

**RUTHENIUM-BASED MODEL CATALYSTS FOR THE LIQUID
PHASE HYDROGENATION OF BIO-BASED ORGANIC ACIDS
AND ALDEHYDES**

By

Xianfeng Ma

A DISSERTATION

**Submitted to
Michigan State University
in partial fulfillment of the requirements
for the degree of**

Chemical Engineering - Doctor of Philosophy

2013

ABSTRACT

RUTHENIUM-BASED MODEL CATALYSTS FOR THE LIQUID PHASE HYDROGENATION OF BIO-BASED ORGANIC ACIDS AND ALDEHYDES

By

Xianfeng Ma

The focus of this thesis was to design heterogeneous ruthenium (Ru)-based catalysts with well-defined structures, and to study the correlation between their structures and their catalytic performance for the liquid phase hydrogenation of bio-derived organic acids and aldehydes.

We evaluated three colloidal-based routes for the preparation of the supported Ru catalysts, and observed that polyol reduction using polymeric stabilizers gave the best results for synthesizing monodisperse colloidal Ru NPs. Sonication-assisted deposition also gave the best results for anchoring the colloidal NPs onto mesoporous silica support (MSU-F). Activation of the supported Ru NPs to remove the stabilizer was explored using three different thermal treatments. The solid catalysts were then characterized and their reactivity was assessed by the aqueous phase hydrogenation of pyruvic acid as a model reaction. These studies showed that argon-protected calcination is the most efficient procedure for activating Ru nanocatalysts on MSU-F support.

We then investigated the effect of particle size on the catalytic performance of the supported Ru NPs, using the liquid phase hydrogenation of cinnamaldehyde (CAL) as the model reaction. Colloidal Ru NPs of various sizes were synthesized by adjusting the polyol reduction parameters. It was observed that the formation of Ru NPs can occur under either thermodynamic or kinetic control, with the final size of the NPs determined by a balance between the two pathways. After

sonication-assisted deposition of the size-tuned Ru NPs on MSU-F and subsequent Ar-protected calcination, we observed well-dispersed Ru NPs on the support with no agglomeration or damage to the ordered structure of the support. The uniformity and crystallinity of the supported Ru NPs in each catalyst also improved with the thermal activation procedure. The hydrogenation of CAL over supported Ru NPs produced cinnamyl alcohol (COL), hydrocinnamaldehyde (HCAL), and hydrocinnamyl alcohol (HCOL), with COL the major product. Varying the size of the NPs did not affect the apparent activation energy or product selectivity, suggesting that the reaction pathway was independent of particle size. However, particle size changed the density of active sites per unit surface area, thus affecting the activity of the catalysts.

Finally, we examined the influence of the metal composition of a series of Ru-Pd bimetallic catalysts on their performance for CAL hydrogenation. The colloidal bimetallic NPs were synthesized by polyol reduction, deposited on MSU-F support by sonication-assisted deposition, and activated through Ar-protected calcination. The NPs in each catalyst were well dispersed on the MSU-F support with an alloyed crystal structure. The bimetallic NPs produced higher turnover frequencies (TOF) for CAL hydrogenation than the monometallic Ru NPs, presumably due to synergetic effects. In contrast to CAL hydrogenation over Ru NPs which produced COL as the major product, the reaction over bimetallic NPs and monometallic Pd NPs produced HCAL or HCOL as the major product, with the ratio of HCAL to HCOL produced dependent on the metal composition of the catalysts.

In summary, this research has provided new routes for the rational design of Ru-based heterogeneous catalysts with well-defined structures, and new insights into the relationship between structure and catalytic performance of Ru-based catalysts for multiphase hydrogenation of bio-based organic acids and aldehydes.

ACKNOWLEDGEMENTS

I would like to express my gratitude to my advisor, Dr. Robert Y. Ofoli, for his support and guidance during my studies over the years. I am thankful to him for the invaluable suggestions he shared with me and for giving me the freedom to try my ideas throughout the research. I would like to thank my committee members, Dr. James E. Jackson, Dr. Dennis J. Miller, and Dr. Sherine O. Obare for their help and guidance throughout my research.

Thanks to the past and current members of the Ofoli Group for their help during my research. I would particularly like to thank Dr. Rui Lin for her collaboration. I also appreciate all the assistance and insights provided by Dr. Lars Peereboom and Dr. Mikhail Y. Redko.

Finally, I would like to express my thanks to my family and friends for their continuous support and encouragement.

TABLE OF CONTENTS

LIST OF TABLES	viii
LIST OF FIGURES	x
Chapter 1	
Introduction and background	1
1.1 Background and motivation	1
1.2 Research objectives	2
1.3 Colloidal routes for design of heterogeneous metal catalysts	3
1.4 Size control of heterogeneous metal catalysts for enhanced reactivity and selectivity	4
1.5 Assessment of supported bimetallic catalysts for reactivity and selectivity	5
1.6 Scope of this thesis	5
REFERENCES	8
Chapter 2	
Exploration of colloidal-based routes for preparing the supported Ru nanocatalysts	16
Abstract	16
2.1. Introduction	17
2.2. Experimental techniques	18
2.2.1. Inductively coupled plasma atomic emission spectroscopy (ICP-AES)	18
2.2.2. Transmission electron microscopy (TEM)	18
2.2.3. Infrared (IR) Spectroscopy	19
2.2.4. Thermogravimetric/Differential Thermal Analysis (TGA-DTG)	19
2.2.5. X-ray Photoelectron Spectroscopy (XPS)	19
2.2.6. Powder x-ray Diffraction (XRD)	19
2.2.7. Physisorption and chemisorption	20
2.2.8. General procedures for assessing reactivity of the supported NPs	20
2.3. Preparation of well-defined Ru nanocatalysts by thermal decomposition	21
2.3.1. Synthesis of Thioether-Stabilized colloidal Ru NPs	21
2.3.2. Preparation of supported Ru nanocatalysts from Ru-nDS colloidal NPs	22
2.3.3. Reactivity Assessment of Ru-nDS NPs Supported on Activated Charcoal (AC)	24
2.4. Phase-transfer protocol for preparation of well-defined Ru nanocatalysts	26
2.4.1. Phase-transfer synthesis of Amine-Stabilized Ru NPs	26
2.4.2. Preparation of supported Ru nanocatalysts from Ru-ODA colloidal NPs	29
2.4.3. Reactivity Assessment of MSU-F supported Ru-ODA NPs	37
2.5. Preparation of Well-defined Ru Nanocatalysts by Polyol reduction	41
2.5.1. Synthesis of polymer-stabilized Colloidal Ru NPs by Polyol Reduction	41
2.5.2. Preparation of supported Ru nanocatalysts from Ru-PVP colloidal NPs	42

2.5.3. Reactivity Assessment of Ru-PVP NPs supported on MSU-F.....	51
2.6. Summary	55
REFERENCES	57

Chapter 3

Effect of particle size on the liquid phase hydrogenation of cinnamaldehyde, using Ru NPs supported on mesoporous silica (MSU-F)	63
Abstract	63
3.1. Introduction.....	64
3.2. Experimental materials and methods.....	65
3.2.1. Synthesis of size-tunable colloidal Ru NPs	65
3.2.2. Preparation of size-tuned Ru NPs supported on MSU-F.....	67
3.2.3. Characterization of different size groups of Ru NPs supported on MSU-F	67
3.2.4. General procedure for catalytic experiments and assessments	68
3.3. Results and Discussion	69
3.3.1. Conditions used to synthesize size-tunable colloidal Ru NPs	69
3.3.1.1. Effect of poyol reduction temperature.....	70
3.3.1.2. Effect of Ru (II) to Ru (III) precursor ratios	72
3.3.1.3. Influence of adding pre-synthesized NPs (seed-mediated growth).....	76
3.3.1.4. Effect of stabilizer	78
3.3.2. Properties of size-tunable Ru NPs supported on MSU-F	81
3.3.2.1. Morphologies and metal compositions of supported Ru NPs	83
3.3.2.2. Structure of Ru NPs supported on MSU-F.....	86
3.3.2.3. Surface properties of Ru NPs supported on MSU-F	89
3.3.3. Catalytic assessment of CAL hydrogenation over Ru NPs supported on MSU-F	91
3.3.3.1. Determination of reaction rates for CAL hydrogenation over Ru NPs.....	94
3.3.3.2. Mass transfer analysis of CAL hydrogenation over Ru NPs supported on MSU-F.....	96
3.3.3.3. Effect of particle size on the activity of Ru NPs for CAL hydrogenation	98
3.3.3.4. Effect of particle size on the selectivity of Ru NPs for CAL hydrogenation.....	102
3.4. Summary	108
REFERENCES	110

Chapter 4

Effect of compositions of Ru-Pd bimetallic NPs on CAL hydrogenation.....	118
Abstract	118
4.1. Introduction.....	119
4.2. Experimental	120
4.2.1. Synthesis of colloidal Ru-Pd bimetallic NPs	120
4.2.2. Preparation of Ru-Pd bimetallic NPs supported on MSU-F.....	122
4.2.3. Characterization of Ru-Pd bimetallic NPs supported on MSU-F.....	122
4.2.4. General procedure for catalytic experiments	123
4.3. Results and Discussion	124
4.3.1. Synthesis of colloidal Pd NPs and Ru-Pd bimetallic NPs	124
4.3.2. Characterization of Ru-Pd NPs supported on MSU-F.....	128
4.3.2.1. Morphologies and chemical compositions of Ru-Pd NPs supported on MSU-F... 129	

4.3.2.2. Structure of Ru-Pd NPs supported on MSU-F	137
4.3.2.3. Surface properties of Ru-Pd NPs supported on MSU-F.....	141
4.3.3. Catalytic assessment of CAL hydrogenation with Ru-Pd NPs supported on MSU-F	143
4.3.3.1. Effect of metal composition on the activity of Ru-Pd NPs supported on MSU-F .	146
4.3.3.2. Effect of composition on the selectivity of Ru-Pd NPs supported on MSU-F.....	149
4.4. Summary	153
REFERENCES	154
Chapter 5	
Conclusions and suggestions for future research.....	159
5.1. Conclusions.....	159
5.2. Suggestions for future research.....	161
5.2.1. Additional characterization to understand the structure of Ru-Pd bimetallic NPs supported on MSU-F.....	161
5.2.2. Mechanism-based kinetic modeling of CAL hydrogenation over the supported Ru-Pd NPs.....	162
REFERENCES	164
APPENDICES	168
Appendix A Reaction profiles for CAL hydrogenation over different size groups of Ru NPs supported on MSU-F.....	169
A. 1 CAL hydrogenation over the catalyst WD170F-5NM.....	169
A. 2 CAL hydrogenation over Ru catalyst SG30F-6NM	173
A. 3 CAL hydrogenation over Ru catalyst TW10F-25NM	177
A. 4 CAL hydrogenation over Ru catalyst TW12F-67NM	181
A. 5 CAL hydrogenation over Ru catalyst TW16F-94NM	185
Appendix B Reaction profiles for CAL hydrogenation over Ru-Pd bimetallic NPs supported on MSU-F	189
B. 1 CAL hydrogenation over the bimetallic catalyst Pd05RuF	189
B. 2 CAL hydrogenation over the bimetallic catalyst Pd20RuF	190
B. 3 CAL hydrogenation over the bimetallic catalyst Pd40RuF	191
B. 4 CAL hydrogenation over the bimetallic catalyst Pd50RuF	192
B. 5 CAL hydrogenation over the bimetallic catalyst Pd60RuF	193
B. 6 CAL hydrogenation over the bimetallic catalyst Pd80RuF	194
B. 7 CAL hydrogenation over the bimetallic catalyst Pd95RuF	195
B. 8 CAL hydrogenation over the bimetallic catalyst Pd100F	196

LIST OF TABLES

Table 2-1 Comparison of elemental composition and metal dispersion of RuDS-AC-350 and Ru/SiO ₂	23
Table 2-2 Catalytic activities of supported Ru nanocatalysts for PyA hydrogenation	25
Table 2-3 Properties of MSU-F supported Ru-ODA NPs after different thermal treatments	37
Table 2-4 Activities of supported Ru-ODA NPs for PyA hydrogenation	40
Table 2-5 Physical properties Ru-PVP NPs supported on MSU-F after thermal treatments	51
Table 2-6 Activities of Ru-PVP NPs supported on MSU-F for PyA hydrogenation.	54
Table 3-1 Reaction progression for the synthesis of Ru NPs at different temperatures.	71
Table 3-2 Summary of reaction conditions for synthesis of Ru NPs by seed-mediated growth. .	77
Table 3-3 A summary of colloidal Ru NPs used to prepare supported Ru catalysts.	82
Table 3-4 Chemical compositions and average size of Ru-PVP NPs supported on MSU-F.....	86
Table 3-5 Ru content and textural properties of the size-tuned Ru NPs supported on MSU-F....	89
Table 3-6 A list of reaction conditions for CAL hydrogenation over Ru NPs in different size groups supported on MSU-F.....	91
Table 3-7 Regression coefficients of substrate concentration against reaction time for CAL hydrogenation over the catalyst SG30F-6NM.....	96
Table 3-8 parameters and observable modulus for intra-particle mass transfer analysis.	98
Table 4-1 Metal concentrations in precursor solution for synthesis of Ru-Pd bimetallic NPs...	121
Table 4-2 A list of colloidal Ru-Pd NPs used to prepare catalysts supported on MSU-F	128
Table 4-3 Chemical compositions and average size of MSU-F supported Ru-Pd NPs.....	133
Table 4-4 Chemisorption and physisorption results of MSU-F supported Ru-Pd NPs	141

Table 4-5 Summary of reaction conditions for CAL hydrogenation over Ru-Pd NPs supported on MSU-F 144

Table 4-6 Regression coefficients of substrate concentration versus reaction time for CAL hydrogenation over the catalyst Pd50RuF.. 145

LIST OF FIGURES

Figure 2-1 TEM images of Ru- <i>n</i> DS NPs synthesized via thermal decomposition.....	22
Figure 2-2 TEM images of Ru- NPs supported on AC (RuDS-AC-350).....	23
Figure 2-3 Reaction profiles of PyA hydrogenation over Ru- <i>n</i> DS NPs supported on AC.....	25
Figure 2-4 Illustration of the phase-transfer method for synthesizing ODA-stabilized Ru NPs..	27
Figure 2-5 TEM images of Ru-ODA NPs synthesized by phase-transfer.	28
Figure 2-6 TEM images of Ru-ODA NPs supported on MSU-F, after different thermal treatments.....	30
Figure 2-7 IR spectra of ODA, MSU-F, and supported Ru-ODA NPs after different thermal treatments.....	31
Figure 2-8 TGA and DTG diagrams of MSU-F, ODA, and supported Ru-ODA NPs after different thermal treatments.....	33
Figure 2-9 XRD patterns of pure MSU-F and supported Ru-ODA NPs after different thermal treatments.....	34
Figure 2-10 XPS spectra of supported Ru–ODA NPs after different thermal treatments.	35
Figure 2-11 Reaction profiles during PyA hydrogenation over Ru-ODA NPs supported on MSU-F..	39
Figure 2-12 TEM images and EDS spectra for Ru-PVP NPs.....	42
Figure 2-13 TEM images of pure MSU-F and MSU-F-supported Ru-PVP NPs..	43
Figure 2-14 FTIR spectra of MSU-F, PVP, and Ru-PVP NPs supported on MSU-F..	44
Figure 2-15 TGA analysis of MSU-F, PVP, and MSU-F supported Ru-PVP NPs.....	46
Figure 2-16 XRD patterns of pure MSU-F and MSU-F supported Ru-PVP NPs after thermal treatment..	47
Figure 2-17 XPS spectra of MSU-F supported Ru-PVP NPs after thermal treatments.....	49

Figure 2-18 Reaction profiles of PyA hydrogenation over Ru-PVP NPs supported on MSU-F..	53
Figure 3-1 Typical TEM images of Ru NPs synthesized at different temperatures..	72
Figure 3-2 Typical TEM images of Ru NPs synthesized at different molar fractions of Ru (II) salt in the precursor solution..	74
Figure 3-3 Average diameter of PVP-Ru NPs as a function of Ru(II) mole fraction (mol%) in the precursor mixture..	76
Figure 3-4 TEM images of Ru NPs synthesized via seed-mediated growth..	78
Figure 3-5 HRTEM images of Ru NPs synthesized at different PVP/precursor ratios and their size distributions ..	80
Figure 3-6 HRTEM images of the size distribution of Ru NPs stabilized by different molecular weights of PVP polymers.....	81
Figure 3-7 FTIR spectra of MSU-F, PVP, and the size-tuned Ru NPs supported on MSU-F.....	83
Figure 3-8 Representative HRTEM images of size-tuned Ru NPs supported on MSU-F.....	84
Figure 3-9 Power XRD pattern of the size-tuned Ru NPs supported on MSU-F.	87
Figure 3-10 SAED patterns of size-tuned Ru NPs supported on MSU-F.....	88
Figure 3-11 Typical reaction profiles for CAL hydrogenation over Ru NPs supported on MSU-F.	93
Figure 3-12 Reaction profiles for CAL hydrogenation over SG30F-6NM and the corresponding regression curves.....	95
Figure 3-13 The activities of each catalyst as a function of initial substrate concentration..	100
Figure 3-14 The activity of Ru NPs for CAL hydrogenation as a function of initial substrate concentration.....	100
Figure 3-15 Projected optimal adsorption configuration for CAL over a Ru (0001) surface....	101
Figure 3-16 Arrhenius plots for CAL hydrogenation over - Ru NPs of different sizes supported on MSU-F.	102
Figure 3-17 Product selectivity as a function of substrate conversion for CAL hydrogenation over Ru NPs supported on MSU-F.	104

Figure 3-18 Product selectivity as a function of the size of Ru NPs supported on MSU-F..	105
Figure 3-19 Arrhenius plots for the production of HCAL and COL over Ru NPs of different sizes supported on MSU-F.....	107
Figure 4-1 Typical TEM images of colloidal Ru-Pd NPs synthesized with Ru(II) as precursor..	125
Figure 4-2 Typical TEM images of colloidal Ru-Pd NPs synthesized with Ru(III) as Ru precursor.	126
Figure 4-3 EDS spectra of colloidal Ru-Pd NPs.....	127
Figure 4-4 FTIR spectra of MSU-F, PVP, and Ru-Pd NPs supported on MSU-F..	129
Figure 4-5 Typical TEM images of Ru-Pd NPs supported on MSU-F.....	130
Figure 4-6 EDS analysis of Ru-Pd NPs supported on MSU-F.	134
Figure 4-7 XRD patterns of Ru-Pd bimetallic NPs and monometallic Pd NPs supported on MSU-F.	137
Figure 4-8 SAED patterns and HRTEM images of Ru-Pd NPs supported on MSU-F..	138
Figure 4-9 CO-TPD spectra of Ru-Pd NPs supported on MSU-F.....	143
Figure 4-10 Reaction profile for CAL hydrogenation over Pd ₅₀ RuF and the corresponding regression curves.....	145
Figure 4-11 Catalytic activity as a function of Pd fraction for CAL hydrogenation over Ru-Pd NPs supported on MSU-F.....	146
Figure 4-12 TOF as a function of Pd fraction for CAL hydrogenation over Ru-Pd NPs supported on MSU-F.	147
Figure 4-13 Arrhenius pots for CAL hydrogenation over bimetallic and monometallic NPs supported on MSU-F.....	148
Figure 4-14 Product selectivity as a function of substrate conversion for CAL hydrogenation over Ru-Pd NPs supported on MSU-F.....	150
Figure 4-15 Product selectivity as a function of Pd fraction in the bimetallic NPs for CAL hydrogenation..	152
Figure A.1-1 Reaction profiles for CAL hydrogenation under reaction temperature of 45°C ..	169

Figure A.1-2	Reaction profiles for CAL hydrogenation under reaction temperature of 65°C..	170
Figure A.1-3	Reaction profiles for CAL hydrogenation under reaction temperature of 85°C..	170
Figure A.1-4	Reaction profiles for CAL hydrogenation under reaction temperature of 105°C.	171
Figure A.1-5	Reaction profiles for CAL hydrogenation under reaction temperature of 125°C.	172
Figure A.2-1	Reaction profiles for CAL hydrogenation under reaction temperature of 45°C...	173
Figure A.2-2	Reaction profiles for CAL hydrogenation under reaction temperature of 65°C...	173
Figure A.2-3	Reaction profiles for CAL hydrogenation under reaction temperature of 85°C...	174
Figure A.2-4	Reaction profiles for CAL hydrogenation under reaction temperature of 105°C.	175
Figure A.2-5	Reaction profiles for CAL hydrogenation under reaction temperature of 125°C.	176
Figure A.3-1	Reaction profiles for CAL hydrogenation under reaction temperature of 45°C..	177
Figure A.3-2	Reaction profiles for CAL hydrogenation under reaction temperature of 65°C..	177
Figure A.3-3	Reaction profiles for CAL hydrogenation under reaction temperature of 85°C..	178
Figure A.3-4	Reaction profiles for CAL hydrogenation under reaction temperature of 105°C.	179
Figure A.3-5	Reaction profiles for CAL hydrogenation under reaction temperature of 125°C.	180
Figure A.4-1	Reaction profiles for CAL hydrogenation under reaction temperature of 45°C..	181
Figure A.4-2	Reaction profiles for CAL hydrogenation under reaction temperature of 65°C..	181
Figure A.4-3	Reaction profiles for CAL hydrogenation under reaction temperature of 85°C..	182
Figure A.4-4	Reaction profiles for CAL hydrogenation under reaction temperature of 105°C.	183
Figure A.4-5	Reaction profiles for CAL hydrogenation under reaction temperature of 125°C.	184
Figure A.5-1	Reaction profiles for CAL hydrogenation under reaction temperature of 45°C..	185
Figure A.5-2	Reaction profiles for CAL hydrogenation under reaction temperature of 65°C..	185
Figure A.5-3	Reaction profiles for CAL hydrogenation under reaction temperature of 85°C..	186
Figure A.5-4	Reaction profiles for CAL hydrogenation under reaction temperature of 105°C.	187

Figure A.5-5 Reaction profiles for CAL hydrogenation under temperature of 125°C.....	188
Figure B.1-1 Reaction profiles for CAL hydrogenation over the catalyst Pd05RuF.....	189
Figure B.2-1 Reaction profiles for CAL hydrogenation over the catalyst Pd20RuF.....	190
Figure B.3-1 Reaction profiles for CAL hydrogenation over the catalyst Pd40RuF.....	191
Figure B.4-1 Reaction profiles for CAL hydrogenation over the catalyst Pd50RuF.....	192
Figure B.5-1 Reaction profiles for CAL hydrogenation over the catalyst Pd60RuF.....	193
Figure B.6-1 Reaction profiles for CAL hydrogenation over the catalyst Pd80RuF.....	194
Figure B.7-1 Reaction profiles for CAL hydrogenation over the catalyst Pd95RuF.....	195
Figure B.8-1 Reaction profiles for CAL hydrogenation over the catalyst Pd100F.	196

Chapter 1 Introduction and background

1.1 Background and motivation

Biomass is a promising class of alternative resources for the production of fuels and value-added chemicals because it has the advantage of being renewable and potentially carbon-neutral. It also offers worldwide accessibility as opposed to fossil reserves, and allows for a variety of chemical transformations.¹⁻³ The general approach for biomass conversion to useful product involves two major steps: conversion of biomass to a variety of platform molecules, and transformation of the platform molecules to either fuel or value-added chemicals. Heterogeneous catalysis is at the heart of the integrated processes for the transformation of biomass. It is generally recognized that the primary factor limiting the catalytic conversion of biorenewable feedstock is the lack of efficient catalysts.⁴⁻⁸

A comprehensive molecular level understanding of catalytic processes is vital to the design of more efficient catalysts. Typical heterogeneous metal catalysts are composed of highly porous supports containing finely dispersed active materials in the form of nanoparticles (NPs).⁹ A good control of structures and composition of the active materials is important to enable more insight into the catalytic reaction process, and has the potential to promote better assessment of the mechanisms of heterogeneous catalysis in a rational manner.¹⁰⁻¹³ However, conventional processes used for preparing heterogeneous catalysts often lead to ill-defined morphologies as well as uneven distributions of active sites on the supports. This generally leads to difficulties in investigating the nature of the catalytic sites at the molecular scale, because they are not ideal catalytic model systems for fundamental studies.¹⁴⁻¹⁶

Recent advances in materials science and nanotechnology have offered promising ways to prepare well-defined heterogeneous catalysts via *in situ* colloidal schemes. With this route, the synthesis of NPs and their deposition on support(s) are separated into two successive steps. The separation of particle synthesis and subsequent deposition onto supports enables independent control of the morphology and composition of the active materials. This separation also provides a high degree of flexibility for particle dispersion on different supports, and produces well-structured catalysts with high densities of specific atomic ensembles as well as the rational design of tunable active sites, which is not possible with conventional catalyst preparation methods.¹⁴⁻¹⁸ Therefore, the incorporation of nanotechnology into heterogeneous catalyst design makes it possible to advance the molecular-level understanding of heterogeneous catalysis. Although this approach is still in its infancy, it has attracted considerable attention, as demonstrated by the increasing number of publications.¹⁷

1.2 Research objectives

The primary objective of this project was to rationally design heterogeneous ruthenium (Ru)-based catalysts for assessment of the correlation between catalyst structure and catalytic performance, using the liquid-phase hydrogenation of bio-derived organic acids and aldehydes as model reactions. Bio-derived organic acids and α , β -unsaturated carbonyls are important building blocks for the production of a number of valuable chemicals used in the manufacturing of polymers, pharmaceuticals, foods, and other commodity materials.¹⁹ In the following sections of this chapter, we will provide a brief survey of the literature relevant to this project.

1.3 Colloidal routes for design of heterogeneous metal catalysts

In the colloidal-based route for preparation of heterogeneous metal catalysts, colloidal metal NPs with well-defined size and shape are first synthesized via a “bottom-up” approach, which involves the formation of metal atoms from the reduction or decomposition of metal precursors, and subsequent agglomeration of atoms to form NPs of a particular size.^{18,20} A liquid phase chemical method is one of the most widely used procedures among the “bottom-up” approaches. Generally, this method can be classified into three main categories: chemical reduction of metal salts, thermal (also photochemical or sonochemical) decomposition of organometallic compounds, and ligand displacement from organometallic compounds.²¹⁻²⁶

The next step in the colloidal route for catalyst preparation is to disperse the colloidal metal NPs onto suitable high-surface-area supports and to achieve clean metal surfaces by activating the supported NPs to remove the organic material used to stabilize the particles in solution.^{27,28}

Common supports include ceramics, metal oxides, silica, carbonaceous materials, and membranes.²⁹⁻³¹ With new advances in materials science, structured supports have attracted more attention in the preparation of heterogeneous catalysts due to their advantages over conventional supports.^{18,20} For instance, their pores and cavities can be precisely regulated at the micro- or nanoscale as needed to deposit nanoparticles of different sizes and shapes.

Although colloidal metal NPs have already been used extensively for quasi-homogeneous catalysis, application of colloidal-based routes for preparation of heterogeneous metal catalysts is still limited.¹⁶ One possible reason for this is the challenge of removing the capping agent used in catalyst fabrication without adversely affecting particle morphology and/or dispersion.

This is a significant challenge because these organic molecules are bound strongly to the particle surface at approximately monolayer coverage. The effective removal of the stabilizer from the catalysts is a subject of many ongoing studies.^{15,16,18,32-35}

1.4 Size control of heterogeneous metal catalysts for enhanced reactivity and selectivity

Understanding the correlation between particle size and the catalytic activity of noble metallic nanoparticles (NPs) is an important area of fundamental catalysis research.³⁶⁻⁴¹ For metal NPs less than 100 nm in size, variation in particle size may change the surface to bulk atom ratios, crystal facets, and corner or edge locations,⁴²⁻⁴⁴ which may lead to changes in their physical and chemical properties.^{39,45} Recent studies have shown that the change in particle size leads to essentially different active site geometries and site distributions, thus influencing catalytic properties, particularly for structure-sensitive catalytic reactions such as alkane isomerization, ammonia synthesis, and hydrogenation of unsaturated hydrocarbons.^{13,32,39,46-63}

The effect of the size of Ru NPs on catalytic properties has been investigated for ammonia synthesis and decomposition reactions.⁶⁰⁻⁶³ The correlation between size and activity of Ru NPs less than 10 nm was estimated theoretically by assuming hexagonal Ru NPs that only expose some specific surface facets during the reactions. A number of experiments have also shown that intermediate-sized Ru NPs have maximum specific activity for ammonia synthesis.⁶⁰⁻⁶³ Another study on correlating Ru NP size to catalytic activity was on Ru-catalyzed carbon monoxide oxidation.³⁸ In that study, monodisperse Ru NPs ranging from 2 to 6 nm were synthesized and

their activity for CO oxidation was measured as a function of particle size. The authors concluded that activity increased with particle size.

1.5 Assessment of supported bimetallic catalysts for reactivity and selectivity

The interest in studying bimetallic catalysts, which consist of two different metal elements, is because they often exhibit electronic and chemical properties distinct from either of their constituent metals. They also promote enhanced selectivity, activity, and stability compared to either of the monometallic catalyst.^{57,59,64-72} These findings, reported after the first industrial applications in the 1960s for hydrocarbon reforming, have inspired extensive investigations on their possible applications.⁷³⁻⁷⁵ Currently, bimetallic catalysts are widely utilized in many catalytic processes, including conversion of biorenewables.^{8,11,67,76-79} From a fundamental point of view, exploring bimetallic catalysts allows a better understanding of the mechanisms and variables involved in their catalytic reactions, which is important for the design of new catalysts.⁸⁰⁻⁸⁷

1.6 Scope of this thesis

This research is concerned with the reactivity and selectivity of heterogeneous Ru-based model catalysts of different sizes and compositions used for the hydrogenation of organic acids and α , β -unsaturated aldehydes. In the next chapter (Chapter 2), we discuss three approaches for the preparation of supported Ru catalysts with well-defined morphology, and the procedures for assessing reactivity of the catalysts. We also present the general experimental techniques used in this research. In Chapter 3, we present a comprehensive study on synthesis conditions for

producing size-tunable Ru NPs ranging in size from 3.5 to 100 nm, the deposition of Ru NPs of different sizes on mesoporous silica support (MSU-F), and their activation and characterization. We then discuss assessments of the dependence of reactivity on the size of the Ru nanoparticles, using the liquid phase hydrogenation of cinnamaldehyde as the model reaction. The effects of size on a number of kinetic parameters were also considered, including reactivity, selectivity, and activation energies.

In chapter 4, we discuss the synthesis of a series of Ru-Pd bimetallic catalysts with different metal compositions for deposition on mesoporous silica (MSU-F). The liquid phase hydrogenation of cinnamaldehyde (CAL) was used as the model reaction to investigate the effect of composition on a number of kinetic parameters.

Chapter 5 gives a summary of the study as well as the major conclusions. We also suggest some areas for further research, based on the potential for additional insights into using Ru-based catalysts for the liquid phase hydrogenation of bio-derived molecules.

REFERENCES

REFERENCES

- (1) Corma, A.; Iborra, S.; Velty, A. Chemical routes for the transformation of biomass into chemicals. *Chemical Reviews*, 2007, *107*, 2411-2502.
- (2) Dapsens, P. Y.; Mondelli, C.; Perez-Ramirez, J. Biobased Chemicals from Conception toward Industrial Reality: Lessons Learned and To Be Learned. *Acs Catalysis*, 2012, *2*, 1487-1499.
- (3) Serrano-Ruiz, J. C.; Luque, R.; Sepulveda-Escribano, A. Transformations of biomass-derived platform molecules: from high added-value chemicals to fuels via aqueous-phase processing. *Chemical Society Reviews*, 2011, *40*, 5266-5281.
- (4) Alonso, D. M.; Bond, J. Q.; Dumesic, J. A. Catalytic conversion of biomass to biofuels. *Green Chemistry*, 2010, *12*, 1493-1513.
- (5) Norskov, J. K.; Abild-Pedersen, F.; Studt, F.; Bligaard, T. Density functional theory in surface chemistry and catalysis. *Proceedings of the National Academy of Sciences of the United States of America*, 2011, *108*, 937-943.
- (6) Fernando, S.; Adhikari, S.; Chandrapal, C.; Murali, N. Biorefineries: Current status, challenges, and future direction. *Energy & Fuels*, 2006, *20*, 1727-1737.
- (7) Gabriele Centi, R. A. v. S. Catalysis for Renewables: From Feedstock to Energy Production. *Wiley-VCH*, 2007.
- (8) Lin, Y. C.; Huber, G. W. The critical role of heterogeneous catalysis in lignocellulosic biomass conversion. *Energy & Environmental Science*, 2009, *2*, 68-80.
- (9) C. H. Bartholomew, R. J. F. Fundamentals of Industrial Catalytic Processes, 2nd Edition. *Wiley-AIChE; 2 edition (October 28, 2005)* 2005.
- (10) Nolte, P.; Stierle, A.; Jin-Phillipp, N. Y.; Kasper, N.; Schulli, T. U.; Dosch, H. Shape changes of supported Rh nanoparticles during oxidation and reduction cycles. *Science*, 2008, *321*, 1654-1658.
- (11) Tian, N.; Zhou, Z. Y.; Sun, S. G.; Ding, Y.; Wang, Z. L. Synthesis of tetrahedral platinum nanocrystals with high-index facets and high electro-oxidation activity. *Science*, 2007, *316*, 732-735.
- (12) Feldheim, D. L. The new face of catalysis. *Science*, 2007, *316*, 699-700.

- (13) Somorjai, G. A.; Tao, F.; Park, J. Y. The nanoscience revolution: Merging of colloid science, catalysis and nanoelectronics. *Topics in Catalysis*, 2008, 47, 1-14.
- (14) Albiter, M. A.; Morales, R.; Zaera, F. Dendrimer-based synthesis of Pt catalysts for hydrocarbon conversion. *Applied Catalysis a-General*, 2011, 391, 386-393.
- (15) Zaera, F. The New Materials Science of Catalysis: Toward Controlling Selectivity by Designing the Structure of the Active Site. *Journal of Physical Chemistry Letters*, 1, 621-627.
- (16) Sonstrom, P.; Baumer, M. Supported colloidal nanoparticles in heterogeneous gas phase catalysis: on the way to tailored catalysts. *Physical Chemistry Chemical Physics*, 2011, 13, 19270-19284.
- (17) Zahmakiran, M.; Ozkar, S. Metal nanoparticles in liquid phase catalysis; from recent advances to future goals. *Nanoscale*, 2011, 3, 3462-3481.
- (18) Jia, C. J.; Schuth, F. Colloidal metal nanoparticles as a component of designed catalyst. *Physical Chemistry Chemical Physics*, 2011, 13, 2457-2487.
- (19) Varadarajan, S.; Miller, D. J. Catalytic upgrading of fermentation-derived organic acids. *Biotechnology Progress*, 1999, 15, 845-854.
- (20) Maki-Arvela, P.; Hajek, J.; Salmi, T.; Murzin, D. Y. Chemoselective hydrogenation of carbonyl compounds over heterogeneous catalysts. *Applied Catalysis a-General*, 2005, 292, 1-49.
- (21) Daniel, M. C.; Astruc, D. Gold nanoparticles: Assembly, supramolecular chemistry, quantum-size-related properties, and applications toward biology, catalysis, and nanotechnology. *Chemical Reviews*, 2004, 104, 293-346.
- (22) Park, J.; Joo, J.; Kwon, S. G.; Jang, Y.; Hyeon, T. Synthesis of monodisperse spherical nanocrystals. *Angewandte Chemie-International Edition*, 2007, 46, 4630-4660.
- (23) Wilcoxon, J. P.; Abrams, B. L. Synthesis, structure and properties of metal nanoclusters. *Chemical Society Reviews*, 2006, 35, 1162-1194.
- (24) Zhang, Q. B.; Xie, J. P.; Yu, Y.; Lee, J. Y. Monodispersity control in the synthesis of monometallic and bimetallic quasi-spherical gold and silver nanoparticles. *Nanoscale*, 2010, 2, 1962-1975.
- (25) Xu, H. X.; Suslick, K. S. Sonochemical Synthesis of Highly Fluorescent Ag Nanoclusters. *Acs Nano*, 2010, 4, 3209-3214.
- (26) Zhou, T. Y.; Rong, M. C.; Cai, Z. M.; Yang, C. Y. J.; Chen, X. Sonochemical synthesis of highly fluorescent glutathione-stabilized Ag nanoclusters and S2- sensing. *Nanoscale*, 2012, 4, 4103-4106.

- (27) Lee, I.; Morales, R.; Albiter, M. A.; Zaera, F. Synthesis of heterogeneous catalysts with well shaped platinum particles to control reaction selectivity. *Proceedings of the National Academy of Sciences of the United States of America*, 2008, *105*, 15241-15246.
- (28) Zaera, F. Nanostructured materials for applications in heterogeneous catalysis. *Chemical Society Reviews*, 2012.
- (29) Narayanan, R.; El-Sayed, M. A. Carbon-supported spherical palladium nanoparticles as potential recyclable catalysts for the Suzuki reaction. *Journal of Catalysis*, 2005, *234*, 348-355.
- (30) Campelo, J. M.; Luna, D.; Luque, R.; Marinas, J. M.; Romero, A. A. Sustainable Preparation of Supported Metal Nanoparticles and Their Applications in Catalysis. *ChemSuschem*, 2009, *2*, 18-45.
- (31) White, R. J.; Luque, R.; Budarin, V. L.; Clark, J. H.; Macquarrie, D. J. Supported metal nanoparticles on porous materials. Methods and applications. *Chemical Society Reviews*, 2009, *38*, 481-494.
- (32) Kuhn, J. N.; Tsung, C. K.; Huang, W.; Somorjai, G. A. Effect of organic capping layers over monodisperse platinum nanoparticles upon activity for ethylene hydrogenation and carbon monoxide oxidation. *Journal of Catalysis*, 2009, *265*, 209-215.
- (33) Rast, L.; Stanishevsky, A. Aggregated nanoparticle structures prepared by thermal decomposition of poly(vinyl)-N-pyrrolidone/Ag nanoparticle composite films. *Applied Physics Letters*, 2005, *87*.
- (34) Zawadzki, M.; Okal, J. Synthesis and structure characterization of Ru nanoparticles stabilized by PVP or gamma-Al₂O₃. *Materials Research Bulletin*, 2008, *43*, 3111-3121.
- (35) Jurgens, B.; Borchert, H.; Ahrenstorf, K.; Sonstrom, P.; Pretorius, A.; Schowalter, M.; Gries, K.; Zielasek, V.; Rosenauer, A.; Weller, H.; Baumer, M. Colloidally Prepared Nanoparticles for the Synthesis of Structurally Well-Defined and Highly Active Heterogeneous Catalysts. *Angewandte Chemie-International Edition*, 2008, *47*, 8946-8949.
- (36) Bezemer, G. L.; Bitter, J. H.; Kuipers, H.; Oosterbeek, H.; Holewijn, J. E.; Xu, X. D.; Kapteijn, F.; van Dillen, A. J.; de Jong, K. P. Cobalt particle size effects in the Fischer-Tropsch reaction studied with carbon nanofiber supported catalysts. *Journal of the American Chemical Society*, 2006, *128*, 3956-3964.
- (37) Zhang, Y. W.; Grass, M. E.; Habas, S. E.; Tao, F.; Zhang, T. F.; Yang, P. D.; Somorjai, G. A. One-step polyol synthesis and langmuir-blodgett monolayer formation of size-tunable monodisperse rhodium nanocrystals with catalytically active (111) surface structures. *Journal of Physical Chemistry C*, 2007, *111*, 12243-12253.

- (38) Joo, S. H.; Park, J. Y.; Renzas, J. R.; Butcher, D. R.; Huang, W. Y.; Somorjai, G. A. Size Effect of Ruthenium Nanoparticles in Catalytic Carbon Monoxide Oxidation. *Nano Letters*, 10, 2709-2713.
- (39) Van Santen, R. A. Complementary Structure Sensitive and Insensitive Catalytic Relationships. *Accounts of Chemical Research*, 2009, 42, 57-66.
- (40) Jin, R. The impacts of nanotechnology on catalysis by precious metal nanoparticles. *Nanotechnology Reviews*, 2012, 1, 31-56.
- (41) Yang, F.; Zhang, Q. F.; Liu, Y. W.; Chen, S. L. A Theoretical Consideration on the Surface Structure and Nanoparticle Size Effects of Pt in Hydrogen Electrocatalysis. *Journal of Physical Chemistry C*, 2011, 115, 19311-19319.
- (42) Semagina, N.; Kiwi-Minsker, L. Recent Advances in the Liquid-Phase Synthesis of Metal Nanostructures with Controlled Shape and Size for Catalysis. *Catalysis Reviews-Science and Engineering*, 2009, 51, 147-217.
- (43) Halperin, W. P. Quantum size effects in metal particles. *Reviews of Modern Physics*, 1986, 58, 533-606.
- (44) Kleis, J.; Greeley, J.; Romero, N. A.; Morozov, V. A.; Falsig, H.; Larsen, A. H.; Lu, J.; Mortensen, J. J.; Dulak, M.; Thygesen, K. S.; Norskov, J. K.; Jacobsen, K. W. Finite Size Effects in Chemical Bonding: From Small Clusters to Solids. *Catalysis Letters*, 2011, 141, 1067-1071.
- (45) Maillard, F. Fuel Cell Catalysis. *John Wiley & Sons, Inc. New York*, 2009, 507-568.
- (46) Somorjai, G. A.; Frei, H.; Park, J. Y. Advancing the Frontiers in Nanocatalysis, Biointerfaces, and Renewable Energy Conversion by Innovations of Surface Techniques. *Journal of the American Chemical Society*, 2009, 131, 16589-16605.
- (47) Somorjai, G. A.; Li, Y. M. Major Successes of Theory-and-Experiment-Combined Studies in Surface Chemistry and Heterogeneous Catalysis. *Topics in Catalysis*, 2010, 53, 311-325.
- (48) Murzin, D. Y.; Simakova, I. L. On quantitative description of metal particles size effect in catalytic kinetics. *Kinetics and Catalysis*, 2010, 51, 828-831.
- (49) Che, M. The Influence of Particle Size on the Catalytic Properties of Supported Metals. *Advances in Catalysis*, 1989, 36, 55-172.
- (50) Li, Y.; Liu, Q. Y.; Shen, W. J. Morphology-dependent nanocatalysis: metal particles. *Dalton Transactions*, 2011, 40, 5811-5826.

(51) Zaera, F. Probing catalytic reactions at surfaces. *Progress in Surface Science*, 2001, 69, 1-98.

(52) Rarog-Pilecka, W.; Miskiewicz, E.; Szmigiel, D.; Kowalczyk, Z. Structure sensitivity of ammonia synthesis over promoted ruthenium catalysts supported on graphitised carbon. *Journal of Catalysis*, 2005, 231, 11-19.

(53) Zhang, C. J.; Liu, Z. P.; Hu, P. Stepwise addition reactions in ammonia synthesis: A first principles study. *Journal of Chemical Physics*, 2001, 115, 609-611.

(54) Honkala, K.; Hellman, A.; Remediakis, I. N.; Logadottir, A.; Carlsson, A.; Dahl, S.; Christensen, C. H.; Norskov, J. K. Ammonia synthesis from first-principles calculations. *Science*, 2005, 307, 555-558.

(55) Borodzinski, A. The effect of palladium particle size on the kinetics of hydrogenation of acetylene-ethylene mixtures over Pd/SiO₂ catalysts. *Catalysis Letters*, 2001, 71, 169-175.

(56) Borodzinski, A.; Bond, G. C. Selective hydrogenation of ethyne in ethene-rich streams on palladium catalysts, Part 2: Steady-state kinetics and effects of palladium particle size, carbon monoxide, and promoters. *Catalysis Reviews-Science and Engineering*, 2008, 50, 379-469.

(57) McClure, S. M.; Lundwall, M. J.; Goodman, D. W. Planar oxide supported rhodium nanoparticles as model catalysts. *Proceedings of the National Academy of Sciences of the United States of America*, 2011, 108, 931-936.

(58) Gavnholt, J.; Schiotz, J. Structure and reactivity of ruthenium nanoparticles. *Phys. Rev. B*, 2008, 77.

(59) Hellman, A.; Baerends, E. J.; Biczysko, M.; Bligaard, T.; Christensen, C. H.; Clary, D. C.; Dahl, S.; van Harrevelt, R.; Honkala, K.; Jonsson, H.; Kroes, G. J.; Luppi, M.; Manthe, U.; Norskov, J. K.; Olsen, R. A.; Rossmeisl, J.; Skulason, E.; Tautermann, C. S.; Varandas, A. J. C.; Vincent, J. K. Predicting catalysis: Understanding ammonia synthesis from first-principles calculations. *Journal of Physical Chemistry B*, 2006, 110, 17719-17735.

(60) Jacobsen, C. J. H.; Dahl, S.; Hansen, P. L.; Tornqvist, E.; Jensen, L.; Topsoe, H.; Prip, D. V.; Moenshaug, P. B.; Chorkendorff, I. Structure sensitivity of supported ruthenium catalysts for ammonia synthesis. *Journal of Molecular Catalysis a-Chemical*, 2000, 163, 19-26.

(61) Rarog-Pilecka, W.; Smigiel, D.; Komornicki, A.; Zielinski, J.; Kowalczyk, Z. Catalytic properties of small ruthenium particles deposited on carbon - Ammonia decomposition studies. *Carbon*, 2003, 41, 589-591.

- (62) Zheng, W. Q.; Zhang, J.; Xu, H. Y.; Li, W. Z. NH₃ decomposition kinetics on supported Ru clusters: Morphology and particle size effect. *Catalysis Letters*, 2007, *119*, 311-318.
- (63) Garcia-Garcia, F. R.; Guerrero-Ruiz, A.; Rodriguez-Ramos, I. Role of B5-Type Sites in Ru Catalysts used for the NH₃ Decomposition Reaction. *Topics in Catalysis*, 2009, *52*, 758-764.
- (64) Berlowitz, P. J.; Goodman, D. W. The adsorption of hydrogen and carbon monoxide on strained nickel overlayers on tungsten(110) and tungsten(100). *Surf. Sci.*, 1987, *187*, 463-480.
- (65) Berlowitz, P. J.; Houston, J. E.; White, J. M.; Goodman, D. W. Properties of monolayer and multilayer nickel films on the ruthenium(0001) surface. *Surf. Sci.*, 1988, *205*, 1-11.
- (66) Chen, J. G.; Menning, C. A.; Zellner, M. B. Monolayer bimetallic surfaces: Experimental and theoretical studies of trends in electronic and chemical properties. *Surf. Sci. Rep.*, 2008, *63*, 201-254.
- (67) Alayoglu, S.; Nilekar, A. U.; Mavrikakis, M.; Eichhorn, B. Ru-Pt core-shell nanoparticles for preferential oxidation of carbon monoxide in hydrogen. *Nat. Mater.*, 2008, *7*, 333-338.
- (68) Besenbacher, F.; Chorkendorff, I.; Clausen, B. S.; Hammer, B.; Molenbroek, A. M.; Norskov, J. K.; Stensgaard, I. Design of a surface alloy catalyst for steam reforming. *Science (Washington, D. C.)*, 1998, *279*, 1913-1915.
- (69) He, B. L.; Chen, Y. X.; Liu, H. F.; Liu, Y. Synthesis of solvent-stabilized colloidal nanoparticles of platinum, rhodium, and ruthenium by microwave-polyol process. *Journal of Nanoscience and Nanotechnology*, 2005, *5*, 266-270.
- (70) Enache, D. I.; Edwards, J. K.; Landon, P.; Solsona-Espriu, B.; Carley, A. F.; Herzing, A. A.; Watanabe, M.; Kiely, C. J.; Knight, D. W.; Hutchings, G. J. Solvent-Free Oxidation of Primary Alcohols to Aldehydes Using Au-Pd/TiO₂ Catalysts. *Science (Washington, DC, U. S.)*, 2006, *311*, 362-365.
- (71) Norskov, J. K. Surface chemistry: Catalysis frozen in time. *Nature (London, U. K.)*, 2001, *414*, 405-406.
- (72) Norskov, J. K. Catalysis frozen in time. *Nature*, 2001, *414*, 405-406.
- (73) Sinfelt, J. H. Catalysis by alloys and bimetallic clusters. *Acc. Chem. Res.*, 1977, *10*, 15-20.

- (74) Sinfelt, J. H. Three Decades of Catalysis by Metals. Chemistry and Physics of Solid Surfaces VI. *Springer Series in Surface Sciences*, 1986, 5, 19-47.
- (75) Sinfelt, J. H. Bimetallic Catalysts: Discoveries, Concepts and Applications. *John Wiley and Sons, New York*, 1983.
- (76) Knudsen, J.; Nilekar, A. U.; Vang, R. T.; Schnadt, J.; Kunkes, E. L.; Dumesic, J. A.; Mavrikakis, M.; Besenbacher, F. A Cu/Pt Near-Surface Alloy for Water-Gas Shift Catalysis. *J. Am. Chem. Soc.*, 2007, 129, 6485-6490.
- (77) Arenz, M.; Mayrhofer, K. J. J.; Stamenkovic, V.; Blizanac, B. B.; Tomoyuki, T.; Ross, P. N.; Markovic, N. M. The effect of the particle size on the kinetics of CO electrooxidation on high surface area Pt catalysts. *Journal of the American Chemical Society*, 2005, 127, 6819-6829.
- (78) Guzzi, L.; Boskovic, G.; Kiss, E. Bimetallic Cobalt Based Catalysts. *Catalysis Reviews-Science and Engineering*, 2010, 52, 133-203.
- (79) Alonso, D. M.; Wettstein, S. G.; Dumesic, J. A. Bimetallic catalysts for upgrading of biomass to fuels and chemicals. *Chemical Society Reviews*, 2012, 41, 8075-8098.
- (80) Jacobs, G.; Ghadiali, F.; Pisanu, A.; Borgna, A.; Alvarez, W. E.; Resasco, D. E. Characterization of the morphology of Pt clusters incorporated in a KL zeolite by vapor phase and incipient wetness impregnation. Influence of Pt particle morphology on aromatization activity and deactivation. *Applied Catalysis a-General*, 1999, 188, 79-98.
- (81) Sikhwivhilu, L. M.; Coville, N. J.; Naresh, D.; Chary, K. V. R.; Vishwanathan, V. Nanotubular titanate supported palladium catalysts: The influence of structure and morphology on phenol hydrogenation activity. *Applied Catalysis a-General*, 2007, 324, 52-61.
- (82) Piccolo, L.; Henry, C. R. NO-CO reaction kinetics on Pd/MgO model catalysts: morphology and support effects. *Journal of Molecular Catalysis a-Chemical*, 2001, 167, 181-190.
- (83) Yanzhe Yua, B. F., Andreas Jentysa, Gary L. Hallera, J.A. Rob van Veenb, Oliver Y. Gutiérreza, Johannes A. Lercher Bimetallic Pt–Pd/silica–alumina hydrotreating catalysts Part I: Physicochemical characterization. *Journal of Catalysis*, 2012, 292, 1-12.
- (84) Campbell, C. T. Bimetallic surface chemistry. *Annu. Rev. Phys. Chem.*, 1990, 41, 775-837.
- (85) Fuggle, J. C.; Madey, T. E.; Steinkilberg, M.; Menzel, D. Photoelectron spectroscopic studies of adsorption of CO and oxygen on Ru(001). *Surface Science*, 1975, 52, 521-541.

(86) Rodriguez, J. A.; Goodman, D. W. The nature of the metal-metal bond in bimetallic surfaces. *Science (Washington, D. C., 1883-)*, 1992, 257, 897-903.

(87) Tao, F.; Grass, M. E.; Zhang, Y. W.; Butcher, D. R.; Aksoy, F.; Aloni, S.; Altoe, V.; Alayoglu, S.; Renzas, J. R.; Tsung, C. K.; Zhu, Z. W.; Liu, Z.; Salmeron, M.; Somorjai, G. A. Evolution of Structure and Chemistry of Bimetallic Nanoparticle Catalysts under Reaction Conditions. *Journal of the American Chemical Society*, 2010, 132, 8697-8703.

Chapter 2: Exploration of colloidal-based routes for preparing the supported Ru nanocatalysts

Abstract

We have evaluated colloidal-based routes for the preparation and activation of supported Ru nanocatalysts. The colloidal Ru NPs were synthesized by thermal decomposition with thioether as stabilizer, a phase-transfer technique with amine as stabilizer, and a polyol reduction protocol with polymers as stabilizer. Of the three protocols, polyol reduction gave the best results for synthesizing monodisperse Ru NPs in high yield in a moderate reaction time over a broad range of reaction temperatures. Sonication-assisted colloidal deposition was also more efficient than direct colloidal deposition for anchoring Ru NPs onto ordered mesoporous silica (MSU-F) support. Activation of the supported Ru NPs to remove the organic stabilizer used in the synthesis was explored using three thermal treatments: gentle oxidation, thermal reduction, and Argon-protected calcination. After treatment, the solid catalysts were characterized by several physical and chemical techniques and their reactivity was assessed by the aqueous phase hydrogenation of pyruvic acid (PyA) to lactic acid (LA) as a model reaction. These studies suggested that argon-protected calcination is the most efficient procedure to activate Ru nanocatalysts supported on MSU-F.

2.1. Introduction

Ruthenium (Ru) is an important catalyst for many reactions that are critical to biomass conversion, including hydrogenation, hydrogenolysis, oxidation, and carbon-carbon coupling.¹⁻⁵

Several protocols based on colloid chemistry have been attempted so far to produce monodisperse Ru NPs, including polyol or hydride reduction of Ru salts like $\text{RuCl}_3 \cdot n\text{H}_2\text{O}$ ⁶⁻¹⁵ and $\text{Ru}(\text{NO})(\text{NO}_3)_3$,¹⁶ hydrogen decomposition of $\text{Ru}(\text{cod})(\text{cot})$,¹⁷⁻²⁰ and thermal decomposition of $\text{Ru}_3(\text{CO})_{12}$.²¹ Stabilizers for nanoparticle synthesis include polymers, amines, acetates, thiols and organosilanes. Common supports for deposition of the Ru NPs include metal oxides, silica, carbonaceous materials, and membranes.²²⁻²⁴ Removal of the stabilizer from the supported Ru NPs has been reported in the technical literature.²⁵ However, to the best of our knowledge, no studies have been reported on a comparison of the efficiency of various strategies for removing the stabilizing agents from Ru NPs.

In this study, we explored three solution-based protocols for synthesizing monodisperse colloidal Ru NPs. Following synthesis, we deposited the Ru NPs on supports to prepare heterogeneous catalysts, and explored several procedures for removing the stabilizer. The structural and surface properties of the as-prepared catalysts were obtained via physical and chemical characterizations such as high resolution transmission electron microscopy (HRTEM), Fourier transform infrared spectroscopy (FT-IR), x-ray photoelectron spectroscopy (XPS), thermogravimetric analysis (TGA), physisorption and chemisorption, inductively coupled plasma atomic emission spectroscopy (ICP-AES), and x-ray diffraction (XRD). The catalytic properties of the activated

Ru NPs were evaluated by the aqueous phase hydrogenation of pyruvic acid (PyA) to lactic acid (LA), with the activity compared to commercial Ru catalysts supported on silica.

2.2. Experimental techniques

2.2.1. Inductively coupled plasma atomic emission spectroscopy (ICP-AES)

ICP-AES was used to determine the Ru and sulfur contents of the samples. Anhydrous RuCl_3 and *n*-dodecyl sulfide were used to prepare standard solutions for system calibration. For analysis of the colloidal sample(s), 0.5 ml of the colloid was transferred to a screw-capped centrifuge tube and the solvent was removed by nitrogen flushing. Then 2.0 ml of *aqua regia* (a mixture of HNO_3 and HCl in a 3:1 volume ratio) was added to the tube. The mixture was heated to 80°C and maintained at this temperature for 3 h, followed by centrifugation at 4000 RPM for 6 min to remove insoluble materials. The supernatant was diluted 15 times by de-ionized water, followed by analysis by ICP-AES. A similar procedure was used for analysis of solid samples, except for weighing the initial sample instead of measuring the volume. All analyses were carried out using a Varian ICP-AES instrument (Vista Pro, Cary, NC).

2.2.2. Transmission electron microscopy (TEM)

We examined the morphologies of the colloid and supported NPs using a JEOL 2200FS electron microscope (Tokyo, Japan) equipped with an energy dispersive x-ray (EDX) spectrometer (Oxford Instrument, UK). The specimens were prepared as follows. Colloidal NPs were diluted 50 times with methanol, and the supported catalysts were dispersed in methanol to form a suspension. One drop of the diluted colloidal suspension was transferred to a 3 nm carbon-coated copper grid. The samples were first dried in vacuum desiccators at room temperature overnight and then dried at 80°C for about 12 h, followed by TEM characterization. TEM

images and selected area electron diffraction (SAED) patterns were acquired with a field emission gun operated at 200 kV. EDS point spectra, line scans, and mapping analyses were conducted under STEM mode for both dark and bright field images of supported NPs from different regions.

2.2.3. Infrared (IR) Spectroscopy

We used Fourier transform infrared spectroscopy (FTIR) to assess the existence of organic residues after catalyst preparation. All Infrared spectra were acquired on a Mattson Galaxy FT-IR spectrometer (Mattson Instruments, Madison, WI) using KBr pellets.

2.2.4. Thermogravimetric/Differential Thermal Analysis (TGA-DTG)

TGA-DTG analysis was carried out on a TGA/DSC thermogravimetric analyzer (Mettler-Toledo Inc., Columbus, OH) to assess the transformation, if any, of the catalysts during calcination. In a typical analysis, about 70 mg of the sample was placed in an alumina sample holder, and heated from room temperature to 700°C at a rate of 10°C/min under a nitrogen atmosphere.

2.2.5. X-ray Photoelectron Spectroscopy (XPS)

To assess the oxidation state and surface composition of the solid samples, XPS measurements of the supported Ru nanocatalysts were performed on a Perkin Elmer Phi 5600 ESCA (Waltham, MA) system with a magnesium K α x-ray source at a take-off angle of 45°.

2.2.6. Powder x-ray Diffraction (XRD)

XRD patterns of the supported NPs were acquired using an x-ray powder diffraction system (D8 ADVANCE, Bruker AXS Inc., Madison, WI) with a Lynx-Eye detector and Cu K α radiation. The samples were scanned with a step size of 0.02° and a dwell time of 1.0 s.

2.2.7. Physisorption and chemisorption

The physical properties (surface area, pore size, pore volume) of each catalyst were determined by nitrogen physisorption at 78K using a Micromeritics ASAP2010 analyzer (Micromeritics Instrument Corporation, Norcross, GA). Prior to measurement, each sample was degassed under vacuum at 220°C for about 24 h. The surface area was calculated from the BET model. The average pore size and pore size (or volume) distribution were estimated by the *t*-plot method. H₂ chemisorption of the prepared catalysts was performed on a Micromeritics ASAP2010C analyzer. For standard analysis, the sample was flushed by flowing H₂ at room temperature for 30 min, heated at a rate of 10°C/min to the target temperature, and maintained at this temperature for 2 h to reduce the catalyst. The sample was then flushed by flowing He for 90 min, evacuated for 30 min, and cooled down to 35°C for analysis.

2.2.8. General procedures for assessing reactivity of the supported NPs.

All reactions for assessing catalyst reactivity were conducted in a Parr multi-batch reactor system (Model 5000, Parr Instrument Co., Moline, IL). In a typical experiment, the target quantity of catalyst was pre-reduced in the reactor by purging with nitrogen, heating to 150°C, charging with hydrogen to 3.4 MPa, and holding for 12 h. After cooling the system to room temperature and flushing it with nitrogen, 35 mL of the substrate was charged into the reactor from a sample cylinder under nitrogen pressure. When the reaction temperature stabilized at the target value, the reactor was pressurized with hydrogen gas to initiate the reaction. Liquid samples (2 mL) were withdrawn periodically for HPLC or GC analysis.

2.3. Preparation of well-defined Ru nanocatalysts by thermal decomposition

The thioether-stabilized monodisperse Ru NPs were synthesized by thermal decomposition of triruthenium dodecacarbonyl toluene with *n*-dodecyl sulfide (*n*DS,) as the stabilizing ligand. The work was done in collaboration with Professor Sherine Obare of the Department of Chemistry, Western Michigan University. The solid catalysts were characterized by several physical and chemical techniques. The reactivity of the supported Ru nanocatalysts was evaluated using the aqueous phase hydrogenation of PyA to LA as a model reaction.

2.3.1. Synthesis of Thioether-Stabilized colloidal Ru NPs

In a typical procedure for the synthesis of *n*DS-stabilized colloidal Ru NPs, 0.0312 g $\text{Ru}_3(\text{CO})_{12}$ (1.95×10^{-4} M) and 0.214 g *n*DS (1.98×10^{-3} M) were added to 30 mL of toluene. The mixture was heated to 40°C, and maintained for 15 min to ensure complete dissolution of the salt. The solution was evacuated at this temperature for 10 min, followed by introduction of nitrogen gas. The solution was then heated to 109°C, and maintained at this temperature for 24 h with magnetic stirring.

TEM observations (Figure 2-1) confirmed the successful synthesis of Ru-*n*DS NPs by thermal decomposition of $\text{Ru}_3(\text{CO})_{12}$. The TEM image in Figure 2-1 shows spherical Ru NPs with an average diameter of 3.4 ± 0.9 nm. The yield of Ru-*n*DS NPs is about 32%, as determined by ICP-AES analysis.

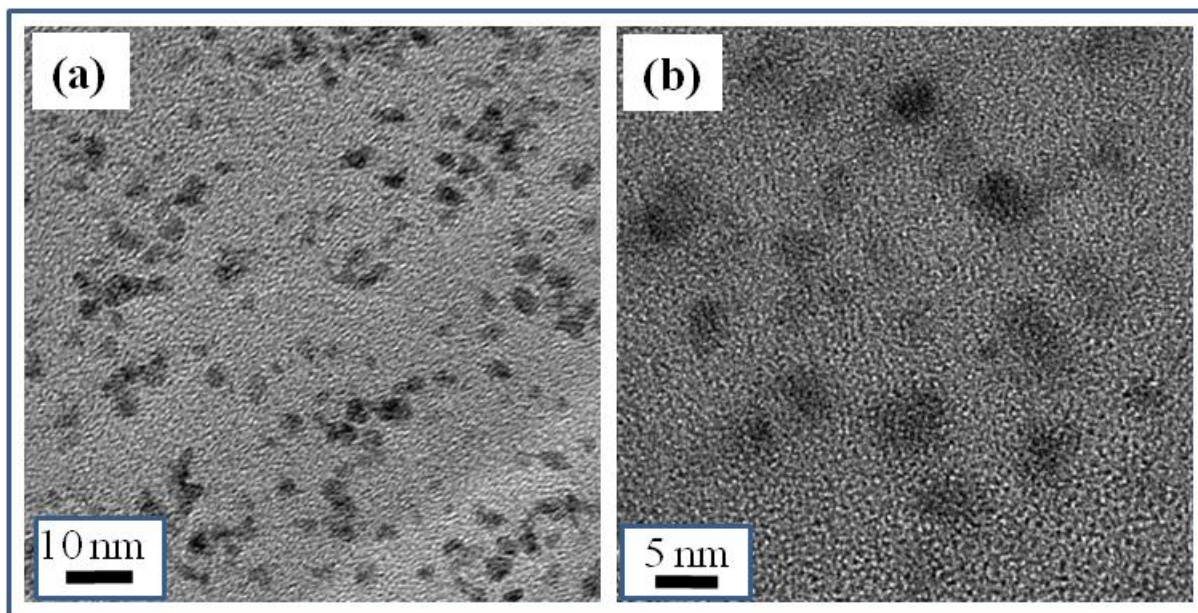


Figure 2-1 TEM images of Ru-*n*DS NPs synthesized via thermal decomposition. (a) TEM image at a magnification of 200K; (b) TEM image at a magnification of 300K

2.3.2. Preparation of supported Ru nanocatalysts from Ru-*n*DS colloidal NPs

Activated charcoal (AC, Sigma-Aldrich) was used to prepare the supported Ru-*n*DS NPs. The preparation includes deposition of particles on the support and removal of the stabilizing ligands from particle surfaces. The Ru-*n*DS NPs were loaded onto AC via a colloidal deposition method. In a typical procedure, 0.4 g AC was added to 50 mL of a Ru-*n*DS colloidal solution. The mixture was evacuated for 10 min and stirred under a nitrogen atmosphere for 24 h at 45°C, followed by nitrogen flushing to remove the toluene. The remaining solid was dried overnight at 120°C, calcined under vacuum at 360°C for 1.5 h, and reduced under a hydrogen atmosphere at 350°C for 3 h. The prepared catalyst was designated RuDS-AC-350.

The TEM image of RuDS-AC-350 (Figure 2-2a) shows Ru NPs dispersed on the AC support. The more magnified image in (Figure 2-2b) shows that the supported particles retained their spherical shape on the support.

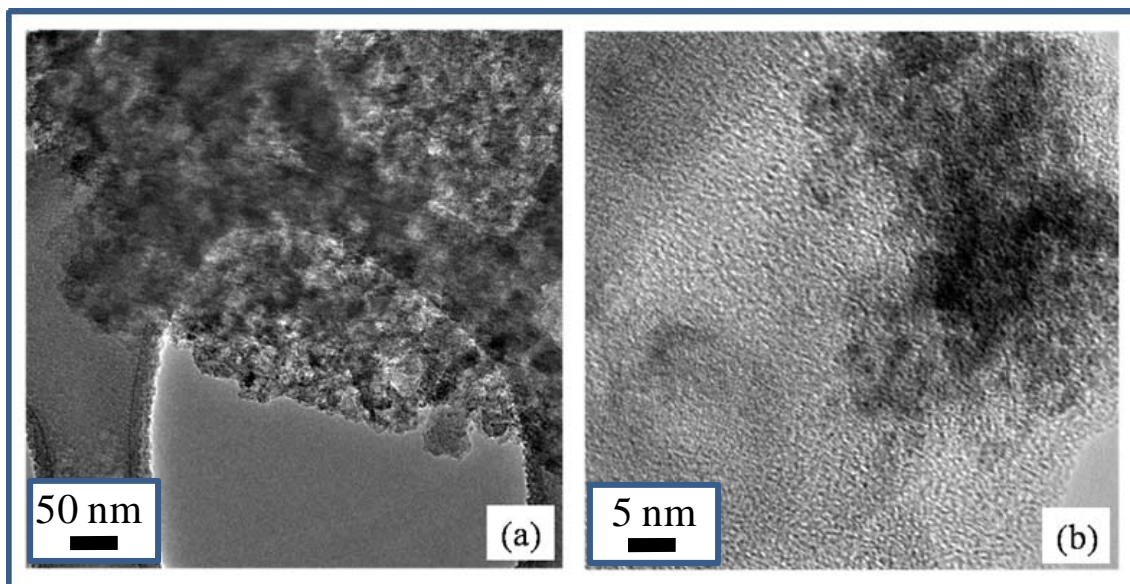


Figure 2-2 TEM images of Ru- NPs supported on AC (RuDS-AC-350). (a) TEM image at a magnification of 30K; (b) TEM image at a magnification of 200K

The data in Table 2-1 are a summary of the elemental composition (Ru and sulfur) and metal dispersion of the prepared catalysts and commercial Ru/SiO₂, as determined by ICP-AES and H₂ chemisorption, respectively. It was observed that thermal reduction at 350°C is not sufficient to fully remove the sulfur from the solid catalyst, and that the remaining sulfur in RuDS-AC-350 likely blocked adsorption of H₂ to the Ru NPs surfaces, as indicated by the value of metal dispersion in Table 2-1.

Table 2-1 Comparison of elemental composition and metal dispersion of RuDS-AC-350 and Ru/SiO₂

Sample ID	Ru content ^a (wt%)	S content ^b (wt%)	Metal dispersion ^c (%)
RuDS-AC-350	3.9±0.05	1.14±0.03	----
Ru/SiO ₂	1.32±0.02	----	17.55±1.37

^{a,b} Determined by ICP-AES. ^c Calculated from H₂ adsorption results.

2.3.3. Reactivity Assessment of Ru-*n*DS NPs Supported on Activated Charcoal (AC)

The reactivity of Ru nanocatalysts supported on AC (RuDS-AC-350) was assessed using the aqueous phase hydrogenation of PyA to LA as a model reaction. The pure support (AC) and commercial Ru/SiO₂ (Kaida Chemical Engineering Co., Shanxi, China) were used for negative and positive control experiments, respectively. All reactions were conducted according to the procedure described in **Section 2.2.9**. The reaction conditions are given in Figure 2-3, and the catalyst loading for each reaction is listed in Table 2-2. The initial reaction rate (mM PyA converted per hour) and activity (mmol PyA per g Ru per h) of each catalyst were calculated by fitting the data collected during the first five hours of reaction to an exponential function, and determining the slope at time $t=0$. The results are summarized in Table 2-2. The activity of RuDS-AC-350 was less than 15% that of the commercial Ru/SiO₂, which is very likely due to the incomplete removal of sulfur, since sulfur-containing compounds have been shown to be strong poisons of transition metal catalysts.²⁶⁻³⁰

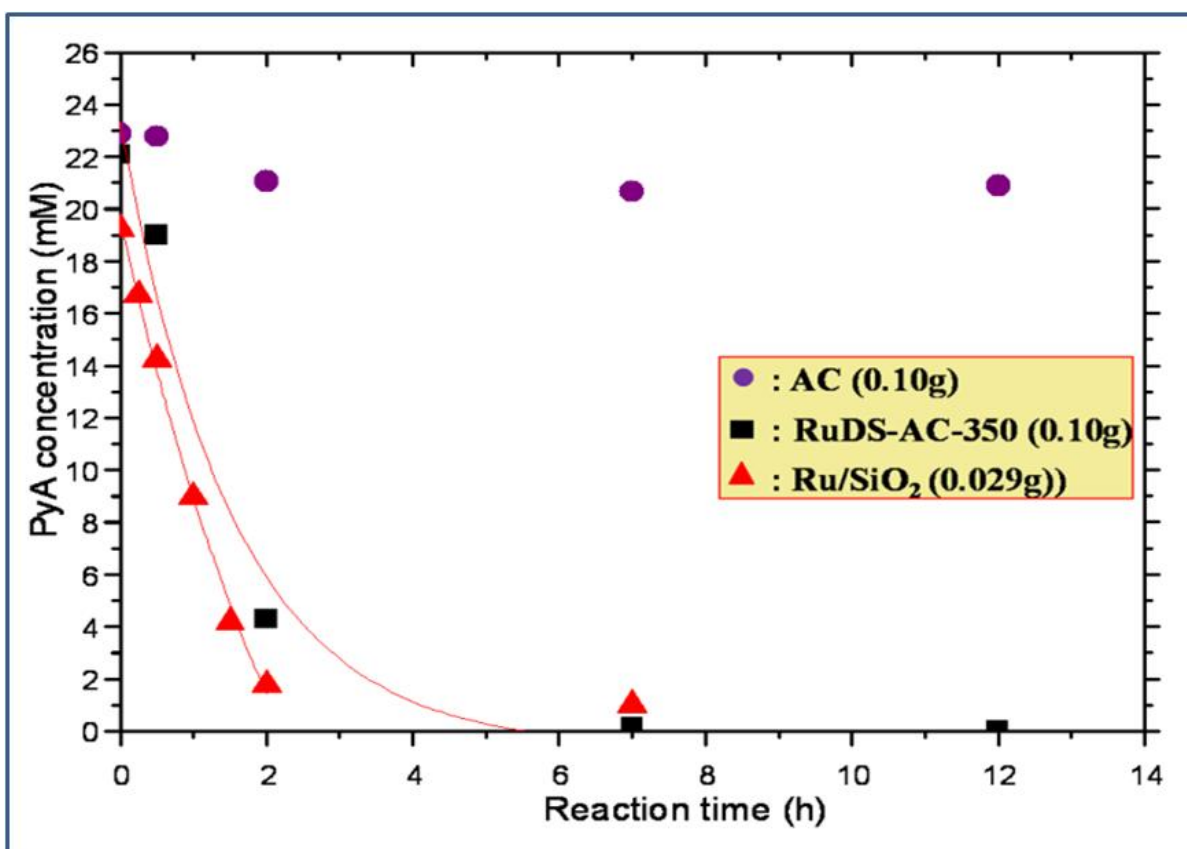


Figure 2-3 Reaction profiles of PyA hydrogenation over Ru-*n*DS NPs supported on AC. PyA hydrogenation was also conducted over pure AC and commercial Ru/SiO₂ as control experiments, respectively. Reaction conditions: $T= 45^{\circ}\text{C}$; $P(\text{H}_2) = 5.0 \text{ bar}$; 35 ml of PyA in water (20 mM). All catalysts were pretreated at 150°C under 33.4 bar of H₂ for 12 h. For interpretation of the references to color in this and all other figures, the reader is referred to the electronic version of this dissertation.

Table 2-2 Catalytic activities of supported Ru nanocatalysts for PyA hydrogenation

Sample ID	amount of catalyst ^a ($\times 10^{-1}$ mg)	amount of Ru ^b ($\times 10^2$ mg)	reaction rate ^c (mM PyA h ⁻¹)	activity ^c ($\times 10^3$ mmol PyA gRu ⁻¹ h ⁻¹)
AC	10.00	---	---	---
RuDS-AC-350	10.00	388.01	-15.57 \pm 2.71	0.14 \pm 0.02
Ru/SiO ₂	2.90	38.28	-12.32 \pm 1.09	1.14 \pm 0.12

^aTotal weight of catalyst. ^bCalculated from catalyst loading (g) and Ru content (wt. %) from ICP-AES measurements on the corresponding catalyst. ^cInitial reaction rate of substrate. ^dInitial activity, calculated as the consumption of PyA in mmol per g of Ru per hour.

2.4. Phase-transfer protocol for preparation of well-defined Ru nanocatalysts

Phase transfer is a promising way of synthesizing monodisperse metal NPs. Phase-transfer uses aqueous soluble metal precursors that are easily obtained compared to other synthesis methods. The method can also be used to effectively functionalize metallic NPs with suitable ligands *in vitro* to create desired chemical functionality and solubility, which are usually obtained by complicated post-synthetic modification in traditional methods.³¹⁻³⁵

We developed a facile phase-transfer protocol to synthesize monodisperse Ru NPs using amine as the stabilizing ligand. Following synthesis, we deposited the Ru NPs on ordered mesoporous silica (MSU-F) to prepare supported catalysts. We also explored several thermal treatment procedures to remove the stabilizing ligand. The reactivity of the supported Ru nanocatalysts was evaluated using the aqueous phase hydrogenation of PyA to LA as a model reaction.

2.4.1. Phase-transfer synthesis of Amine-Stabilized Ru NPs

Amine-stabilized Ru NPs (Ru-ODA colloidal NPs) were synthesized by a facile phase-transfer protocol using Ru (III) acetylacetonate ($\text{Ru}(\text{acac})_3$, 99%, Strem Chemical Inc.) as the metal precursor and octadecylamine (ODA, 99%, Alfa Aesar) as the stabilizing agent. In a typical synthesis, $\text{Ru}(\text{acac})_3$ (0.079 g, 2.0×10^{-4} mol) and ODA (0.53 g, 2.0×10^{-3} mol) were dissolved in 20 mL 1,4-butanediol in a 100 mL round bottom Schlenk flask. The solution was heated from room temperature to 130°C and evacuated at this temperature for 10 min under magnetic stirring, followed by introduction of argon. The solution was then heated to 210°C and maintained at this temperature for 5 min to reduce the Ru salt and form ODA-stabilized NPs (Ru-ODA). Ten (10) mL of toluene was then injected into the solution, followed by vigorous mixing of the biphasic mixture to extract the hydrophobic NPs from the hydrophilic medium.

The resulting colloidal solution in toluene was centrifuged at 6500 RPM for 5 min to remove trace insolubles.

The synthesis of Ru-ODA NPs by phase-transfer is illustrated in Figure 2-4. The NPs formed in a hydrophilic medium (polyol) can be completely extracted to a hydrophobic medium (toluene), as indicated by the colorless polyol phase (Figure 2-4a and b). Following addition of a polar solvent (methanol) to the solution of toluene and colloidal Ru-ODA NPs, a flocculated suspension with no phase separation was easily produced (Figure 2-4c). Centrifugation at 12000 RPM for 5min produced the black precipitates, with a nearly colorless supernatant (Figure 2-4d and e). The precipitate can be easily re-dispersed in toluene to obtain the purified Ru-ODA NPs (Figure 2-4f).

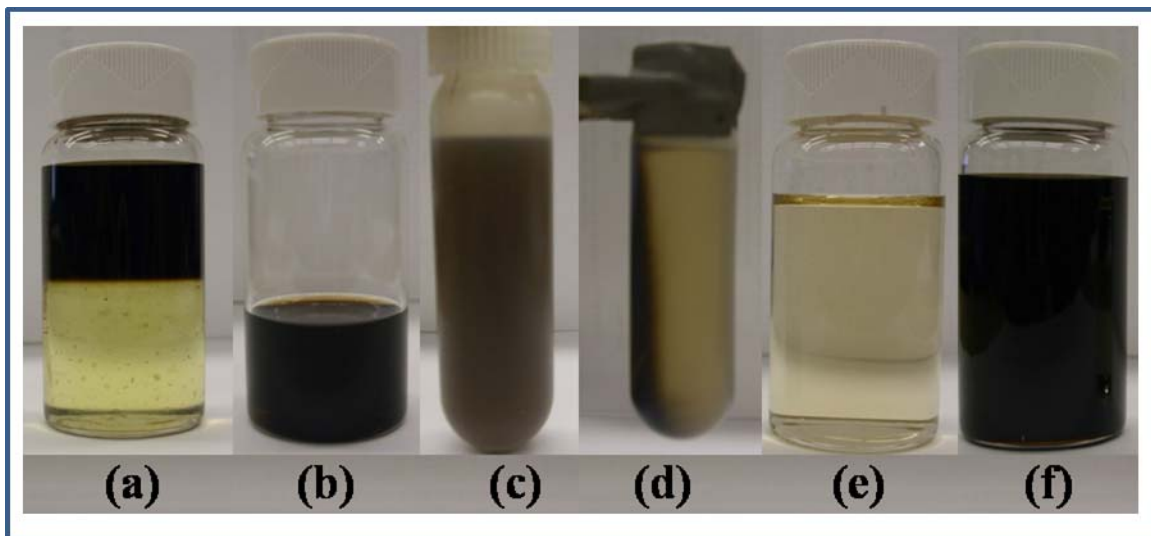


Figure 2-4 Illustration of the phase-transfer method for synthesizing ODA-stabilized Ru NPs. (a) Complete migration of ODA-Ru NPs from polyol to toluene phase, top layer toluene, bottom layer polyol; (b) separated colloidal ODA-Ru NPs in toluene after removal of trace insolubles by centrifugation; (c) flocculated mixture induced by addition of methanol to ODA-Ru NPs in toluene; (d) accumulation of black precipitate after centrifugation; (e) colorless supernatant after centrifugation; (f) ODA-Ru NPs re-dispersed in toluene.

The representative TEM images of Ru-ODA NPs are shown in Figure 2-5. The NPs are spherical and well dispersed with no agglomeration, suggesting good colloid stability (Figure 2-5a-b). The

more magnified image (Figure 2-5c) shows the highly crystalline structure of the NPs. The particles have a fairly narrow size distribution, with an average particle size estimated at 4.5 ± 1.0 nm (Figure 2-5d). More than 80% of the Ru precursor was converted to Ru-ODA NPs, based on the results of ICP-AES analysis. This is much higher than was obtained with the thermal decomposition method.

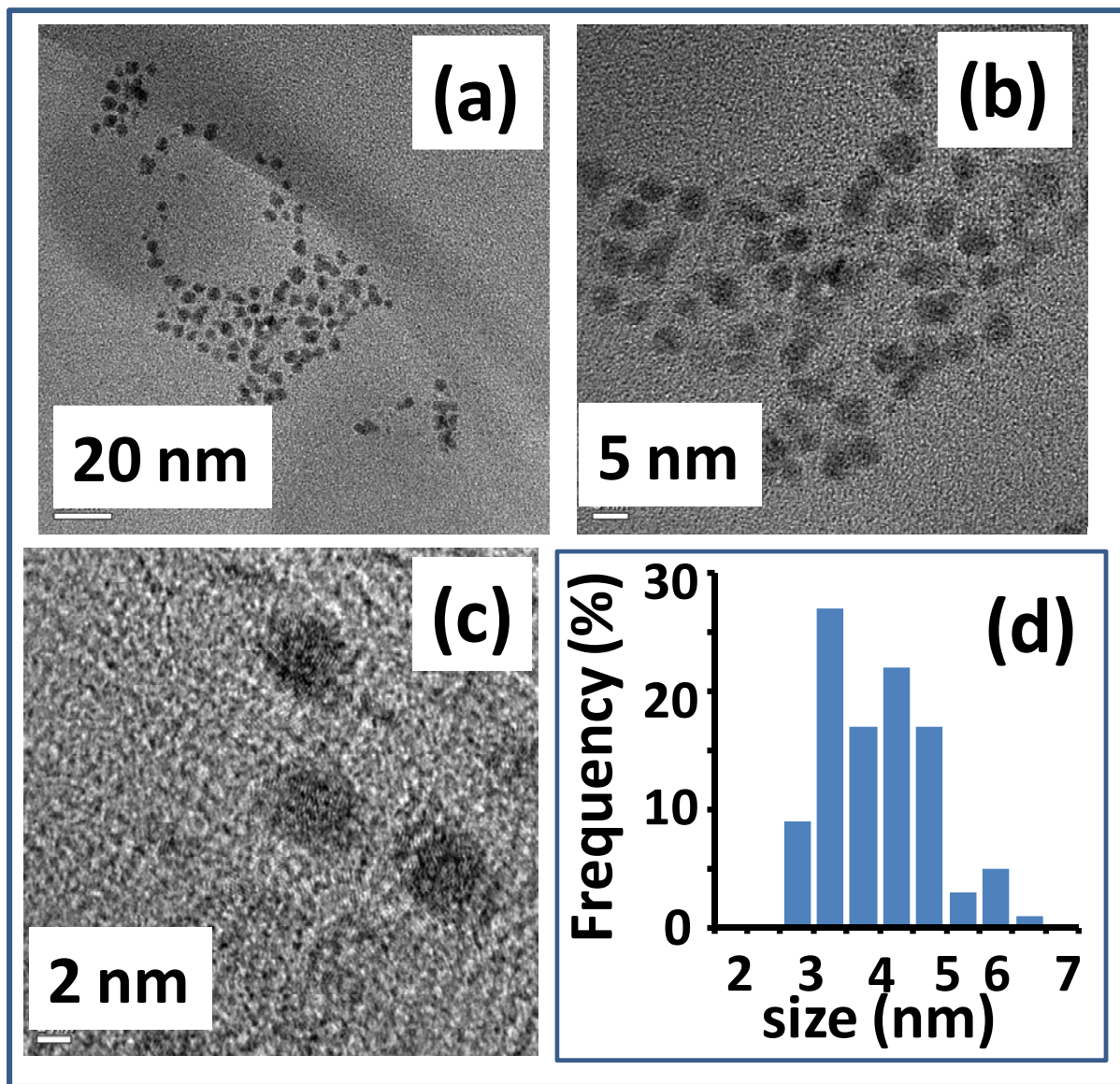


Figure 2-5 TEM images of Ru-ODA NPs synthesized by phase-transfer. (a) HRTEM image of the Ru-ODA NPs at a magnification of 100K, (scale bar of 20 nm); (b) HRTEM image of Ru-ODA NPs at a magnification of 300K, (scale bar of 5 nm); (c) HRTEM image of Ru NPs at a magnification of 600K showing an inter-lattice-spacing of 2.1\AA , (scale bar of 2 nm); (d) size distribution histogram of the Ru-ODA NPs, with an average particle size of $4.5 \pm 1.0\text{nm}$.

2.4.2. Preparation of supported Ru nanocatalysts from Ru-ODA colloidal NPs

Mesoporous silica is an ideal support for heterogeneous catalysis due to its high surface area, tunable pore size and shape, and inert properties. Here, we used ordered mesoporous silica (MSU-F, Sigma-Aldrich) as the support for Ru-ODA NPs. The MSU-F by itself has a hexagonal cellular foam in a mesoporous framework with a cell window size of ~15 nm and unit cell size of ~22 nm.^{36,37}

Preparation of supported Ru nanocatalysts involves the assembly of Ru-ODA NPs on MSU-F and removal of the organic stabilizing shells from the surface of the supported NPs. Loading of colloidal Ru-ODA NPs on MSU-F was accomplished by sonication-assisted colloidal deposition.^{38,39} In a typical procedure, the required amount of MSU-F support was placed in 20 mL of colloidal Ru solution. The mixture was sonicated (VWR Ultrasonic, 75T/120 W/45 kHz) at room temperature for 3 h, followed by centrifugation at 5000 RPM for 10 min. The precipitates were washed twice with methanol. After removing excess methanol by nitrogen flushing at room temperature, the sample was transferred to a vacuum desiccator for further treatment.

Three different procedures were explored to remove the stabilizer from the sample. In the first, the sample was heated in static air to 150°C and maintained at this temperature for 12 h, then cooled to room temperature to obtain the catalyst labeled RuODAF-150. We refer to this procedure as the gentle oxidation method. The second was a thermal reduction protocol, which involved reduction of the sample at 350°C for 2 h under flowing hydrogen to obtain the catalyst RuODAF-350. In the third procedure, the sample was heated in flowing Argon to 650°C at a rate of 10°C min⁻¹, held at this temperature for 2 h, and then cooled to room temperature to get the

catalyst RuODAF-650. We named this procedure the argon-protected calcination protocol. Successful deposition of Ru-ODA NPs was confirmed by the color change of MSU-F before and after Ru NP deposition, from initially white to gray. Figure 2-6 shows the HRTEM images of Ru NPs supported on MSU-F following the different treatments.

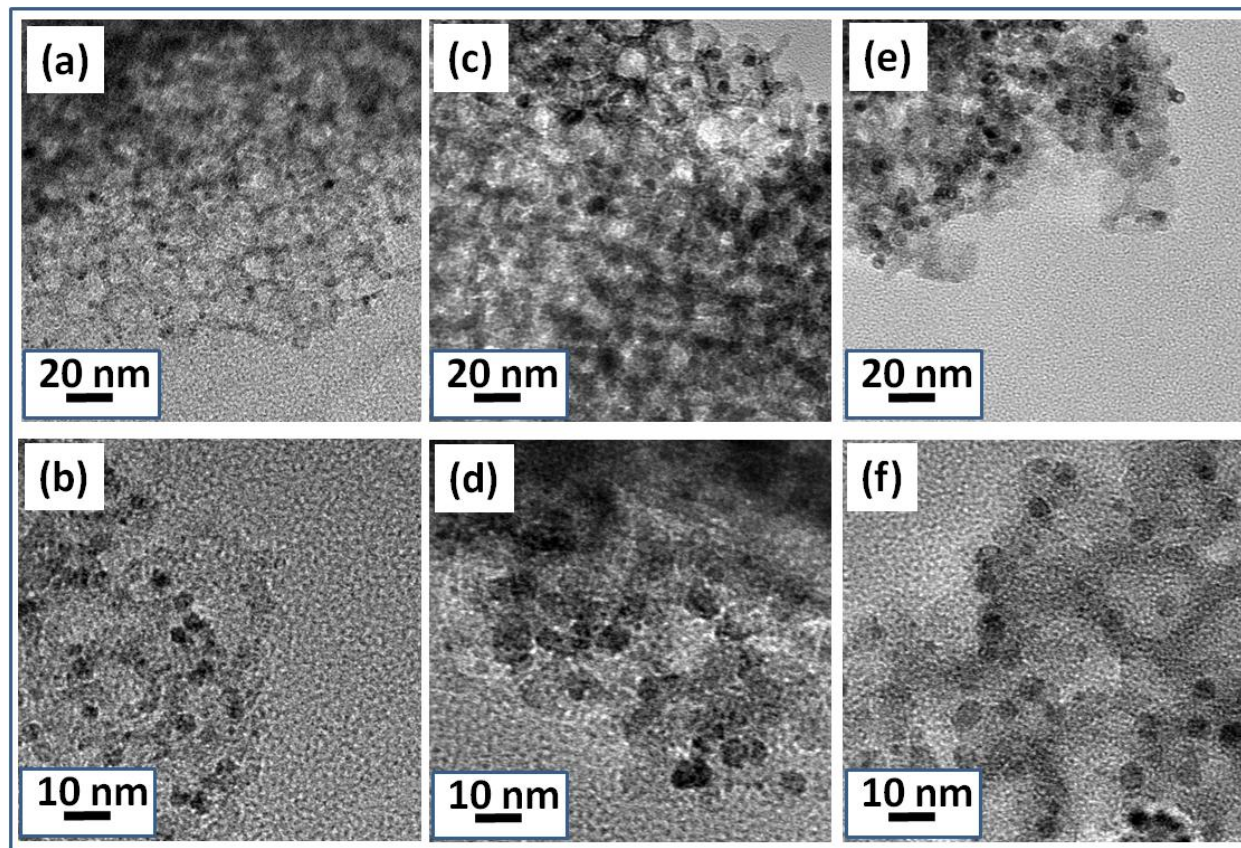


Figure 2-6 TEM images of Ru-ODA NPs supported on MSU-F, after different thermal treatments. (a and b) RuODAF-150 at scale bars of 20 nm 10 nm, respectively, showing well-dispersed NPs of the same size as the colloidal Ru particles; (c and d) RuODAF-350 at scale bars of 20 nm and 10 nm, respectively, showing well-dispersed particles with no damage to the support after thermal reduction; (e and f) RuODAF-650 at scale bars of 20 nm and 10 nm, respectively, showing well-dispersed particles after Argon-protected calcination.

After gentle thermal oxidation, the Ru NPs were still well-dispersed on MSU-F without agglomeration and with no damage to the structure of the support (Figure 2-6a). The more magnified image in Figure 2-6b shows that the particles on the support match the size of the original unsupported colloidal Ru NPs shown earlier in Figure 2-6. The images in Figures 2-6 c

and d show that the Ru NPs remain individually dispersed on the support, with no obvious morphology change after thermal reduction at 350°C, and that the support preserved its ordered structure. Excellent dispersion and morphology were also achieved upon treatment under inert gas-protected calcination at 650°C (Figure 2-6 e and f).

Figure 2-7 summarizes the FT-IR spectroscopy for pure MSU-F, the ligand ODA and the three supported catalysts following the different thermal treatments.

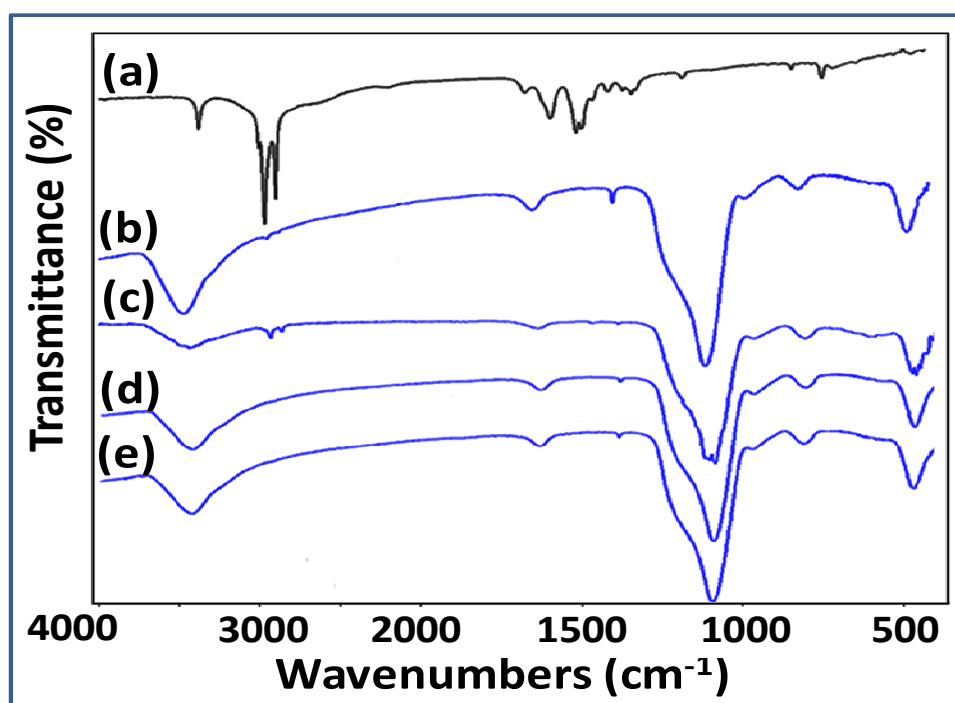


Figure 2-7 IR spectra of ODA, MSU-F, and supported Ru-ODA NPs after different thermal treatments. (a) ODA; (b) pure MSU-F support; (c) RuODAF-150; (d) RuODAF-350; (e) RuODAF-650. MSU-F shows a strong adsorption peak at 1100 cm^{-1} and a weak band at 1636 cm^{-1} . Pure ODA has CH_2 symmetric and asymmetric stretching vibration bands at 2850 and 2919 cm^{-1} , respectively. The band at 1570 cm^{-1} is assigned to the N–H vibration bend of amine groups. The band at 1450 cm^{-1} is assigned to the scissoring of methylene from the hydrocarbon chains of ODA.

The absorption peaks for pure MSU-F (Figure 2-7b) and ligand (ODA, Figure 2-7a) are consistent with those in previous reports.⁴⁰⁻⁴⁵ RuODAF-150 shows the characteristic absorption

peaks of MSU-F, while the disappearance of the N–H vibration peaks indicates complete decomposition of ODA during gentle oxidation. However, the remaining CH₂ stretching bands (2850 and 2919 cm⁻¹) suggest attachment of the decomposed ODA residuals to the surface of the Ru NPs. By contrast, the IR spectra of RuODAF-350 and RuODAF-650 only show the characteristic peaks of pure MSU-F, indicating complete removal of ODA by both thermal reduction at 350°C and heating under inert gas at 650°C.

The TGA curves in Figure 2-8a show the thermal stability of each sample, and the DTG curves provide information on the rate of weight loss during the thermal treatments (Figure 2-8b). It can be seen from Figure 2-8 that MSU-F is thermally stable from room temperature to at least 700°C. ODA experiences a rapid weight loss starting at 200°C, with about 90% weight loss by 260°C. The DTG curve for pure ODA suggests that it undergoes a single stage thermal decomposition. The TGA and DTG curves for RuODAF-150 suggest that most of the stabilizing ODA on the Ru NPs is decomposed under gentle oxidation. However, the approximately 4% sample weight loss by 340°C suggests that the decomposed ODA residuals remained on the Ru metal surface after gentle oxidation. It can be deduced from the TGA curves of RuODAF-350 and RuODAF-650 that more than 98% of ODA was removed by either thermal reduction at 350°C or calcination under an argon atmosphere at 650°C. These results are in agreement with the FT-IR spectra discussed earlier.

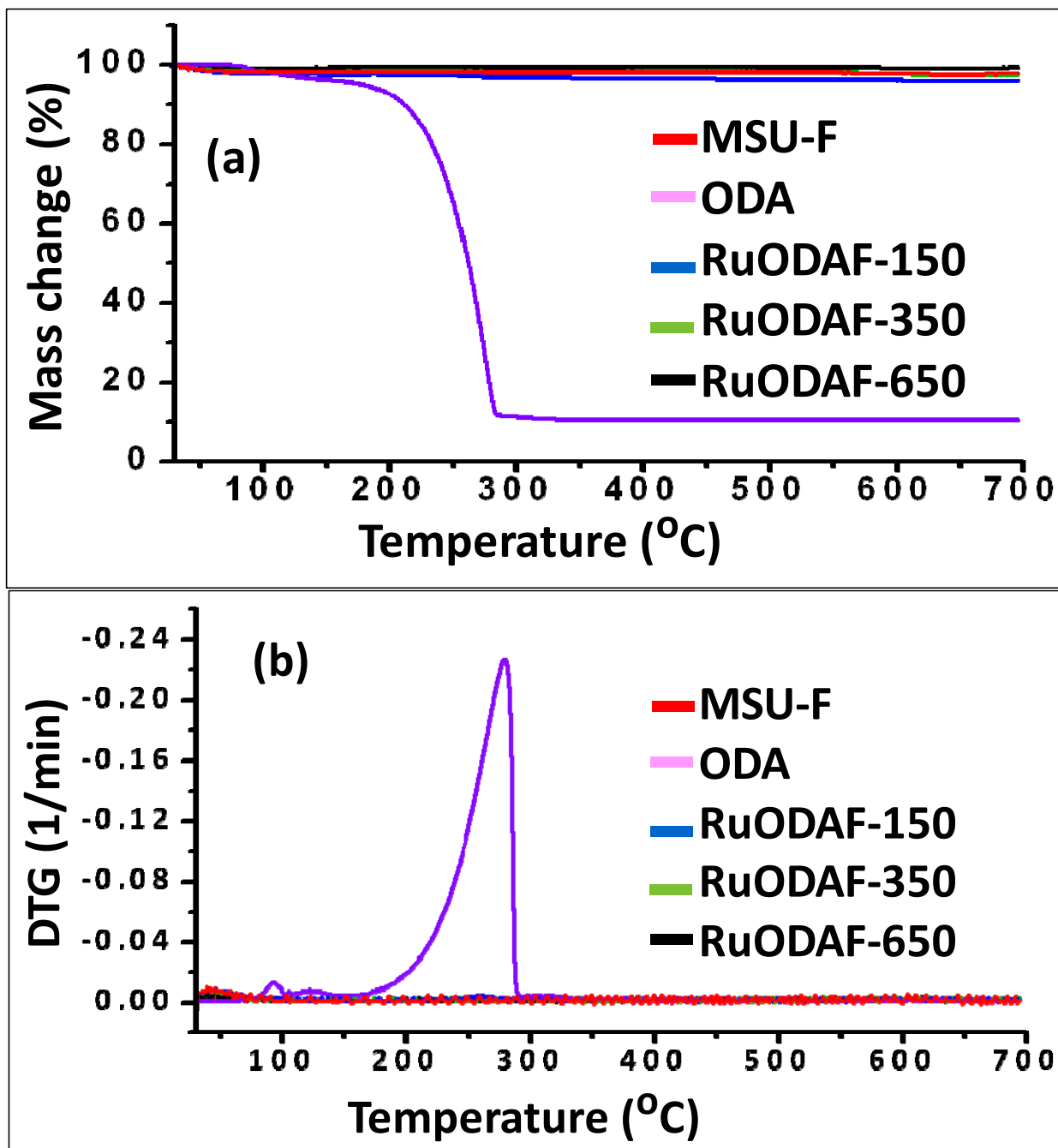


Figure 2-8 TGA and DTG diagrams of MSU-F, ODA, and supported Ru-ODA NPs after different thermal treatments. (a) TGA diagram, (b) DTG diagram. The temperature was raised from 25°C to 700°C at a rate of 10°C/min. MSU-F is thermally stable over the entire temperature range. The decomposition of pure ODA began at about 200°C and was complete at 260°C. The relatively negligible changes in the TGA and DTG curves for RuODAF-150, RuODAF-350 and RuODAF-650 are an indication of complete decomposition of ODA during the thermal treatments.

The XRD results of the pure support and all three supported Ru catalysts also provide important information on particle crystallinity (Figure 2-9). All three samples exhibit the characteristic peak of the (101) facet of hexagonal close packed (*hcp*) crystalline Ru metal in the powder XRD measurements shown in Figure 2-9.^{46,47} This diffraction peak (43.5°) is weaker in RuODAF-150 than in RuODAF-350 and RuODAF-650, suggesting that the thermal treatments at higher temperatures resulted in more annealing and therefore greater crystallinity. As expected, no characteristic peaks were observed for the pure support between 2θ values of 30° and 50° .

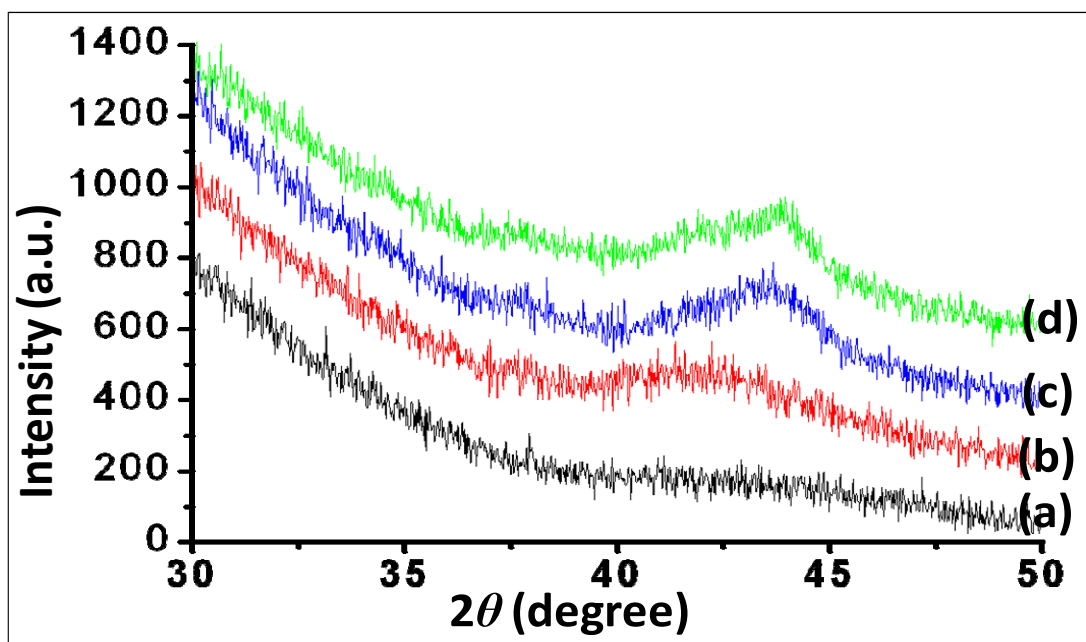


Figure 2-9 XRD patterns of pure MSU-F and supported Ru-ODA NPs after different thermal treatments. (a) MSU-F; (b) RuODAF-150; (c) RuODAF-350; (d) RuODAF-650. The peak at the 2θ value of 43.5° is consistent with the (101) facet of hexagonal close packed (*hcp*) Ru nanocrystals. The intensity of the peak is an indication of the degree of crystallinity of each sample.

XPS measurements were performed on all samples to further investigate the effects of thermal treatment on the atomic composition and oxidation states of the catalysts (Figure 2-10). Three peaks were observed in the Ru 3p binding energy region. The peak at the lowest binding energy

is assigned to metallic Ru(0), while the two at higher binding energies correspond to Ru (IV) and Ru (VI) oxidation states, respectively.⁴⁸⁻⁵¹

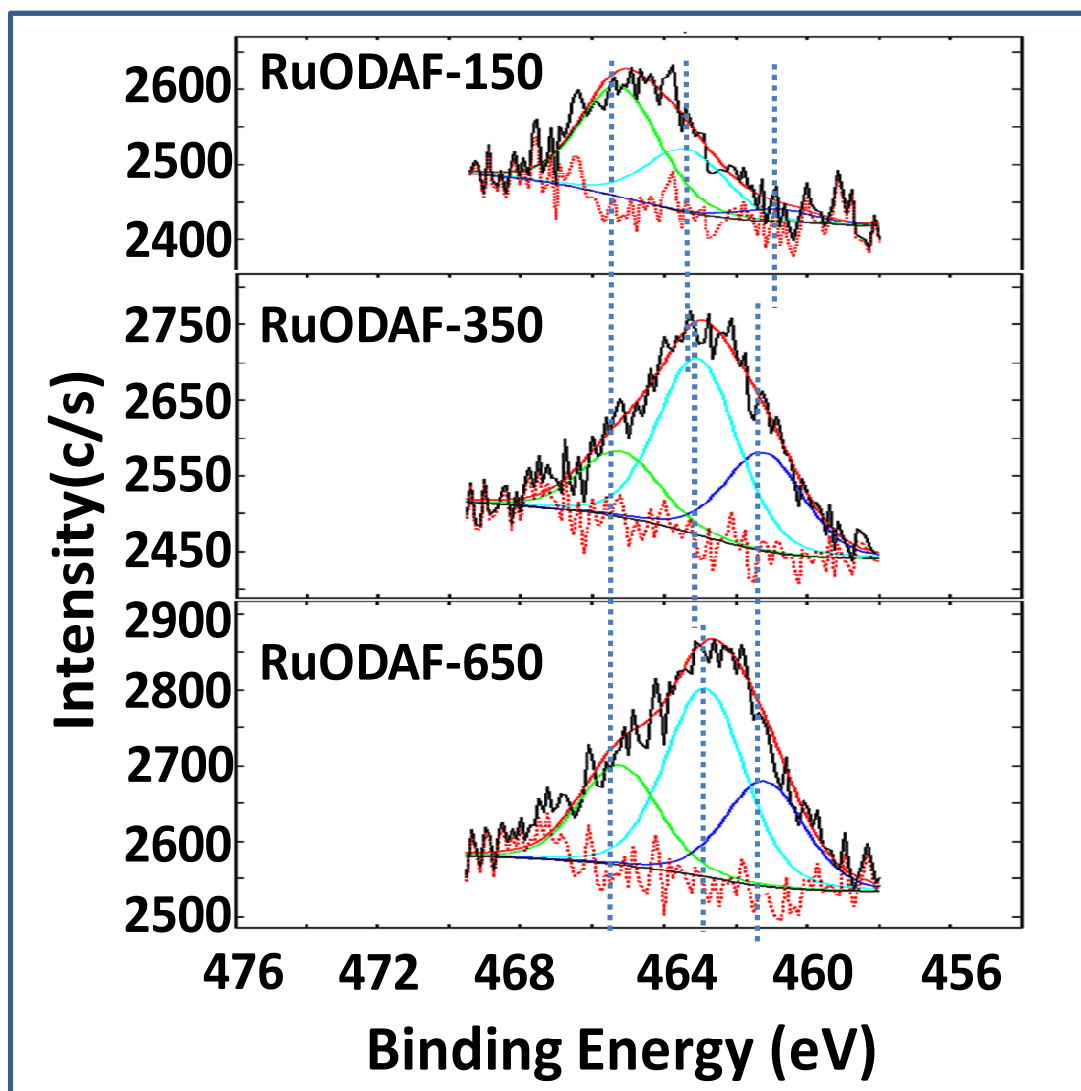


Figure 2-10 XPS spectra of supported Ru-ODA NPs after different thermal treatments. The three peaks from low to high binding energy in each diagram correspond to Ru(0), Ru (IV), and Ru (VI). The binding energy of Ru(0) in RuODAF-150 displays a negative shift compared to that of bulk metallic Ru (461.2-461.5 eV^{48,49}) and a positive shift compared to the bulk Ru (IV) which is at 462.4-463.2eV⁵², indicating incomplete removal of the ODA stabilizer. The XPS spectra of RuODA-350 and RuODA-650 are in good agreement with that of the bulk Ru,⁴⁸⁻⁵² suggesting complete removal of ODA.

The binding energy of metallic Ru in RuODAF-150 was 460.81 eV, which is slightly lower than the values for bulk Ru in the zero valence state (461.2-461.5 eV).^{48,49} However, the binding

energy of Ru(IV) in RuODAF-150 (463.39eV) shows a positive shift compared to that of the bulk RuO₂. These shifts in binding energies are attributed to the incomplete removal of residuals in RuODAF-150. The binding energies of Ru(0) in both RuODAF-350 (461.22 eV) and RuODAF-650 (461.20 eV) are in agreement with the data for bulk Ru (0), indicating complete removal of ODA. The binding energies of Ru(IV) in both RuODAF-350 (463.06eV) and RuODAF-650 (462.84 eV) are also consistent with those of Ru 3p_{3/2} for bulk RuO₂ (462.4-463.2eV).⁵² The presence of Ru (IV) and Ru (VI) in all samples indicates that the surface atoms of the Ru NPs can be easily oxidized when exposed to air, even under ambient conditions.

The BET surface area, Ru content, and metal dispersion of each catalyst are summarized in Table 2-3. The surface area of RuODAF-150 (537.28 m²g⁻¹) is slightly larger than that of pure MSU-F (503.33 m²g⁻¹), possibly because the immobilized Ru NPs were located at the edge of the support, thus extending the dimensions of the mesopores. When the capping ODA and its decomposed residuals were completely removed by either thermal reduction at 350°C or calcination at 650°C under argon, the surface area increased to 645.17 m²g⁻¹ for RuODAF-350 and 822 m²g⁻¹ for RuODAF-650. The larger surface area for RuODAF-650 compared to that of RuODAF-350 can be attributed to restructuring of the silica framework in MSU-F via bond rearrangements.^{37,53} The Ru contents in RuODAF-350 (0.72±0.01 wt%) and RuODAF-650 (0.78±0.08 wt%) are lower than in RuODAF-150 (1.27±0.02 wt%), indicating a loss of Ru from the catalysts treated under thermal reduction or Ar protected calcination. One possible explanation for this result is the formation of low boiling point compounds between the surface Ru atoms and the residuals of decomposed ODA.^{46,54,55} Structural rearrangement of the support

could also lead to loss of mass of the support and subsequently result in a slight increase of Ru content in RuODAF-650 compared to RuODAF-350. RuODAF-150 has a metal dispersion of approximately 17.0%. This value increased to 30.4% for RuODAF-350, which can be attributed to complete removal of ODA during thermal reduction. The slight increase of metal dispersion in RuODAF-650 (34.59%) compared to RuODAF-350 is attributed to restructuring of the support during the high temperature (650°C) calcination.

Table 2-3 Properties of MSU-F supported Ru-ODA NPs after different thermal treatments

Sample ID	BET Surface area ^a (m ² g ⁻¹)	Ru content ^b (wt%)	Metal dispersion ^c (%)
MSU-F	503.33 ± 1.20	---	---
Ru/SiO ₂	139.64 ± 0.78	1.32 ± 0.02	17.55 ± 1.37
RuODAF-150	537.28 ± 1.22	1.27 ± 0.02	17.03 ± 0.71
RuODAF-350	645.17 ± 1.60	0.72 ± 0.01	30.40 ± 0.72
RuODAF-650	822.36 ± 1.74	0.78 ± 0.03	34.59 ± 0.58

^aFrom N₂ adsorption. ^bFrom ICP-AES. ^cFrom H₂ adsorption results.

2.4.3. Reactivity Assessment of MSU-F supported Ru-ODA NPs

We used the aqueous phase hydrogenation of PyA to LA to assess the activity of the supported Ru catalysts. The catalyst loading in each reaction is listed in Table 2-4. The detailed reaction conditions are listed in Figure 2-11. Figure 2-11a shows the conversion of substrate as a function of reaction time for pure MSU-F, commercial Ru/SiO₂, and the three as-prepared Ru nanocatalysts. A 100% selectivity to LA was observed in all the reactions. Less than 5% of the PyA was converted in 7 h with pure MSU-F, indicating that the reaction is catalytic. Ninety percent (90%) conversion of the substrate was achieved within 1.5 h for all the catalysts

developed in this work, while 80% of the substrate was converted by the commercial Ru/SiO₂ over the same interval. These results compare very favorably to previous reports on the hydrogenation of PyA in ethanol-water media under harsher reaction conditions than used here.⁵⁶

Figure 2-11b is a plot of substrate concentration as a function of reaction time. The initial reaction rates (mM PyA per h), activities (mmol PyA per g Ru per h) and turnover frequencies (TOF, h⁻¹) of the catalysts, as shown in Table 2-4, were calculated by regression of the data collected during the first 1.5 h of each reaction, and taking the derivatives of the regression function at time $t=0$. All three Ru nanocatalysts prepared in this study showed higher reaction rates and activity than the commercial Ru/SiO₂. The activities of RuODAF-350 and RuODAF-650 were significantly higher than that of RuODAF-150, demonstrating the need for complete removal of the stabilizer. As expected, RuODAF-350 and RuODAF-650 have similar TOF values, since they have the same surface structures and the reactions were conducted under the same conditions. The high TOF value of RuODAF-150 may be the result of a different behavior of the decomposed ODA residues on particle surface in the aqueous phase. It is possible that the residuals in the chemisorption environment attach tightly to the particles and inhibit hydrogen adsorption on Ru surfaces, leading to fewer measured active sites. However, the hydrophilic residuals may extend away from the catalyst surface into the aqueous reaction media, and enabled easier access to active sites. The possible result is that, the low H₂ adsorption would lead to underestimation of the metal dispersion values used to calculate activity and TOF for RuODAF-150, which would subsequently produce a higher than expected activity and TOF.

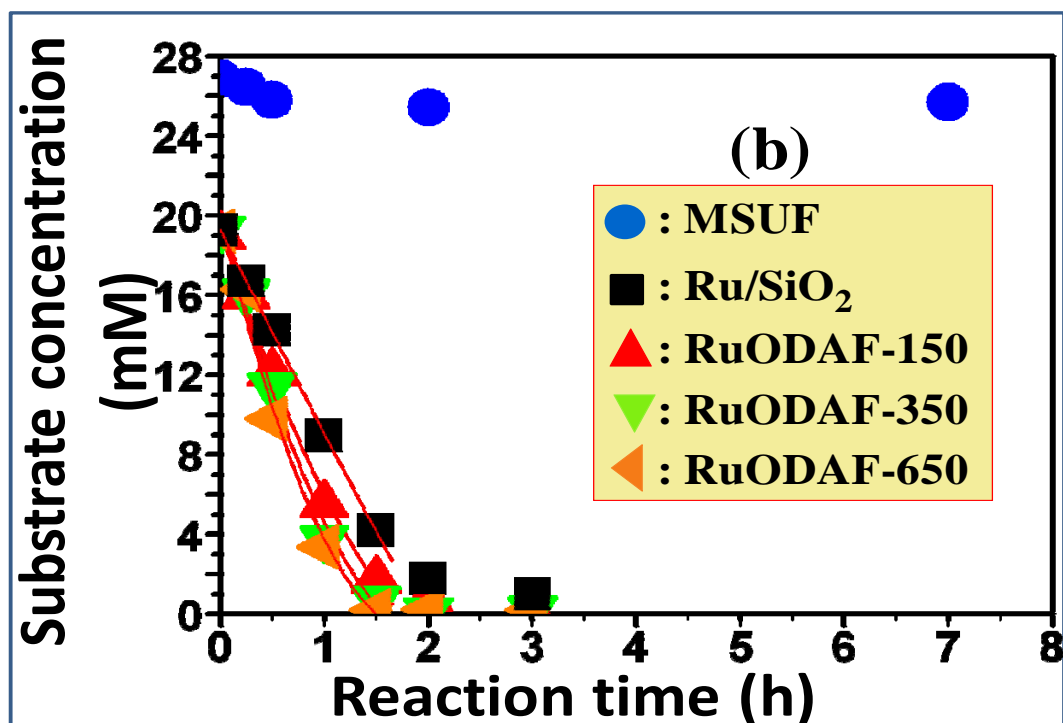
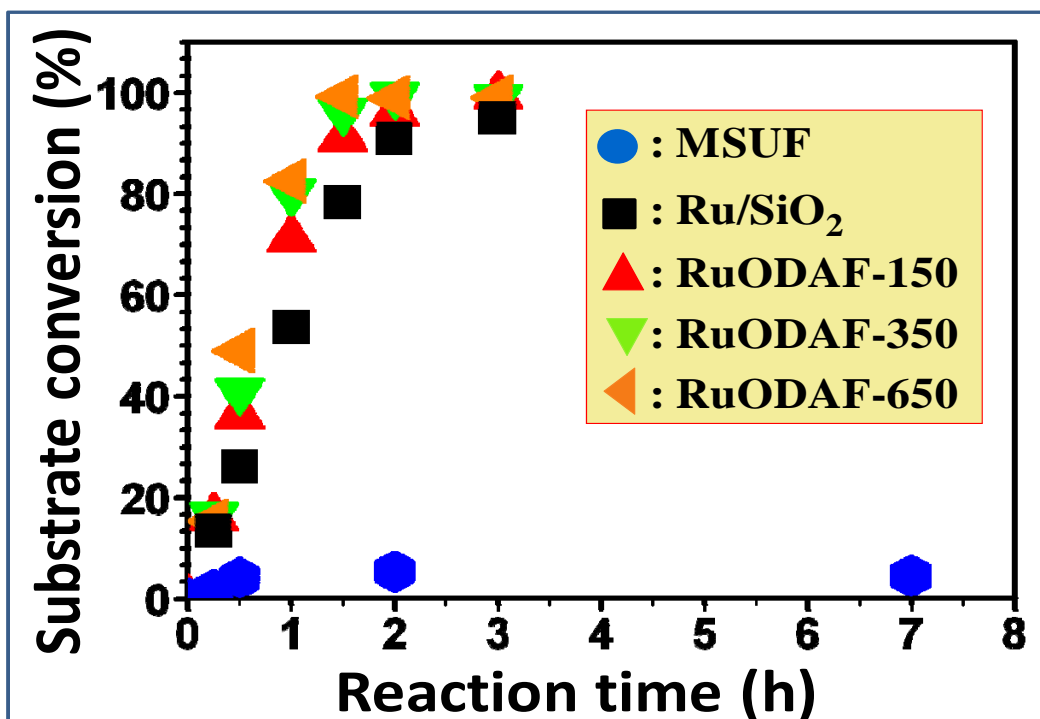


Figure 2-11 Reaction profiles during PyA hydrogenation over Ru-ODA NPs supported on MSU-F. (a) PyA conversion vs. reaction time for different catalysts; (b) PyA concentration vs. reaction time for different catalysts. The curves are the polynomial regressions of each data set. Reaction conditions: $T = 45^{\circ}\text{C}$; $P(\text{H}_2) = 5.0 \text{ bar}$; 35 ml of Pya in water (20 mM). All catalysts were pretreated at 150°C overnight under 33.4 bar of H_2 .

Table 2-4 Activities of supported Ru-ODA NPs for PyA hydrogenation

Sample ID	Amount of catalyst ^a ($\times 10^1$ mg)	Amount of Ru ^b ($\times 10^{-2}$ mg)	Initial Reaction rate ^c (mM PyA h ⁻¹)	Initial Activity ^d ($\times 10^3$ mmol PyA gRu ⁻¹ h ⁻¹)	TOF ^e ($\times 10^2$ h ⁻¹)
MSU-F	5.00	---	---	---	
Ru/SiO ₂	2.90	38.28	12.32 \pm 1.09	1.14 \pm 0.12	6.49
RuODAF-150	3.11	21.56	16.33 \pm 1.79	1.45 \pm 0.16	8.58
RuODAF-350	5.34	21.36	19.96 \pm 3.18	1.82 \pm 0.29	6.07
RuODAF-650	4.91	21.42	22.01 \pm 3.98	2.01 \pm 0.36	5.86

^aTotal weight of catalyst in the corresponding system. ^bCalculated from catalyst loading (g) and Ru content (wt. %). ^cInitial reaction rate of substrate. ^dInitial activity calculated as the consumption of PyA in mmol per g of Ru per h. ^eTOF calculated from initial activity and metal dispersion from hydrogen adsorption experiments, unit consumption of PyA in mmol per mmol of available Ru active sites per h, with each Ru atom considered as one active site.

2.5. Preparation of Well-defined Ru Nanocatalysts by Polyol reduction

We synthesized monodisperse Ru NPs by a polyol reduction method modified from previous reports.^{6,11,57} The Ru NPs were deposited on MSU-F to prepare supported catalysts. We evaluated several thermal treatments to remove the PVP capping agent. Both the supported Ru nanocatalysts and the unsupported Ru NPs were characterized via a number of physical and chemical techniques. The reactivity of the supported Ru nanocatalysts was evaluated using the aqueous phase hydrogenation of PyA to LA as a model reaction.

2.5.1. Synthesis of polymer-stabilized Colloidal Ru NPs by Polyol Reduction

The polymer-stabilized colloidal Ru NPs were synthesized by polyol reduction of Ru(acac)₃ using Poly-N-vinyl-2-pyrrolidone (PVP) as the stabilizing agent. In a typical synthesis, 0.079 g Ru(acac)₃ (99%, Alfa Aesar) and 0.222 g PVP (MW \approx 55K, Sigma-Aldrich), were dissolved in 20 mL of 1,4-butanediol (99%, Alfa Aesar) in a 50 mL round bottom Schlenk flask. The solution was heated from room temperature to 130°C and evacuated at this temperature for 10 min under magnetic stirring. Argon was then introduced, and the solution was heated to 175°C and maintained at that temperature for 1.5 h. When the mixture was cooled down to room temperature after the prescribed period of time, acetone was poured into the solution till a cloudy black suspension was formed. This suspension was separated by centrifugation at 5000 RPM for 6 min. The precipitated Ru NPs were collected, washed once in acetone, and re-dispersed in methanol.

Figures 2-12a and b show typical TEM images of the PVP-stabilized Ru NPs at different magnifications. The Ru NPs are spherical and well-dispersed with no agglomeration. EDS data shown in Figure 2-12c confirm that the NPs contain Ru. It can also be seen from the histogram in

Figure 1d that the particles have a fairly narrow size distribution, with an average particle size estimated at 3.5 ± 0.5 nm. We also determined from ICP-AES data that 89% of the $\text{Ru}(\text{acac})_3$ precursor was converted to colloidal Ru NPs.

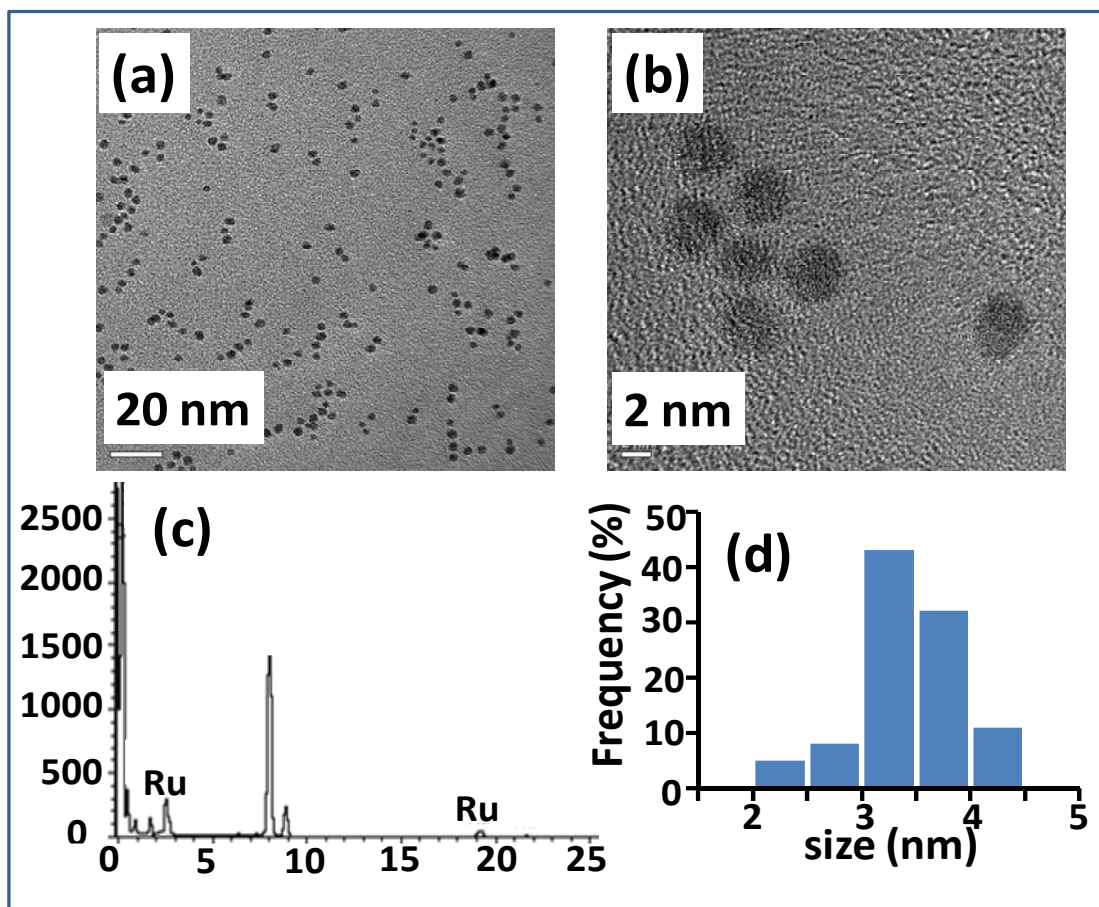


Figure 2-12 TEM images and EDS spectra for Ru-PVP NPs. (a) TEM image of well-dispersed Ru NPs at a magnification of 100K (scale bar of 20 nm); (b) TEM image of Ru NPs at a magnification of 600K showing very stable NPs (scale bar of 2 nm); (c) EDS spectrum showing the elemental Ru content of the NPs at a magnification of 100K; (d) histogram showing the size distribution of Ru NPs, with an average particle size (diameter) of 3.5 ± 0.5 nm.

2.5.2. Preparation of supported Ru nanocatalysts from Ru-PVP colloidal NPs

We used MSU-F as the support for Ru-PVP NPs. Preparation of the supported Ru nanocatalysts was accomplished following the same procedures described in **Section 2.4.2**, including particle deposition and thermal treatments to remove the capping PVP agent. The catalysts treated by the three procedures described in **Section 2.4.2** were named RuF-150, RuF-350, and RuF-650,

respectively. The TEM images of the MSU-F and the MSU-F supported Ru nanocatalysts following the three thermal treatments are shown in Figure 2-13.

Following gentle thermal oxidation at 150°C, the Ru NPs were still well-dispersed in the pores of MSU-F, with no signs of agglomeration and no damage to the structure of the support (Figure 2-13a and 2b). The more magnified images in Figures 2-13 c and d show that the particles visible on the support match the size of the unsupported colloidal Ru NPs. The TEM images in Figure 2-13e and f show that the Ru NPs remain individually dispersed on the support, with no obvious morphology changes after thermal reduction, and that the support preserved its ordered structure during treatment. Good dispersion and uniformity were also achieved upon treatment under an inert gas atmosphere at 650°C, as shown in Figures 2-13 g and h

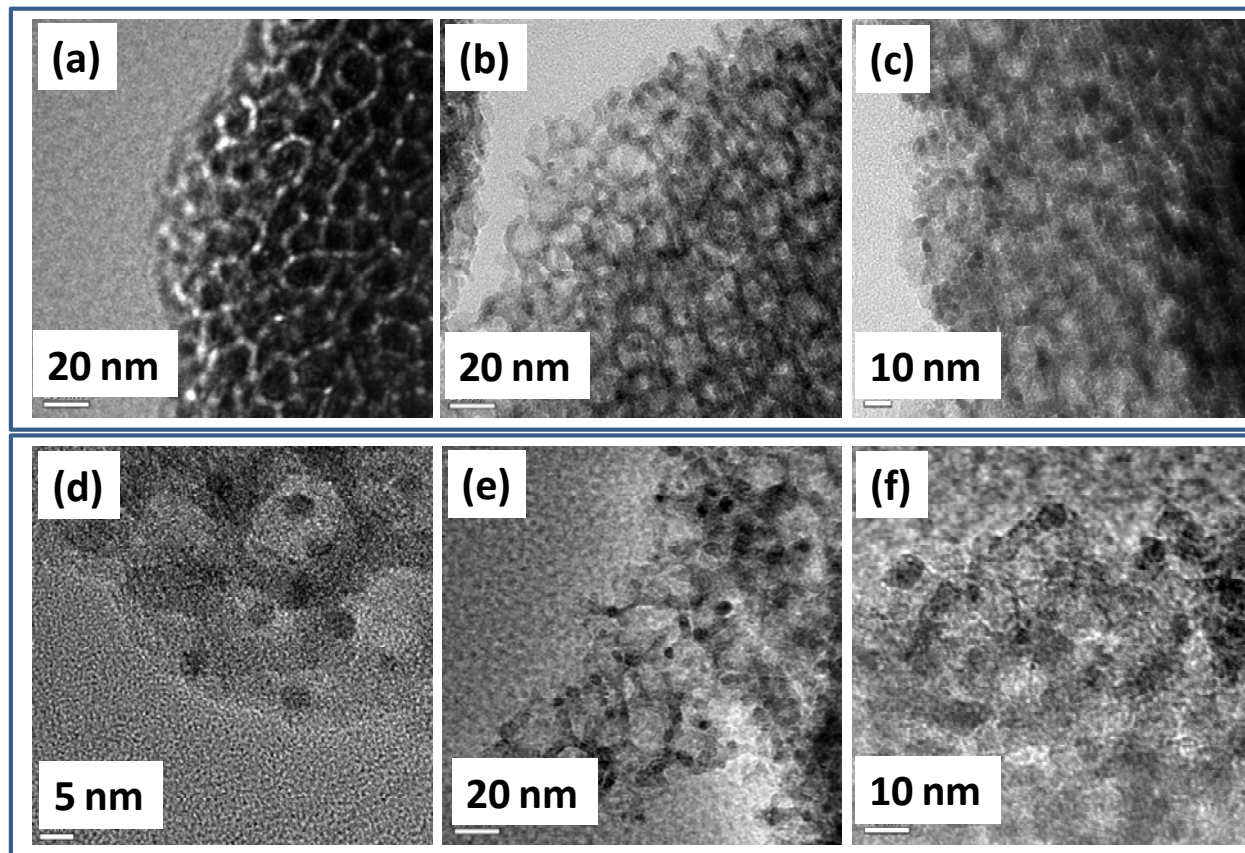
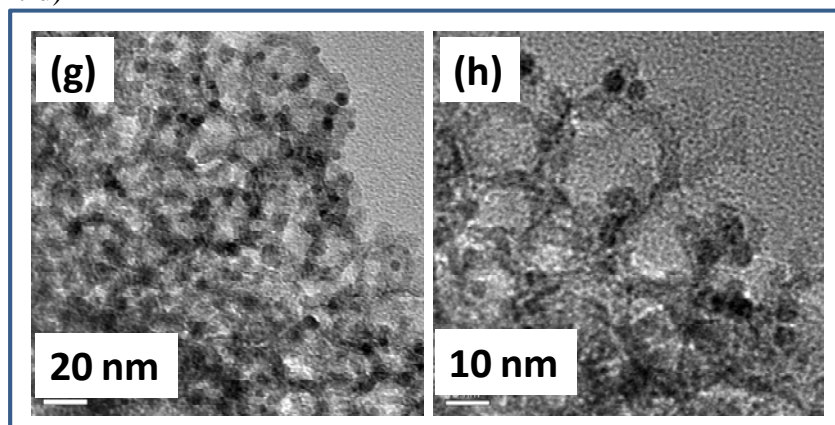


Figure 2-13 TEM images of pure MSU-F and Ru-PVP NPs supported on MSU-F. (a) pure MSU-F support; (b, c, and d) RuF-150; (e and f) RuF-350; (g and h) RuF-650.

Figure 2-13 (cont'd)



FT-IR analysis was performed on the starting material, as well as after each step of catalyst preparation, and the results are summarized in Figures 2-14.

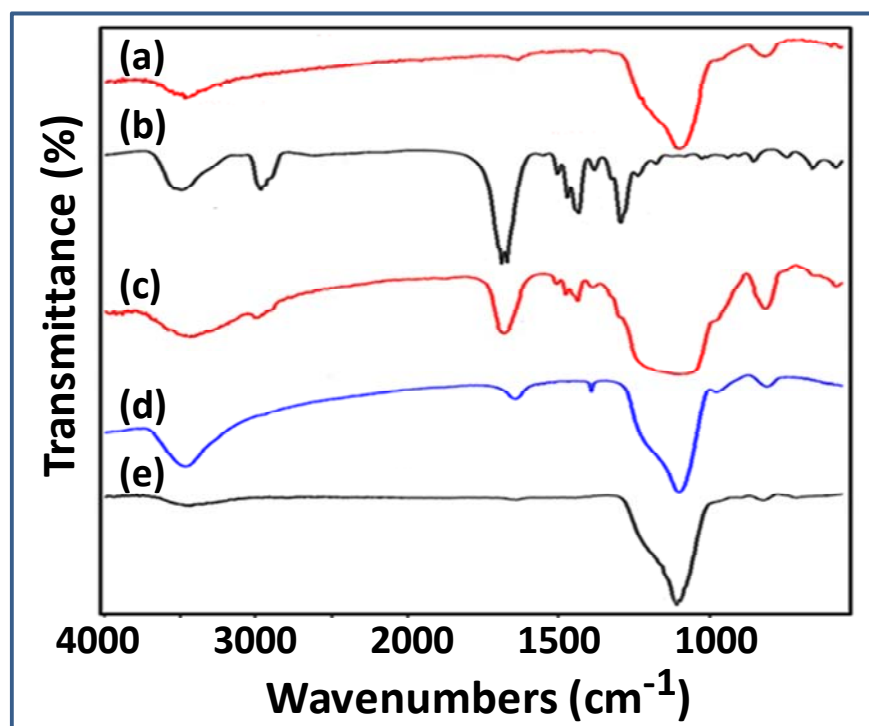


Figure 2-14 FTIR spectra of MSU-F, PVP, and Ru-PVP NPs supported on MSU-F. (a) pure MSU-F support; (b) PVP; (c) RuF-150; (d) RuF-350; and (e) RuF-650. MSU-F shows consistent characteristic peaks as in the absorption spectra (Figure 4.3-4). Pure PVP has C=O and C-N stretch bands at 1694 and 1674 cm^{-1} , asymmetric CH_2 stretches at 2950 cm^{-1} for the pyrrolidone ring and at 2922 cm^{-1} for the polymer backbone, a CH bending band at 1371 cm^{-1} , and a CH_2 scissor band at 1461 cm^{-1} ; the spectrum also contains a series of bands in the range 750 cm^{-1} to 1300 cm^{-1} , corresponding to the spectra of the C-C ring and C-C chain of PVP.

The IR spectra of MSU-F and ODA have transmission peaks in agreement with previous reports.^{58,59} RuF-150 shows the characteristic peaks of MSU-F and PVP, suggesting that only partial decomposition of the capping PVP agent occurred during the gentle oxidation treatment. The spectrum for RuF-350 in Figure 2-14 shows the characteristic peaks of MSU-F, but the disappearance of some PVP characteristic bands is an indication that PVP was completely decomposed during thermal reduction at 350°C. However, the remaining bands for the C=O stretch, C-N stretch, and CH bend (1636 cm⁻¹, 1674 cm⁻¹, and 1371 cm⁻¹, respectively) demonstrate that the decomposed PVP residuals are still attached to the surface of the Ru NPs. By contrast, the IR spectra of RuF-650 only shows the characteristic peaks for pure MSU-F, providing evidence of complete decomposition and removal of the capping polymer agent from the supported catalyst.

The TGA curves in Figure 2-15 show that the thermal decomposition of pure PVP started at about 390°C and was complete by the time the system reached 480°C, with about 95% of total weight loss. The differential thermal gravimetric (DTG) curve of pure PVP suggests that it undergoes thermal decomposition in two stages. The onset decomposition temperature of RuF-150 is close to that of pure PVP, with the total weight loss reaching a maximum of about 13% at 480°C. It is also observed that RuF-150 displays only one stage of PVP decomposition as indicated in its DTG curve. From the TGA curve of RuF-650, it can be deduced that more than 98% of the capping PVP was decomposed by heating under argon at 650°C. We observed less than 3% weight loss for RuF-350 in the TGA curve, which suggests that most of the capping

PVP agent on the Ru NPs was decomposed by calcination under hydrogen at 350°C. This temperature is lower than the decomposition temperature of pure PVP (390°C-410°C)⁶⁰.

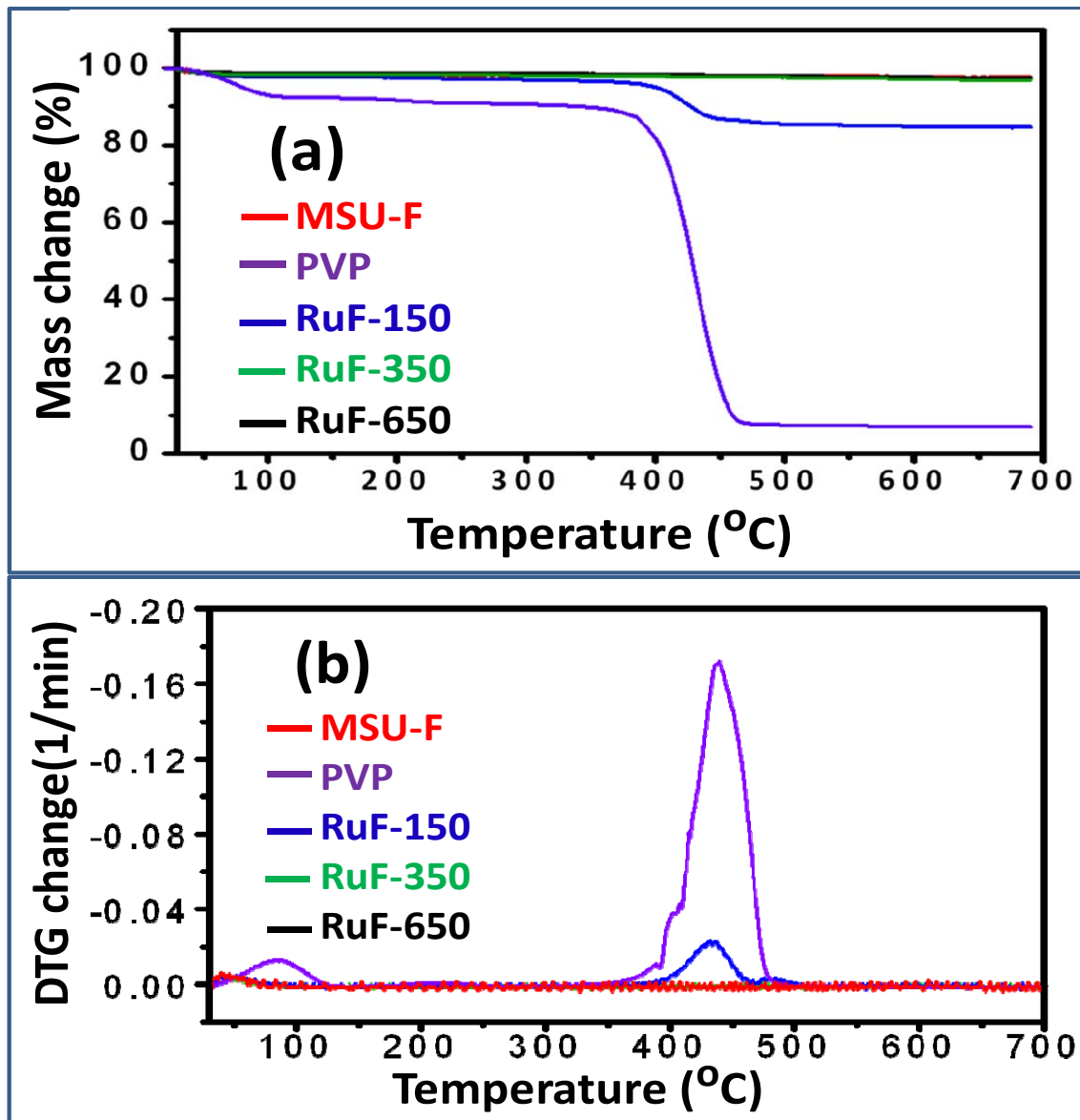


Figure 2-15 TGA analysis of MSU-F, PVP, and Ru-PVP NPs supported on MSU-F. (a) TGA curves of MSU-F, PVP, and MSU-F supported Ru-PVP NPs after thermal treatments, (b) DTG curve of each sample. MSU-F is thermally stable over the entire temperature range. The decomposition of pure PVP began at about 390°C and was complete by the time the system reached 480°C. The decomposition of RuF-150 is similar to that of pure PVP. The relatively negligible changes in the TGA and DTG curves for RuF-350 and RuF-650 are an indication of complete decomposition of PVP during the calcination process.

Powder XRD measurements (Figure 2-16) for all three preparations show a diffraction peak at $2\theta = 43.5^\circ$ characteristic of the (101) facet of hexagonal close packed, crystalline Ru metal.^{32,46}

This marker peak is weaker in RuF-150 than in RuF-350 and RuF-650, suggesting that thermal treatment under higher temperature allows more annealing and therefore greater crystallinity of Ru in the catalysts. As expected, no characteristic diffraction peaks were observed for the pure support between 2θ values of 30° and 50° .

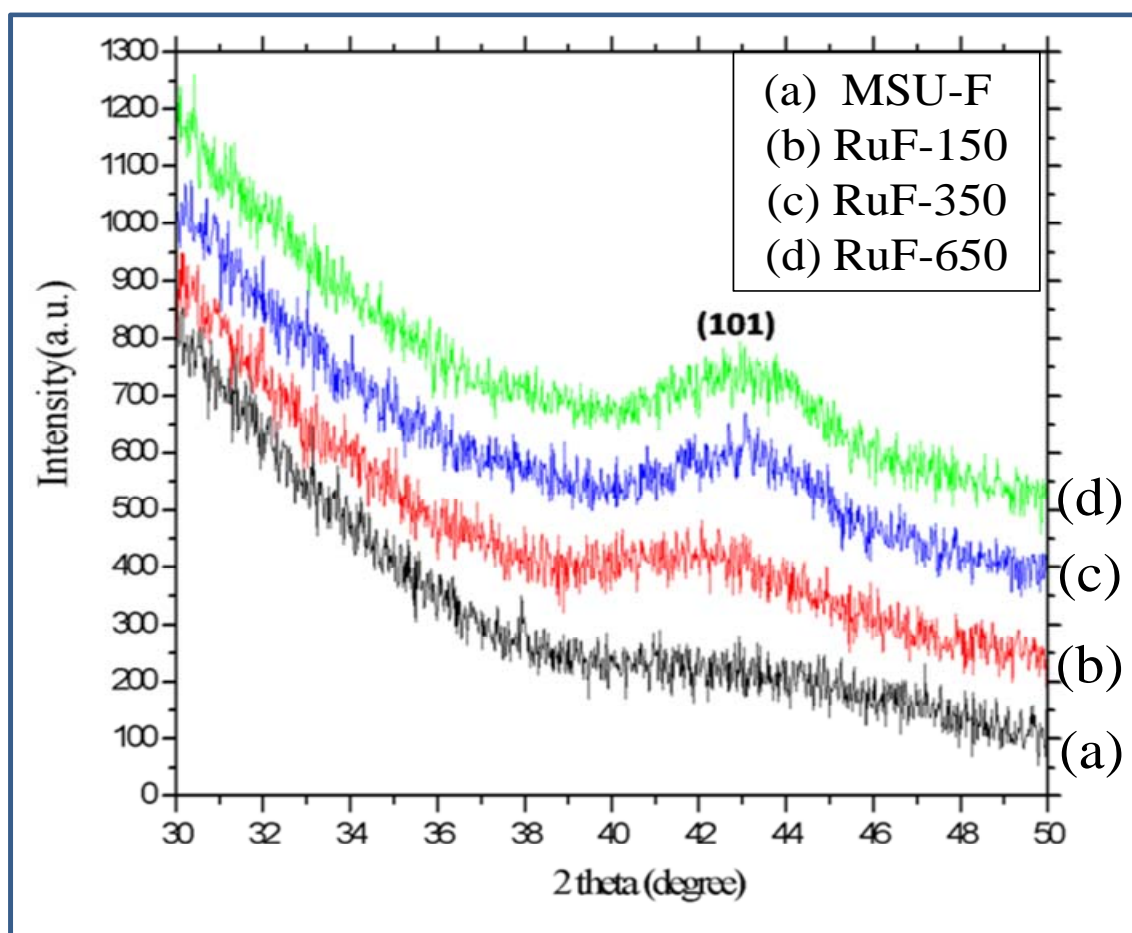


Figure 2-16 XRD patterns of pure MSU-F and Ru-PVP NPs supported on MSU-F after thermal treatment. The peak at the 2θ value of 43.5° is consistent with the (101) face of hexagonal close packed (*hcp*) Ru nanocrystals. The intensity of the peak is an indication of the crystallinity of each sample.

XPS measurements were performed on all samples to investigate the effect of thermal treatment on the atomic composition and oxidation states of the NPs. Figure 2-17 shows the XPS spectra of the catalysts in the Ru 3p region. The binding energy around 461 eV was assigned to Ru in the metallic form. The other two signals at higher binding energies (462.5 eV and 465 eV) were assigned to Ru (IV) and Ru (VI), respectively (Figure 2-17). The binding energy of metallic Ru in RuF-150 was 460.80 eV, which is slightly lower than that of standard metallic Ru (461.5 eV). This negative shift in binding energy is likely the result of the incomplete removal of the PVP capping agent. A similar effect was observed in RuF-350, likely the result of decomposed PVP residues still bonded to the surface of the Ru atoms. The binding energy of metallic Ru in RuF-650 (461.18 eV) is very close to that of the pure Ru metal, indicating that most of the capping polymer and its residues were removed at 650°C under argon. A similar trend in binding energy shift for Ru (VI) is observed among the three catalysts. The presence of Ru (IV) and Ru (VI) in all the samples indicates that Ru NPs can be easily oxidized when exposed to air, even under ambient conditions, making pre-reduction necessary prior to hydrogenation reactions.

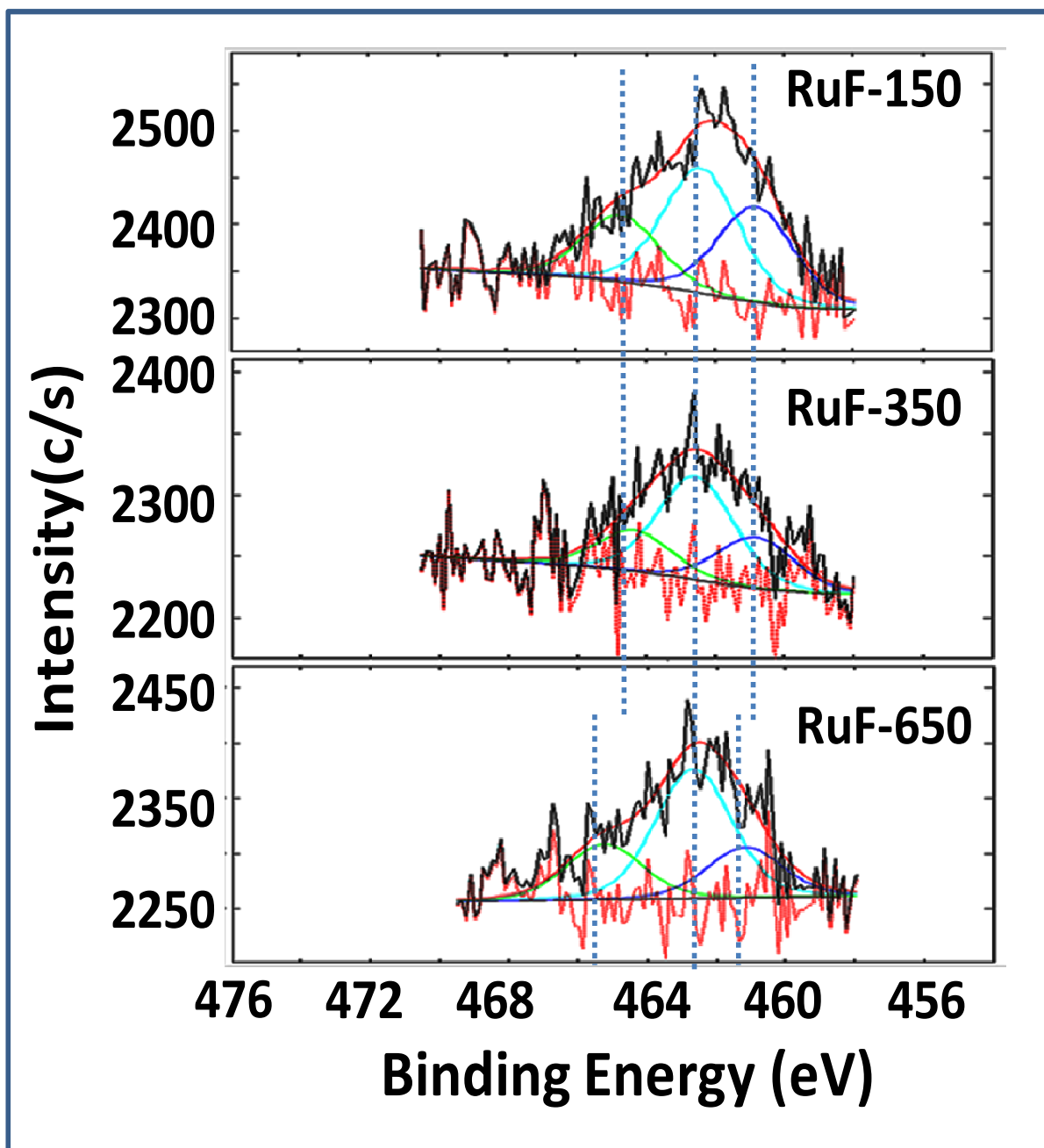


Figure 2-17 XPS spectra of Ru-PVP NPs supported on MSU-F after thermal treatments. The three characteristic peaks from high bonding energy to low in each diagram correspond to metallic Ru(0), Ru (IV) and Ru (VI). The binding energies of metallic Ru in RuF-150 and RuF-350 display a negative shift compared to that of standard metallic Ru (461.2-461.5 eV). A similar trend was observed for the binding energies of Ru (VI) in RuF-150 and RuF-350. The presence of Ru (IV) and Ru (VI) in all samples also indicates that the surface atoms of the Ru NPs can be easily oxidized when exposed to air, even under ambient conditions.

The physical properties and Ru content of the catalysts are summarized in Table 2-5, including the surface areas determined by physisorption, Ru metal content from ICP-AES characterization, metal dispersion from hydrogen adsorption, and the ratio of nitrogen to Ru atomic concentrations (N/Ru) from XPS measurements. The surface area of pure MSU-F decreased from 503 m²/g to 320 m²/g for RuF-150, possibly the result of deposition of Ru NPs inside the pores of the support as shown in the TEM image (Figure 2-13d). It is also possible that partially decomposed PVP on RuF-150 may have covered the pores on the support, leading to an apparently reduced surface area. The surface area of RuF-350 increased to 579 m²/g, and the Ru content from 0.77 wt% (RuF-150) to 0.89 wt%, which could be attributed to the migration of NPs from the inner pores to the edges of the support (Figure 2-13e). The surface area of RuF-650 increased to 649 m²/g, but the Ru content decreased to 0.42 wt%, the lowest among the three. The increase in surface area for RuF-650 relative to RuF-350 suggests complete removal of decomposed PVP residues from nanoparticle surfaces. The decreased Ru content is likely the result of formation of low boiling point compounds from surface Ru atoms and decomposed PVP residues, based on other studies in the published literature.^{46,54} With partially decomposed PVP surrounding the Ru NPs, RuF-150 has a metal dispersion of approximately 2.5%. This value increased by 7.5-fold (to 18.6%) for RuF-650. The increase can be attributed to complete removal of PVP at 650°C. On the other hand, the metal dispersion of RuF-350 decreased to 0.55% relative to the value for RuF-150. The most logical explanation for this is that the residues of degraded PVP were still attached to the Ru surface. A nitrogen to ruthenium (N: Ru) molar ratio of 7.36 was calculated from the peak intensities in the XPS spectra for RuF-150. By contrast, the ratios for RuF-350 and

RuF-650 were negligible, suggesting that the N-containing PVP side rings were eliminated during calcination.

Table 2-5 Physical properties MSU-F supported Ru-PVP NPs after thermal treatments

Sample ID	BET Surface area ^a (m ² g ⁻¹)	Ru content ^b (wt%)	Metal dispersion ^c (%)	N/Ru atomic ratio ^d
MSU-F	503.33 ± 1.20	---	---	---
Ru/SiO ₂	139.64± 0.78	1.32±0.02	17.55±1.37	---
RuF-150	320.70 ± 7.38	0.77±0.01	2.49±0.88	7.36
RuF-350	579.23 ± 1.48	0.89±0.03	0.55±0.57	0.00
RuF-650	649.89± 1.59	0.42±0.01	18.65±0.43	0.00

^aFrom N₂ adsorption. ^bFrom ICP-AES. ^cFrom H₂ adsorption results. ^dBased on intensities of Ru 3p and N 1s peaks in XPS analysis.

2.5.3. Reactivity Assessment of Ru-PVP NPs supported on MSU-F

The activity of the Ru catalysts was assessed using the aqueous phase hydrogenation of PyA to LA. The catalyst loading and Ru loading in each catalyst are listed in Table 2-6. The reaction conditions are described in Figure 2-18.

Figure 2-18a shows the conversion profiles as a function of reaction time at 45°C for pure MSU-F, commercial Ru/SiO₂, and the three thermally-treated Ru nanocatalysts supported on MSU-F. A 100% selectivity to LA was observed in all the reactions. Less than 5% of the PyA was converted in 7 h with pure MSU-F, indicating that the reaction is catalytic. Both the commercial Ru/SiO₂ and RuF-650 achieved complete conversion within 3 h, while RuF-150 and RuF-350 required 5 h. These results compare favorably to previous reports on the catalytic performance of

nanocatalysts for PyA hydrogenation in ethanol-water mixtures at 100°C and 10 bar hydrogen pressure.⁵⁶

Figure 2-18b is a plot of substrate (PyA) concentration as a function of reaction time for pure MSU-F, commercial Ru/SiO₂ and the three treated Ru nanocatalysts. The initial reaction rates (mM PyA per h) and activities (mmol PyA per g of Ru catalyst per hour) of the Ru catalysts were calculated by regressing each of the data collected during the first two hours of reaction, and calculating the derivatives at time zero. The results, summarized in Table 2-6, show that all three Ru nanocatalysts prepared in this study demonstrated higher activity than the commercial Ru/SiO₂ catalyst.

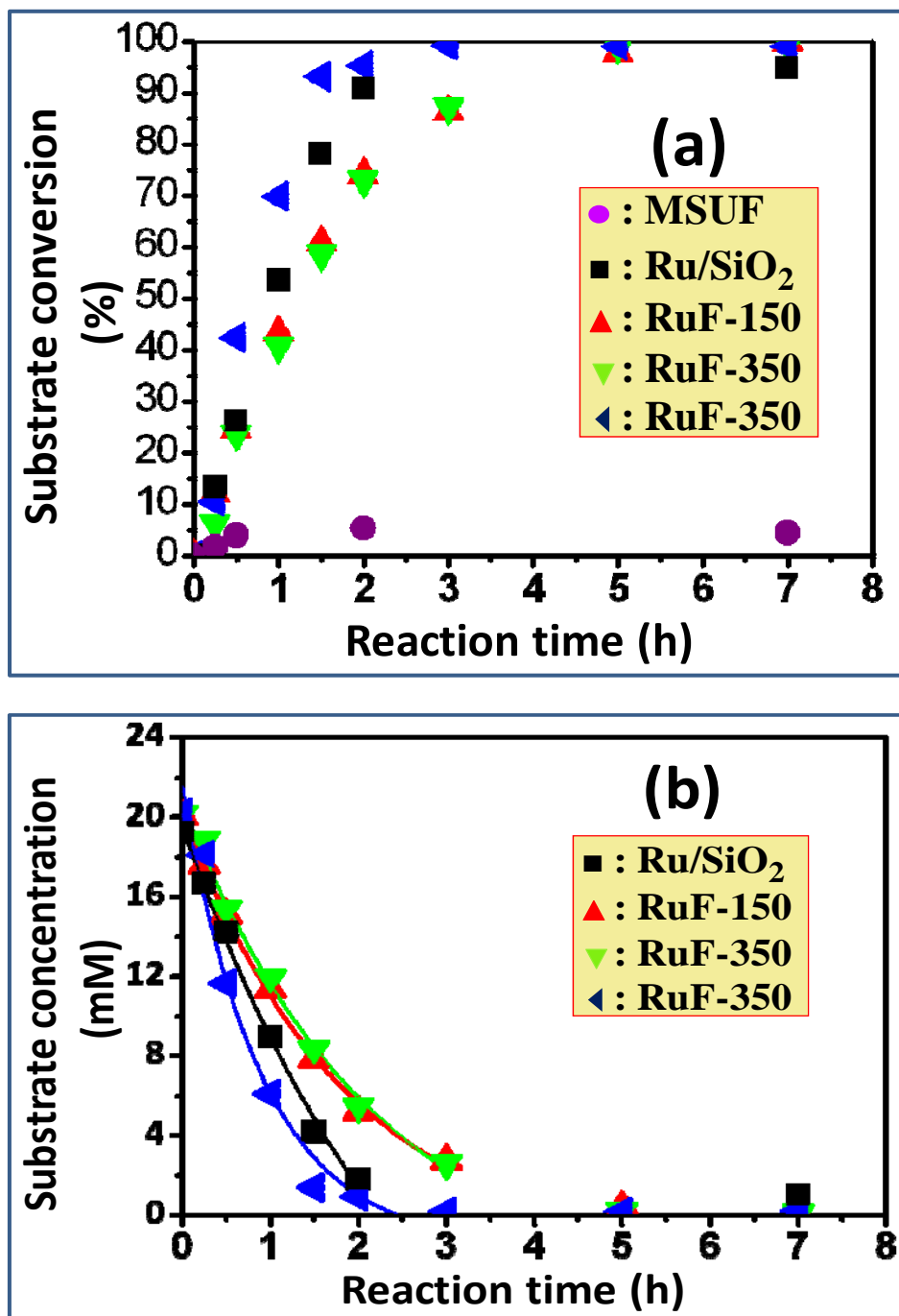


Figure 2-18 Reaction profiles of PyA hydrogenation over Ru-PVP NPs supported on MSU-F. (a) PyA conversion vs reaction time for different catalysts; (b) PyA concentration vs reaction time. The solid lines are the polynomial regressions of each data set. Reaction conditions: $T = 45^{\circ}\text{C}$; $P(\text{H}_2) = 5.0 \text{ bar}$; 35 ml of PyA in water (20 mM). All catalysts were pretreated at 150°C overnight under H_2 pressure of 33.4 bar.

Table 2-6 Activities of MSU-F supported Ru-PVP NPs for PyA hydrogenation.

Sample ID	Amount of catalyst ^a ($\times 10^1$ mg)	Ru loading ^b ($\times 10^{-2}$ mg)	Reaction rate ^c (mM PyA h ⁻¹)	Activity ^d ($\times 10^3$ mmol PyA g _{Ru} ⁻¹ h ⁻¹)
MSU-F	5.00	---	---	---
Ru/SiO ₂	2.90	38.28	12.48 \pm 1.34	1.14 \pm 0.12
RuF-150	3.11	39.50	11.93 \pm 0.06	1.93 \pm 0.01
RuF-350	5.34	38.29	11.30 \pm 0.24	1.85 \pm 0.04
RuF-650	4.91	38.40	25.25 \pm 0.49	4.13 \pm 0.08

^aTotal weight of catalyst in corresponding system. ^bCalculated from catalyst loading (g) and Ru content (wt. %) from ICP-AES measurements on the corresponding catalyst. ^cInitial reaction rate of substrate. ^dInitial activity was calculated as the consumption of PyA in mmol per g of Ru per h.

The activity of RuF-650 is nearly three times that of the commercial Ru/SiO₂ supported catalyst, and twice as high as RuF-150 and RuF-350. This can be attributed to the much better accessibility to surface catalytic sites following the complete decomposition and removal of the PVP capping agent, and to the much better dispersion of the nanocatalysts on the support. The activities of RuF-150 and RuF-350 are about 1.5 times higher than the commercial Ru/SiO₂ catalyst, even though their metal dispersions are comparatively lower. The fact that metal dispersion does not necessarily predict catalytic activity in the aqueous phase could be attributed to the behavior of catalysts in different media.

2.6. Summary

We have developed and systematically evaluated three solution-based routes to synthesize uniform colloidal Ru NPs. All the Ru NPs are spherical with narrow size distributions. Thermal decomposition of organometallic compounds ($\text{Ru}_3(\text{CO})_{12}$) using thioether (nDS) as stabilizer can produce monodisperse Ru NPs with high stability in non-polar solvents (toluene). However, this method leads to a slow reaction rate and a low yield of Ru NPs from expensive metal precursors. In addition, harsh conditions are required to remove the stabilizing thioether compound from the supported NPs. The phase-transfer method readily reduces cheaper Ru salts only soluble in hydrophilic media and produces hydrophobic amine-stabilized Ru NPs in high yield and in a much shorter reaction time. However, the process is difficult to control due to the fast reaction rate. On the other hand, the polyol reduction method enables synthesis of Ru NPs with high yield in a moderate reaction time over a broad range of reaction temperatures. Also, the polymer stabilizer contains no poisonous elements in the Ru catalyst. Among the three synthetic routes, polyol reduction offers the best way of easily controlling the morphology and composition of the Ru NPs, simply by manipulating synthesis parameters.

MSU-F has proven to be better than activated carbon as a support for heterogeneous catalysts. The sonication-assisted colloidal deposition method has several advantages over direct colloidal deposition for immobilization of Ru NPs onto supports. By comparing the reactivity and various properties of the supported Ru nanocatalysts treated in different ways, we concluded that calcination at 650°C under an inert gas is the best thermal treatment for removing the capping agent from Ru nanocatalysts supported on MSU-F.

REFERENCES

REFERENCES

- (1) Astruc, D. Rhodium and Ruthenium nanoparticles in catalysis. *Nanoparticles and Catalysis*, 2007, *11*, 349-388.
- (2) Koh, A. C. W.; Leong, W. K.; Chen, L. W.; Ang, T. P.; Lin, J.; Johnson, B. F. G.; Khimyak, T. Highly efficient ruthenium and ruthenium-platinum cluster-derived nanocatalysts for hydrogen production via ethanol steam reforming. *Catalysis Communications*, 2008, *9*, 170-175.
- (3) Braden, D. J.; Henao, C. A.; Heltzel, J.; Maravelias, C. T.; Dumesic, J. A. Production of liquid hydrocarbon fuels by catalytic conversion of biomass-derived levulinic acid. *Green Chemistry*, 2011, *13*, 1755-1765.
- (4) Deng, W. P.; Tan, X. S.; Fang, W. H.; Zhang, Q. H.; Wang, Y. Conversion of Cellulose into Sorbitol over Carbon Nanotube-Supported Ruthenium Catalyst. *Catalysis Letters*, 2009, *133*, 167-174.
- (5) Yoon, S. J.; Kim, Y. K.; Lee, J. G. Catalytic Oxidation of Biomass Tar over Platinum and Ruthenium Catalysts. *Industrial & Engineering Chemistry Research*, 2011, *50*, 2445-2451.
- (6) Yan, X. P.; Liu, H. F.; Liew, K. Y. Size control of polymer-stabilized ruthenium nanoparticles by polyol reduction. *Journal of Materials Chemistry*, 2001, *11*, 3387-3391.
- (7) Harpeness, R.; Peng, Z.; Liu, X. S.; Pol, V. G.; Koltypin, Y.; Gedanken, A. Controlling the agglomeration of anisotropic Ru nanoparticles by the microwave-polyol process. *Journal of Colloid and Interface Science*, 2005, *287*, 678-684.
- (8) Lu, F.; Liu, J.; Xu, J. Synthesis of chain-like Ru nanoparticle arrays and its catalytic activity for hydrogenation of phenol in aqueous media. *Materials Chemistry and Physics*, 2008, *108*, 369-374.
- (9) He, B. L.; Chen, Y. X.; Liu, H. F.; Liu, Y. Synthesis of solvent-stabilized colloidal nanoparticles of platinum, rhodium, and ruthenium by microwave-polyol process. *Journal of Nanoscience and Nanotechnology*, 2005, *5*, 266-270.
- (10) Viau, G.; Brayner, R.; Poul, L.; Chakroune, N.; Lacaze, E.; Fievet-Vincent, F.; Fievet, F. Ruthenium nanoparticles: Size, shape, and self-assemblies. *Chemistry of Materials*, 2003, *15*, 486-494.

- (11) Joo, S. H.; Park, J. Y.; Renzas, J. R.; Butcher, D. R.; Huang, W. Y.; Somorjai, G. A. Size Effect of Ruthenium Nanoparticles in Catalytic Carbon Monoxide Oxidation. *Nano Letters*, 2010, 10, 2709-2713.
- (12) Tsukatani, T.; Fujihara, H. New method for facile synthesis of amphiphilic thiol-stabilized ruthenium nanoparticles and their redox-active ruthenium nanocomposite. *Langmuir*, 2005, 21, 12093-12095.
- (13) Yang, J.; Lee, J. Y.; Deivaraj, T. C.; Too, H. P. Preparation and characterization of positively charged ruthenium nanoparticles. *Journal of Colloid and Interface Science*, 2004, 271, 308-312.
- (14) Chakroune, N.; Viau, G.; Ammar, S.; Poul, L.; Veautier, D.; Chehimi, M. M.; Mangeney, C.; Villain, F.; Fievet, F. Acetate- and thiol-capped monodisperse ruthenium nanoparticles: XPS, XAS, and HRTEM studies. *Langmuir*, 2005, 21, 6788-6796.
- (15) Katarzyna Morawa Eblagon, T. V.-S., K.M. Kerry Yu, Anibal J. Ramirez-Cuesta, Shik Chi Tsang Size-controlled preparation of ruthenium nanoparticles using polyaromatic amine-containing compounds as hydrogenation nanocatalyst precursors. *International Journal of Nanoparticles*, 2010, 3, 104-122.
- (16) Chen, Y.; Liew, K. Y.; Li, J. L. Size-controlled synthesis of Ru nanoparticles by ethylene glycol reduction. *Materials Letters*, 2008, 62, 1018-1021.
- (17) Pelzert, K.; Laleu, B.; Lefebvre, F.; Philippot, K.; Chaudret, B.; Candy, J. P.; Basset, J. M. New Ru nanoparticles stabilized by organosilane fragments. *Chemistry of Materials*, 2004, 16, 4937-4941.
- (18) Pelzer, K.; Vidoni, O.; Philippot, K.; Chaudret, B.; Colliere, V. Organometallic synthesis of size-controlled polycrystalline ruthenium nanoparticles in the presence of alcohols. *Advanced Functional Materials*, 2003, 13, 118-126.
- (19) Jansat, S.; Picurelli, D.; Pelzer, K.; Philippot, K.; Gomez, M.; Muller, G.; Lecante, P.; Chaudret, B. Synthesis, characterization and catalytic reactivity of ruthenium nanoparticles stabilized by chiral N-donor ligands. *New Journal of Chemistry*, 2006, 30, 115-122.
- (20) Tristany, M.; Chaudret, B.; Dieudonne, P.; Guari, Y.; Lecante, P.; Matsura, V.; Moreno-Manas, M.; Philippot, K.; Pleixats, R. Synthesis of ruthenium nanoparticles stabilized by heavily fluorinated compounds. *Advanced Functional Materials*, 2006, 16, 2008-2015.
- (21) Brink, M. V.; Peck, M. A.; More, K. L.; Hoefelmeyer, J. D. Alkylamine stabilized ruthenium nanocrystals: Faceting and branching. *Journal of Physical Chemistry C*, 2008, 112, 12122-12126.

- (22) Narayanan, R.; El-Sayed, M. A. Carbon-supported spherical palladium nanoparticles as potential recyclable catalysts for the Suzuki reaction. *Journal of Catalysis*, 2005, 234, 348-355.
- (23) Campelo, J. M.; Luna, D.; Luque, R.; Marinas, J. M.; Romero, A. A. Sustainable Preparation of Supported Metal Nanoparticles and Their Applications in Catalysis. *Chemsuschem*, 2009, 2, 18-45.
- (24) White, R. J.; Luque, R.; Budarin, V. L.; Clark, J. H.; Macquarrie, D. J. Supported metal nanoparticles on porous materials. Methods and applications. *Chemical Society Reviews*, 2009, 38, 481-494.
- (25) Zawadzki, M.; Okal, J. Synthesis and structure characterization of Ru nanoparticles stabilized by PVP or gamma-Al₂O₃. *Materials Research Bulletin*, 2008, 43, 3111-3121.
- (26) Montassier, C.; Menezo, J. C.; Hoang, L. C.; Renaud, C.; Barbier, J. Aqueous polyol conversions on ruthenium and on sulfur-modified ruthenium. *Journal of Molecular Catalysis*, 1991, 70, 99-110.
- (27) Lahr, D. G.; Shanks, B. H. Effect of sulfur and temperature on ruthenium-catalyzed glycerol hydrogenolysis to glycols. *Journal of Catalysis*, 2005, 232, 386-394.
- (28) Osada, M.; Hiyoshi, N.; Sato, O.; Arai, K.; Shirai, M. Subcritical water regeneration of supported ruthenium catalyst poisoned by sulfur. *Energy & Fuels*, 2008, 22, 845-849.
- (29) Schwarz, J. A. Adsorption-desorption kinetics of H₂ from clean and sulfur covered Ru(001). *Surface Science*, 1979, 87, 525-538.
- (30) Rodriguez, J. A.; Hrbek, J. Interaction of sulfur with well-defined metal and oxide surfaces: Unraveling the mysteries behind catalyst poisoning and desulfurization. *Accounts of Chemical Research*, 1999, 32, 719-728.
- (31) Yang, J.; Lee, J. Y.; Ying, J. Y. Phase transfer and its applications in nanotechnology. *Chemical Society Reviews*, 2011, 40, 1672-1696.
- (32) Yang, J.; Ying, J. Y. A general phase-transfer protocol for metal ions and its application in nanocrystal synthesis. *Nature Materials*, 2009, 8, 683-689.
- (33) Zhang, J.; Ting, B. P.; Koh, Y. T.; Ying, J. Y. Synthesis of Metallic Nanoparticles Using Electrogenerated Reduced Forms of alpha-SiW(12)O(40) (4-) as Both Reductants and Stabilizing Agents. *Chemistry of Materials*, 2011, 23, 4688-4693.

- (34) Yuan, X.; Luo, Z. T.; Zhang, Q. B.; Zhang, X. H.; Zheng, Y. G.; Lee, J. Y.; Xie, J. P. Synthesis of Highly Fluorescent Metal (Ag, Au, Pt, and Cu) Nanoclusters by Electrostatically Induced Reversible Phase Transfer. *Acs Nano*, 2011, 5, 8800-8808.
- (35) Wang, X.; Zhuang, J.; Peng, Q.; Li, Y. D. A general strategy for nanocrystal synthesis. *Nature*, 2005, 437, 121-124.
- (36) Karkamkar, A.; Kim, S. S.; Pinnavaia, T. J. Hydrothermal restructuring of the cell and window sizes of silica foams. *Chemistry of Materials*, 2003, 15, 11-13.
- (37) Kim, S. S.; Pauly, T. R.; Pinnavaia, T. J. Non-ionic surfactant assembly of ordered, very large pore molecular sieve silicas from water soluble silicates. *Chemical Communications*, 2000, 1661-1662.
- (38) Rioux, R. M.; Song, H.; Hoefelmeyer, J. D.; Yang, P.; Somorjai, G. A. High-surface-area catalyst design: Synthesis, characterization, and reaction studies of platinum nanoparticles in mesoporous SBA-15 silica. *Journal of Physical Chemistry B*, 2005, 109, 2192-2202.
- (39) Konya, Z.; Molnar, E.; Tasi, G.; Niesz, K.; Somorjai, G. A.; Kiricsi, I. Pre-prepared platinum nanoparticles supported on SBA-15 - preparation, pretreatment conditions and catalytic properties. *Catalysis Letters*, 2007, 113, 19-28.
- (40) Zhang, F. A.; Lee, D. K.; Pinnavaia, T. J. PMMA-mesocellular foam silica nanocomposites prepared through batch emulsion polymerization and compression molding. *Polymer*, 2009, 50, 4768-4774.
- (41) Leff, D. V.; Brandt, L.; Heath, J. R. Synthesis and characterization of hydrophobic, organically-soluble gold nanocrystals functionalized with primary amines. *Langmuir*, 1996, 12, 4723-4730.
- (42) Ray, K.; Nakahara, H. Adsorption behaviour of alizarine violet molecules onto the Langmuir-Blodgett films of octadecylamine. *Physical Chemistry Chemical Physics*, 2001, 3, 4784-4790.
- (43) Gole, A.; Kumar, A.; Phadtare, S.; Mandale, A. B.; Sastry, M. Glucose induced in-situ reduction of chloroaurate ions entrapped in a fatty amine film: formation of gold nanoparticle-lipid composites. *Physchemcomm*, 2001, art. no.-19.
- (44) Park, S. J.; Li, K.; Hong, S. K. Preparation and characterization of layered silicate-modified ultrahigh-molecular-weight polyethylene nanocomposites. *Journal of Industrial and Engineering Chemistry*, 2005, 11, 561-566.
- (45) Lin, Z. Y.; Liu, Y.; Wong, C. P. Facile Fabrication of Superhydrophobic Octadecylamine-Functionalized Graphite Oxide Film. *Langmuir*, 2010, 26, 16110-16114.

(46) Su, F. B.; Lv, L.; Lee, F. Y.; Liu, T.; Cooper, A. I.; Zhao, X. S. Thermally reduced ruthenium nanoparticles as a highly active heterogeneous catalyst for hydrogenation of monoaromatics. *Journal of the American Chemical Society*, 2007, *129*, 14213-14223.

(47) Fiechter, S.; Dorbandt, I.; Bogdanoff, P.; Zehl, G.; Schulenburg, H.; Tributsch, H.; Bron, M.; Radnik, J.; Fieber-Erdmann, M. Surface modified ruthenium nanoparticles: Structural investigation and surface analysis of a novel catalyst for oxygen reduction. *Journal of Physical Chemistry C*, 2007, *111*, 477-487.

(48) Fuggle, J. C.; Madey, T. E.; Steinkilberg, M.; Menzel, D. Photoelectron spectroscopic studies of adsorption of CO and oxygen on Ru(001). *Surface Science*, 1975, *52*, 521-541.

(49) Nyholm, R.; Martensson, N. Core level binding energies for the elements Zr-Te (Z=40-52). *Journal of Physics C-Solid State Physics*, 1980, *13*, L279-L284.

(50) Arico, A. S.; Creti, P.; Kim, H.; Mantegna, R.; Giordano, N.; Antonucci, V. Analysis of the electrochemical characteristics of a direct methanol fuel cell based on a Pt-Ru/C anode catalyst. *Journal of the Electrochemical Society*, 1996, *143*, 3950-3959.

(51) Zhang, X.; Chan, K. Y. Water-in-oil microemulsion synthesis of platinum-ruthenium nanoparticles, their characterization and electrocatalytic properties. *Chemistry of Materials*, 2003, *15*, 451-459.

(52) Charles Daniel Wagner, W. M., Davis, L. E., Moulder, J. F., Muilenberg, G. E., Eds.; Handbook of x-ray photoelectron spectroscopy: a reference book of standard data for use in x-ray photoelectron spectroscopy. *Physical Electronics Division, Perkin-Elmer: Eden Prairie, MN*, 1979, *55*, 344.

(53) Bagshaw, S. A.; Bruce, I. J. Rapid calcination of high quality mesostructured MCM-41, MSU-X, and SBA-15 silicate materials: A step towards continuous processing? *Microporous and Mesoporous Materials*, 2008, *109*, 199-209.

(54) Tulevski, G. S.; Myers, M. B.; Hybertsen, M. S.; Steigerwald, M. L.; Nuckolls, C. Formation of catalytic metal-molecule contacts. *Science*, 2005, *309*, 591-594.

(55) Chen, W.; Davies, J. R.; Ghosh, D.; Tong, M. C.; Konopelski, J. P.; Chen, S. W. Carbene-functionalized ruthenium nanoparticles. *Chemistry of Materials*, 2006, *18*, 5253-5259.

(56) Luque, R.; Clark, J. H. Water-tolerant Ru-Starbon (R) materials for the hydrogenation of organic acids in aqueous ethanol. *Catalysis Communications*, 2010, *11*, 928-931.

(57) Brayner, R.; Viau, G.; Bozon-Verduraz, F. Liquid-phase hydrogenation of hexadienes on metallic colloidal nanoparticles immobilized on supports via coordination capture

by bifunctional organic molecules. *Journal of Molecular Catalysis a-Chemical*, 2002, 182, 227-238.

(58) Zhang, F.-A.; Lee, D.-K.; Pinnavaia, T. J. PMMA-mesocellular foam silica nanocomposites prepared through batch emulsion polymerization and compression molding. *Polymer*, 2009, 50, 4768-4774.

(59) Borodko, Y.; Habas, S. E.; Koebel, M.; Yang, P. D.; Frei, H.; Somorjai, G. A. Probing the interaction of poly(vinylpyrrolidone) with platinum nanocrystals by UV-Raman and FTIR. *Journal of Physical Chemistry B*, 2006, 110, 23052-23059.

(60) Borodko, Y.; Lee, H. S.; Joo, S. H.; Zhang, Y. W.; Somorjai, G. Spectroscopic Study of the Thermal Degradation of PVP-Capped Rh and Pt Nanoparticles in H₂ and O₂ Environments. *Journal of Physical Chemistry C*, 2010, 114, 1117-1126.

Chapter 3: Effect of the size of Ru nanoparticles on the liquid phase hydrogenation of cinnamaldehyde

Abstract

We investigated the effect of particle size on the catalytic activity of the supported Ru NPs, using the liquid phase hydrogenation of cinnamaldehyde (CAL) as the model reaction. The size-tunable colloidal Ru NPs were produced via extension of polyol reduction to various synthesis conditions. It was observed that the formation of Ru NPs can occur under either thermodynamic or kinetic control, with the final size of the NPs determined by a balance between the two pathways. After sonication-assisted deposition of the size-tunable Ru NPs on MSU-F and subsequent Ar-protected calcination, we observed that the NPs were well-dispersed on the support with no signs of agglomeration and no damage to the ordered structure of the support. The uniformity and crystallinity of the supported Ru NPs in each catalyst also improved, possibly due to sintering and annealing effects during the thermal treatments. The primary product of CAL hydrogenation over all the supported Ru NPs was cinnamyl alcohol (COL), and variation in the size of the NPs did not affect product selectivity. The relationship between the size of the Ru NPs and their reactivities was non-linear, indicating that not all the surface atoms of the NPs were active sites.

3.1. Introduction

Selective hydrogenation of α,β -unsaturated aldehydes is an important catalytic process for the industrial production of fine chemicals used for pharmacological products, perfumes, and flavors.¹⁻⁵ A fundamental understanding of the mechanisms for competitive hydrogenation of C=C and C=O bonds in α,β -unsaturated aldehydes offers the opportunity to design efficient catalysts for converting unsaturated aldehydes to more desirable products. Many studies have been conducted to investigate the factors governing the hydrogenation pathways of α,β -unsaturated aldehydes in heterogeneous catalysis, including the type of metal(s),² surface structures of the metal and pore accessibility of the supports,⁶⁻¹⁶ steric hindrance to adsorption of substrates on metallic surfaces,^{5,7-9,17} and effects of promoters.^{2,18,19}

In this work, we use cinnamaldehyde (CAL) as the probe molecule to investigate the correlation between Ru NP size and catalytic performance for hydrogenation of α, β -unsaturated aldehydes. This reaction has been studied previously using traditional Ru catalysts.²⁰⁻²⁸ However, in this study, by using Ru NPs of relatively uniform size, it is possible to do a more quantitative and rational investigation of the effect of particle size on catalytic performance. The size-tunable Ru NPs ranged from 3.5 nm to 130 nm were synthesized using the polyol reduction method described previously. Control of particle size was achieved by varying a number of synthesis parameters, including temperature, type of Ru precursor, and precursor to stabilizer ratios. The resulting Ru NPs were immobilized onto a mesoporous silica support (MSU-F) and activated by the Ar-protected calcination protocol described in Chapter 2. Several physical and chemical techniques were used to characterize the colloidal and supported Ru NPs in each size group. Experiments to assess the reaction sensitivity of CAL hydrogenation to Ru particle size were

conducted in a stirred batch reactor system. We quantified the effect of size on a number of key kinetic parameters, including reactivity, selectivity, and activation energy.

3.2. Experimental materials and methods

Methanol (reagent grade, 99.9%), isopropanol (HPLC grade, 99.9%), polyvinylpyrrolidone (PVP, MW: 55K), acetone (ACS reagent, $\geq 99.5\%$), and ordered mesoporous silica (MSU-F) were purchased from Sigma-Aldrich (St. Louis, MO). Ruthenium acetylacetonate [Ru(acac)₃] (99%), dichlorotricarbonylruthenium (II) dimer, 98% [RuCl₂(CO)₃]₂ and palladium acetylacetonate ([Pd(acac)₂], 99%) were purchased from Strem Chemicals (Newburyport, MA). Phenyl ether (99%) and 1,4-butanediol (99%) were purchased from Alfa Aesar (Ward Hill, MA). High purity argon gas (99.99%) was purchased from Airgas (Lansing, MI). All chemicals were used without further purification. Copper grids with 3-nm carbon film coatings for TEM analysis were purchased from Ted Pella, Inc. (Redding, CA).

3.2.1. Synthesis of size-tunable colloidal Ru NPs

We conducted comprehensive studies using the polyol reduction method described in Chapter 2 to synthesize size-tunable Ru NPs. First, we studied the role of the polyol reduction temperature in controlling the size of Ru NPs. In a typical synthesis, 0.079 g Ru(acac)₃ (0.2×10^{-3} mol) and 0.222 g PVP (0.4×10^{-5} mol) were dissolved in 20 mL of 1,4-butanediol in a 50 mL round bottom Schlenk flask equipped with a reflux condenser and a Teflon-coated magnetic stirring. The solution was heated from room temperature to 125°C and evacuated at this temperature for 10

min under magnetic stirring. Argon was then introduced, and the solution was heated to the desired temperature to initiate the reaction. The reaction temperature was adjusted from 130°C to 200°C. To monitor the progression of each reaction, 0.2 ml of sample was periodically retrieved from the reaction mixture using a long needle syringe, mixed with acetone to form a suspension, and centrifuged to determine the color of the supernatant. The reaction was terminated when the supernatant became colorless.

We then used a combination of Ru (II) and (III) salts as the metal precursors to control the size of the colloidal Ru NPs. In a standard synthesis, a mixture of metal precursors containing Ru (II) salt (dichlorotricarbonylruthenium (II) dimer) and Ru(III) salt (Ru(acac)₃ and 0.222 g PVP (0.4x10⁻⁵ mol) were placed in a 50 mL round bottom Schlenk flask equipped with a reflux condenser and a Teflon-coated magnetic stirring bar, followed by addition of 20 mL of 1,4-butanediol to dissolve the chemicals. The amounts of Ru(II) and Ru(III) were pre-calculated to obtain a constant total Ru concentration of 10 mM in the reaction solution. The solution was heated from room temperature to 125°C and evacuated at this temperature for 10 min under magnetic stirring. Argon was then introduced, and the solution was heated to 150°C to initiate the reaction.

The influence of stabilizer molecular weight and stabilizer to precursor ratio was also investigated. The stabilizer to precursor ratio was adjusted, using Ru(III) as the sole precursor and varying the amount of PVP stabilizer. All reactions were conducted at 150°C. We also studied the effects of the molecular weight of the PVP stabilizer (29K and 55K) on the size of NPs. The reactions were conducted at 150°C, with a stabilizer to precursor ratio of 200 to 1.

Finally, we investigated how the addition of seed (previously-synthesized NPs) affects the particle size (seed-mediated growth). Ru NPs (3.5 nm) prepared via the protocol described in Chapter 2 were used as the seeds. In a typical synthesis, a target volume of the as-prepared colloidal seeds and calculated amounts of Ru(acac)₃ and 0.222 g PVP were added to a 50 mL Schlenk flask equipped with a reflux condenser and a Teflon-coated magnetic stirring bar. Ten (10) mL 1,4-butanediol was then added to form the reaction mixture. The mixture was heated from room temperature to 130°C and evacuated at this temperature for 10 min under magnetic stirring. Argon was then introduced, and the solution was heated to 170°C and maintained at that temperature for 1.5 h.

All the Ru NPs synthesized in each run were purified by repeated precipitation-centrifugation, followed by re-dispersion in 20 mL of methanol prior to further experiments.

3.2.2. Preparation of size-tuned Ru NPs supported on MSU-F

Ru catalysts supported on MSU-F were prepared via the sonication-assisted deposition method described in Chapter two. The Ar-protected calcination procedure was used to remove the capping PVP stabilizer from the supported NPs to activate the catalysts.

3.2.3. Characterization of different size groups of Ru NPs supported on MSU-F

The structures and morphologies of the supported catalysts were analyzed using a Model JEOL 2200FS electron microscope (Tokyo, Japan) under the operation conditions described in Chapter 2. The chemical compositions of the supported catalysts were determined by ICP-AES on an Agilent 720 Series ICP-AES Spectrometer. The specific surface areas and average pore diameters of the catalysts were determined by nitrogen adsorption–desorption measurements

carried out at liquid nitrogen temperature (~78K) with a Micromeritics ASAP 2010 M instrument. X-ray diffraction (XRD) patterns were obtained using a Bruker D8 diffractometer with Ru K α source. Infrared spectra of the samples were obtained on a Mattson Galaxy FT-IR spectrometer (Mattson Instruments, Madison, WI) using KBr pellets. In a typical experiment for H₂ chemisorption, the catalyst was first flushed with helium at 110°C for 30 min, and then reduced by H₂ at 350°C for 60 min, followed by evacuation at 360°C for 90 min. After cooling to 35°C, the catalysts were evacuated again for 30 min before analysis at 35°C. The total number of exposed Ru atoms in each catalyst was calculated from the amount of H₂ adsorbed and extrapolated to zero pressure, assuming a one-to-one stoichiometry of H to Ru surface atom.²⁹ A similar procedure was used for CO chemisorption experiments.

3.2.4. General procedure for catalytic experiments and assessments

All the catalytic hydrogenations were conducted in a Parr multi-batch reactor system (Model 5000, Parr Instrument Co., Moline, Illinois) equipped with a magnetically-coupled stirring unit. The system contains six 75 mL reactors, each equipped with a heating mantle and sampling port. In a typical experiment, the target quantity of catalyst was pre-reduced in the reactor by purging with nitrogen, heating to 150°C, charging with hydrogen to 3.4 MPa, and holding for 12 h. After cooling the system to room temperature and flushing it with nitrogen, 35 mL of CAL in isopropyl alcohol (IPA) was charged into the reactor from a sample cylinder under nitrogen pressure. When the reaction stabilized at the target temperature, the reactor was pressurized with hydrogen gas at 2.0 MPa to initiate the reaction. To monitor the progress of the reaction, liquid

samples (2 mL) were withdrawn periodically and analyzed by a Bruker 450 GC-FID equipped with a DB-1 capillary column. Prior to GC analysis, each sample was centrifuged at 300RPM for 3 min to remove the solid catalyst.

3.3. Results and Discussion

3.3.1. Conditions used to synthesize size-tunable colloidal Ru NPs

Formation of colloidal metal NPs is generally considered to involve two consecutive stages: nucleation and particle growth.³⁰⁻³² Nucleation can take place in a homogeneous process where seed particles are formed *in situ* to initiate particle growth; or in a heterogeneous process where pre-synthesized particles are added to serve as nucleation sites for particle growth. The subsequent growth of metal particles from seed can occur via conventional monomer addition in which the nuclei can grow by attracting molecular precursors from the surrounding solution. It could also be achieved through multiple coalescence, in which several preformed small particles combine and re-crystallize to form new larger particles.^{31,33-36}

The two stages are controlled by thermodynamics, kinetics or a combination of the two. The final morphology (size/shape) of the NPs is determined by a balance between the thermodynamic and kinetic pathways in the stepwise nucleation and growth stages. Under thermodynamic control, which is characterized by fast equilibrated nucleation and growth, the equilibrium particles with the lowest overall surface energy are preferentially formed. By contrast, under non-equilibrium kinetic control, which is directly associated with the nucleation and growth rates, formation of particles is favored along the direction with lower activation energy barriers. Reaction parameters can be manipulated to regulate the balance between the kinetic and thermodynamic regimes, and thus control the morphology of the resulting NPs.^{35,37-39}

3.3.1.1. Effect of polyol reduction temperature

The reaction temperature is one of the major variables in controlling the size of NPs, since it affects both the reduction rate of metal precursors and particle formation.^{40,41} The influence of reaction temperature on the size of Ru NPs synthesized by polyol reduction was studied over a temperature range of 130 to 200°C, as shown in Table 3-1. The progress of the reaction in each experiment was monitored by observing solution color changes during synthesis. All synthesis temperatures were kept constant during each procedure by continuous heating and careful monitoring. At a synthesis temperature of 130°C, the initially red solution turned slightly to orange after 5 hours. The color of the solution gradually turned from orange to brown during the subsequent 23 hours, indicating the reduction of the Ru precursors by 1,4-butanediol and the steady formation of Ru nuclei. The brown solution gradually darkened as the reaction proceeded, and finally became black after 39 hours of reaction. It is possible that a considerable number of Ru nuclei would have been formed at this stage, in which case the subsequent reaction progress would consist mainly of particle growth. After 39 hours, 0.1 mL of sample was taken out periodically using a long needle syringe and mixed with 1 mL of acetone. The mixture was then centrifuged and the color of the supernatant was used as an indicator for the extent of the conversion of Ru precursors. It was observed that the supernatant became colorless at 70 h and did not change after that, suggesting a complete reaction. The time required for each color-change stage decreased rapidly with increased reaction temperature up to 170°C. For reactions conducted above 170°C, the time interval required for solution color change was relatively insensitive to increases in reaction temperature.

Table 3-1 Reaction progression for the synthesis of Ru NPs at different temperatures.

Sample ID	Reaction temperature (°C)	Progression of the reaction					
		Red	Orange	Brown	Dark brown	Black	Completed
00200	200	 0h	 1min	 2min	 3min	 8min	 60min
00180	180	0h	2min	3min	6min	17min	95min
00170	170	0h	12min	20min	50min	80min	130min
00150	150	0h	15min	60min	120min	180min	20h
00130	130	0h	5h	28h	35h	39h	70h

The TEM images of Ru NPs synthesized at different temperatures are presented in Figure 3-1. These figures show that all the Ru NPs are mono-disperse and near-spherical polyhedral at all synthesis temperatures. When the reaction was conducted between 170°C and 200°C, no obvious changes in particle size and size distribution were observed (T170, T180, and T200 in Figure 3-1). This is attributed to thermodynamic control in the synthesis process, since the high reaction temperature (above 170°C) facilitated fast system equilibrium.^{35,37} By contrast, particle size increased with a decrease in reaction temperatures when the reactions were conducted below 170°C (T170, T150, and T130 in Figure 3-1). We believe this is due to kinetic control predominating over thermodynamic control. In a low temperature regime, the slow rates of nucleation and particle growth result in availability of Ru atoms that can diffuse to the surface of the nuclei to induce continuous growth, leading to larger NPs.

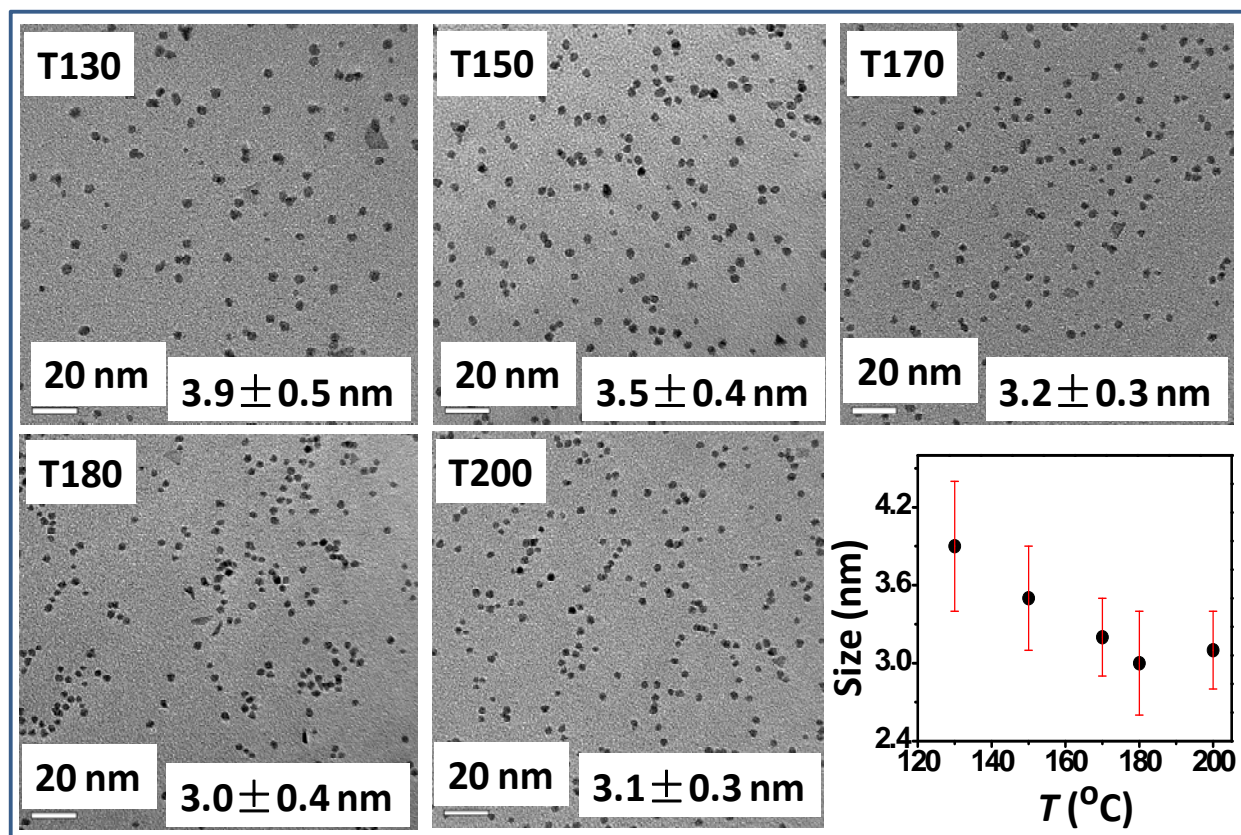


Figure 3-1 Typical TEM images of Ru NPs synthesized at different temperatures. The plot of particle size as a function of reaction temperature is also shown (inset). The size distribution of each sample was calculated by counting 200 randomly-selected NPs in each image.

3.1.1.2. Effect of Ru (II) to Ru (III) precursor ratios

To further understand the mechanism for Ru particle formation, we replaced part of the original Ru(III) precursor by the more-easily-reduced Ru (II) salt (dichlorotricarbonylruthenium (II) dimer) to assess the effect of different compositions of precursors. The mole fraction of Ru (II) salt in the total metal precursor mixture varied from 0 mol% to 100 mol%.

The TEM results on particle size and size distribution as a function of the fraction of Ru (II) in the metal precursor mixtures are presented in Figure 3-2 and Figure 3-3, respectively. When 20% of Ru (III) ions were replaced by Ru (II) in the initial precursor solution (Figure 3-2a), the final particle size was 2.8 nm, which is smaller than those obtained when pure Ru (III) ions were used as precursor (Figure 3-1, sample ID T150). It is possible that the metal reduction and nucleation

as precursor (Figure 3-1, sample ID T150). It is possible that the metal reduction and nucleation rates increased with addition of the more-easily-reduced Ru(II) salt, but the particle growth rate remained relatively unchanged due to the low percentage of precursor replacement. By contrast, when the fraction of Ru (II) was further increased in the precursor mixture, the particle size significantly increased and reached 129 nm at a Ru (II) salt fraction of 80% (Figure 3-2b-e). We believe this is because multiple coalescence events occurred in addition to monomer addition during the particle growth stage. This argument is supported by the bimodal particle size distributions when the fraction of Ru (II) was between 40% and 60%. Furthermore, the broad size distribution of Ru NPs observed in Figure 3-3 suggests that the particle growth (more specifically, multiple coalescence events) and nucleation occur simultaneously instead of in stepwise fashion. In the case of pure Ru (II) salt as a precursor, particle size was essentially the same as that of 80% Ru(II) in the precursor mixture. It is very likely that only multiple coalescence events occurred during the growth stage. The needle-like edges of the NPs visible in the HRTEM images of Figure 3-2e and 3f suggest that formation of big NPs occurs through coalescence. The EDS point spectra and elemental line scan spectra confirm the existence of Ru elements in each size of the NPs.

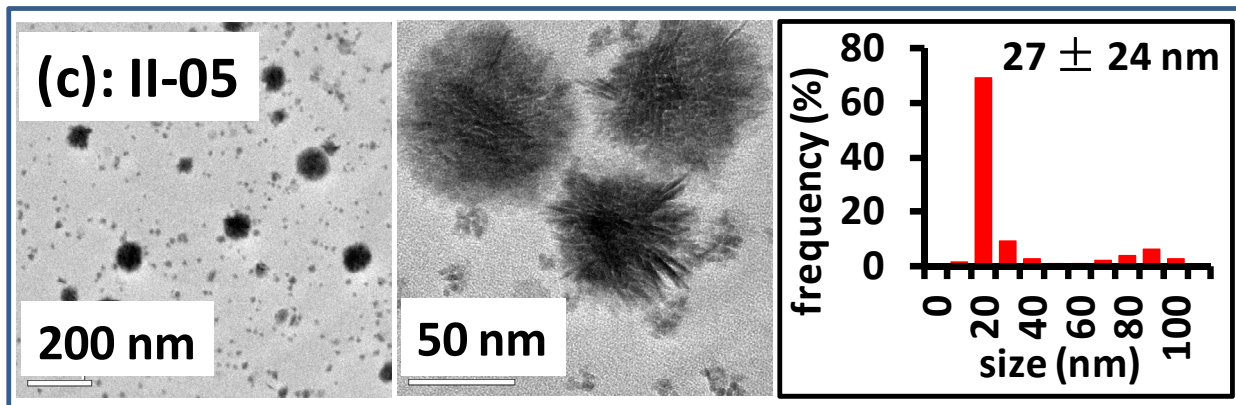
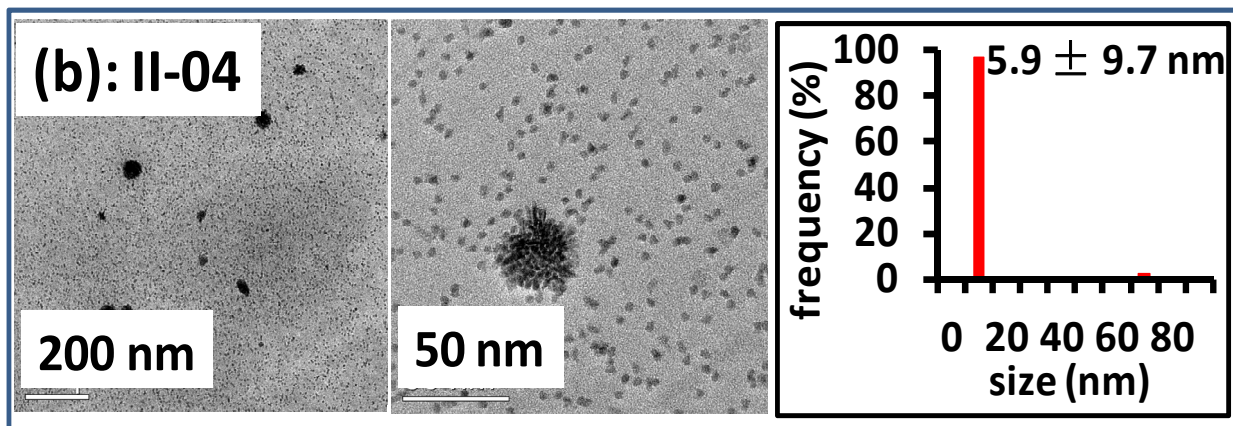
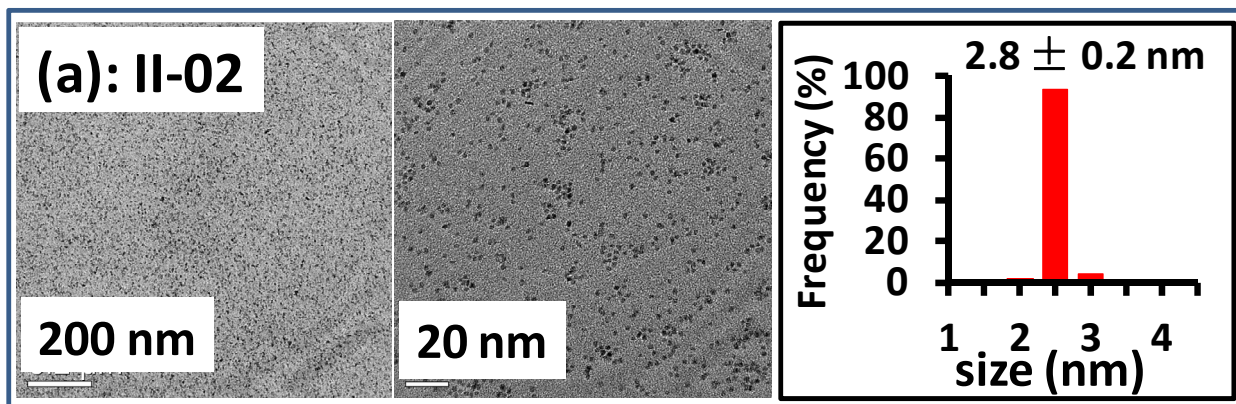
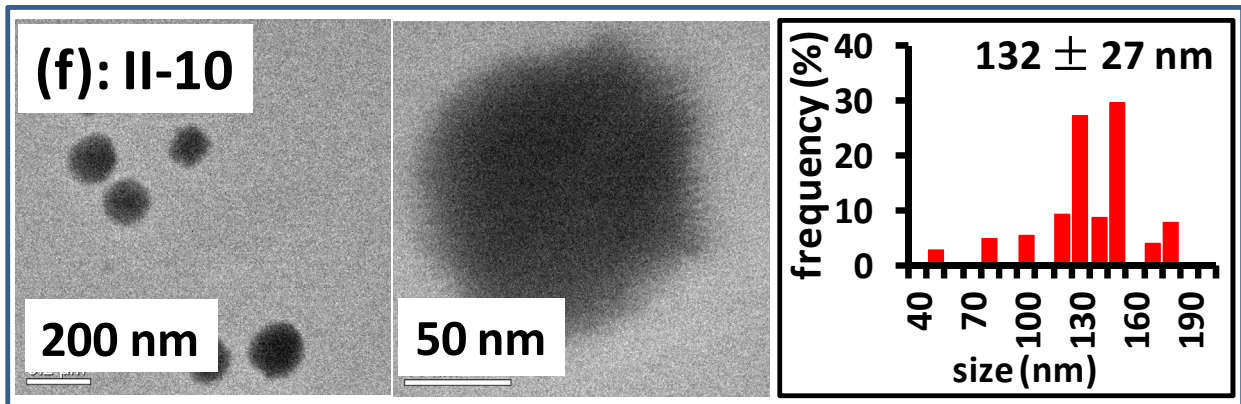
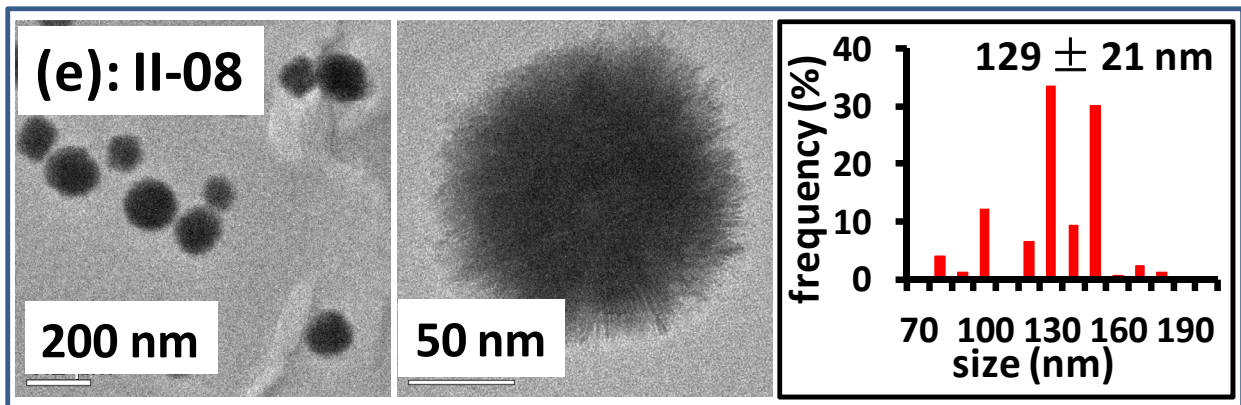
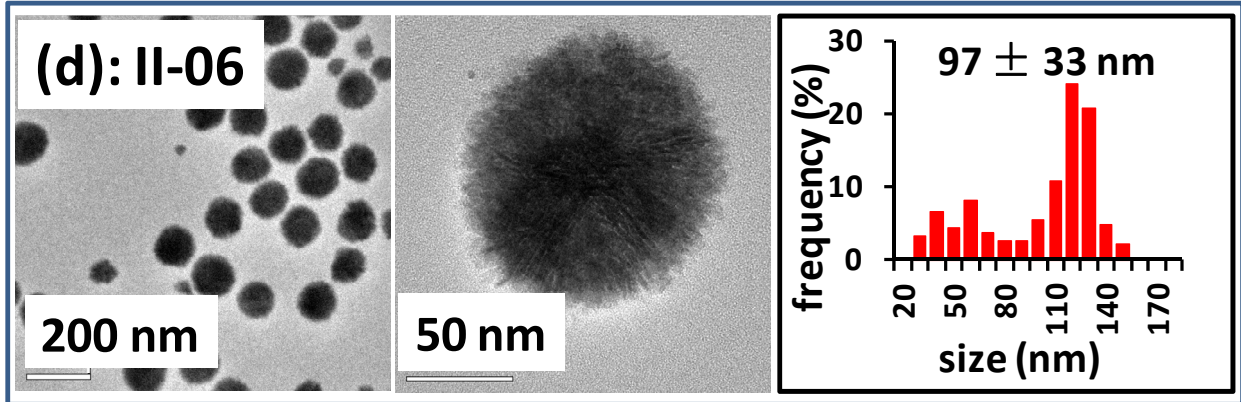


Figure 3-2 Typical TEM images of Ru NPs synthesized at different molar fractions of Ru (II) salt in the precursor solution. II-10: 100% fraction of Ru (II) salt; II-8: 80% fraction of Ru (II) salt; II-06: 60% fraction of Ru (II) salt; II-05: 50% fraction of Ru (II) salt; II-04: 40% fraction of Ru (II) salt; II-02: 20% fraction of Ru (II) salt. Synthesis conditions: 20mM of Ru ions concentration in precursor solution, 20 ml of reaction volume, $T=150^{\circ}\text{C}$.

Figure 3-2 (cont'd)



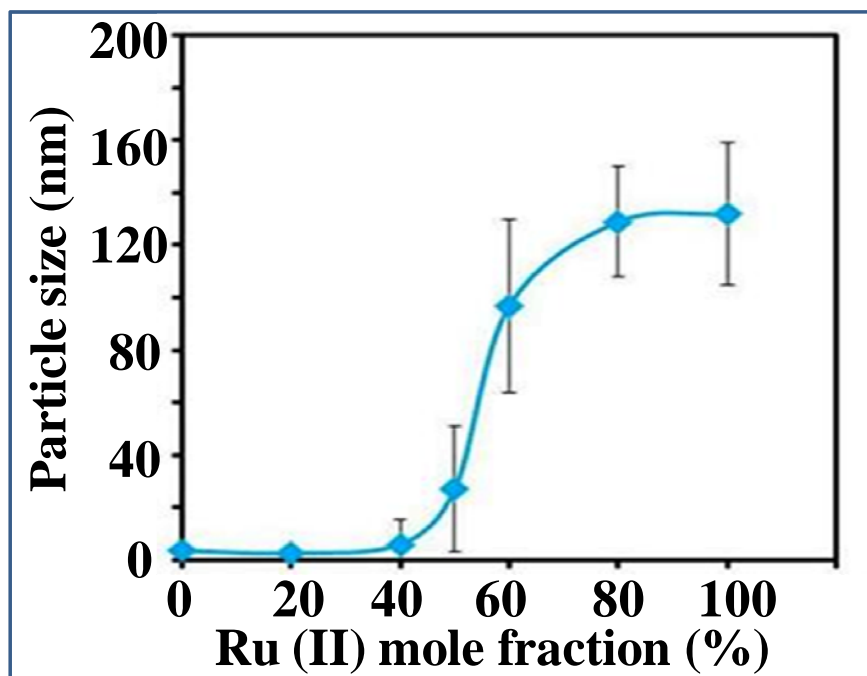


Figure 3-3 Average diameter of PVP-Ru NPs as a function of the mole fraction (mol%) of Ru(II) in the precursor mixture. While there appears to be significant overlap between samples (based on the error bars), ANOVA analyses showed that the means of the samples are significantly different.

3.3.1.3. Influence of adding pre-synthesized NPs (seed-mediated growth)

Addition of pre-synthesized seed particles to serve as nucleation sites for metal reduction (seed-mediated growth) can drastically change the resulting nanoparticle growth kinetics. This so-called seed-mediated growth mechanism offers an alternative way to control the size of NPs by simply changing the amount and type (size/shape) of seed particles added to the growth medium. The resulting separation of nucleation and subsequent growth events offers more flexibility in controlling the size and size distribution of the final NPs. The concept of seed-mediated growth was initially developed for the synthesis of Au NPs and has been extended to other metals including Pd, Pt, and Ag.⁴²⁻⁵⁴

Here we describe the preparation of Ru NPs via seed-mediated growth to study the influence of the amount of added seed on the morphology of the resulting NPs. The synthesis of Ru NPs requires two steps as described in the experimental section. The seed used was from sample T170, which has an average size of 3.2 ± 0.3 nm. Different amounts of Ru seed were added to the reaction mixture, each sample designated as Seed0 to Seed8.0, as shown in Table 3-2.

Table 3-2 Summary of reaction conditions for synthesis of Ru NPs by seed-mediated growth.

Sample ID	Seed added (Ru elemental concentration in the seed colloid is 0.8 mM)	Ru salt concentration in the precursor mixture (mM)
Seed0	0 mL	10
Seed0.5	0.5 mL	9.5
Seed1.5	1.5 mL	8.5
Seed3.0	3.0mL	7.0
Seed4.5	4.5 mL	5.5
Seed6.0	6.0 mL	4.0
Seed8.0	8.0 mL	2.0

The elemental concentration of Ru in colloidal Ru NPs was about 1.0 mg/ml (determined by ICP-AES). Precursor: Ru(III) acetylacetonate; stabilizer: PVP-55K; precursor to stabilizer ratio: 1:10; reaction temperature: 170°C ; total Ru concentration: 10 mM; total reaction solution volume: 10 mL.

Figures 3-4 shows the effects of the amount of seed added on the size of the resulting Ru NPs. When a relatively small amount of seed (0.5 and 1.5mL per 10.0 mL) was added to the reaction solution, the resulting NPs increased in size to an average diameter of 3.9 nm. As the fraction of Ru seed in the reaction solution increased to 30% (3.0 mL/10.0 mL), the resulting Ru NPs increased to a maximum diameter of 5.5 ± 0.6 nm. When the fraction of Ru seed was increased further to 45% (4.5 mL/10.0 mL), the size of the resulting NPs decreased slightly and then remained basically constant as the fraction of seed increased to 80% (8.0 mL/10.0 mL). The standard deviation in size distribution is reasonably small for each sample, and essentially constant with variation of Ru seed concentration. The Ru NPs were generally uniform with a

narrow size distribution. They maintained the spherical shape of the seeds, indicating little influence of seed concentration on the shape of the Ru NPs.

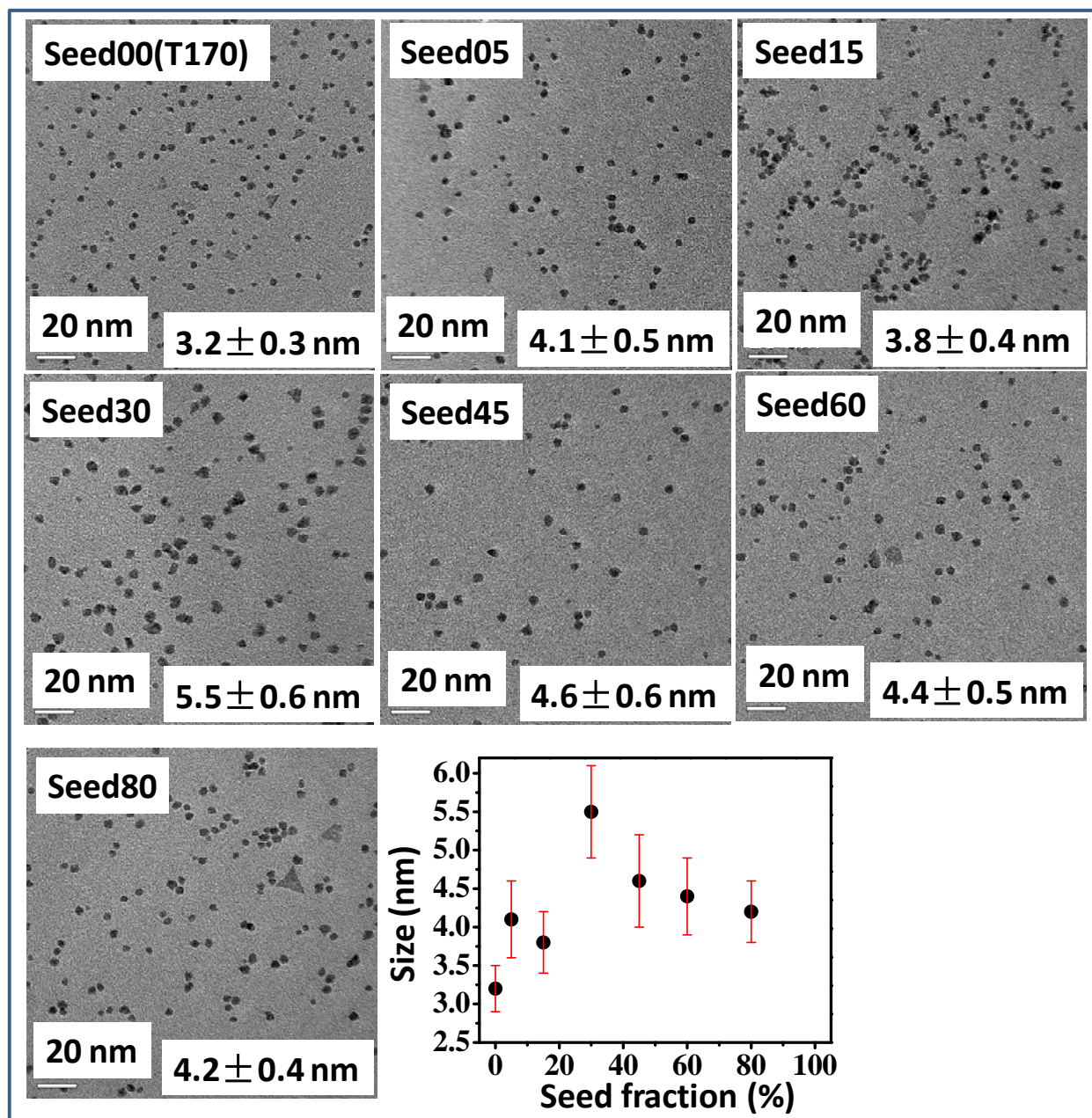


Figure 3-4. TEM images of Ru NPs synthesized via seed-mediated growth. All images were taken at a magnification of 100 K.

3.3.1.4. Effect of stabilizer

To minimize the negative effect of the capping agent on particle dispersion on catalyst support and minimize complications in the subsequent removal of the stabilizer, it is necessary to lower the ratio of the stabilizing polymer to metal precursor as much as possible during synthesis of the colloidal particles.^{55,56} Figure 3-5 shows HRTEM images of five samples synthesized at different PVP to precursor molar ratios. It is observed that, for PVP/precursor molar ratios ranging from 5 to 80, the process yielded mainly spherical Ru NPs with similar average sizes and size distributions. It is likely that, at the low PVP/precursor molar ratios, one PVP molecule stabilizes several NPs (Figure 3-5 R50 and R100). This may lead to particle aggregation after deposition on the support.

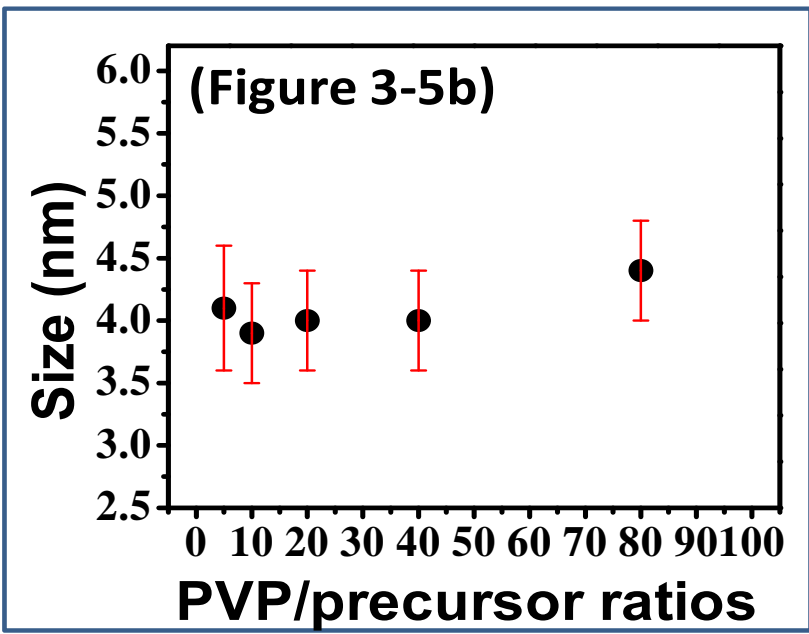
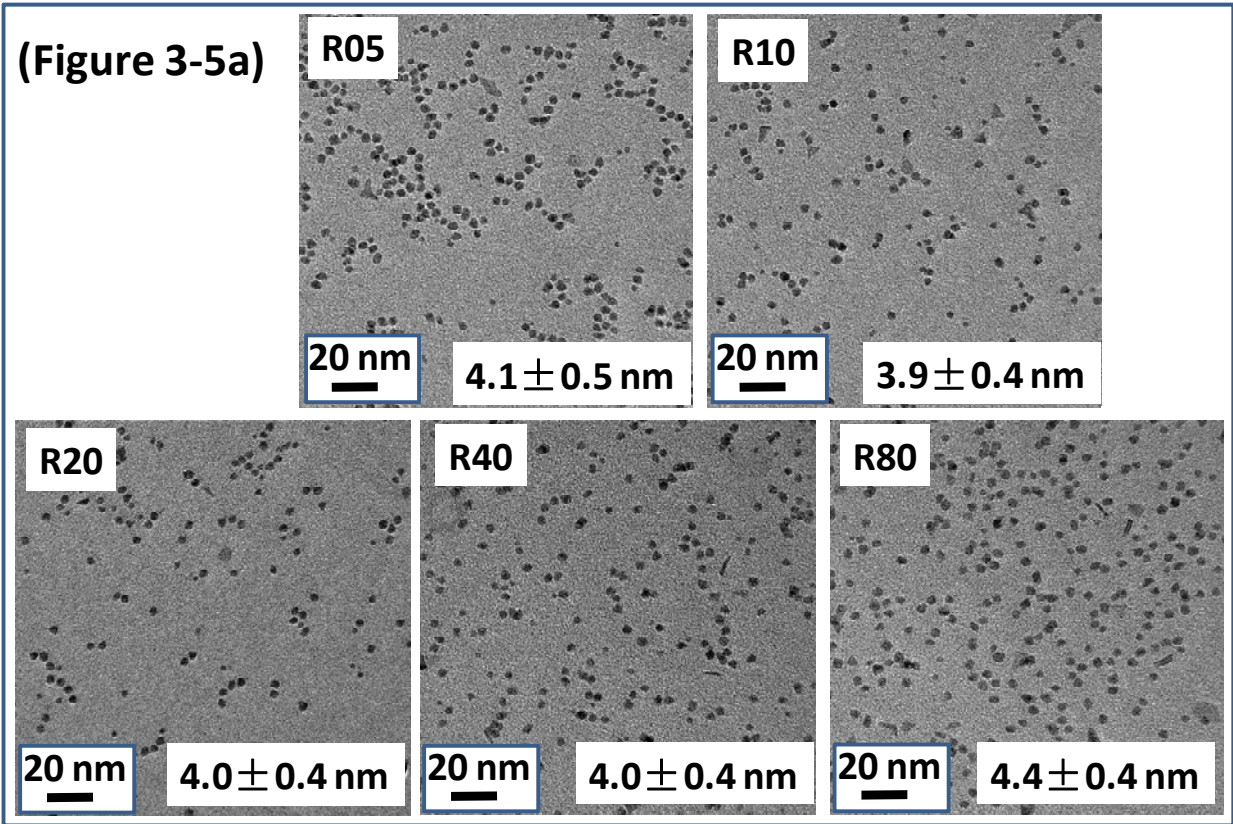


Figure 3-5. HRTEM images of Ru NPs synthesized at different PVP/precursor ratios and their size distributions. (a): HRTEM images; (b) particle size against the stabilizer to precursor ratio. R50: PVP/precursor ratios =5/1; R10: PVP/precursor ratios =10/1; R20: PVP/precursor ratios =20/1; R40: PVP/precursor ratios =40/1; R800: PVP/precursor ratios =80/1.

In addition to changing PVP/precursor molar ratios, we compared the sizes and shapes of Ru NPs stabilized with PVP of molecular weights 29K and 55K Daltons, respectively. The resulting data show that there is no significant difference in the size or shape of the resulting Ru NPs (Figure 3-6).

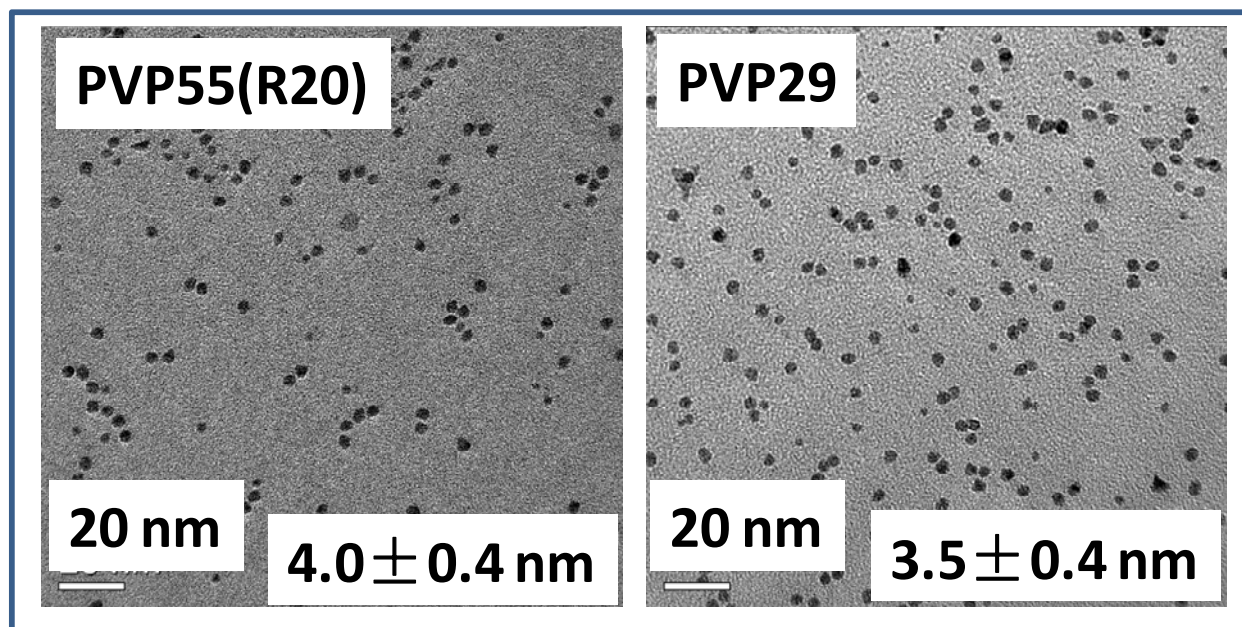


Figure 3-6. HRTEM images of the size distribution of Ru NPs stabilized by different molecular weights of PVP. PVP55: PVP with MW \approx 55K; PVP29: PVP with MW \approx 29K.

3.3.2. Properties of size-tunable Ru NPs supported on MSU-F

We used the TEM data to select the colloidal Ru NPs to prepare the supported catalysts. These supported NPs were used to investigate the effects of particle size on their catalytic performance. Table 3-3 gives information on Ru NPs used for the preparation of supported Ru NPs of different sizes. The labels assigned to the prepared catalysts are also given in Table 3-3.

Table 3-3 A summary of colloidal Ru NPs used to prepare supported Ru catalysts.

Colloidal NPs ID	00170	Seed30	II05	II06	II08
Synthesis method	Polyol reduction at 170 °C	Seed mediated growth	Mixed metal precursor	Mixed metal precursor	Mixed metal precursor
Average size (nm)	3.2	5.5	27	97	129
Supported catalyts ID	WD170-5NM	SG30F-6NM	TW10F-25NM	TW12F-67NM	TW16F-94NM

FT-IR spectra of the pure support (MSU-F), PVP, and each catalyst are shown in Figure 3-7. The spectra of the pure support (MSU-F) and pure PVP has characteristic absorption peaks in agreement with previously reported results.⁵⁷ By contrast, the IR spectra of the catalysts activated through Ar-protected calcination show only the characteristic peaks of pure MSU-F, indicating complete decomposition and removal of the capping polymer agent from the supported catalyst.

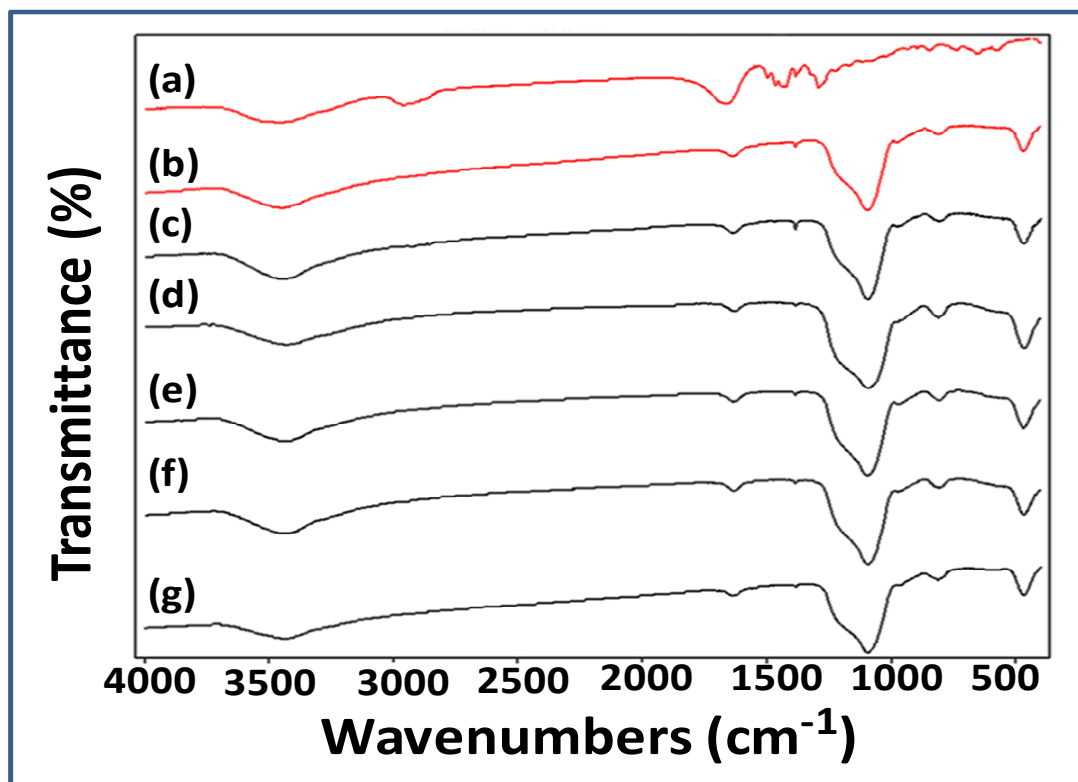


Figure 3-7 FTIR spectra of MSU-F, PVP, and the size-tuned Ru NPs supported on MSU-F. (a) PVP; (b) pure MSU-F support; (c) WD170F-5NM; (d) SG30F-6.1NM; (e) TW10F-25NM; (f) TW12F-67NM, and (e) TW16F-94NM.

3.3.2.1. Morphologies and metal compositions of supported Ru NPs

The morphologies of the supported Ru catalysts were investigated by a combination of TEM, STEM, SAED, and EDS. Typical characterization results are shown in Figure 3-8. After thermal activation of the supported NPs under the Ar-protected calcinations at 650°C, the MSU-F support retained its typical structure, which consists of a hexagonal cellular foam mesoporous framework with a cell window size of ~15 nm and unit cell size of ~22 nm. The Ru NPs were still well-dispersed on the support with no signs of agglomeration and no damage to the framework and structure of the support. Additionally, no stray NPs were observed in any TEM images, even though the supported catalysts were washed by methanol before they were dropped onto the TEM grid. This is an indication of strong interaction of the NPs with the support. The

more magnified images in Figure 3-8 show that the particles on the support are spherical in shape.

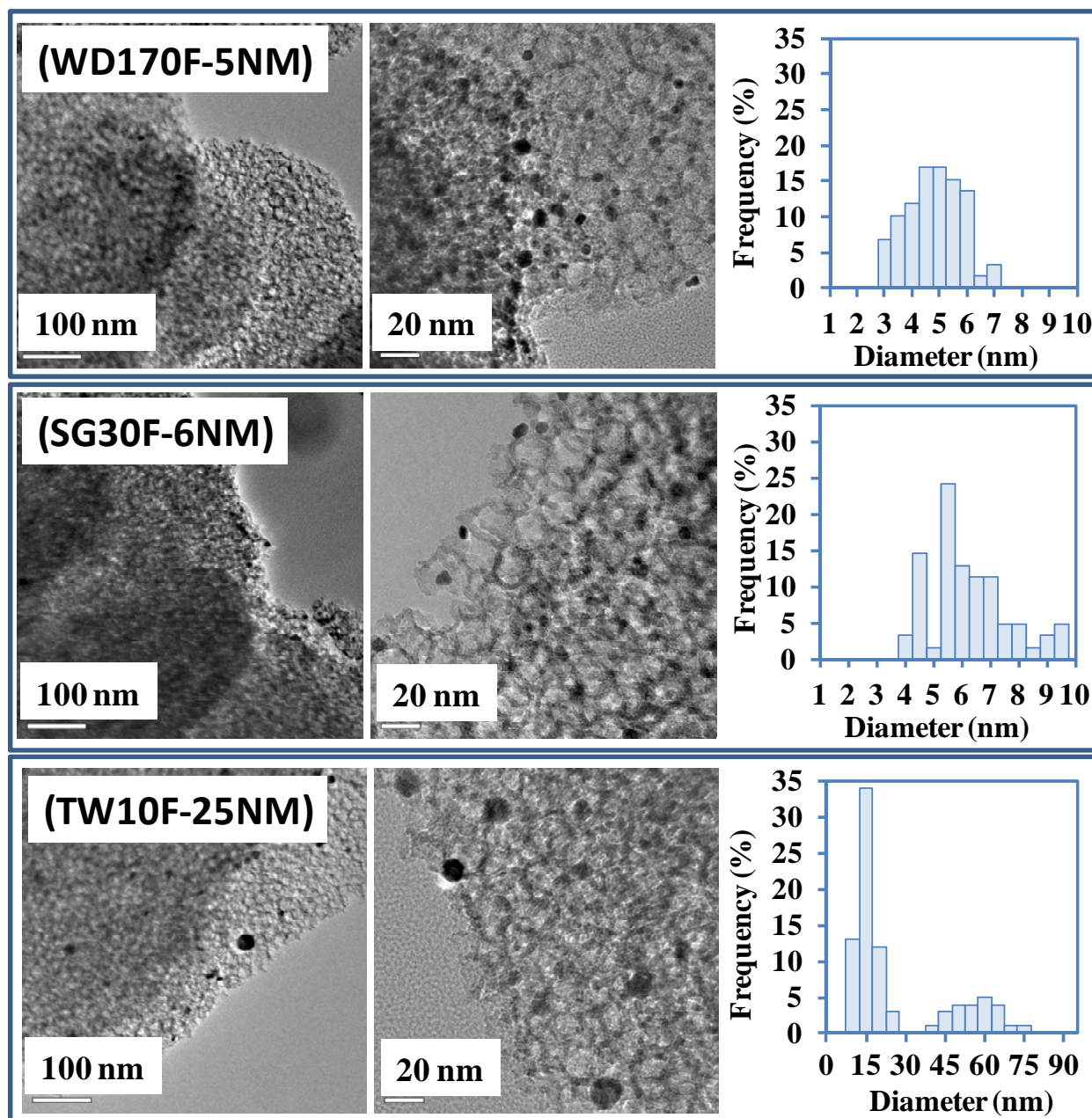
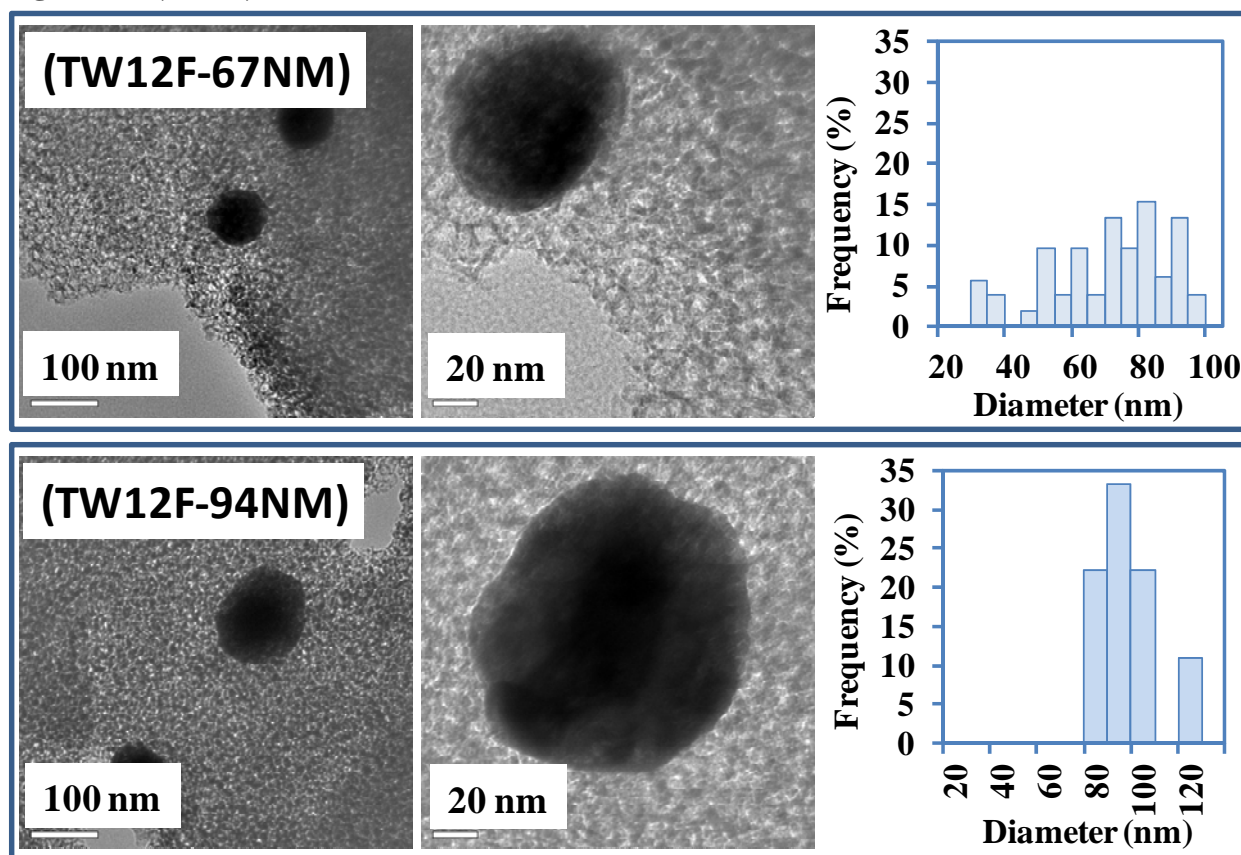


Figure 3-8 Typical HRTEM images of size-tuned Ru NPs supported on MSU-F. The HRTEM images for each sample have scale bars of 100 nm and 20 nm from left to right, respectively.

Figure 3-8 (cont'd)



The average diameters of the supported NPs and the Ru content of each catalyst are summarized in Table 3-4. The mean particle size determined from the TEM observation are 6 nm for the catalyst WD170F-5NM, 6 nm for SG30F-6.1NM, 25 nm for TW10F-25NM, 67 nm for TW12F-67NM, and 94 nm for TW16F-94NM. The Ru content in WD170F-5NM is about 0.55wt%. The sample SG30F-6NM has a similar metal content (0.58wt %). Further increases in particle size resulted in a decrease in catalyst metal content.

Table 3-4 Chemical compositions and average sizes of Ru NPs supported on MSU-F.

Sample ID	Ru content	Average size of
	(WT)%	NPs (nm)
MSU-F	---	
WD170F-5NM	0.55	4.7±1.3
SG30F-6NM	0.58	6.1±1.6
TW10F-25NM	0.49	24.8±18.8
TW12F-67NM	0.31	66.7±18.3
TW16F-94NM	0.28	93.8±2.8

The Ru content in each sample was determined by ICP-AES. Average size of the NPs in each sample was determined by counting ~100 NPs in the TEM images.

3.3.2.2. Structure of Ru NPs supported on MSU-F

The crystal structure of the supported Ru NPs was analyzed by powder XRD. The patterns for each catalyst as well as the support are presented in Figure 3-9. No peak was observed in the diffraction pattern of the pure support over the range of 2θ values from 30 to 50°. Peaks observed at $2\theta = 38.2^\circ$, 42.2° , and 43.5° for the supported catalysts are attributable to the (100), (002), and (101) facets of *hcp* Ru crystal. While these features are very weak and broad in the case of the catalysts WD170F-5NM and SG30F-6NM due to the small size of Ru NPs, they are much sharper and more intensive in the case of the TW10F-25NM, TW12F-67NM, and TW16F-94NM, indicating greater crystallinity. This is consistent with the SAED observations.

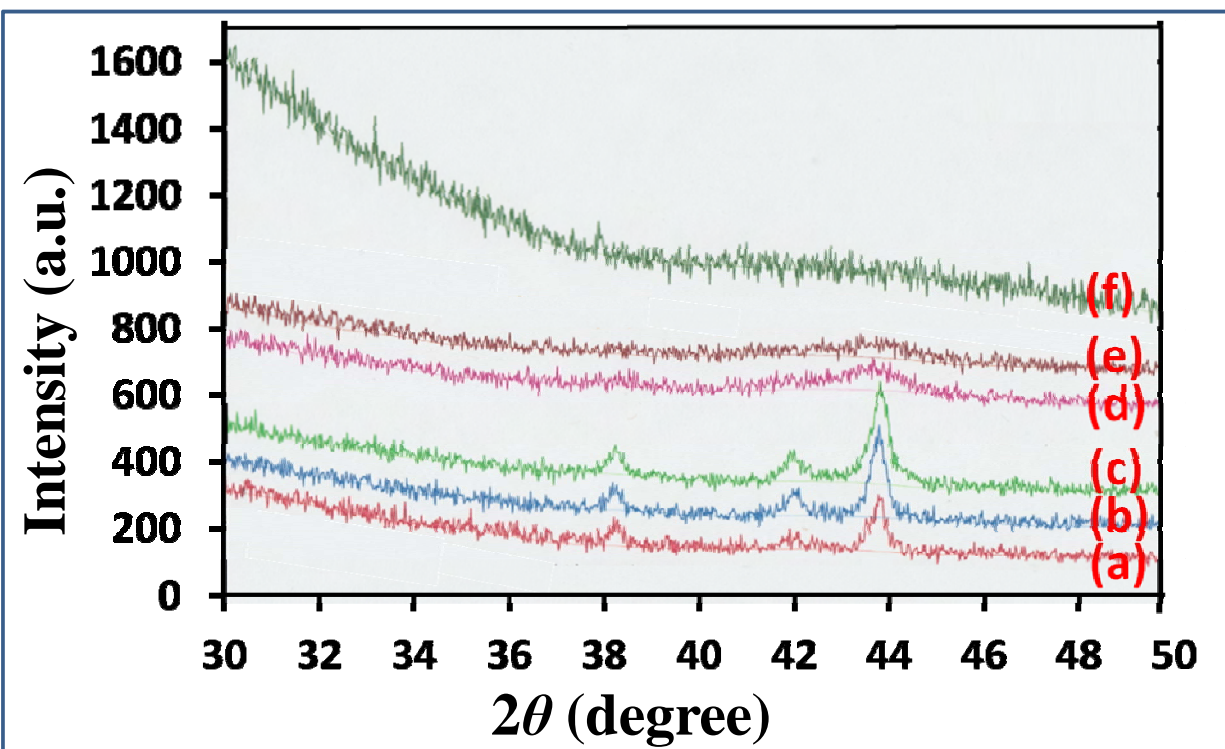


Figure 3-9 Power XRD pattern of the size-tuned Ru NPs supported on MSU-F. The peak at the 2θ value of 43.5° is consistent with the (101) facet of hexagonal close packed Ru nanocrystals. The intensity of the peak indicates the crystallinity of each sample. (a) TW16F-94NM; (b) TW12F-67NM; (c) TW10F-25NM; (d) SG30F-6.1NM; (e) WD170F-5NM; (f) pure MSU-F support

The crystallinity of the supported Ru NPs was also confirmed by the SAED pattern of each catalyst, as shown in Figure 3-10. The array of bright spots in the SAED pattern of each sample indicates the crystal structure of the supported NPs.

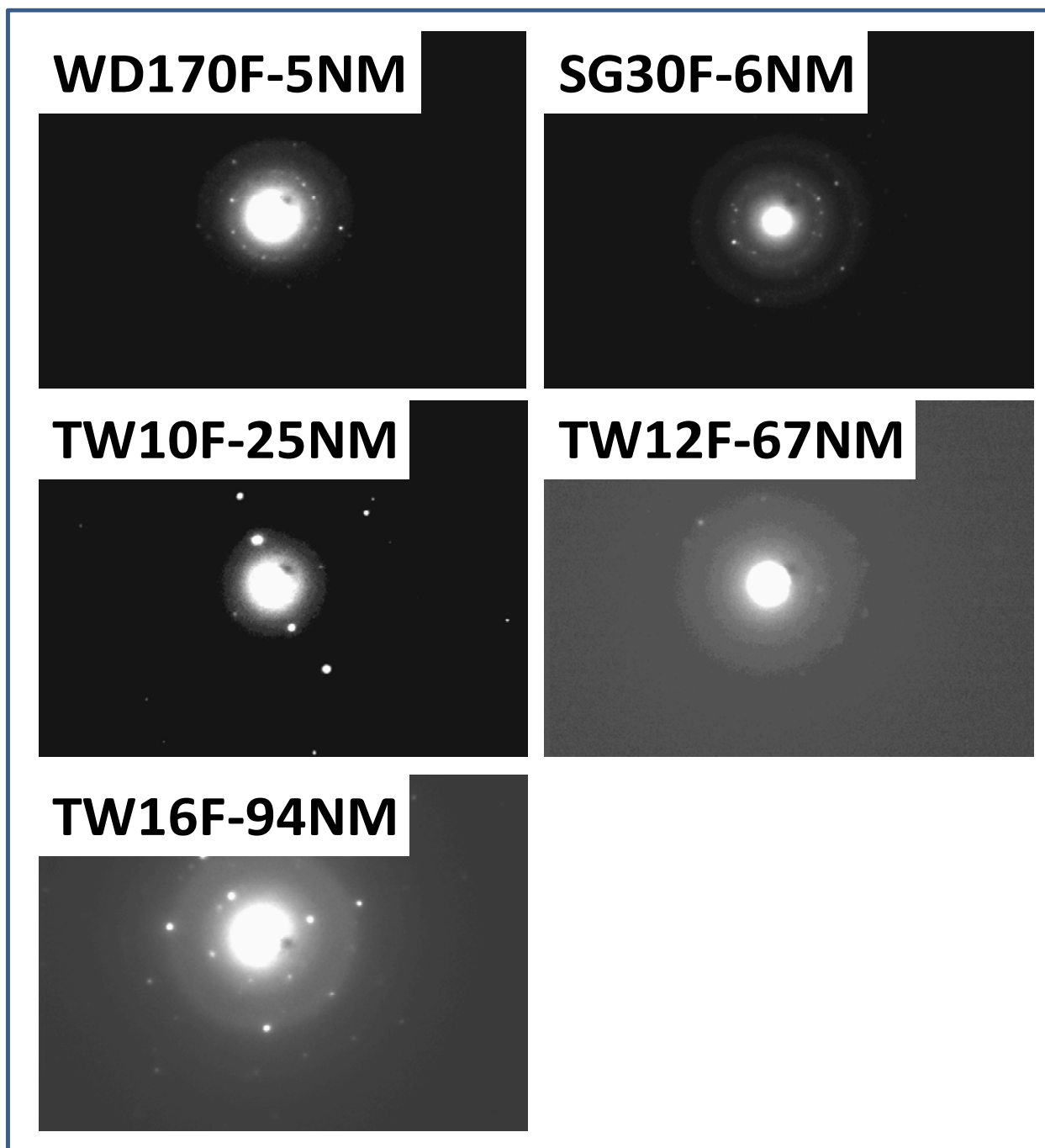


Figure 3-10 SAED patterns of size-tuned Ru NPs supported on MSU-F. The SAED characterizations were performed on randomly selected NPs in each sample. The array of bright spots in the pattern indicates the crystallinity of the NPs.

3.3.2.3. Surface properties of Ru NPs supported on MSU-F

A summary of the surface properties of the supported Ru catalysts is given in Table 3.3-4. The total surface area of each catalyst after thermal treatment was close to that of the MSU-F support. Table 3-5 also shows that, for all catalysts, the diameter of the silica pores remained essentially unchanged. These results suggest that the pores of the mesoporous silica were not clogged, even by Ru NPs with sub-10 nm diameters, and that NPs are situated predominantly on the outer surface of the silica framework rather than in the pores, which is in good agreement with the TEM observations.

Table 3-5 Ru content and textural properties of the size-tuned Ru NPs supported on MSU-F.

Sample ID	Ru content (wt%)	BET Surface area ($\text{m}^2 \text{g}^{-1}$)	Average pore diameter (nm)
MSU-F	---	503.33 ± 1.20	---
WD170F-4.7NM	0.55	479.12 ± 1.14	15.31
SG30F-6.1NM	0.58	542.84 ± 1.67	15.06
TW10F-49.3NM	0.49	533.77 ± 1.58	14.93
TW12F-66.8NM	0.31	574.16 ± 1.71	14.95
TW16F-93.8NM	0.28	560.44 ± 1.65	15.13

The Ru content was determined by ICP-AES. BET surface area was determined by nitrogen adsorption at 77K. The average pore diameters were determined by the BJH method.

The metal dispersion can be determined experimentally from H_2 (or CO) chemisorption data.

The metal dispersion of Ru in each catalyst can also be calculated using the spherical clusters model,⁵⁸⁻⁶⁰ based on the average size of the Ru NPs:

theoretical metal dispersion (MD_{th})

$$\begin{aligned}
 & \frac{\left(\frac{\text{surface area of one Ru NP}}{\text{surface area of one Ru atom}} \right)}{\left(\frac{\text{volume of one Ru NP}}{\text{volume of one Ru atom}/\alpha} \right)} = \frac{\left(4\pi R^2 \right) / \left(6 \times \left(\frac{1}{2} \times \frac{2\sqrt{3}}{3} r \times r \right) \right)}{\left(\frac{4\pi}{3} R^3 \right) / \left(\left(\frac{4\pi}{3} r^3 \right) / 0.74 \right)} \\
 & = \frac{4.90r}{R} = \frac{4.90 \times 0.134}{R} = \frac{0.66}{R}
 \end{aligned} \tag{3.1}$$

where R is the average radius of the Ru NPs as determined from TEM measurements (nm); r is the radius of one Ru atom (0.134 nm); and α is the atomic packing factor, taken as 0.74 by assuming the crystal structure of Ru to be hexagonal close-packed (*hcp*).

For supported Ru NPs with an average diameter of 4.7 nm (sample WD170-5NM), the theoretical metal dispersion is:

$$MD_{th} = \frac{0.66}{R} = \frac{0.66}{(4.7/2)} = 0.281 \tag{3.2}$$

The experimental metal dispersion of the catalyst WD170F-5NM obtained by H₂ chemisorption (0.152) and CO chemisorption (0.146) are very close, but equal to only about 50% of the theoretical estimate. This suggests that only 50% of the surface Ru atoms served as actual active sites, which is in good agreement with the observation for bulk Ru metal.⁶¹ It is experimentally challenging to determine the metal dispersion of supported Ru NPs with average diameters larger than 20 nm (TW10F-49NM, TW12F-67NM, and TW16F-94NM, for example) because a large amount of sample is required to obtain detectable levels of chemisorbed H₂ or CO.

3.3.3. Catalytic assessment of CAL hydrogenation over Ru NPs supported on MSU-F

A list of the reaction conditions investigated for CAL hydrogenation over supported Ru-Pd NPs is given in Table 3-6. Under the described conditions, cinnamyl alcohol (COL) and hydrocinnamaldehyde (HCAL), and hydrocinnamyl alcohol (HCOL) are the only products observed within the reaction time (see Figure 3-11 and more details in Appendix A-1 to A-5).

Table 3-6 A Reaction conditions used for CAL hydrogenation over Ru NPs of different size groups supported on MSU-F

Catalyst	Metal loading ($\times 10^{-6}$ mole)	Initial concentration of CAL (mM)	T ($^{\circ}\text{C}$)	$P(\text{H}_2)$ (bar)	time (hour)
WD170F-5NM	1.1	20	45	20	7
	1.6	40	45	20	7
	1.1	20	65	20	7
	1.6	40	65	20	7
	1.1	20	85	20	7
	1.6	40	85	20	7
	1.5	10	105	20	7
	1.5	20	105	20	7
	1.5	40	105	20	7
	1.1	60	105	20	7
	1.5	80	105	20	7
	1.1	20	125	20	7
	1.6	40	125	20	14
	SG30F-6NM	1.2	20	45	20
1.2		20	65	20	14
1.2		20	85	20	14
1.2		10	105	20	14
1.2		20	105	20	14
1.2		40	105	20	14
1.2		60	105	20	14
1.2		80	105	20	14
1.2		20	125	20	14

Table 3-6 (cont'd)

Catalyst	Metal loading ($\times 10^{-6}$ mole)	Initial concentration of CAL (mM)	T ($^{\circ}\text{C}$)	$P(\text{H}_2)$ (bar)	time (hour)
TW10F-25NM	1.1	20	45	20	24
	1.1	20	65	20	24
	1.1	20	85	20	24
	1.1	10	105	20	24
	1.1	20	105	20	24
	1.1	40	105	20	24
	1.1	60	105	20	24
	1.1	80	105	20	24
	1.1	20	125	20	24
TW12F-67NM	1.1	20	45	20	24
	1.1	20	65	20	24
	1.1	20	85	20	24
	1.1	10	105	20	24
	1.1	20	105	20	24
	1.1	40	105	20	24
	1.1	60	105	20	24
	1.1	80	105	20	24
	1.1	20	125	20	24
TW16F-94NM	1.1	20	45	20	24
	1.1	20	65	20	24
	1.1	20	85	20	24
	1.1	10	105	20	24
	1.1	20	105	20	24
	1.1	40	105	20	24
	1.1	60	105	20	24
	1.1	80	105	20	24
	1.1	20	125	20	24

A very small but measurable amount of HCAL, COL and HCOL ($\sim 2.6 \times 10^{-6}$ moles in total) was observed at time $t=0$ of the reaction (i.e., prior to feeding hydrogen into the reactor), as shown in the data for CAL hydrogenation using WD170-5NM (Figures 3-11 and Appendix A). Similar results were observed in reactions with other Ru NPs, with HCAL being the primary product in each case. We speculate on two possible explanations for this. First, it is known that IPA can be dehydrogenated over metal catalysts to produce acetone and hydrogen.⁶² Thus, this reaction

could, in principle, provide hydrogen to induce the hydrogenation of CAL. A more plausible explanation is that H₂ was strongly adsorbed on the surface of the Ru NPs during catalyst pre-reduction. The subsequent purging of the system with nitrogen did not completely remove the chemically-bound H₂ from the catalyst surface. As a result, H₂ was already available on the catalyst surfaces to initiate the reaction as soon as the system was charged with the reactant (CAL), prior to the introduction of exogenous hydrogen into the reactor.

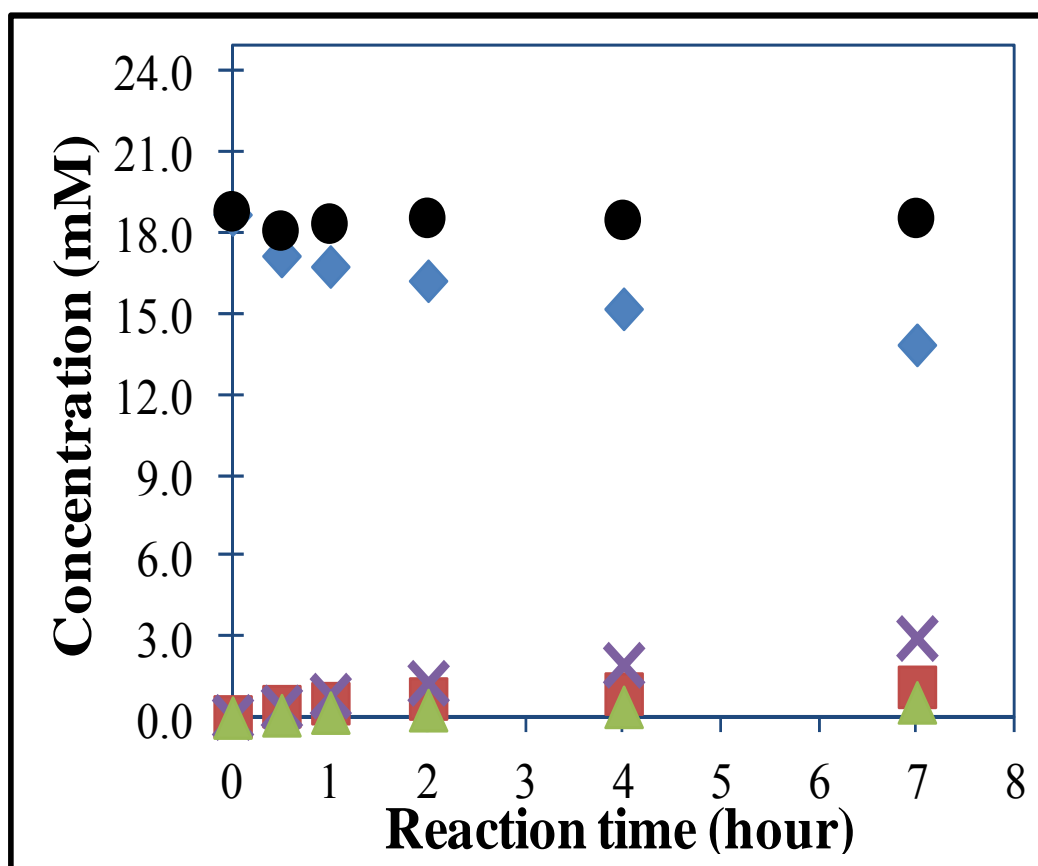


Figure 3-11 Typical reaction profiles for CAL hydrogenation over Ru NPs supported on MSU-F. Reaction conditions: 1.12×10^{-4} g of Ru loading with WD170-5NM as catalyst, 35 ml solution of CAL in IPA (20 mM of CAL), reaction temperature of 45°C, hydrogen pressure of 20 bar, and a stirring speed of 800 RPM. [Key: ●C-balance, ◆CAL, ■HCAL, ✕COL, ▲HCOL.]

3.3.3.1. Determination of reaction rates for CAL hydrogenation over Ru NPs

The initial rate of each reaction was determined by a differential approach.^{63,64} In a typical analysis, the CAL concentration versus reaction time data were fit to an n^{th} order polynomial (where $n = 2$ or 3). Since there was some substrate conversion prior to feeding H_2 into the reaction chamber (as discussed above), the regression equation was not forced through time $t=0$. The equation was differentiated, and the initial rate was calculated by taking the derivative at time $t=0$. One example of the analysis is illustrated below for CAL hydrogenation over the catalyst SG30F-6NM (Figure 3-12 and Table 3-7)

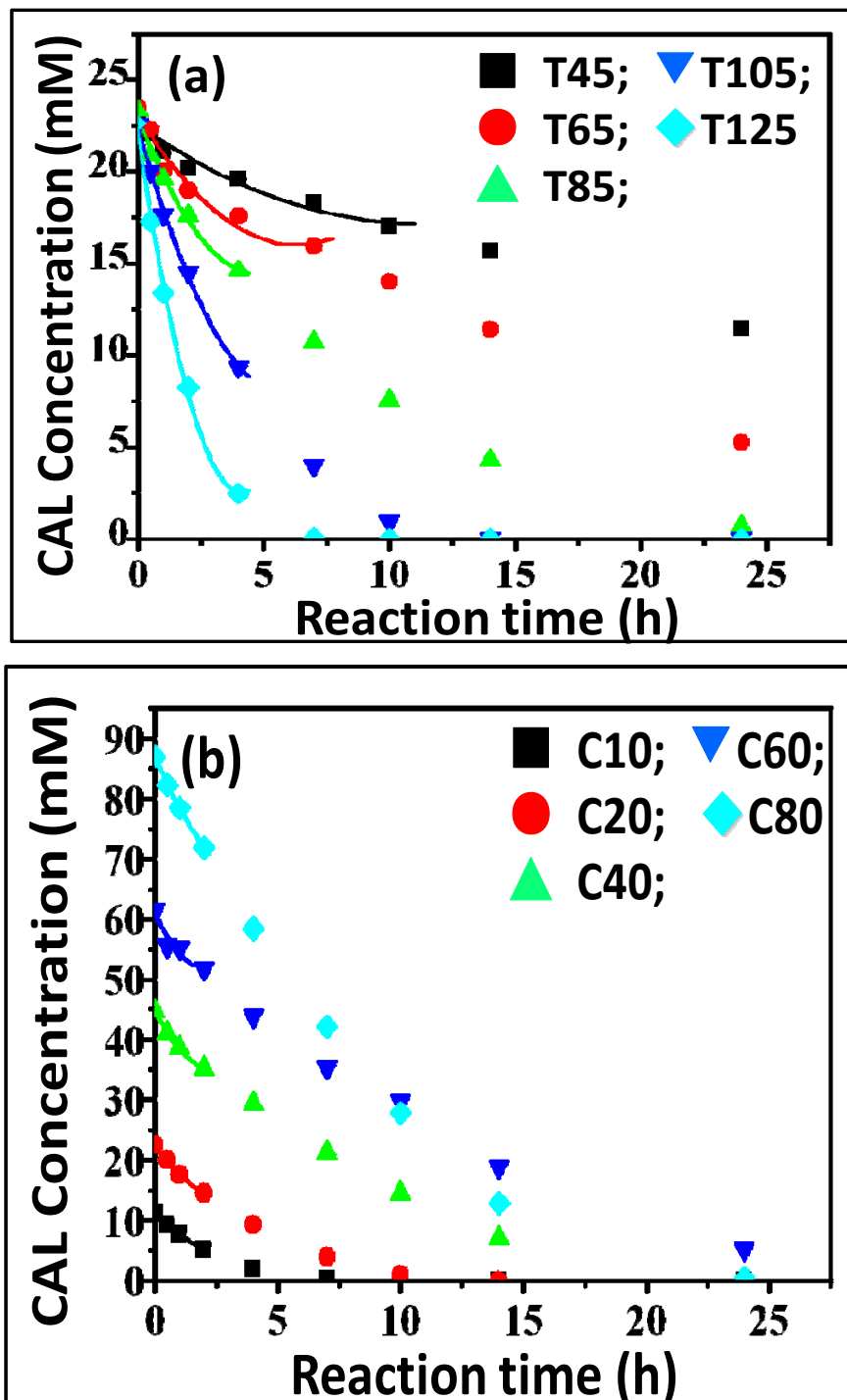


Figure 3-12 Reaction profiles for CAL hydrogenation over SG30F-6NM and the corresponding regression curves: (a) reaction profiles at different temperatures, (b) reaction profiles at different initial substrate concentrations. Reaction conditions: 35 ml CAL solution in IPA; $T = 45^{\circ}\text{C} - 105^{\circ}\text{C}$; $P(\text{H}_2) = 20$ bar; Stirring speed = 800 RPM. The numbers T## are the reaction temperatures, and C## are the initial substrate concentrations.

Table 3-7 Regression coefficients of substrate concentration versus reaction time for CAL hydrogenation over the catalyst SG30F-6NM. Reaction conditions: 35 ml CAL solution in IPA (10 - 80mM); T = 45°C -105°C; P(H₂) = 20 bar; Stirring speed = 800 RPM.

Reaction ID	Regression function $Y = A + B1*X + B2*X^2$					
	A		B1		B2	
	value	error	value	error	value	error
C20T45	22.52	0.38	-0.96	0.24	0.04	0.02
C20T65	23.02	0.56	-2.22	0.49	0.18	0.07
C20T85	22.96	0.36	-3.58	0.51	0.38	0.12
C20T105	22.57	0.11	-5.73	0.27	0.84	0.12
C20T125	22.16	0.53	-9.51	0.75	1.15	0.18
C10T105	11.10	0.05	-3.81	0.14	0.41	0.06
C40T105	44.68	0.22	-7.67	0.55	1.45	0.26
C60T105	60.93	1.78	-8.93	4.51	2.23	2.09
C80T105	86.96	0.12	-9.57	0.31	1.02	0.14

3.3.3.2. Mass transfer analysis of CAL hydrogenation over Ru NPs supported on MSU-F

The assessment of mass transfer influences is necessary for further investigation of NP size effects on catalytic performance during CAL hydrogenation. The three-phase reaction involves the transport of hydrogen through liquid to catalyst surfaces (gas-liquid mass transfer), transport of dissolved reactants from the bulk liquid to catalyst surfaces (liquid-solid mass transfer), and reaction at the catalyst surface and transfer of product from the NP interface back into the bulk liquid (intra-catalyst mass transfer). Based on previous literature reports,⁶⁴⁻⁶⁶ we assume our reaction is free of gas-liquid mass transfer and liquid-solid mass transfer limitations under the hydrogenation conditions used. So we are only focused on the intra-catalyst mass transfer. The effect of intra-catalyst mass transfer was examined by the Weisz-Prater criterion via the observable modulus:⁶⁷

$$\eta\phi^2 = \frac{(-r)L^2}{C_s D_e} \dots\dots\dots (3.3)$$

where $\eta\phi^2$ is the observable modulus, r is the initial reaction rate [$\text{mol}\times\text{L}\times\text{s}^{-2}$], L is the characteristic length of the catalysts, C_s is the reactant concentration at the solid-liquid interface, $D_e = \varepsilon^2 D_j$ is the effective diffusivity [$\text{cm}^2 \times \text{s}^{-1}$], ε is the catalyst support porosity, and D_j is the diffusivity of reactant j in the liquid phase, which can be estimated by the Wilke-Chang equation:⁶⁸

$$D_j = 7.4 \times 10^{-8} \frac{(\phi_B M_B)^{0.5} T}{\mu V_j^{0.6}} \dots\dots\dots (3.4)$$

where D_j is the diffusivity of reactant j in liquid, T is the absolute temperature [K], μ is the viscosity of the solution [cp], V_j is the molar volume of reactant j as a liquid at its normal boiling point [$\text{cm}^3 \times \text{mol}^{-1}$], ϕ_B is the association parameter for the solvent (which is 1.4 for IPA), and M_B is the molecular weight of IPA (60).

The absence of intra-catalyst mass transfer could be justified if the value of the observable modulus is less than 0.3 for reaction orders of 2 or less. We evaluated the effect of the intra-catalyst diffusion for the experiment with the highest reaction rate we observed because it is most likely to reflect the mass transfer limitation. The values of the related parameters under the reaction conditions and calculated results of the observable modulus are summarized in Table 3-

8. The values of the observable modulus for both CAL and H₂ are much smaller than 0.3, indicating that mass transport resistance is negligible under the experimental conditions.

Table 3-8 parameters and observable modulus for intra-particle mass transfer analysis.

Parameters for IPA		viscosity (cP)	association factor		molecular weight	
		0.20	1.4		60	
Parameters for catalyst		Pore volume (cm ³ /g)	Density (cm ² /g)	Porosity	monolayer thickness (nm)	characteristic length (cm)
		1.88	0.15	0.28	4nm	40×10 ⁻⁶
Parameters for reactant		Concentration (mol/L)	D _j (cm ² ·s ⁻¹)	De (cm ² ·s ⁻¹)	initial rate (mol L ⁻¹ ·s ⁻¹)	Observable modulus
	CAL	0.02	3.08×10 ⁻⁵	2.45×10 ⁻⁵	-3.23×10 ⁻⁶	1.06×10 ⁻⁷
	H ₂	0.08	4.91×10 ⁻⁵	3.90×10 ⁻⁵	-3.23×10 ⁻⁶	0.17×10 ⁻⁷

The reaction was conducted under the conditions of 1.12×10⁻⁴ g of Ru loading, 35 ml substrate (20 mM of CAL in IPA), temperature of 125°C, hydrogen pressure of 20 bars, and a stirring speed of 800rpm. The association factor was 1.4.⁶⁹ The viscosity (cP) of IPA was calculated by $\lg(\mu) = -0.7009 + 8.4150 \times 10^2 \times T^{-1} - 8.6068 \times 10^{-3} \times T + 8.2964 \times 10^{-6} \times T^2$.⁷⁰

Total pore volume of the catalysts was determined by N₂ adsorption-desorption and the density of the catalysts was estimated from literature. Monolayer thickness of the catalysts was estimated from TEM observations by assuming 2D properties of the catalyst. The catalyst characteristic length was calculated assuming 10 layers overlap. The H₂ concentration in IPA was estimated from literature values.⁷¹ The concentration of reactant at the catalyst surface was assumed to be the same as in bulk liquid based on our assumption of negligible liquid-solid mass transfer limitations.

3.3.3.3. Effect of particle size on the activity of Ru NPs for CAL hydrogenation

The activity of the supported NPs was calculated as the ratio of substrate conversion rate and catalyst surface area, as shown in the equation below:

$$\text{activity (moleCAL} \times \text{m}^{-2} \times \text{h}^{-1}) = \frac{\text{initial rate} \times \text{volume of substrate solution}}{\text{Total metal surface area (SA) of catalyts}} \dots (3.5)$$

The total metal surface area (TSA) of the catalyst was calculated by the following equation:

$$TSA = \frac{4\pi R^2 \cdot m_{\text{cat}} \cdot \text{wt\% Ru}}{\frac{4\pi R^3 \rho}{3}} = \frac{3m_{\text{cat}} \cdot \text{wt\% Ru}}{R \cdot \rho} \dots (3.6)$$

where m_{cat} is the total amount of catalyst (NP and support) used in each reaction (g); wt% Ru is the weight percent of Ru in the catalyst (%); R is the average radius of the Ru NPs in the catalyst (m); and ρ is the density of the Ru NPs, which is assumed constant at $12.45 \times 10^3 \text{ g/m}^3$.

We conducted the reactions using initial CAL concentrations ranging from 10 to 80 mol%. The data (Fig 3-13) show that the activity of each catalyst has a nonlinear dependence on the initial substrate concentration. This is an indication that the hydrogenation of CAL is not a first order reaction, and that a Langmuir-Hinshelwood type of mechanism may be more suitable to describe the reaction kinetics. Figure 3-14 shows the catalyst activity as a function of Ru NP size under different initial substrate (CAL) concentrations. The activities of Ru NPs with sub-10 nm diameters (WD170F-5NM and SG30F-6nm) are similar to each other over the same initial substrate concentrations, but larger particles appear to improve activity. This suggests that the larger Ru NPs have a higher density of active sites per unit surface area for CAL adsorption and hydrogenation than smaller NPs.

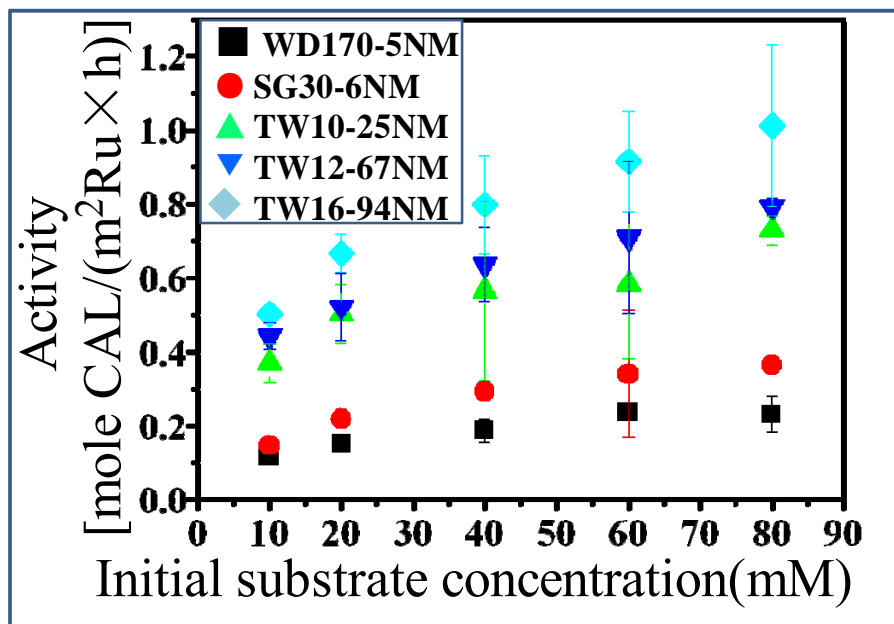


Figure 3-13 Activities of catalysts as a function of initial substrate concentration. All the reactions were conducted under conditions of 35 ml solution of CAL in isopropyl alcohol, reaction temperature of 105°C, hydrogen pressure of 20 bar, and a stirring speed of 800 RPM. The amount of Ru used in each reaction was given in Table 3-6.

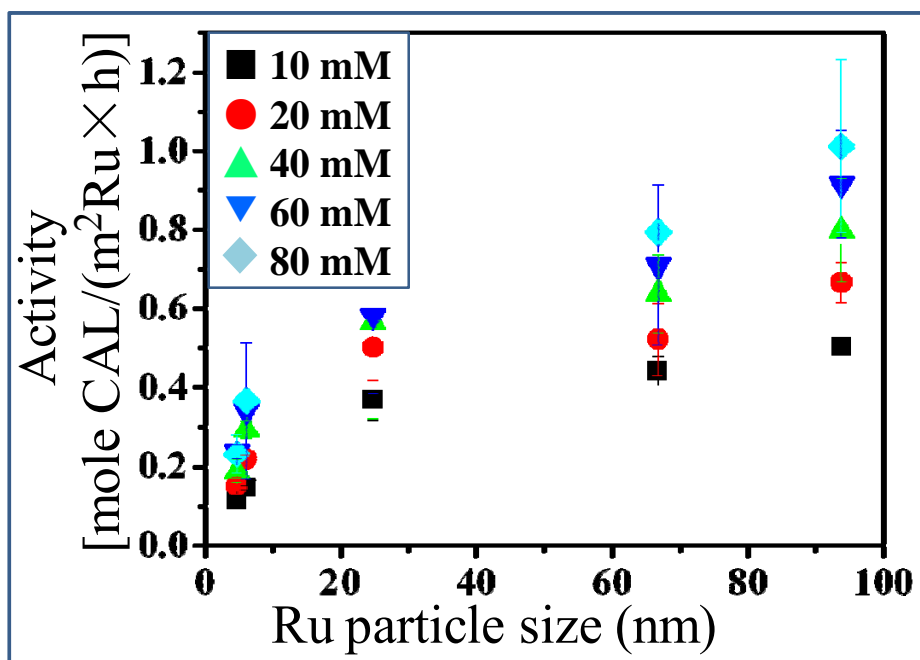


Figure 3-14 Activity of Ru NPs for CAL hydrogenation as a function of initial substrate concentration. All reactions were conducted under conditions of 35 ml solution of CAL in isopropyl alcohol, reaction temperature of 105°C, hydrogen pressure of 20 bar, and a stirring speed of 800 RPM. The amount of Ru used in each reaction was given in Table 3-6.

The dependence of active site density on particle size can be explained by the geometry of the metal surface. Theoretical calculations have shown that the optimal structure of benzalacetone on Ru (0001) surface is a planar benzalacetone molecule adsorbed parallel to a flat metal surface⁷².

We believe the optimal structure of CAL on Ru (0001), which is the primary facet of the supported NPs (Figure 3-15), is likely similar to that of benzalacetone on Ru (0001), because the two have similar molecular structures. Larger Ru NPs provide surface areas with reduced curvatures than smaller NPs as reflected in the equation below:

$$\kappa = 360^\circ \times l / (\pi \times d) = 1.1 / (\pi D) \dots\dots\dots (3.7)$$

where κ is the reduced curvature of a CAL molecule adsorbed on the surface of Ru NPs ($^\circ$); l is the length of a CAL molecule, assumed to be 1.1nm,; D is the average diameter of Ru NPs in the catalyst (nm). Therefore, increasing particle size can improve the density of usable active sites per unit surface area.

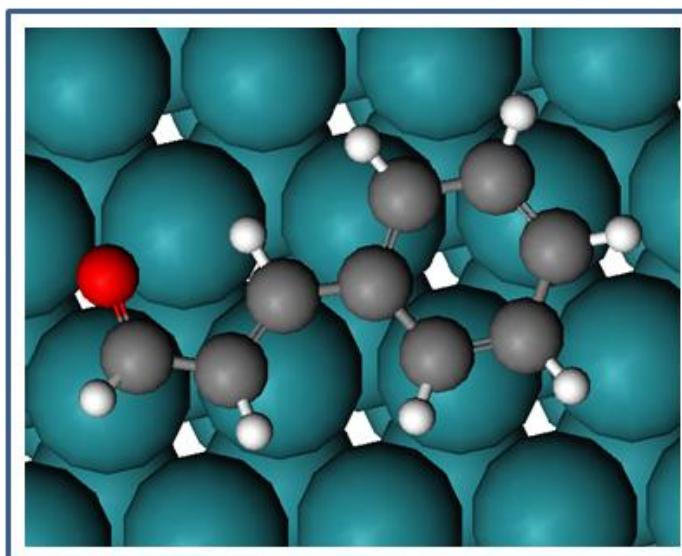


Figure 3-15 Projected optimal adsorption configuration for CAL over a Ru (0001) surface. The optimized structure was obtained by DFT calculations using the projector-augmented wave (PAW) method with the revised Perdew–Burke–Ernzerhof (revPBE) approximation coded in GPAW software program package.⁷³⁻⁷⁵

The apparent activation energy (E_a) for CAL hydrogenation was estimated from Arrhenius plots of the natural logarithm of the activity versus reciprocal absolute temperature (Figure 3-16). The values are independent of particle size, suggesting that variations in Ru NP size do not affect the reaction pathway for CAL hydrogenation.

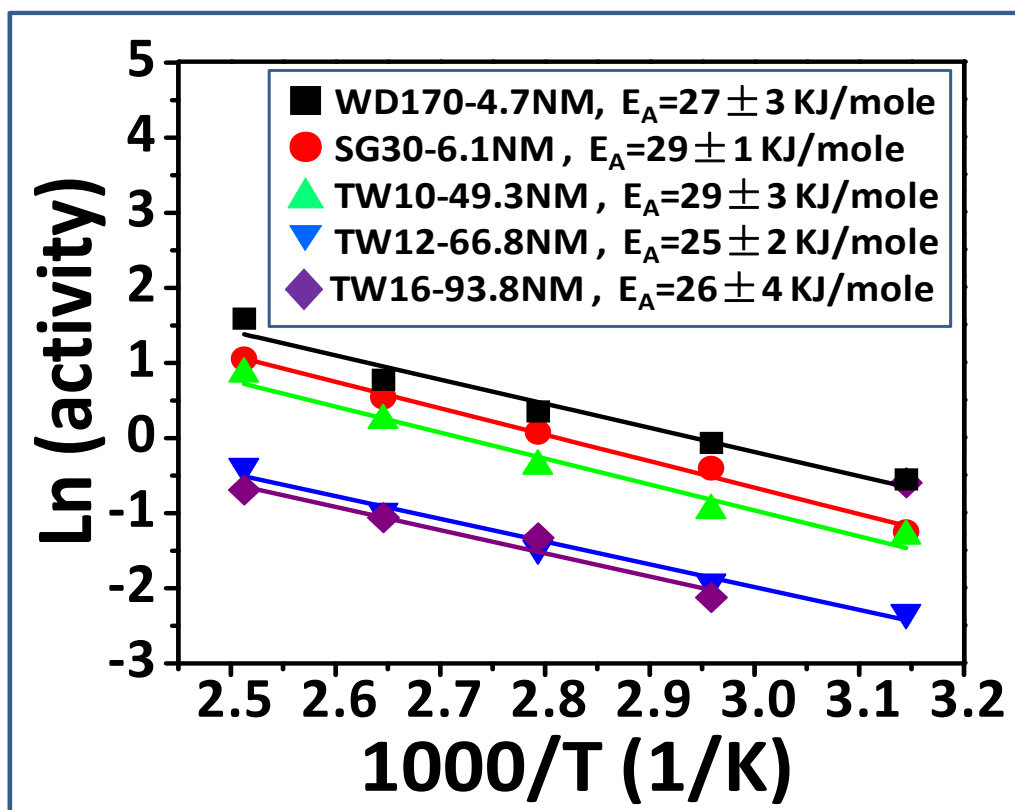


Figure 3-16 Arrhenius plots for CAL hydrogenation over Ru NPs of different sizes supported on MSU-F. The apparent activation energies were obtained by linear regression [$\ln(r) = \ln(r_0) - E_A/RT$]. The unit of activity is mole CAL per m^2 Ru per h (equation 3.5). All reactions were conducted under 35 ml substrate (20 mM CAL in IPA), $P(H_2) = 20$ bar, and a stirring speed of 800 RPM, over reaction temperatures ranging from 45°C to 125°C. The amount of Ru used in each reaction was given in Table 3-6. One point for TW16-93.8NM was excluded from the regression due to abnormal temperature fluctuations during the experiment.

3.3.3.4. Effect of particle size on the selectivity of Ru NPs for CAL hydrogenation

The selectivity to each product was defined as the ratio of the moles of the target product to the moles of total products formed. The profiles of product selectivity as a function of time for the

reaction over different size groups of supported Ru NPs are shown in Figure 3-17. The selectivity of COL increased with the increase of substrate conversion and reached a maximum of 55% at a substrate conversion of 35%. This value remained constant but began to decrease after conversions higher than 70%. The selectivity of HCAL is about 60% at the beginning of the reaction and continuously decreased with increase in substrate conversion; in particular, a sharp rate of decrease was observed at high degrees of conversion (>85%); all HCAL is consumed at 100% conversion of the substrate. The selectivity of HCOL remained at 18% for conversions less than 70%, but increased after that. The selectivity of products for reactions over SG30F-6NM show a similar behavior to those of WD170F-5NM, except for a slight difference in conversion values at which the sharp decrease of HCAL selectivity occurs.

By contrast, increasing the size of Ru NPs to 49.3nm (TW10F-25NM) leads to less than 80% conversion of CAL within 24 hours of reaction. The selectivity of COL increased at the beginning of the reaction and reached a maximum of 55% at lower substrate conversion (20%), in comparison to reactions over smaller Ru NPs (~35%). This selectivity remains constant till the substrate is completely converted. The selectivity for HCAL is the same as in the reactions over smaller Ru NPs at the beginning of the reaction and continuously decreased with increased substrate conversion, but no sharp decreases in rates were observed. The initial selectivity for HCOL is about 15%, and increased slowly as the reaction proceeded. Increasing the Ru NP size to 67 nm (TW12F-67NM) does not affect the product selectivity profiles compared to reactions over the catalyst TW10F-25NM, but it decreased the conversion of substrate within 24 hours. The reaction over 94 nm Ru NPs (TW16F-94NM) has a similar trend in substrate concentration and product selectivity relative to the reaction conducted with the catalyst TW12F-67NM.

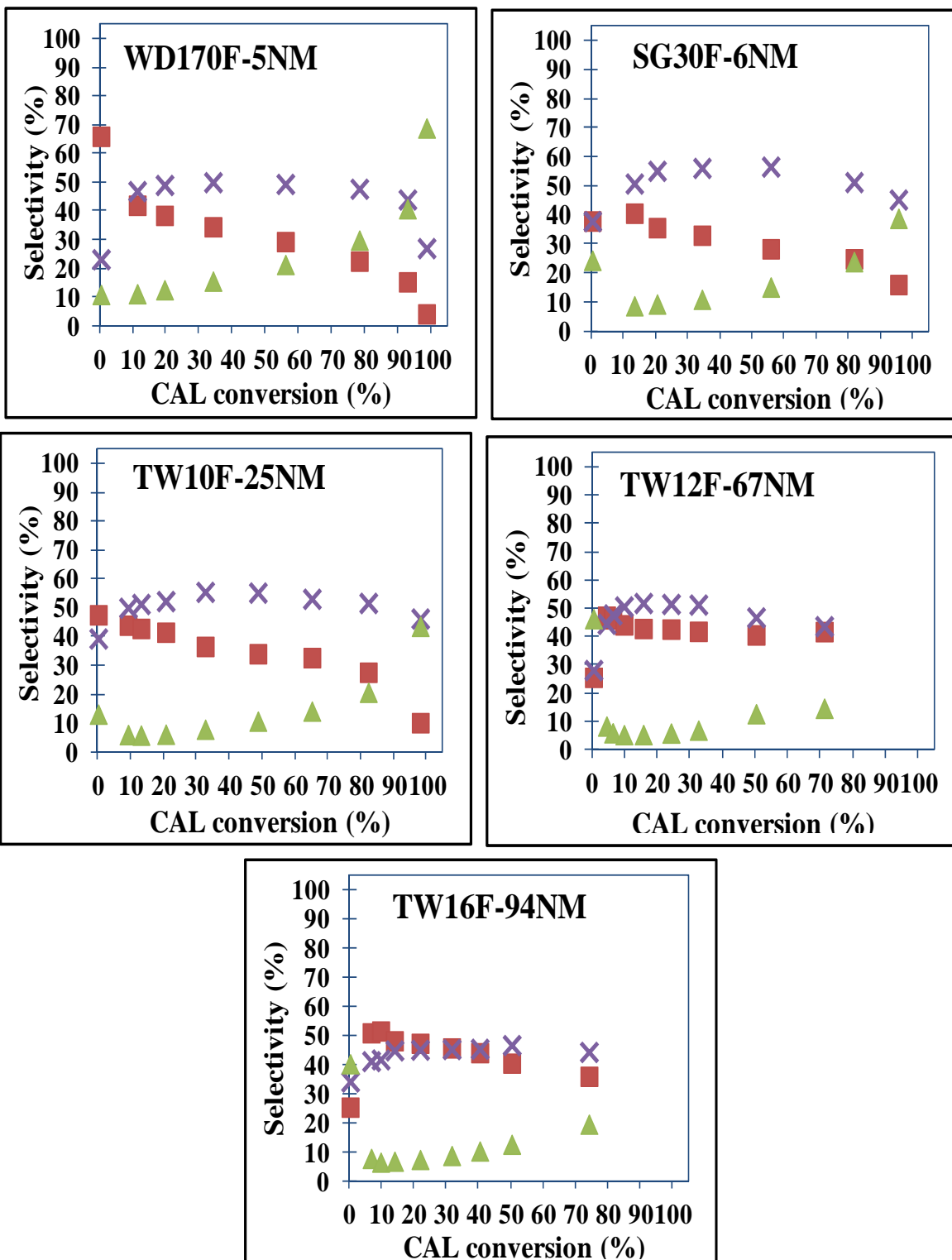


Figure 3-17 Product selectivity as a function of substrate conversion for CAL hydrogenation over Ru NPs supported on MSU-F. ■ HCAL; × COL; ▲ HCOL. Reaction conditions: 35 ml CAL solution in IPA (20mM); $T = 105^{\circ}\text{C}$; Stirring speed = 800 RPM.

The effect of NP size on the selectivity of each product was also investigated at 50% substrate conversion. The choice of 50% conversion for this evaluation is reasonable for our experimental data, since the profiles in Figure 3-17 show that the product distribution remains relatively constant for CAL conversions between 35 and 60%. The profiles in Figure 3-18 also show no obvious variations in product selectivity with respect to NP size, which is in good agreement with the results of CAL hydrogenation using Ru/Al₂O₃ particles in the sub-10 nm range.⁷⁶ This also provides confirmation of our earlier observation that particle size does not affect the reaction pathway for CAL hydrogenation.

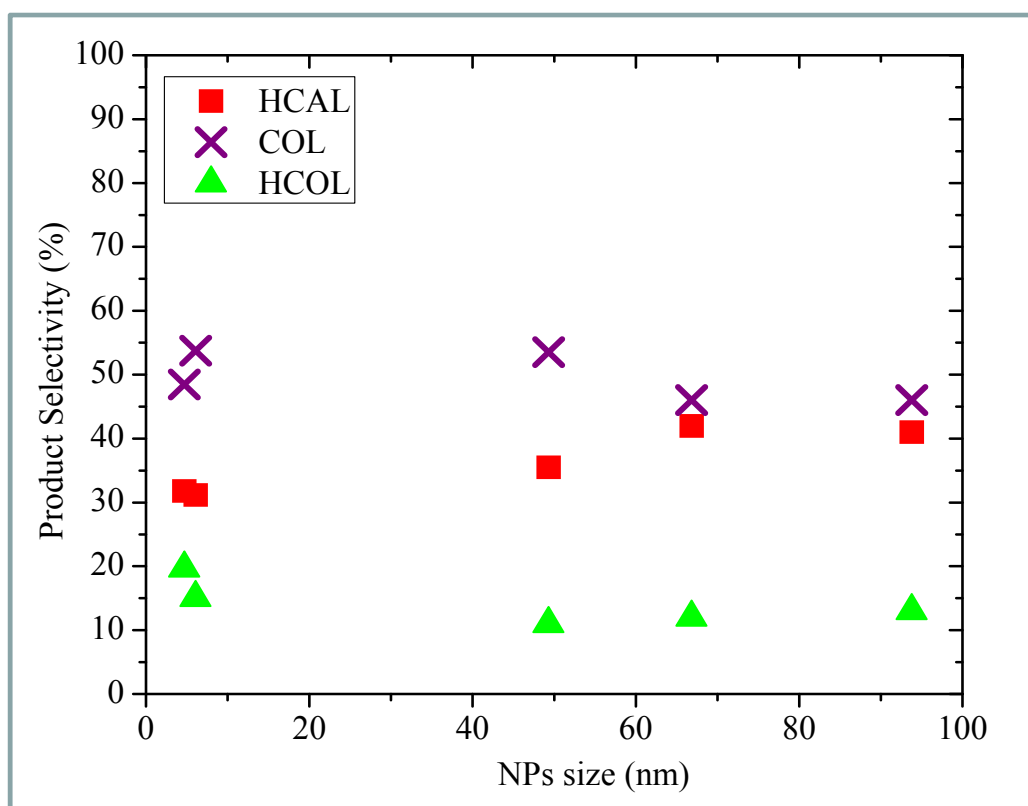


Figure 3-18 Product selectivity as a function of the size of Ru NPs supported on MSU-F. All the reactions were conducted under conditions of 35 ml solution of CAL in IPA (20mM CAL), reaction temperature of 378 K, hydrogen pressure of 20 bar, and a stirring speed of 800 RPM. The amount of Ru used in each reaction was given in Table 3-6.

The apparent activation energies (E_a) for production of HCAL and COL during CAL hydrogenation were also estimated by Arrhenius plots of the natural logarithm of the initial rates of HCAL or COL production versus reciprocal absolute temperature (Figures 3-19a and b). These activation energies are independent of particle size, confirming our earlier observation that particle size does not affect the reaction pathway for CAL hydrogenation.

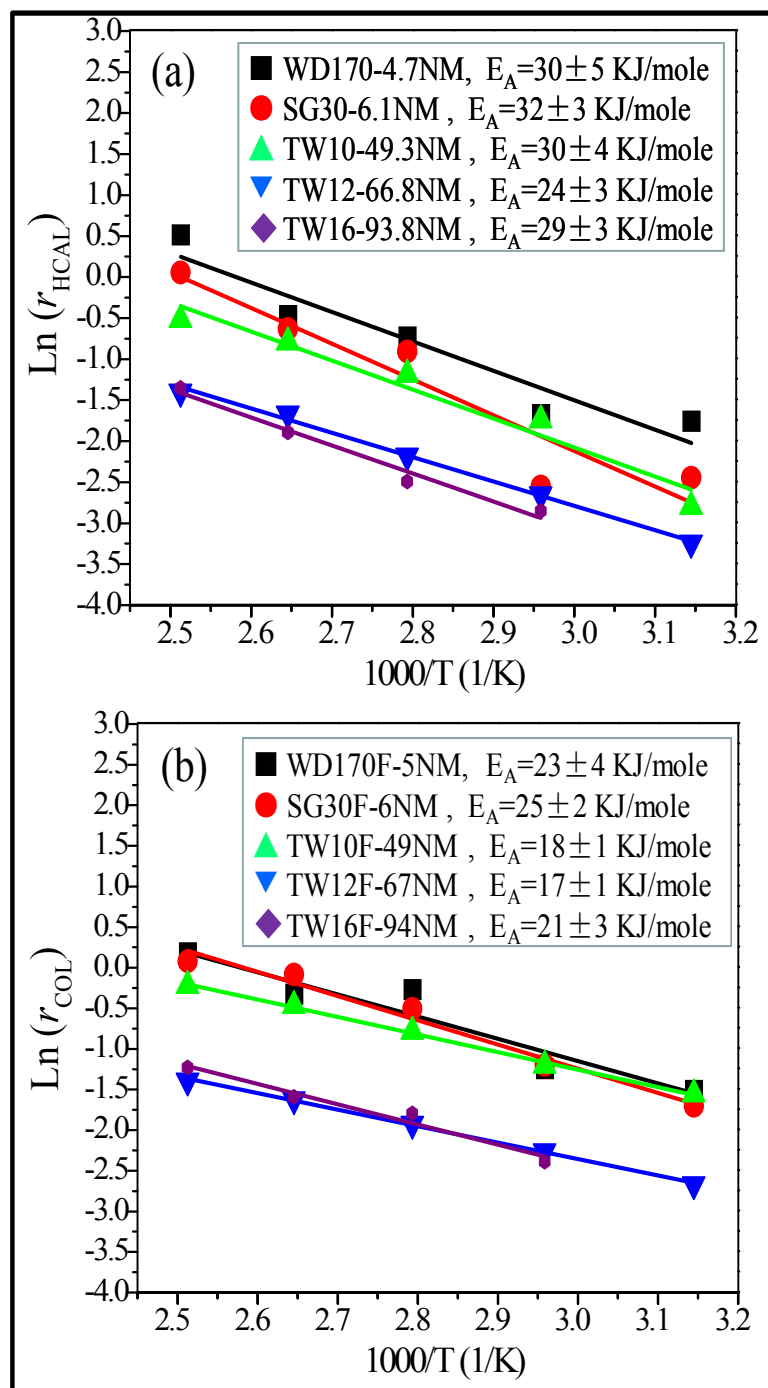


Figure 3-19 Arrhenius plots for the production of HCAL and COL over Ru NPs of different sizes supported on MSU-F. (a): the plot for HCAL; (b): the plot for COL. The apparent activation energies were obtained by linear regression [$\ln(r) = \ln(r_0) - E_A/RT$]. All the reactions were conducted under conditions of 35 ml solution of CAL in IPA (20 mM CAL), hydrogen pressure of 20 bar, and a stirring speed of 800 RPM, over reaction temperatures ranging from 318 K to 398 K. The amount of Ru used in each reaction was given in Table 3-6.

The published literature contains several mechanism-based kinetic analyses for liquid phase hydrogenation of CAL over traditional Ru catalysts.^{13,15,16,20,26,69,77} The most recent kinetic model was based on the Langmuir–Hinshelwood reaction mechanism, under the assumption of non-competitive hydrogen adsorption and competitive adsorption of other molecules, adsorption and hydrogenation of C=O and C=C bonds on different active sites, and irreversible reactions in all the hydrogenation steps.^{69,77} We attempted to apply this model to estimate the reaction parameters for our Ru NPs, but the regression analyses did not provide a good fit. A possible reason for the deviation between the model and our data could be the significant delocalization effect of reaction intermediates for COL and HCAL during the hydrogenation steps, which results in a Braess-like reaction network.⁷⁸

3.4. Summary

We have successfully synthesized spherical Ru NPs ranging from 3.5 to 130 nm by adjusting synthesis parameters using a polyol reduction protocol. The formation of Ru NPs can occur under either thermodynamic or kinetic control. The size of NPs is determined by a balance between the two pathways, and can be regulated through manipulation of the reaction parameters. The reaction temperature was found to have a significant effect on the balance between thermodynamic and kinetic control during the formation of Ru NPs. Manipulating the fraction of the more-easily-reduced Ru (II) salt in the initial precursor solution can substantially change the particle formation kinetics and provide a reliable tuning parameter for Ru NPs over a broad range of size. The concentration and molecular weight of the stabilizing PVP agent have no obvious effect on the final morphology of the Ru NPs.

The size-tunable Ru NPs were successfully immobilized on mesoporous silica support (MSU-F) via sonication-assisted deposition. For all the catalysts activated by Ar-protected calcination, the Ru NPs remained well-dispersed on the support with no signs of agglomeration and no damage to the framework and structure of the support. Thermal activation also improved the crystallinity of the supported NPs.

The reaction products for CAL hydrogenation over supported Ru NPs with different sizes are COL, HCAL, and HCOL. The reaction pathway of CAL hydrogenation over the supported Ru NPs is independent of particle size. However, particle size changes the density of active sites per unit surface area, thus affecting the activity of the catalysts.

REFERENCES

REFERENCES

- (1) Gallezot, P.; Richard, D. Chemoselective hydrogenation of unsaturated carbonyl compounds. *Erdol & Kohle Erdgas Petrochemie*, 1994, 47, 283-286.
- (2) Gallezot, P.; Richard, D. Selective hydrogenation of alpha,beta-unsaturated aldehydes. *Catalysis Reviews-Science and Engineering*, 1998, 40, 81-126.
- (3) Jerdev, D. I.; Olivas, A.; Koel, B. E. Hydrogenation of crotonaldehyde over Sn/Pt(111) alloy model catalysts. *Journal of Catalysis*, 2002, 205, 278-288.
- (4) Murillo, L. E.; Goda, A. M.; Chen, J. G. Selective hydrogenation of the CO bond in acrolein through the architecture of bimetallic surface structures. *Journal of the American Chemical Society*, 2007, 129, 7101-7105.
- (5) Loffreda, D.; Delbecq, F.; Vigne, F.; Sautet, P. Chemo-regioselectivity in heterogeneous catalysis: Competitive routes for C=O and C=C hydrogenations from a theoretical approach. *Journal of the American Chemical Society*, 2006, 128, 1316-1323.
- (6) Blackmond, D. G.; Oukaci, R.; Blanc, B.; Gallezot, P. Geometric and electronic effects in the selective hydrogenation of alpha,beta-unsaturated aldehydes over zeolite-supported metals. *Journal of Catalysis*, 1991, 131, 401-411.
- (7) Haubrich, J.; Loffreda, D.; Delbecq, F.; Sautet, P.; Krupski, A.; Becker, C.; Wandelt, K. Adsorption of alpha,beta-Unsaturated Aldehydes on Pt(111) and Pt-Sn Alloys: II. Crotonaldehyde. *Journal of Physical Chemistry C*, 2009, 113, 13947-13967.
- (8) Haubrich, J.; Loffreda, D.; Delbecq, F.; Sautet, P.; Jugnet, Y.; Krupski, A.; Becker, C.; Wandelt, K. Adsorption and vibrations of alpha,beta-unsaturated aldehydes on pure pt and Pt-Sn alloy (111) surfaces I. Prenal. *Journal of Physical Chemistry C*, 2008, 112, 3701-3718.
- (9) Haubrich, J.; Loffreda, D.; Delbecq, F.; Sautet, P.; Jugnet, Y.; Becker, C.; Wandelt, K. Adsorption and Vibrations of alpha,beta-Unsaturated Aldehydes on Pt(111) and Pt-Sn Alloy (111) Surfaces. 3. Adsorption Energy vs Adsorption Strength. *Journal of Physical Chemistry C*, 2010, 114, 1073-1084.
- (10) Toebes, M. L.; Zhang, Y. H.; Hajek, J.; Nijhuis, T. A.; Bitter, J. H.; van Dillen, A. J.; Murzin, D. Y.; Koningsberger, D. C.; de Jong, K. P. Support effects in the hydrogenation of cinnamaldehyde over carbon nanofiber-supported platinum catalysts: characterization and catalysis. *Journal of Catalysis*, 2004, 226, 215-225.

- (11) Toebes, M. L.; Nijhuis, T. A.; Hajek, J.; Bitter, J. H.; van Dillen, A. J.; Murzin, D. Y.; de Jong, K. P. Support effects in hydrogenation of cinnamaldehyde over carbon nanofiber-supported platinum catalysts: Kinetic modeling. *Chemical Engineering Science*, 2005, *60*, 5682-5695.
- (12) Hajek, J.; Kumar, N.; Nieminen, V.; Maki-Arvela, P.; Salmi, T.; Murzin, D. Y.; Cerveny, L. Deactivation in liquid-phase hydrogenation of cinnamaldehyde over aluminosilicate-supported ruthenium and platinum catalysts. *Chemical Engineering Journal*, 2004, *103*, 35-43.
- (13) Hajek, J.; Kumar, N.; Maki-Arvela, P.; Salmi, T.; Murzin, D. Y. Selective hydrogenation of cinnamaldehyde over Ru/Y zeolite. *Journal of Molecular Catalysis a-Chemical*, 2004, *217*, 145-154.
- (14) Handjani, S.; Marceau, E.; Blanchard, J.; Krafft, J. M.; Che, M.; Maki-Arvela, P.; Kumar, N.; Warna, J.; Murzin, D. Y. Influence of the support composition and acidity on the catalytic properties of mesoporous SBA-15, Al-SBA-15, and Al₂O₃-supported Pt catalysts for cinnamaldehyde hydrogenation. *Journal of Catalysis*, 2011, *282*, 228-236.
- (15) Hajek, J.; Maki-Arvela, P.; Toukoniitty, E.; Kumar, N.; Salmi, T.; Murzin, D. Y.; Cerveny, L.; Paseka, I.; Laine, E. The effect of chemical reducing agents in the synthesis of sol-gel Ru-Sn catalysts: Selective hydrogenation of cinnamaldehyde. *Journal of Sol-Gel Science and Technology*, 2004, *30*, 187-195.
- (16) Hajek, J.; Kumar, N.; Salmi, T.; Murzin, D. Y.; Karhu, H.; Vayrynen, J.; Cerveny, L.; Paseka, I. Impact of catalyst reduction mode on selective hydrogenation of cinnamaldehyde over Ru-Sn sol-gel catalysts. *Industrial & Engineering Chemistry Research*, 2003, *42*, 295-305.
- (17) Delbecq, F.; Loffreda, D.; Sautet, P. Heterogeneous Catalytic Hydrogenation: Is Double Bond/Surface Coordination Necessary? *Journal of Physical Chemistry Letters*, 2010, *1*, 323-326.
- (18) Chen, X. F.; Li, H. X.; Dai, W. L.; Wang, J.; Ran, Y.; Qiao, M. H. Selective hydrogenation of cinnamaldehyde to cinnamyl alcohol over the Co-La-B/SiO₂ amorphous catalyst and the promoting effect of La-dopant. *Applied Catalysis a-General*, 2003, *253*, 359-369.
- (19) Hammoudeh, A.; Mahmoud, S. Selective hydrogenation of cinnamaldehyde over Pd/SiO₂ catalysts: selectivity promotion by alloyed Sn. *Journal of Molecular Catalysis a-Chemical*, 2003, *203*, 231-239.
- (20) Neri, G.; Bonaccorsi, L.; Mercadante, L.; Galvagno, S. Kinetic analysis of cinnamaldehyde hydrogenation over alumina-supported ruthenium catalysts. *Industrial & Engineering Chemistry Research*, 1997, *36*, 3554-3562.
- (21) Coq, B.; Kumbhar, P. S.; Moreau, C.; Moreau, P.; Warawdekar, M. G. Liquid phase hydrogenation of cinnamaldehyde over supported ruthenium catalysts: Influence of

particle size, bimetallics and nature of support. *Journal of Molecular Catalysis*, 1993, 85, 215-228.

(22) Braun, T.; Wohlers, M.; Belz, T.; Schlogl, R. Fullerene-based ruthenium catalysts: A novel approach for anchoring metal to carbonaceous supports .2. Hydrogenation activity. *Catalysis Letters*, 1997, 43, 175-180.

(23) Toebes, M. L.; Prinsloo, F. F.; Bitter, J. H.; van Dillen, A. J.; de Jong, K. P. Influence of oxygen-containing surface groups on the activity and selectivity of carbon nanofiber-supported ruthenium catalysts in the hydrogenation of cinnamaldehyde. *Journal of Catalysis*, 2003, 214, 78-87.

(24) Lashdaf, M.; Krause, A. O. I.; Lindblad, M.; Tiitta, A.; Venalainen, T. Behaviour of palladium and ruthenium catalysts on alumina and silica prepared by gas and liquid phase deposition in cinnamaldehyde hydrogenation. *Applied Catalysis a-General*, 2003, 241, 65-75.

(25) Bachiller-Baeza, B.; Rodriguez-Ramos, I.; Guerrero-Ruiz, A. Influence of Mg and Ce addition to ruthenium based catalysts used in the selective hydrogenation of alpha,beta-unsaturated aldehydes. *Applied Catalysis a-General*, 2001, 205, 227-237.

(26) Hajek, J.; Kumar, N.; Maki-Arvela, P.; Salmi, T.; Murzin, D. Y.; Paseka, I.; Heikkila, T.; Laine, E.; Laukkanen, P.; Vayrynen, J. Ruthenium-modified MCM-41 mesoporous molecular sieve and Y zeolite catalysts for selective hydrogenation of cinnamaldehyde. *Applied Catalysis a-General*, 2003, 251, 385-396.

(27) Fujita, S. I.; Sano, Y.; Bhanage, B. M.; Arai, M. Supported liquid-phase catalysts containing ruthenium complexes for selective hydrogenation of alpha, beta-unsaturated aldehyde: importance of interfaces between liquid film, solvent, and support for the control of product selectivity. *Journal of Catalysis*, 2004, 225, 95-104.

(28) Liu, H. L.; Yuan, M. L.; Guo, C. H.; Li, R. X.; Fu, H. Y.; Chen, H.; Li, X. J. Selective Hydrogenation of Cinnamaldehyde to Cinnamyl Alcohol over Ru/ZrO₂ center dot xH(2)O Catalyst. *Chinese Journal of Catalysis*, 2011, 32, 1256-1261.

(29) Zawadzki, M.; Okal, J. Synthesis and structure characterization of Ru nanoparticles stabilized by PVP or gamma-Al₂O₃. *Materials Research Bulletin*, 2008, 43, 3111-3121.

(30) Tao, A. R.; Habas, S.; Yang, P. D. Shape control of colloidal metal nanocrystals. *Small*, 2008, 4, 310-325.

(31) Shevchenko, E. V.; Talapin, D. V.; Schnablegger, H.; Kornowski, A.; Festin, O.; Svedlindh, P.; Haase, M.; Weller, H. Study of nucleation and growth in the organometallic synthesis of magnetic alloy nanocrystals: The role of nucleation rate in size control of CoPt₃ nanocrystals. *Journal of the American Chemical Society*, 2003, 125, 9090-9101.

- (32) Park, J.; Joo, J.; Kwon, S. G.; Jang, Y.; Hyeon, T. Synthesis of monodisperse spherical nanocrystals. *Angewandte Chemie-International Edition*, 2007, *46*, 4630-4660.
- (33) Pacholski, C.; Kornowski, A.; Weller, H. Self-assembly of ZnO: From nanodots, to nanorods. *Angewandte Chemie-International Edition*, 2002, *41*, 1188.
- (34) Zheng, H. M.; Smith, R. K.; Jun, Y. W.; Kisielowski, C.; Dahmen, U.; Alivisatos, A. P. Observation of Single Colloidal Platinum Nanocrystal Growth Trajectories. *Science*, 2009, *324*, 1309-1312.
- (35) Jun, Y. W.; Lee, J. H.; Choi, J. S.; Cheon, J. Symmetry-controlled colloidal nanocrystals: Nonhydrolytic chemical synthesis and shape determining parameters. *Journal of Physical Chemistry B*, 2005, *109*, 14795-14806.
- (36) Wu, D.; Zheng, Z.; Gao, S.; Cao, M.; Cao, R. Mixed-phase PdRu bimetallic structures with high activity and stability for formic acid electrooxidation. *Physical Chemistry Chemical Physics*, 2012, *14*, 8051-8057.
- (37) Berhault, G.; Bausach, M.; Bisson, L.; Becerra, L.; Thomazeau, C.; Uzio, D. Seed-mediated synthesis of Pd nanocrystals: Factors influencing a kinetic- or thermodynamic-controlled growth regime. *Journal of Physical Chemistry C*, 2007, *111*, 5915-5925.
- (38) Leff, D. V.; Ohara, P. C.; Heath, J. R.; Gelbart, W. M. Thermodynamic Control of Gold Nanocrystal Size: Experiment and Theory. *Journal of Physical Chemistry*, 1995, *99*, 7036-7041.
- (39) Yin, Y.; Alivisatos, A. P. Colloidal nanocrystal synthesis and the organic-inorganic interface. *Nature*, 2005, *437*, 664-670.
- (40) Mazumder, V.; Sun, S. H. Oleylamine-Mediated Synthesis of Pd Nanoparticles for Catalytic Formic Acid Oxidation. *Journal of the American Chemical Society*, 2009, *131*, 4588-+.
- (41) Zhang, Y. W.; Grass, M. E.; Huang, W. Y.; Somorjai, G. A. Seedless Polyol Synthesis and CO Oxidation Activity of Monodisperse (111)- and (100)-Oriented Rhodium Nanocrystals in Sub-10 nm Sizes. *Langmuir*, 2006, *26*, 16463-16468.
- (42) Jana, N. R.; Gearheart, L.; Murphy, C. J. Wet chemical synthesis of high aspect ratio cylindrical gold nanorods. *J. Phys. Chem. B*, 2001, *105*, 4065-4067.
- (43) Wu, H. L.; Kuo, C. H.; Huang, M. H. Seed-Mediated Synthesis of Gold Nanocrystals with Systematic Shape Evolution from Cubic to Trisoctahedral and Rhombic Dodecahedral Structures. *Langmuir*, 2010, *26*, 12307-12313.

- (44) Kim, D. Y.; Li, W. Y.; Ma, Y. Y.; Yu, T.; Li, Z. Y.; Park, O. O.; Xia, Y. N. Seed-Mediated Synthesis of Gold Octahedra in High Purity and with Well-Controlled Sizes and Optical Properties. *Chemistry-a European Journal*, 2011, 17, 4759-4764.
- (45) Xue, C.; Millstone, J. E.; Li, S. Y.; Mirkin, C. A. Plasmon-driven synthesis of triangular core-shell nanoprisms from gold seeds. *Angewandte Chemie-International Edition*, 2007, 46, 8436-8439.
- (46) Lim, B.; Jiang, M. J.; Tao, J.; Camargo, P. H. C.; Zhu, Y. M.; Xia, Y. N. Shape-Controlled Synthesis of Pd Nanocrystals in Aqueous Solutions. *Advanced Functional Materials*, 2009, 19, 189-200.
- (47) Zhang, L.; Niu, W. X.; Xu, G. B. Seed-mediated growth of palladium nanocrystals: The effect of pseudo-halide thiocyanate ions. *Nanoscale*, 2011, 3, 678-682.
- (48) Chen, Y. H.; Hung, H. H.; Huang, M. H. Seed-Mediated Synthesis of Palladium Nanorods and Branched Nanocrystals and Their Use as Recyclable Suzuki Coupling Reaction Catalysts. *Journal of the American Chemical Society*, 2009, 131, 9114-9121.
- (49) He, B. L.; Chen, Y. X.; Liu, H. F.; Liu, Y. Synthesis of solvent-stabilized colloidal nanoparticles of platinum, rhodium, and ruthenium by microwave-polyol process. *Journal of Nanoscience and Nanotechnology*, 2005, 5, 266-270.
- (50) Alayoglu, S.; Nilekar, A. U.; Mavrikakis, M.; Eichhorn, B. Ru-Pt core-shell nanoparticles for preferential oxidation of carbon monoxide in hydrogen. *Nature Materials*, 2008, 7, 333-338.
- (51) Zhang, Q. A.; Li, W. Y.; Moran, C.; Zeng, J.; Chen, J. Y.; Wen, L. P.; Xia, Y. N. Seed-Mediated Synthesis of Ag Nanocubes with Controllable Edge Lengths in the Range of 30-200 nm and Comparison of Their Optical Properties. *Journal of the American Chemical Society*, 2010, 132, 11372-11378.
- (52) Xiong, Y. J.; Cai, H. G.; Wiley, B. J.; Wang, J. G.; Kim, M. J.; Xia, Y. N. Synthesis and mechanistic study of palladium nanobars and nanorods. *Journal of the American Chemical Society*, 2007, 129, 3665-3675.
- (53) Zhang, Y. W.; Grass, M. E.; Habas, S. E.; Tao, F.; Zhang, T. F.; Yang, P. D.; Somorjai, G. A. One-step polyol synthesis and langmuir-blodgett monolayer formation of size-tunable monodisperse rhodium nanocrystals with catalytically active (111) surface structures. *Journal of Physical Chemistry C*, 2007, 111, 12243-12253.
- (54) Fan, F. R.; Liu, D. Y.; Wu, Y. F.; Duan, S.; Xie, Z. X.; Jiang, Z. Y.; Tian, Z. Q. Epitaxial growth of heterogeneous metal nanocrystals: From gold nano-octahedra to palladium and silver nanocubes. *Journal of the American Chemical Society*, 2008, 130, 6949.

- (55) Lee, J. N.; Park, C.; Whitesides, G. M. Solvent compatibility of poly(dimethylsiloxane)-based microfluidic devices. *Analytical Chemistry*, 2003, 75, 6544-6554.
- (56) Lee, I.; Morales, R.; Albiter, M. A.; Zaera, F. Synthesis of heterogeneous catalysts with well shaped platinum particles to control reaction selectivity. *Proceedings of the National Academy of Sciences of the United States of America*, 2008, 105, 15241-15246.
- (57) Borodko, Y.; Habas, S. E.; Koebel, M.; Yang, P. D.; Frei, H.; Somorjai, G. A. Probing the interaction of poly(vinylpyrrolidone) with platinum nanocrystals by UV-Raman and FTIR. *Journal of Physical Chemistry B*, 2006, 110, 23052-23059.
- (58) R. Van Hardeveld, F. H. The statistics of surface atoms and surface sites on metal crystals. *Surface Science*, 1969, 15, 189-230.
- (59) Pushkarev, V. V.; An, K.; Alayoglu, S.; Beaumont, S. K.; Somorjai, G. A. Hydrogenation of benzene and toluene over size controlled Pt/SBA-15 catalysts: Elucidation of the Pt particle size effect on reaction kinetics. *Journal of Catalysis*, 2012, 292, 64-72.
- (60) Crespo-Quesada, M.; Yarulin, A.; Jin, M. S.; Xia, Y. N.; Kiwi-Minsker, L. Structure Sensitivity of Alkynol Hydrogenation on Shape- and Size-Controlled Palladium Nanocrystals: Which Sites Are Most Active and Selective? *Journal of the American Chemical Society*, 133, 12787-12794.
- (61) Chen, Y. Aqueous-phase catalytic hydrogenation of organic acids and their mixtures. *dissertation, Michigan State University*, 2007.
- (62) Rioux, R. M.; Vannice, M. A. Dehydrogenation of isopropyl alcohol on carbon-supported Pt and Cu-Pt catalysts. *Journal of Catalysis*, 2005, 233, 147-165.
- (63) Zhang, Z. G.; Jackson, J. E.; Miller, D. J. Kinetics of aqueous-phase hydrogenation of lactic acid to propylene glycol. *Industrial & Engineering Chemistry Research*, 2002, 41, 691-696.
- (64) Chen, Y. Q.; Miller, D. J.; Jackson, J. E. Kinetics of aqueous-phase hydrogenation of organic acids and their mixtures over carbon supported ruthenium catalyst. *Industrial & Engineering Chemistry Research*, 2007, 46, 3334-3340.
- (65) yuqing, c. Kinetics of Aqueous Phase Hydrogenation of Organic Acids and their Mixtures over Carbon-supported Ruthenium Catalyst. *Dissertation, Michigan State University*, 2007.
- (66) Zhang, Z. Aqueous-phase hydrogenation of biomass derived lactic acid to propylene glycol. *Dissertations & Theses. Michigan State University*, 2000.
- (67) Weisz, P. B.; Prater, C. D. Interpretation of measurements in experimental catalysis. *Advances in Catalysis*, 1954, 6, 143-196.

(68) Wilke, C. R.; Chang, P. Correlation of diffusion coefficients in dilute solutions. *Aiche Journal*, 1955, *1*, 264-270.

(69) Hajek, J.; Murzin, D. Y. Liquid-phase hydrogenation of cinnamaldehyde over a Ru-Sn sol-gel catalyst. 1. Evaluation of mass transfer via a combined experimental/theoretical approach. *Industrial & Engineering Chemistry Research*, 2004, *43*, 2030-2038.

(70) Yaws, C. Chemical Properties Handbook: Physical, Thermodynamics, Environmental Transport, Safety & Health Related Properties for Organic & Inorganic Chemical. 1998.

(71) Brunner, E. Solubility of Hydrogen in Alcohols. *Berichte Der Bunsen-Gesellschaft-Physical Chemistry Chemical Physics*, 1979, *83*, 715-721.

(72) Ide, M. S.; Hao, B.; Neurock, M.; Davis, R. J. Mechanistic Insights on the Hydrogenation of alpha,beta-Unsaturated Ketones and Aldehydes to Unsaturated Alcohols over Metal Catalysts. *Acs Catalysis*, *2*, 671-683.

(73) Mortensen, J. J.; Hansen, L. B.; Jacobsen, K. W. Real-space grid implementation of the projector augmented wave method. *Phys. Rev. B*, 2005, *71*.

(74) Zhang, Y.; Yang, W. Comment on "Generalized Gradient Approximation Made Simple". *Physical Review Letters*, 1998, *80*, 890-890.

(75) The GPAW program package is freely available at <https://wiki.fysik.dtu.dk/gpaw/>.

(76) Mercadante, L.; Neri, G.; Milone, C.; Donato, A.; Galvagno, S. Hydrogenation of alpha,beta-unsaturated aldehydes over Ru/Al₂O₃ catalysts. *Journal of Molecular Catalysis a-Chemical*, 1996, *105*, 93-101.

(77) Hajek, J.; Warna, J.; Murzin, D. Y. Liquid-phase hydrogenation of cinnamaldehyde over a Ru-Sn sol-gel catalyst. 2. Kinetic modeling. *Industrial & Engineering Chemistry Research*, 2004, *43*, 2039-2048.

(78) Lepore, D. M.; Barratt, C.; Schwartz, P. M. Computational models of chemical systems inspired by Braess' paradox. *Journal of Mathematical Chemistry*, 2011, *49*, 356-370.

Chapter 4: Effect of compositions of Ru-Pd bimetallic NPs on CAL hydrogenation

Abstract

We assessed how the composition of Ru-based bimetallic catalysts affects their selectivity and catalytic activity for cinnamaldehyde (CAL) hydrogenation. The colloidal Ru-Pd bimetallic NPs as well as their monometallic counterparts were synthesized by polyol reduction of the metal precursors, impregnated into MSU-F support via sonication-assisted deposition, and activated through Ar-protected calcination. The supported NPs in each catalyst complex were well dispersed on MSU-F as uniform spheres with sizes ranging from 10 to 12 nm. We also observed that the supported bimetallic NPs have an alloyed crystal structure, with uniform distribution of the two metals in each particle. The hydrogenation of CAL over all the supported Ru-Pd bimetallic NPs and the monometallic Pd NPs produced either hydrocinnamaldehyde (HCAL) or hydrocinnamyl alcohol (HCOL) as the major product, with the molar ratio of HCAL to HCOL strongly dependent on the metal composition of the catalysts. The supported bimetallic NPs produced higher turnover frequencies (TOF) than the monometallic Ru NPs, with the enhancement proportional to the Pd fraction up to 53 mol%, presumably due to synergetic effects. Similarly, we observed that the apparent activation energy is strongly dependent on the metal composition of the supported NPs.

4.1. Introduction

Extensive efforts have been made to elucidate the effects of catalyst composition and structure on catalytic behavior. It is generally recognized that the surface structure and bulk composition of bimetallic catalysts depend on a number of parameters, including the precursors of the constituent metals, type of support, catalyst preparation procedures, and metal-metal and metal-support interactions.¹⁻¹⁴

Our goal in this study was to investigate the effect of metallic composition on the reactivity and selectivity of Ru-Pd bimetallic nanocatalysts supported on mesoporous silica (MSU-F), using the catalytic hydrogenation of CAL as a model reaction. Different compositions of Ru-Pd bimetallic NPs were synthesized by polyol co-reduction of the two metal precursors. The monodisperse bimetallic NPs were then immobilized on mesoporous silica support (MSU-F) following the procedures described in Chapter 2. The characteristics of the supported Ru-Pd bimetallic catalysts as well as the colloidal bimetallic NPs were measured by several physical and chemical techniques including TEM, SAED, EDS, FTIR, physisorption, chemisorption, and TPD. The liquid phase hydrogenation of CAL was used as the model reaction to investigate the relationship between catalyst composition and a number of key kinetic parameters, including reactivity, selectivity, activation energies, and pre-exponential factors. We believe this work provides the first attempt to link composition and structure (NP morphology and crystallinity) of supported Ru-Pd bimetallic nanocatalysts to catalytic performance for the liquid phase hydrogenation of α , β -unsaturated aldehydes.

4.2. Experimental

Poly-N-vinyl-2-pyrrolidone (PVP, MW=55K), acetone (ACS reagent, $\geq 99.5\%$), and mesoporous silica (MSU-F) were purchased from Sigma-Aldrich (St. Louis, MO). Ruthenium acetylacetonate $[\text{Ru}(\text{acac})_3]$ (99%), dichlorotricarbonylruthenium (II) dimer, 98% $[\text{RuCl}_2(\text{CO})_3]_2$, and palladium acetylacetonate ($[\text{Pd}(\text{acac})_2]$, 99%) were purchased from Strem Chemicals (Newburyport, MA). Phenyl ether (99%) and 1,4-butanediol (99%) were purchased from Alfa Aesar (Ward Hill, MA). High purity argon gas (99.99%) was purchased from Airgas (Lansing, MI). All chemicals were used without further purification. Copper grids with 3-nm carbon film coatings for TEM analysis were purchased from Ted Pella, Inc. (Redding, CA). All the solvents were of analytical grade and were used without further purification.

4.2.1. Synthesis of colloidal Ru-Pd bimetallic NPs

The Ru-Pd bimetallic NPs were synthesized by polyol co-reduction of Ru and Pd metal precursors, using PVP as the stabilizing agent. In a typical synthesis, a total amount of 0.2 mmol metal precursors consisting of $\text{Ru}(\text{acac})_3$ (or $[\text{RuCl}_2(\text{CO})_3]_2$) and $\text{Pd}(\text{acac})_2$ was transferred into a 50 mL round bottom Schlenk flask equipped with a reflux condenser and a Teflon-coated magnetic stirring bar, followed by addition of 0.222 g PVP. After that, 10 mL of 1,4-butanediol was transferred into the system at room temperature to dissolve the precursors and stabilizer. The mixture was heated from room temperature to 65°C under magnetic stirring to completely dissolve the salt, followed by 10 min of evacuation and introduction of argon into the system. The solution was then heated from 80°C to 180°C at a rate of $10^\circ\text{C}/\text{min}$. To monitor the progression of each reaction, 0.2 ml of sample was retrieved periodically from the reaction

mixture using a long needle syringe, mixed with acetone to form a suspension, and centrifuged to observe the color of the supernatant. The reaction was terminated when the supernatant became clear. When the reaction was complete, the colloidal product was cooled to room temperature and an excess of acetone was poured into the mixture to induce a cloudy brown suspension. This suspension was separated by centrifugation at 5000 RPM for 8 min and the black product was collected after discarding the colorless supernatant. The precipitated NPs were washed once with acetone, and then re-dispersed in methanol prior to being used for experiments. The concentrations of precursors used in each synthesis are listed in Table 4-1. The samples were labeled Pd#RuII or Pd#RuIII, where # represents the molar percentage of Pd in the precursor mixture, and the Roman numeral is the type of Ru precursor used in the synthesis.

Table 4-1 Metal concentrations in precursor solution for synthesis of Ru-Pd bimetallic NPs

Sample ID ^a	Ru concentration in precursor solution (mM)	Pd concentration in precursor solution (mM)	Pd fraction in metal precursor (<i>mol%</i> Pd)
Pd00Ru(II/III)	20.0	0.0	0
Pd05Ru(II/III)	19.0	1.0	5
Pd20Ru(II/III)	16.0	4.0	20
Pd40Ru(II/III)	14.0	6.0	40
Pd50Ru(II/III)	10.0	10.0	50
Pd60Ru(II/III)	8.0	12.0	60
Pd80Ru(II/III)	4.0	16.0	80
Pd100Ru(II/III)	0.0	20.0	100

^aThe Roman numerals represent the type of Ru precursor used. RuII represents the precursor Ru(acac)₃; RuIII represents the precursor [RuCl₂(CO)₃]₂

The procedure used to synthesize the Pd NPs was similar to that used to synthesize the bimetallic NPs, except that 0.2 mmol Pd(acac)₂ was added to the reaction mixture (Table 4-1), and the reaction temperature was 110°C .

The particle size and shape were analyzed using a Model JEOL 2200FS electron microscope (Tokyo, Japan) under the operating conditions described in Chapter 2.

4.2.2. Preparation of Ru-Pd bimetallic NPs supported on MSU-F

The colloidal NPs were put on MSU-F support by the sonication-assisted deposition method described in Chapter 2. The catalysts were stored in vacuum desiccators prior to their use for experiments. Ar-protected calcination was used to remove the capping PVP agent from the supported NPs.

4.2.3. Characterization of Ru-Pd bimetallic NPs supported on MSU-F

The morphologies of the supported catalysts were analyzed by TEM under the conditions described in Chapter 2. The elemental distribution of the NPs was characterized by a combination of STEM-EDS point analysis, mapping, and line scan. SAED was used to characterize the crystal structures of the NPs. The elemental compositions of the supported bimetallic catalysts were determined by ICP-AES on an Agilent 720 Series ICP-AES Spectrometer. The specific surface area and average pore diameter of the catalysts were obtained by nitrogen adsorption–desorption measurements at liquid nitrogen temperature (~78 K) with a Micromeritics ASAP 2010 M instrument. The metal dispersion of each catalyst was evaluated by a combination of H₂ chemisorption and CO chemisorption, respectively. XRD patterns were obtained with a Bruker D8 diffractometer with a Ru K α source. Infrared spectra of the samples were obtained on a Mattson Galaxy FT-IR spectrometer (Mattson Instruments, Madison, WI) using KBr pellets. CO temperature-programmed deposition (CO-TPD) measurements were performed on a Micromeritics AutoChem II 2920 instrument using helium as the carrier gas and

10% H₂ in helium as the analysis gas. All measurements were carried out in a U-shaped quartz tube heated by an automatic furnace. For each CO-TPD experiment, 0.30 g sample was first reduced by 10% H₂ in helium at 350°C. The catalyst was then flushed by helium 360°C to remove the adsorbed H₂ and then flushed by 10 % CO in Ar to adsorb CO. After cooling to room temperature, the catalyst was flushed with helium at 360°C to remove the physically adsorbed CO, followed by TPD analysis over a temperature range of 40°C to 450°C at a ramp rate of 10°C/min. The amount of CO consumed was determined by a thermal conductivity detector (TCD).

4.2.4. General procedure for catalytic experiments

CAL hydrogenation over Ru-Pd NPs supported on MSU-F was conducted in a Parr multi-batch reactor system (Model 5000, Parr Instrument Co., Moline, IL) equipped with a magnetically coupled stirring unit. The experimental procedures were described in Chapter 3. Liquid samples (2 mL) were withdrawn periodically and analyzed by a Bruker 450 GC-FID equipped with a DB-1 capillary column. Prior to GC analysis, each sample was centrifuged at 300 RPM for 3 min to remove the solid catalyst.

4.3. Results and Discussion

4.3.1. Synthesis of colloidal Pd NPs and Ru-Pd bimetallic NPs

Generally, core-shell, alloy, and aggregate mixtures are the three main types of structures for bimetallic NPs.¹⁵⁻¹⁹ With recent advances in nanotechnology, several liquid-based methods have been explored for synthesis of bimetallic NPs, including co-reduction, seed-mediated growth, galvanic replacement reactions, and noble-metal-induced-reduction (NMIR).¹⁹⁻²²

Co-reduction is one of the widely used colloidal methods for preparation of bimetallic NPs because of its easy operation and high flexibility. To avoid separate nucleation of the two metals during co-reduction, it is necessary to select the proper reducing agent and reaction conditions such as temperature. In principle, this method can be used to control the structure of the bimetallic NPs by using two metal precursors with different redox potentials. Figures 4-1 and 4-2 show typical TEM images of Ru-Pd NPs synthesized with a mixture of $[\text{RuCl}_2(\text{CO})_3]_2$ and $\text{Pd}(\text{acac})_2$ as metal precursors, and a mixture of $\text{Ru}(\text{acac})_3$ and $\text{Pd}(\text{acac})_2$ as metal precursors, respectively. When the more-easily-reduced Ru compound (Ru II, $[\text{RuCl}_2(\text{CO})_3]_2$) was used as the Ru precursor, the resulting Ru-Pd bimetallic NPs underwent a drastic change in morphology (Figure 4-1) with variation of metal composition in the precursor mixtures. At a Pd composition of 20 mol% and 40 mol% in the metal precursor mixtures, a large number of rod-shaped NPs were visible in the HRTEM images in addition to the small irregularly-shaped NPs which may serve as building-blocks for further particle growth. It is likely that the production of poly-disperse NPs is due to the significant difference in redox potentials of the two metal precursors in the polyol solution. As the Pd composition in the metal precursor mixture was increased to 50 mol% and 60 mol%, fewer rod-shaped NPs were observed and particle uniformity improved.

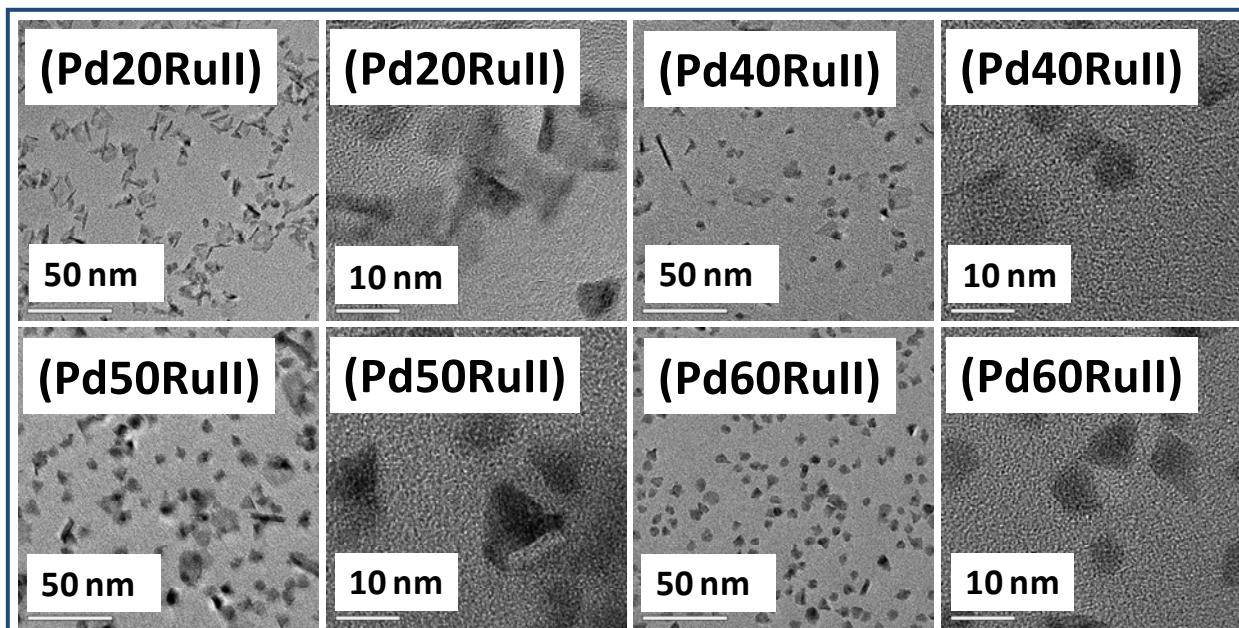


Figure 4-1 Typical TEM images of colloidal Ru-Pd NPs synthesized with Ru(II) as precursor. The number in each notation of the images represents the mole fraction of Pd salt in the metal precursor mixture. The Roman numeral “II” in the notations means that $[\text{RuCl}_2(\text{CO})_3]_2$ was used as the Ru precursor.

By contrast, when Ru (III) salt ($\text{Ru}(\text{acac})_3$) instead of Ru (II) was used as the Ru precursor, the predominant shape of the NPs in each sample is a truncated sphere, although other shapes such as hexagons, pentagons, triangles and cubes are also present (Figure 4-2). A small quantity of branched and multiple twinned shapes can also be observed in Figure 4-2. The monometallic Ru NPs were mostly spherical with an average diameter of 3.2 nm. Using the metal precursor mixture with 5 mol% Pd had little effect on particle morphology, but it resulted in increasing the particle size to about 8 nm. When the percent of Pd was increased to 20 mol%, the NPs appeared less monodisperse and less uniform in size, varying from 5 to 12 nm. In contrast, the NPs synthesized with 40 mol% Pd in the precursor mixture produced relatively monodisperse spherical NPs with an average diameter of 12 nm. The distribution of size and shape of the NPs did not change significantly following further increases in the fraction of Pd in the metal precursor mixture.

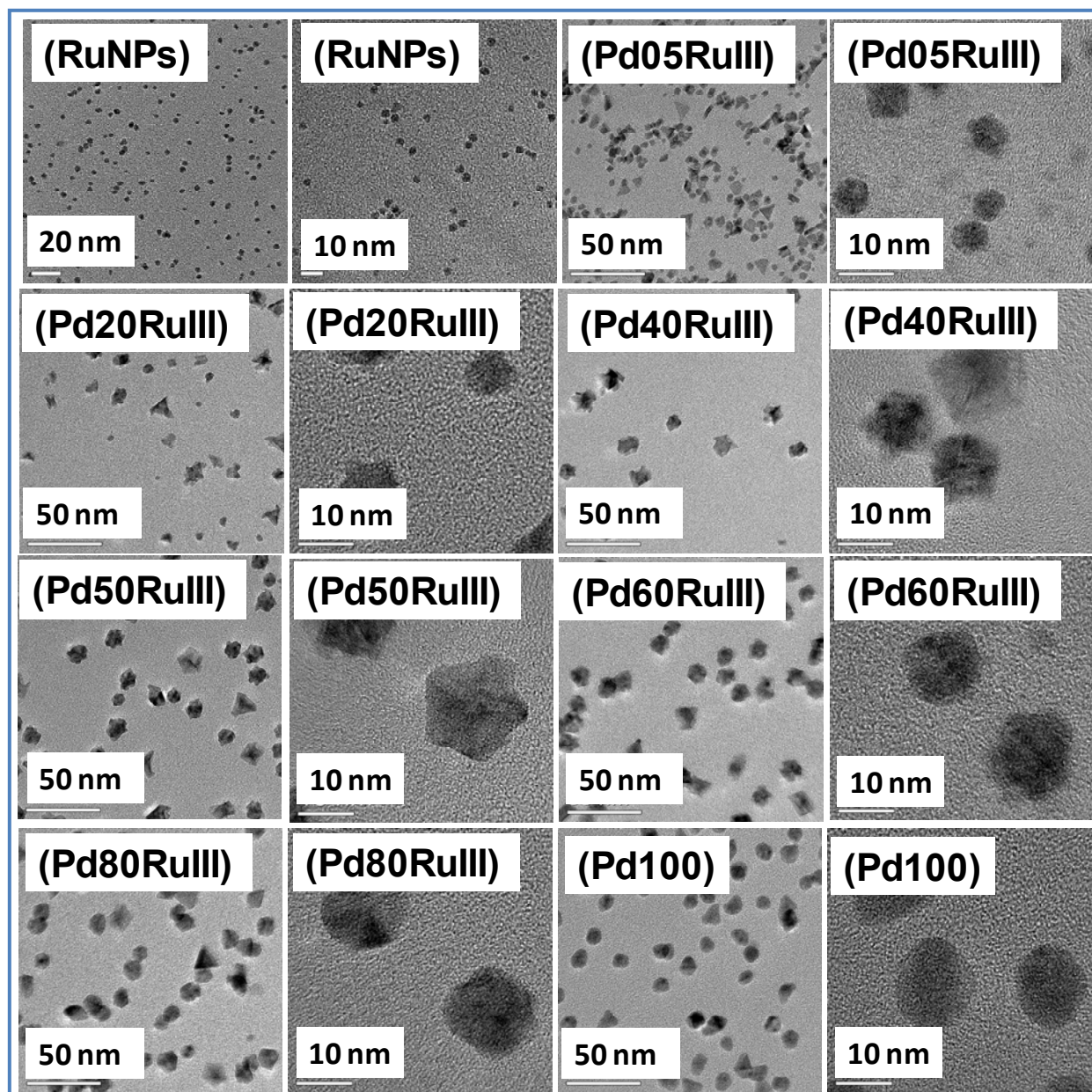


Figure 4-2 Typical TEM images of colloidal Ru-Pd NPs synthesized with Ru(III) as Ru precursor. The number in each figure is the mole fraction of Pd salt used in the metal precursor mixture. The Roman numeral “III” in the notations means Ru(acac)₃ was the Ru salt used in the metal precursor mixture.

The metal compositions of colloidal NPs synthesized with metal precursor mixtures of Ru (III) and Pd(acac)₂ were determined by EDS elemental mapping and line scan of various regions in each sample. The EDS spectra (Figure 4-3) show that all the NPs were composed of Ru and Pd

elements, and no monometallic NPs were observed in any of the samples, demonstrating that the NPs from the various syntheses are bimetallic in nature. The EDS line scan of each sample (except for Pd05RuIII whose size was too small for a EDS line scan) show single Gaussian distributions of signals for both Ru and Pd elements, indicating that the NPs have an alloy structure with random distribution of atoms in the particle.^{16,23}

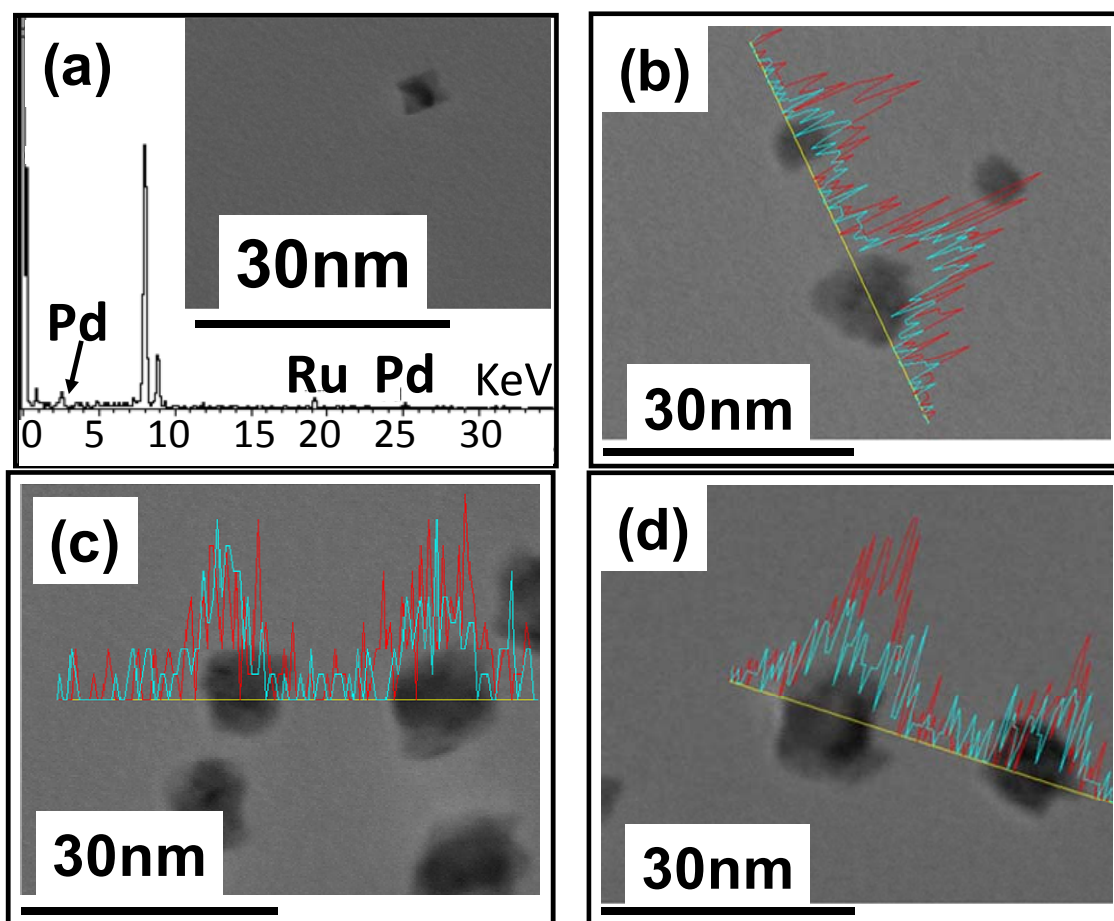
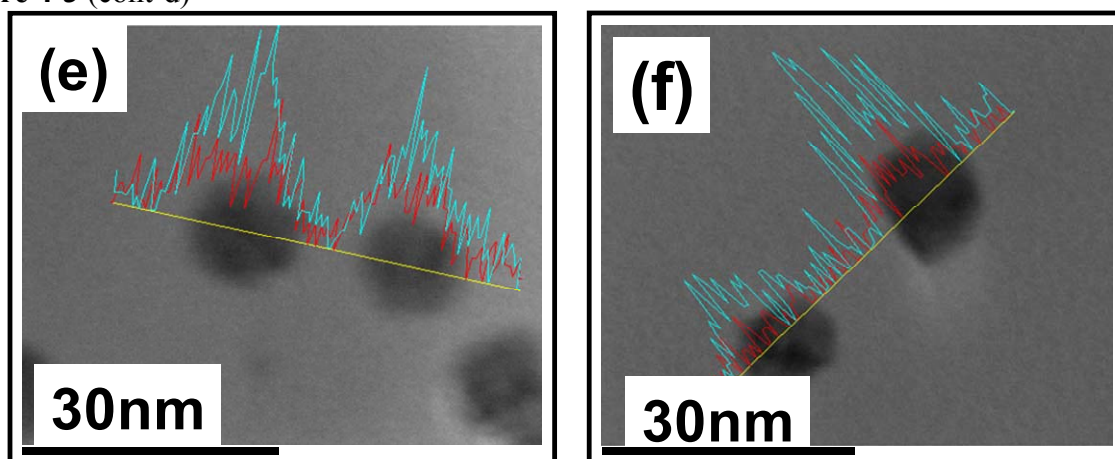


Figure 4-3 EDS spectra of colloidal Ru-Pd NPs. (a) Pd05RuIII, (b) Pd20RuIII, (c) Pd40RuIII, (d) Pd50RuIII, (e) Pd60RuIII, (f) Pd80RuIII. All the analyses were done under a STEM model with a point resolution of 0.19 nm and a high angle dark field resolution of 0.13 nm. The elemental line scans were done at a magnification of 3.0M. The EDS spectra were taken through the line across the selected NPs, where the x-axis represents the length of the line in the image and the y-axis the elemental signal strength at the corresponding location of the line.

Figure 4-3 (cont'd)



4.3.2. Characterization of Ru-Pd NPs supported on MSU-F

A list of the colloidal Ru-Pd NPs used for the preparation of Ru-Pd catalysts supported on mesoporous silica (MSU-F) and the labels for the corresponding catalysts are given in Table 4-2.

Table 4-2 A list of colloidal Ru-Pd NPs used to prepare catalysts supported on MSU-F

colloidal NPs	Pd05RuIII	Pd20RuIII	Pd40RuIII	Pd50RuIII	Pd60RuIII	Pd80RuIII	Pd100
supported NPs	Pd05RuF	Pd20RuF	Pd40RuF	Pd50RuF	Pd60RuF	Pd80RuF	Pd100F

The FT-IR spectra of the pure support (MSU-F), the capping agent (PVP), and each catalyst are displayed in Figure 4-4. The spectra of the support (MSU-F) and the PVP stabilizer have characteristic absorption peaks in agreement with previous reports²⁴. The IR spectra of the catalysts activated through the Ar-protected calcination only have the characteristic peaks of the pure support, indicating complete removal of the capping polymer agent from the surface of the supported NPs.

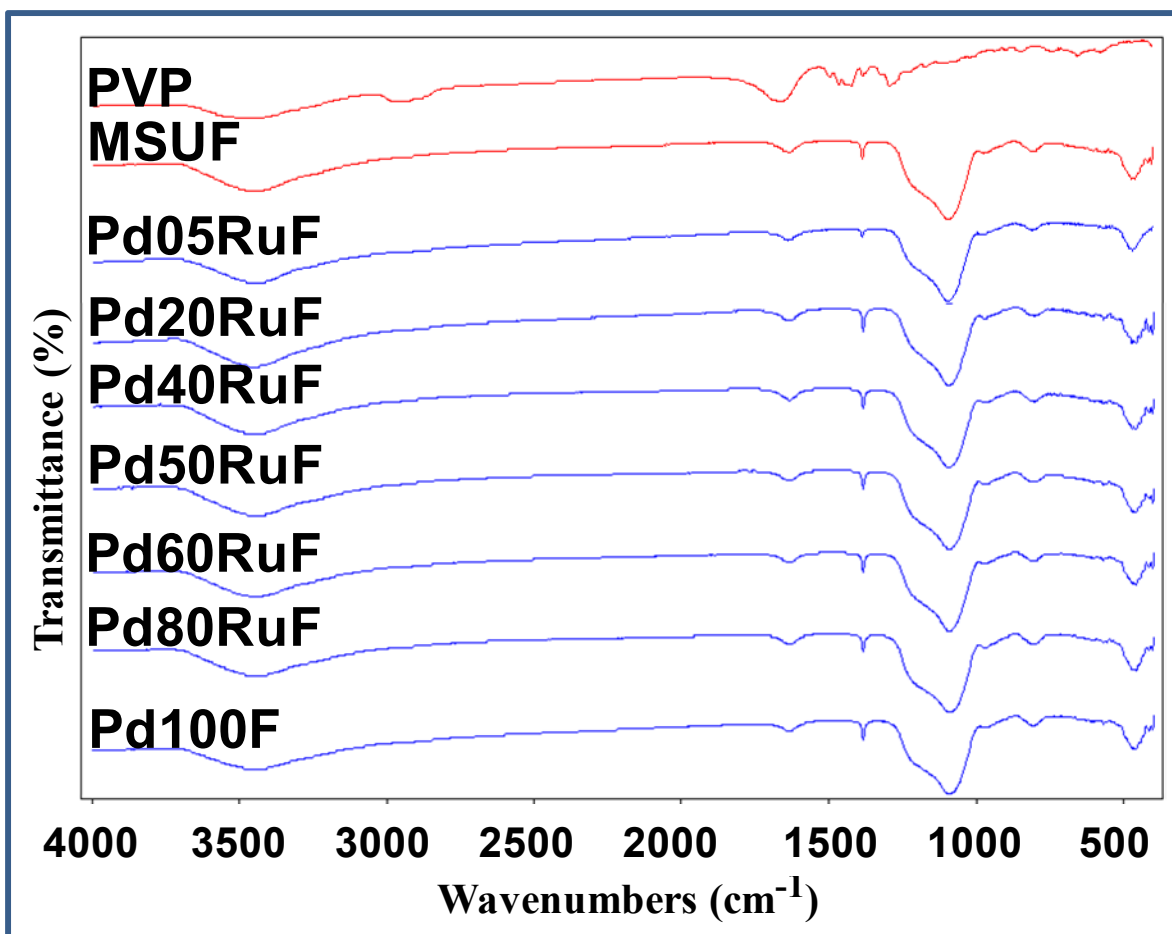


Figure 4-4 FTIR spectra of MSU-F, PVP, and Ru-Pd NPs supported on MSU-F. As was observed for the monometallic samples, MSU-F shows a strong adsorption peak at 1100 cm^{-1} corresponding to the Si-O stretch. Pure PVP has C=O and C-N stretch bands at 1694 and 1674 cm^{-1} , asymmetric CH_2 stretches at 2950 cm^{-1} for the pyrrolidone ring and at 2922 cm^{-1} for the polymer backbone, a CH bending band at 1371 cm^{-1} , and a CH_2 scissor band at 1461 cm^{-1} . The spectrum also contains a series of bands in the range 750 cm^{-1} to 1300 cm^{-1} , corresponding to the spectra of the C-C ring and C-C chain of PVP. The catalysts activated through the Ar-protected calcination only have the characteristic peaks of the pure support.

4.3.2.1. Morphologies and chemical compositions of Ru-Pd NPs supported on MSU-F

Typical TEM images of Ru-Pd bimetallic NPs and Pd monometallic NPs (each supported on MSU-F) are shown in Figure 4-5. For all catalysts, the support still has a layered structure after thermal activation under Ar-protected calcination at 650°C . The support (MSU-F) also retained its typical mesoporous structure, which consists of a hexagonal framework with a cell window

size of ~15 nm. The NPs are well-dispersed on the support with no signs of agglomeration and no damage to the framework or structure of the support. No unsupported NPs were observed in any of the TEM images, indicating a strong interaction between the NPs and the support.

The images at higher magnification (scale bar of 20 nm) in Figure 4-4 show that all the NPs on the support are mostly spherical in shape after thermal treatment. These results are quite different from those of the colloidal Ru-Pd bimetallic NPs, which had various shapes in addition to the predominantly polyhedral shape (Figure 4-2). These results suggest that the thermal treatment significantly improved uniformity in the size and shape of the supported NPs. This improvement can be attributed to sintering and annealing effects during calcination. The particle size distribution of each catalyst was determined by measuring about 100 randomly selected particles over multiple areas in the TEM image of each sample.

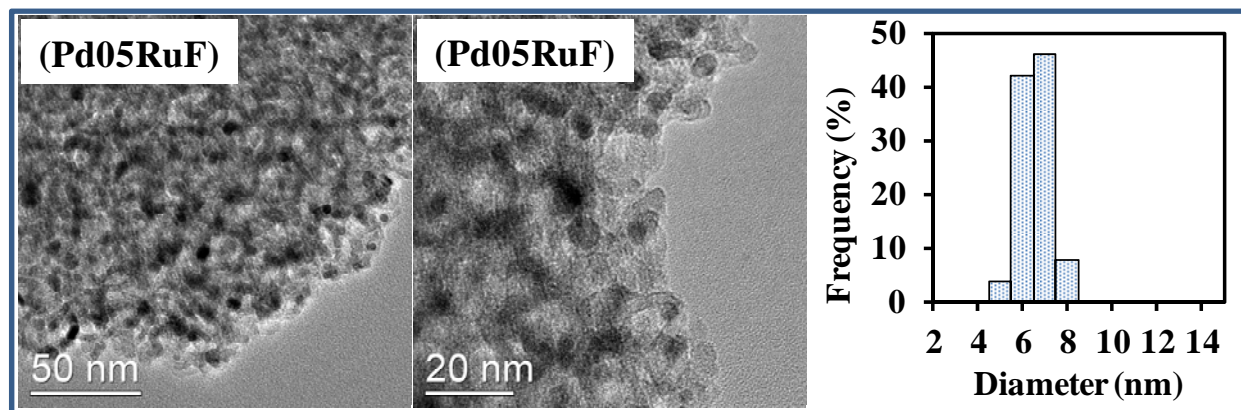


Figure 4-5 Typical TEM images of Ru-Pd NPs supported on MSU-F. The images with scale bar of 50 nm were taken at a magnification of 100 K; the images with scale bar of 20 nm were taken at a magnification of 400 K. The size distribution of NPs in each sample was determined by measuring the diameters of randomly selected NPs (~100 counts) from various TEM images of each sample.

Figure 4-5 (cont'd)

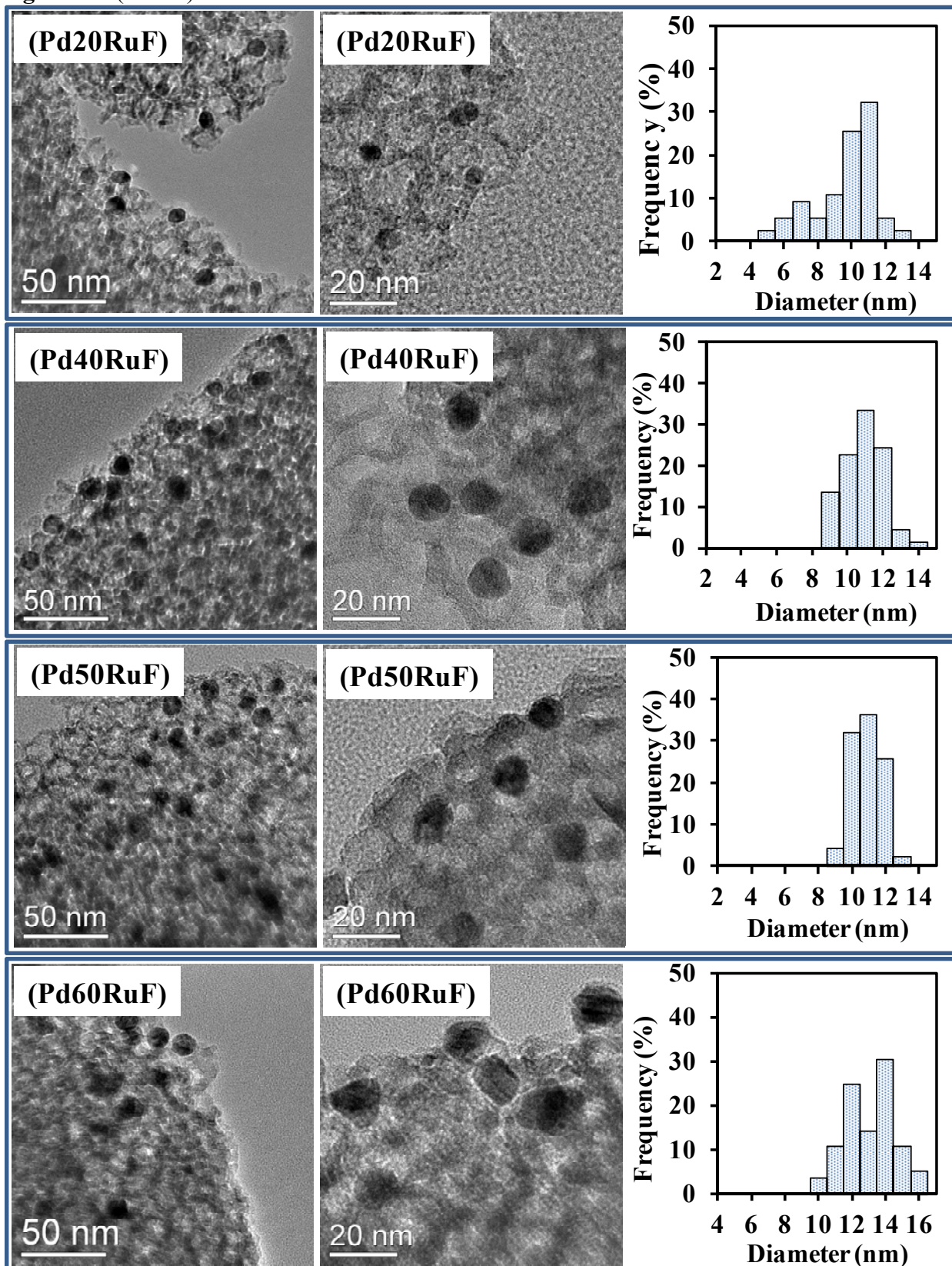
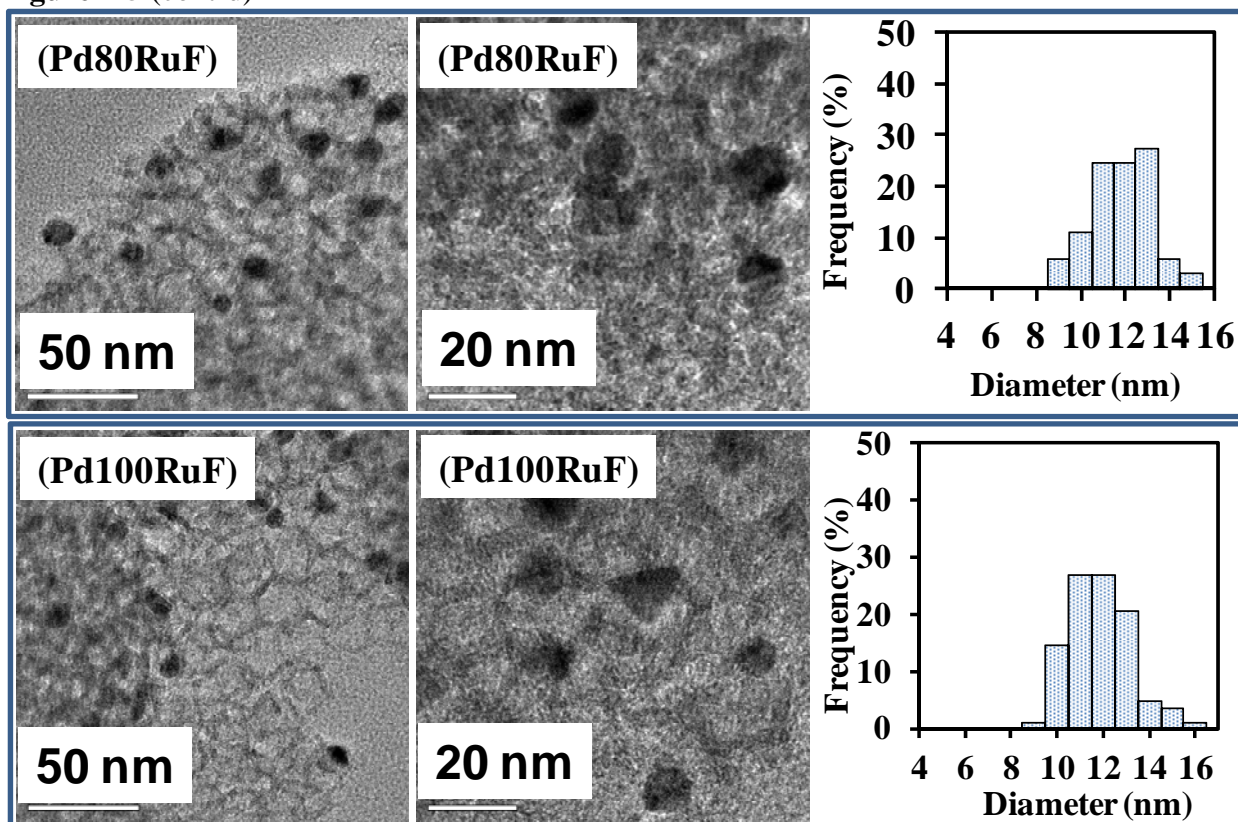


Figure 4-5 (cont'd)



The average diameters of the NPs supported on MSU-F and the metal composition of the bulk catalysts are summarized in Table 4-3. The metal contents obtained from the ICP-AES data show that the mole fraction of Pd in each catalyst is close to that of the Pd compound used in the corresponding metal precursor mixture during the NPs synthesis, demonstrating the high efficiency of polyol co-reduction for producing the Ru-Pd bimetallic NPs. The average diameters of the supported NPs were calculated from the particle size distribution of each catalyst (Figure 4-5). The mean particle size on the MSU-F support increased from 4.7 nm for monometallic Ru NPs (WD170F-5NM) to 10.5 nm for Ru-Pd bimetallic NPs with Pd molar fraction of 44% (Pd40RuF). Further increases in the Pd fraction had no obvious effect on the average size of the

supported NPs. The narrow size distribution, evident from the low standard deviations, is an indication of the uniformity of the NPs.

Table 4-3 Chemical compositions and average size of Ru-Pd NPs supported on MSU-F

Sample ID	Ru content (gRu/gCat.)%	Pd content (gPd/gCat.)%	Molar fraction of Pd in NPs (%)	Average size of NPs (nm)
WD170F-5NM	0.72	0.00	0	4.7±1.3
Pd05RuF	0.76	0.01	2	6.2±0.7
Pd20RuF	0.58	0.07	10	9.2±1.8
Pd40RuF	0.59	0.49	44	10.4±1.0
Pd50RuF	0.62	0.74	53	10.5±1.0
Pd60RuF	0.57	0.97	62	11.6±1.4
Pd80RuF	0.41	1.45	77	11.3±1.4
Pd100F	0.00	1.03	100	11.3±1.3

Chemical compositions in each sample were determined by ICP-AES. Average size (diameter, nm) of the NPs in each sample was determined by counting ~100 NPs in the TEM images.

The metal distribution of the supported Ru-Pd NPs were evaluated by a combination of EDS point analysis, line scan, and elemental mapping. The results summarized in Figure 4-6 show that all the NPs in each sample are composed of both Ru and Pd elements, with no isolated monometallic NPs in any of the samples. This demonstrates that the supported bimetallic NPs have an alloyed structure after thermal activation. The EDS point spectra of each sample acquired from different regions of the NPs show a random arrangement of Pd and Ru atoms in the NPs. The EDS line scan spectra of each sample across the particles shows both Ru and Pd elements, and the elemental mapping of each sample shows a homogeneous distribution of the two elements.

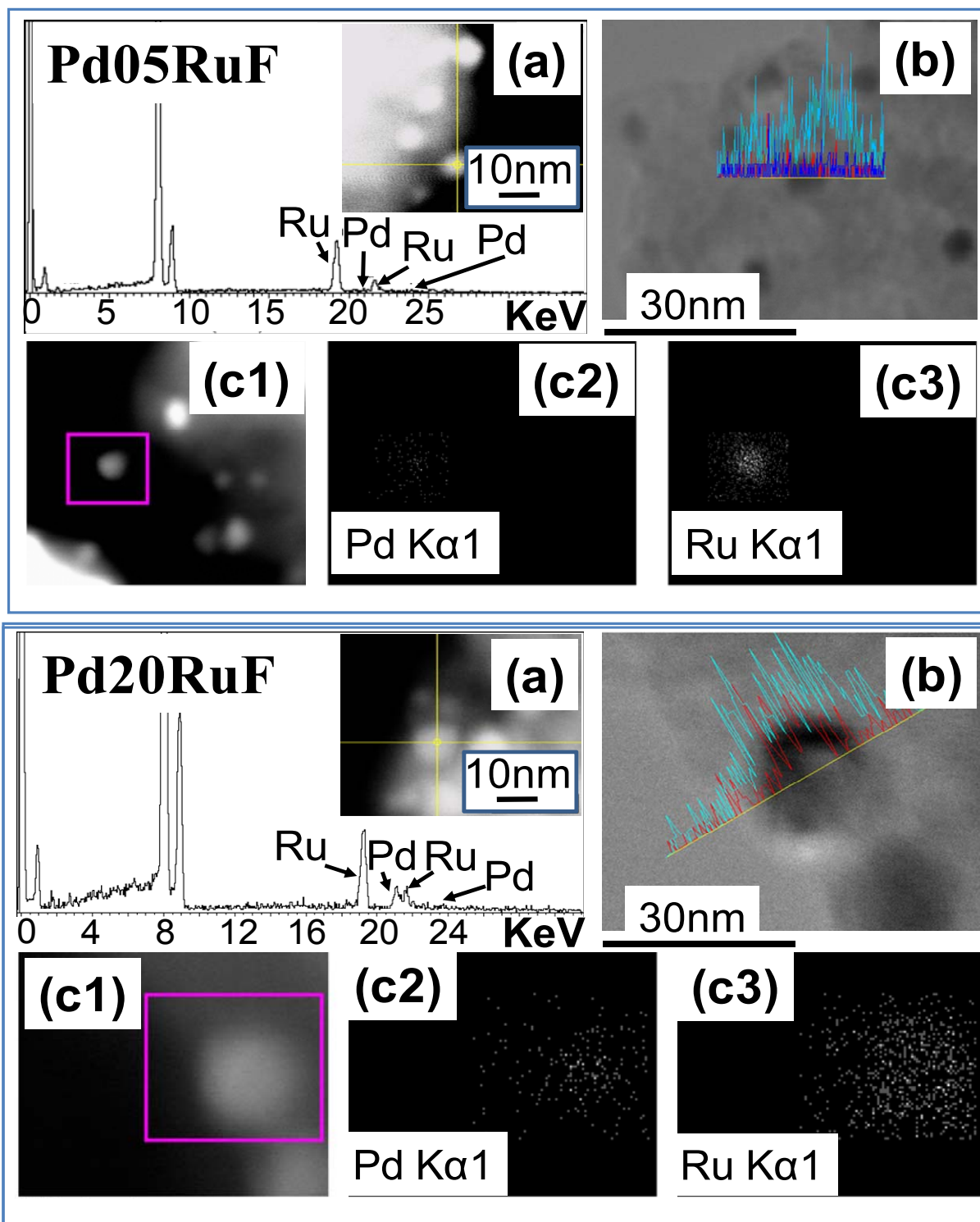


Figure 4-6 EDS analysis of Ru-Pd NPs supported on MSU-F. (a) Randomly selected point on the NPs and the corresponding spectrum of EDS point analysis. (b) EDS line scan profiles of elemental distribution (cyan for Ru and red for Pd) along a line across selected NPs. (c) HRTEM image of a representative NP (c1) and the corresponding elemental mapping images from Pd K α 1 emission (c2) and Ru K α 1 emission (c3). All the analyses were done under STEM conditions with a point resolution of 0.19 nm and a high angle dark field resolution of 0.13 nm.

Figure 4-6 (cont'd)

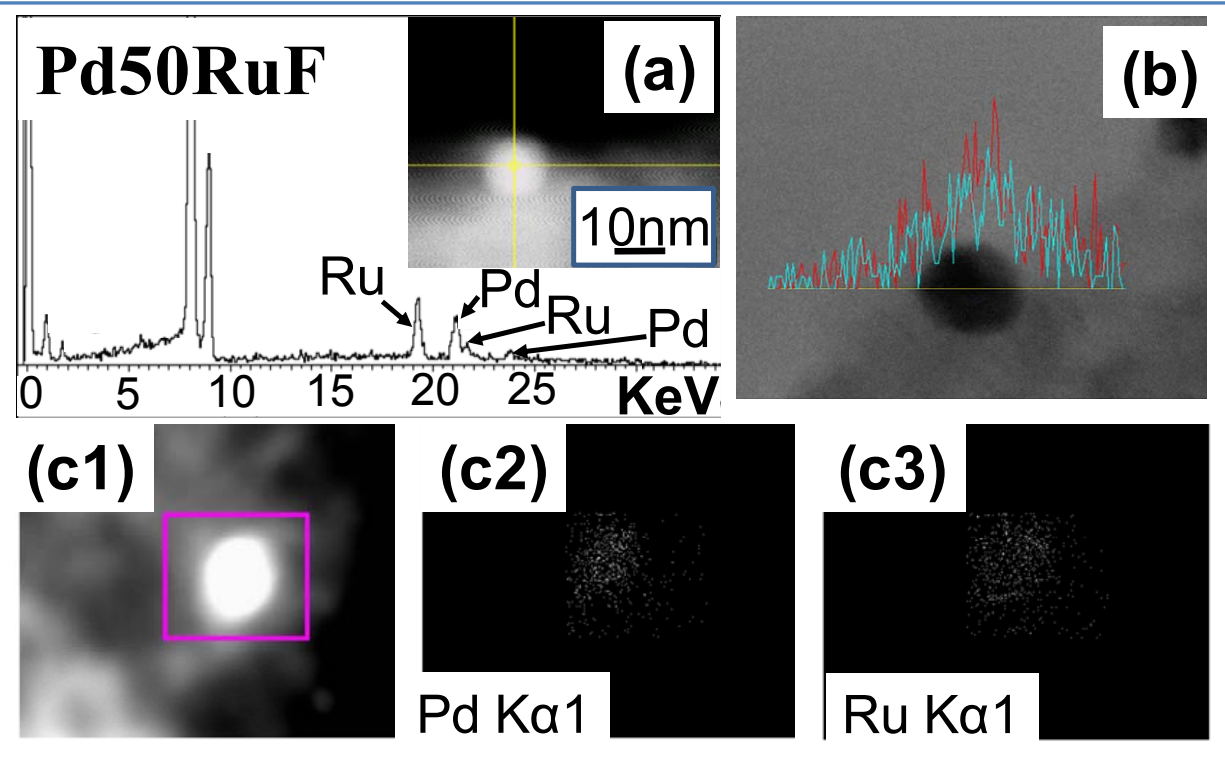
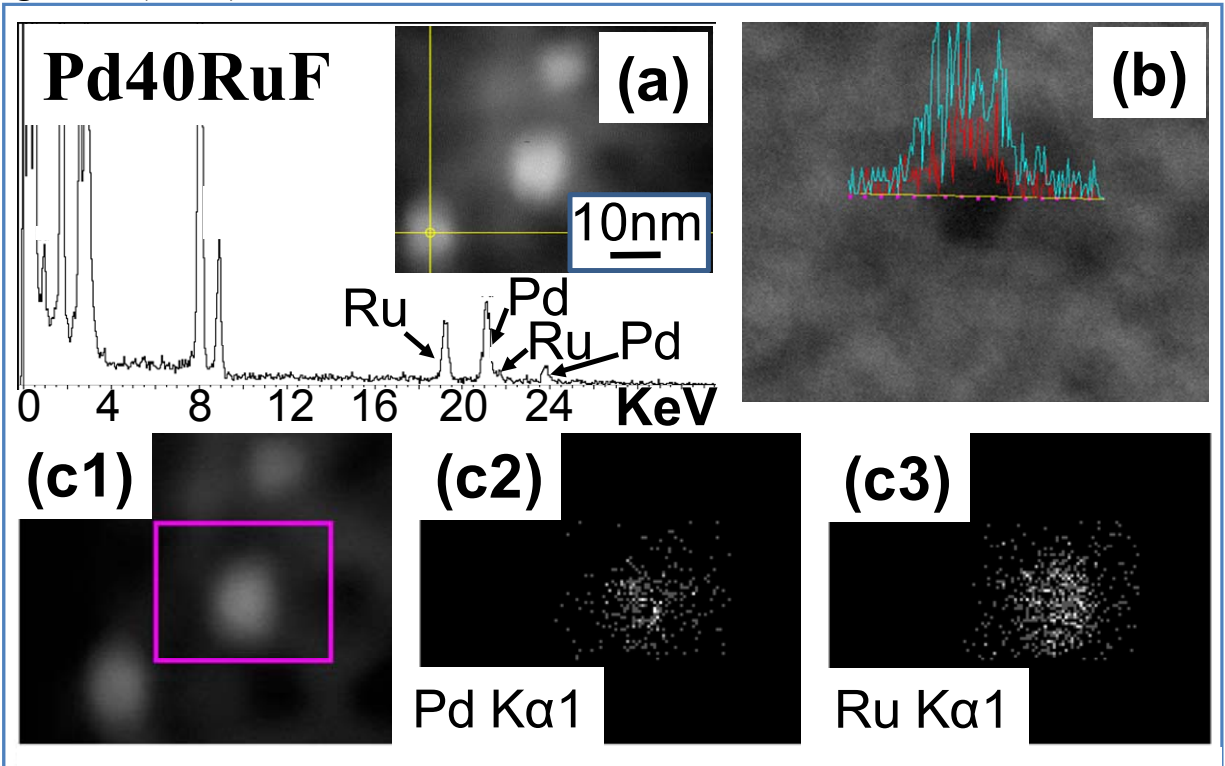
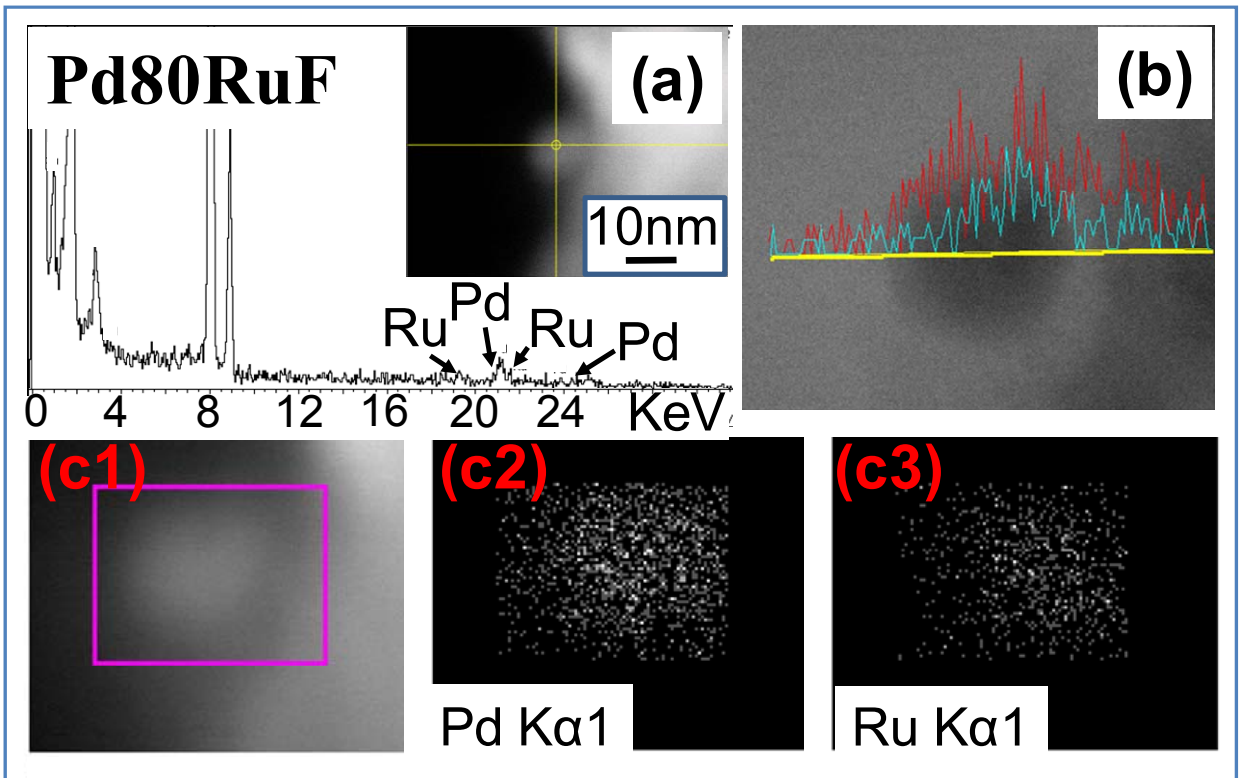
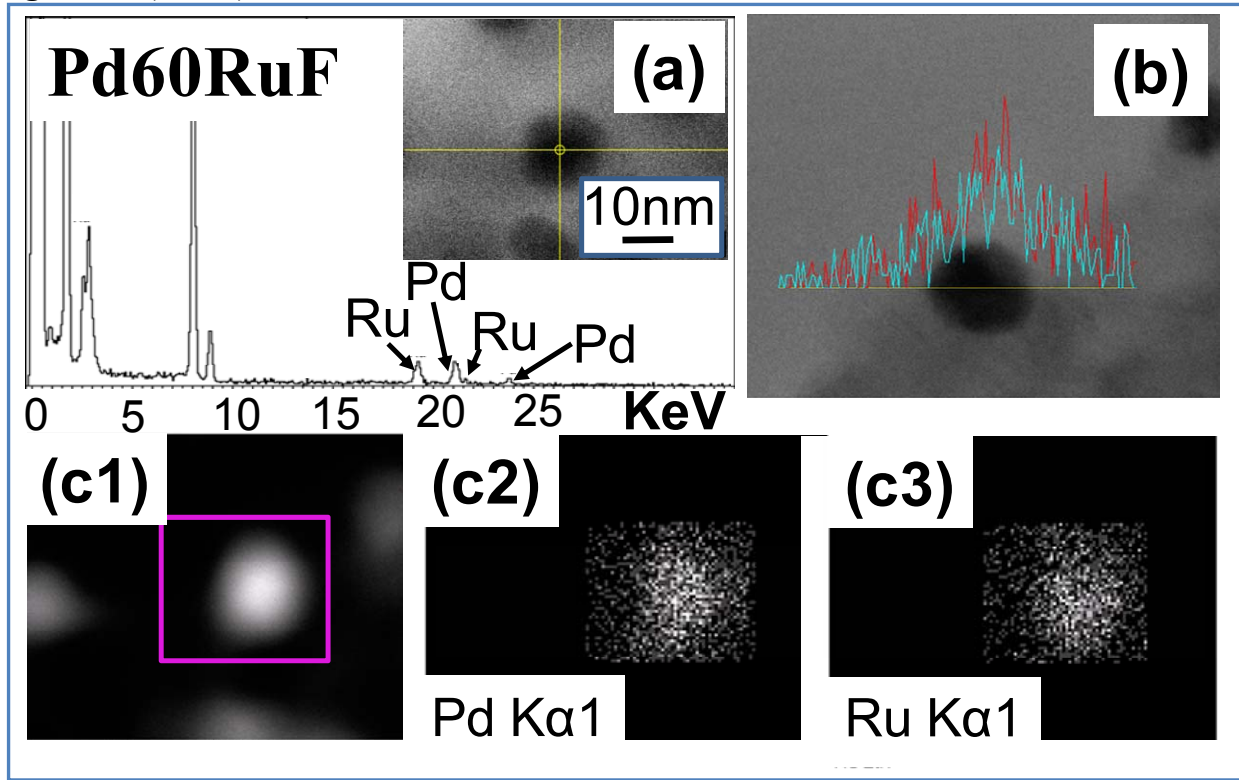


Figure 4-6 (cont'd)



4.3.2.2. Structure of Ru-Pd NPs supported on MSU-F

The crystal structure of the supported Ru-Pd NPs was analyzed by powder XRD diffraction, as shown in Figure 4-7.

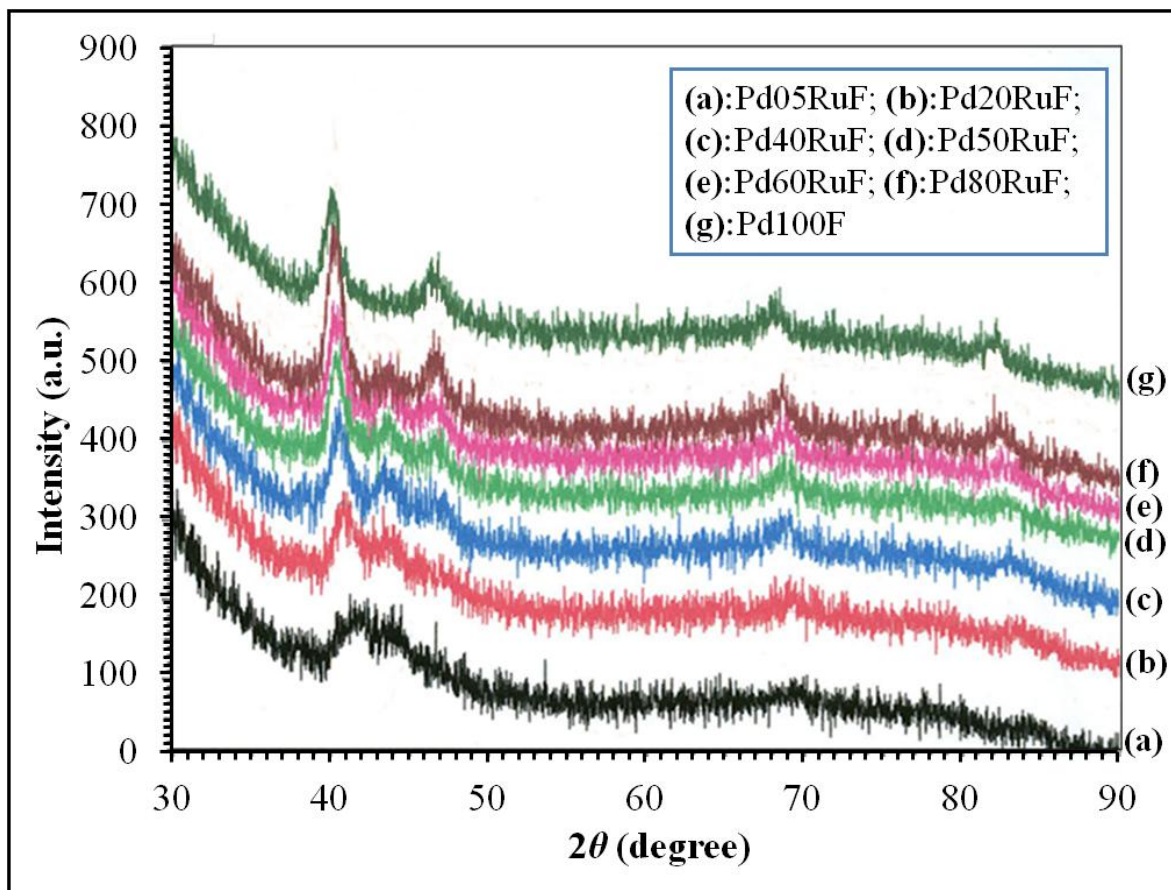


Figure 4-7 XRD patterns of Ru-Pd bimetallic NPs and monometallic Pd NPs supported on MSU-F. The diffraction peaks at $2\theta = 39.1^\circ$, 45.4° , 66.2° , and 79.6° correspond to the (111), (200), (220), (311) facets of Pd with *fcc* crystal structure. Ru with *hcp* crystal structure has a strong diffraction peak at $2\theta = 42.3^\circ$, which corresponds to the (101) facet.

The supported monometallic Pd NPs have diffraction peaks at $2\theta = 39.1^\circ$, 45.4° , 66.2° , and 79.6° , which correspond to the (111), (200), (220), (311) facets of an *fcc* Pd crystal. A new diffraction peak was observed in the XRD patterns of the supported bimetallic NPs, which confirmed the earlier observation that the supported Ru-Pd NPs have an alloyed crystal structure. The peak for Pd05RuF was located at $2\theta = 42^\circ$ which is slightly lower than that of the

monometallic Ru NPs ($2\theta = 42.2^\circ$), suggesting that 2 mol% of Pd in the precursor mixture does not significantly affect the crystal structure of the NPs. It is also evident that increasing the Pd fraction significantly facilitates the transformation of the crystal structure of the bimetallic NPs from the Ru *hcp* structure to the Pd *fcc* structure.

The crystallinity of the supported NPs was also confirmed by the SAED pattern and high resolution TEM (HRTEM) images of each sample (Figure 4-8). Both the array of bright spots in the SAED patterns and the lattice fringes in the HRTEM images correspond to a group of reflection planes within the particles, indicating that the NPs are alloyed crystals.

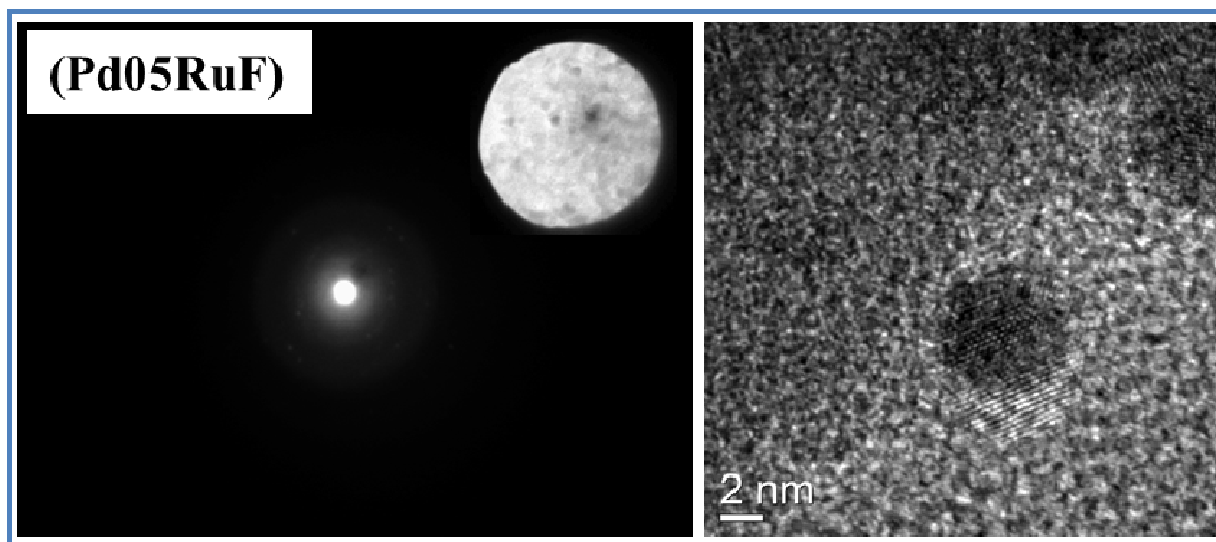


Figure 4-8 SAED patterns and HRTEM images of Ru-Pd NPs supported on MSU-F. The insets represent the area selected for SAED. The HRTEM images of each sample were taken at a magnification of 800 K (scale bar of 2 nm).

Figure 4-8 (cont'd)

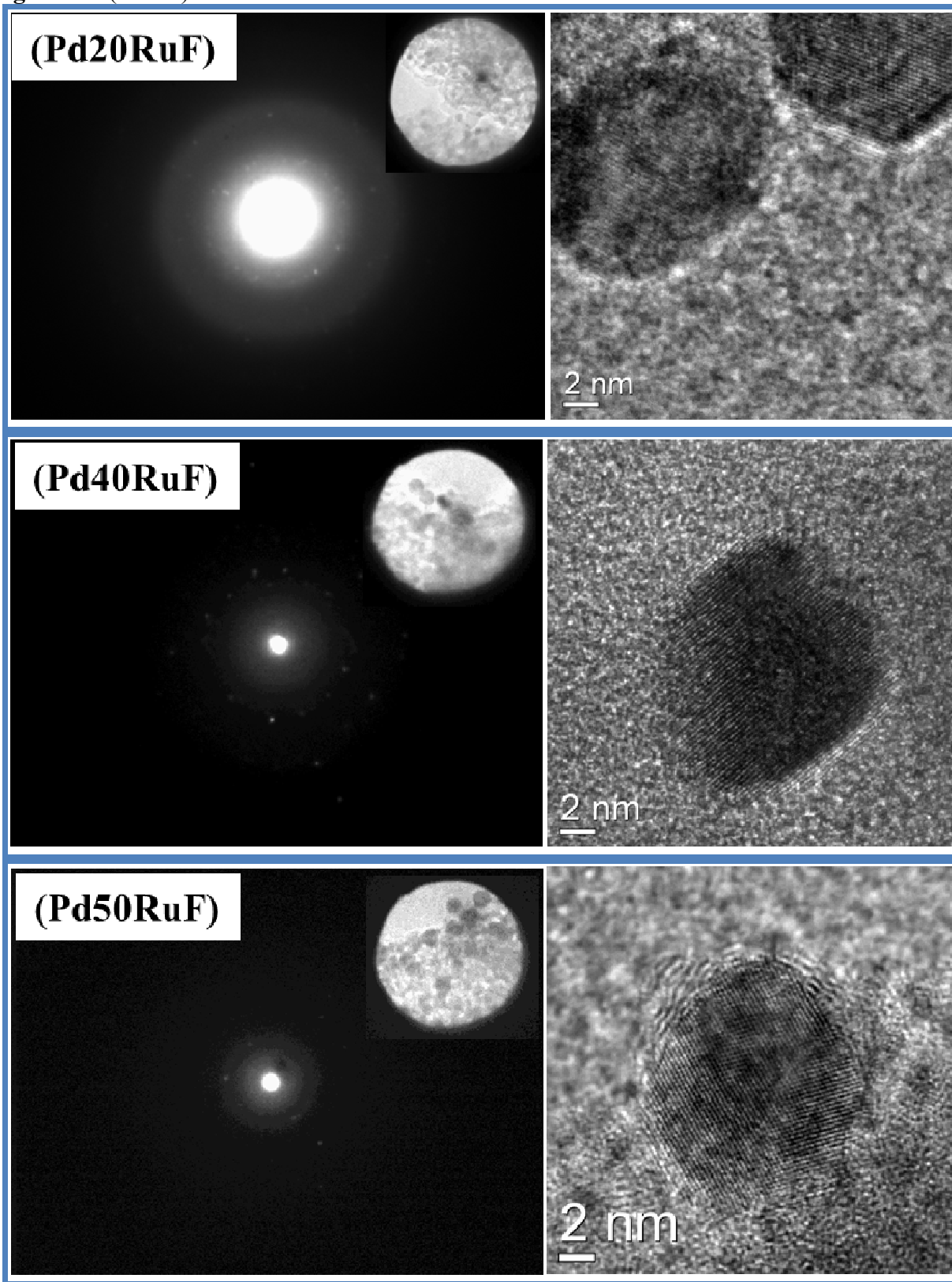
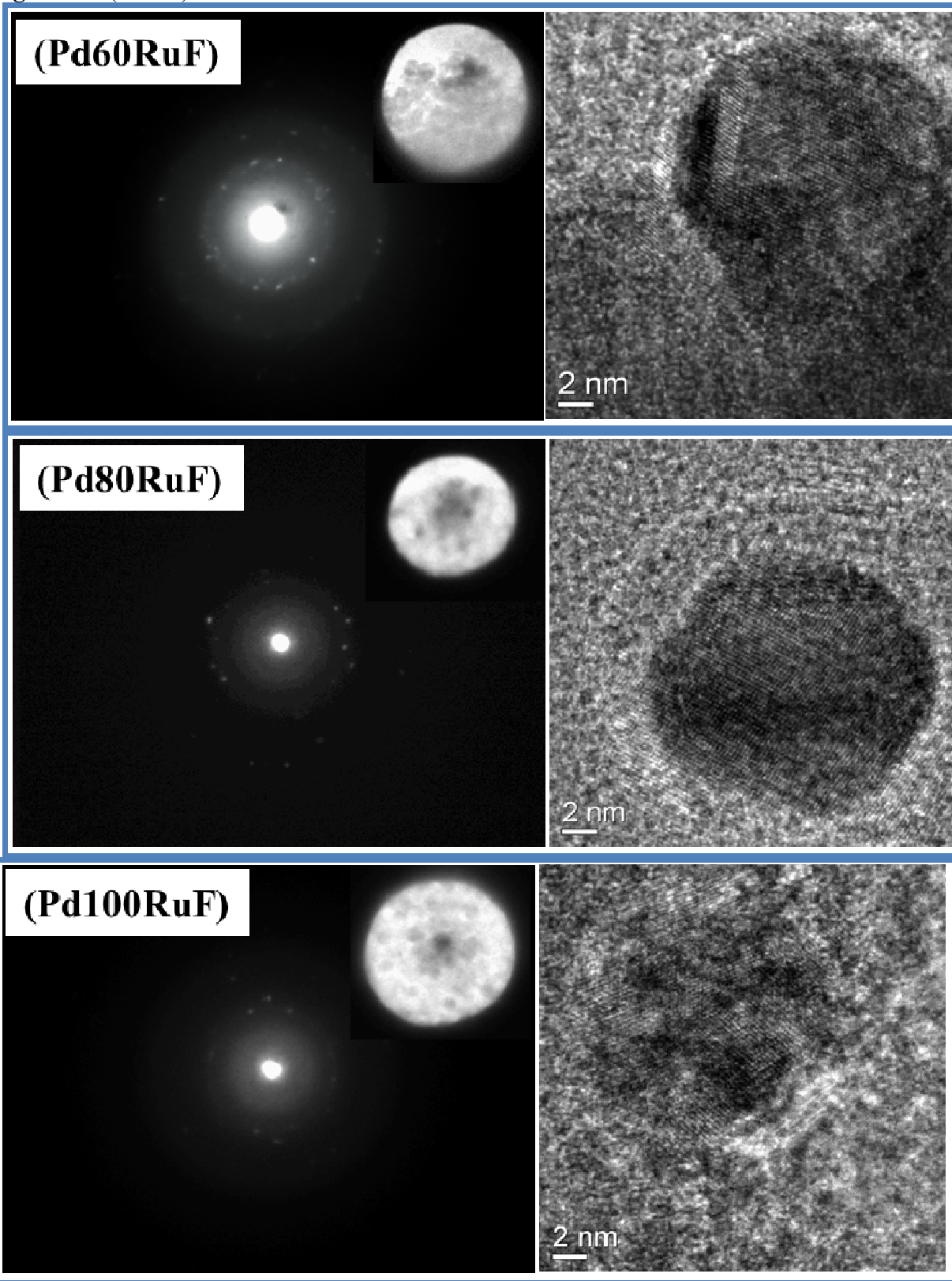


Figure 4-8 (cont'd)



4.3.2.3. Surface properties of Ru-Pd NPs supported on MSU-F

The BET surface area, average pore diameters, and metal dispersion of each catalyst are summarized in Table 4-4. The total surface area of each catalyst after thermal treatment was close to that of the support (MSU-F). The diameter of the pores also remained essentially unchanged. These results suggest that no damage occurred to the structure of the support during the thermal activation of the catalyst. The metal dispersion of each catalyst obtained from H₂ chemisorption is lower than the value from CO chemisorption, except for the supported monometallic Ru NPs (WD170-5NM). This is possibly due to the difference in the adsorption stoichiometry of H₂ and CO. The metal dispersions obtained from CO chemisorption decreased continuously with increases in the Pd fraction of the NPs, and reached a minimum at a Pd fraction of 60 mol%. Increasing the Pd fraction further does not have a significant effect on metal dispersion. The metal dispersions obtained by H₂ chemisorption have a similar trend.

Table 4-4 Chemisorption and physisorption results of MSU-F supported Ru-Pd NPs

Sample ID	BET Surface area (m ² g ⁻¹)	Average pore diameter (nm)	Metal dispersion by chemisorption	
			H ₂	CO
MSU-F	503.33 ± 1.20	---	---	---
WD170F-5NM	479.12 ± 1.14	15.31	15.2%	14.7%
Pd05RuF	506.23 ± 1.16	15.37	6.6%	7.5%
Pd20RuF	498.34 ± 1.26	15.36	7.3%	8.8%
Pd40RuF	504.78 ± 1.27	15.39	2.0%	2.9%
Pd50RuF	462.00 ± 1.14	15.4	0.5%	2.4%
Pd60RuF	525.47 ± 1.40	15.27	0.3%	1.2%
Pd80RuF	477.73 ± 1.23	15.29	0.5%	1.1%
Pd100F	511.92 ± 1.27	15.44	0.4%	1.7%

The BET surface area of each sample was determined from N₂ adsorption. Average size (diameter, nm) of the NPs in each sample was determined by counting ~100 NPs in the TEM images. The metal dispersion of each sample was determined from H₂ and CO adsorption results, respectively.

The CO-TPD spectra of the supported Ru-Pd NPs are shown in Figure 4-9. All CO desorption peaks are within the temperature range of 40°C to 150°C. The CO-TPD profile of the monometallic Ru NPs has a broad CO desorption signal with a maximum at about 80°C, possibly due to CO adsorption on under-coordinated Ru sites. A shoulder at about 60°C was also observed, which originated from CO adsorption on terrace sites. Addition of a little amount of Pd in the NPs (Pd05RuF, 2 mole % of Pd in the NPs) did not completely change the CO desorption pattern, but the maximum desorption peak shifted to a lower temperature (60°C) and a shoulder remained at a higher temperature (80°C). Increasing the Pd fraction to 10 mol% in the bimetallic NPs (Pd20RuF) resulted in a single CO desorption peak with a maximum at 60°C, with no shoulder peaks. The CO desorption pattern was similar for NPs with Pd fractions between 10 mol% (Pd20RuF) and 77 mol% (Pd80RuF). Monometallic Pd NPs also displayed a single CO desorption peak and the temperature for peak maximum is a little lower than that of Pd80RuF.

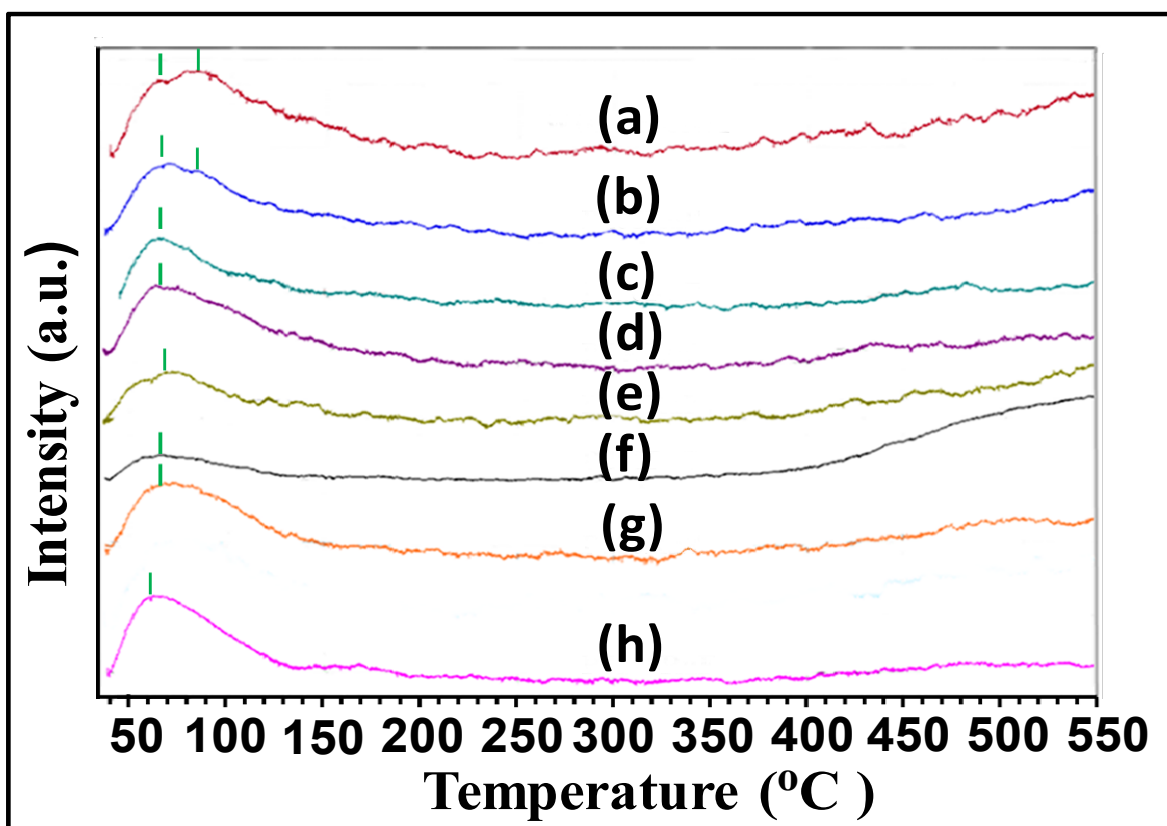


Figure 4-9 CO-TPD spectra of Ru-Pd NPs supported on MSU-F. All CO desorption peaks are within the temperature range of 40°C to 150°C. (a) WD170-5NM; (b) Pd05RuF; (c) Pd20RuF; (d) Pd40RuF; (e) Pd50RuF; (f) Pd60RuF; (g) Pd80RuF; (h) Pd 100F. Monometallic Ru NPs has a broad CO desorption signal with a maximum at about 80°C and a shoulder at about 60°C. Addition of a little amount of Pd in the NPs (Pd05RuF, 2 mole % of Pd in the NPs) did not change the CO desorption pattern. Increasing the Pd fraction to 10 mol% in the bimetallic NPs (Pd20RuF) resulted in a single CO desorption peak with maximum at 60°C, with no shoulder peaks. The CO desorption pattern remained similar for NPs with Pd fractions between 10 mol% (Pd20RuF) and 77 mol% (Pd80RuF). Monometallic Pd NPs has a single CO desorption peak.

4.3.3. Catalytic assessment of CAL hydrogenation with Ru-Pd NPs supported on MSU-F

A list of the reaction conditions investigated for CAL hydrogenation over supported Ru-Pd NPs was given in Table 4-5. The products observed within the reaction time under the described reaction conditions are COL, HCOL, and HCOL (see the plots of substrate and products concentration against reaction time in Appendix B-1 to B-8).

Table 4-5 Summary of reaction conditions for CAL hydrogenation over Ru-Pd NPs supported on MSU-F

Catalyst	Metal loading ($\times 10^{-6}$ mole)	Initial concentration of CAL (mM)	T ($^{\circ}\text{C}$)	$P(\text{H}_2)$ (bar)	time (hour)
Pd05RuF	1.9	40	65	20	7
Pd20RuF	2.0	40	45	20	7
	1.8	40	65	20	7
	2.0	40	85	20	7
	2.0	40	105	20	7
Pd40RuF	2.0	40	65	20	7
Pd50RuF	2.0	40	45	20	7
	1.8	40	65	20	7
	2.0	40	85	20	7
	2.0	40	105	20	7
Pd60RuF	2.0	40	65	20	7
Pd80RuF	1.6	40	45	20	7
	1.6	40	65	20	7
	1.6	40	85	20	7
	1.6	40	105	20	7
Pd100RuF	1.6	40	45	20	7
	1.6	40	65	20	7
	1.6	40	85	20	7
	1.6	40	105	20	7

The initial reaction rates were determined by the differential analysis procedure described in Chapter 3. One example of the analysis is illustrated by the reaction over the catalyst Pd50RuF (Figure 4-10 and Table 4-6).

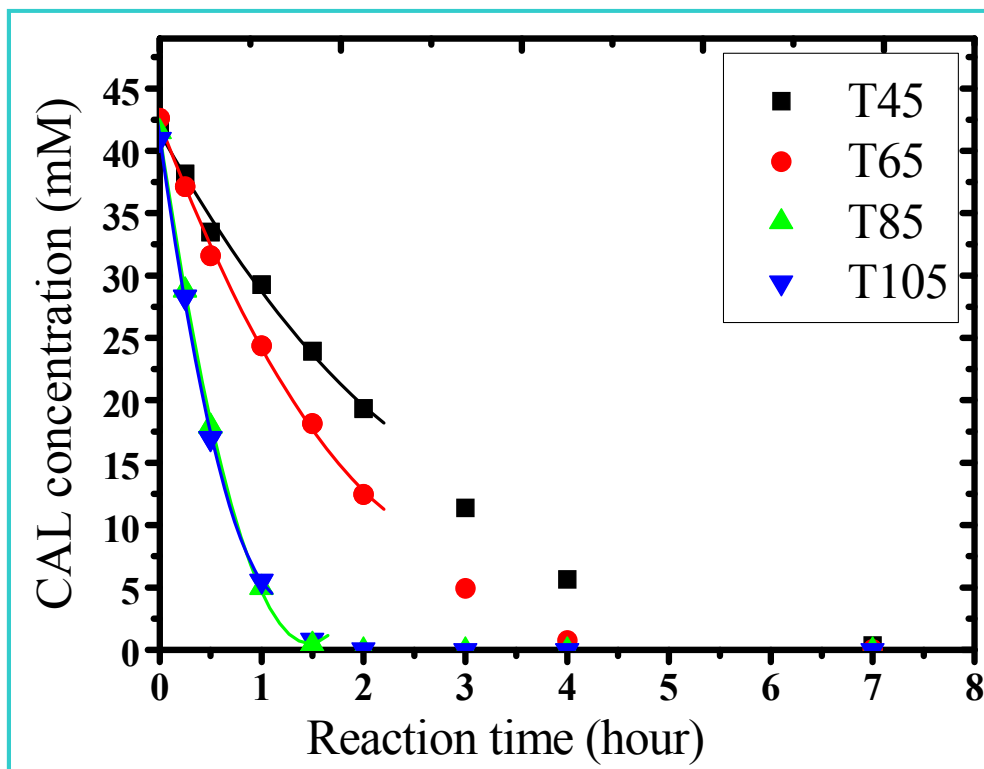


Figure 4-10 Reaction profile for CAL hydrogenation over Pd50RuF and the corresponding regression curves. Reaction conditions: 35 ml CAL solution in IPA (40mM); $T = 45^{\circ}\text{C} - 105^{\circ}\text{C}$; $P(\text{H}_2) = 20$ bar; Stirring speed = 800 RPM. The numbers in T## means the reaction temperature.

Table 4-6 Regression coefficients of substrate concentration versus reaction time for CAL hydrogenation over the catalyst Pd50RuF. Reaction conditions: 35 ml CAL solution in IPA (40mM); $T = 45^{\circ}\text{C} - 105^{\circ}\text{C}$; $P(\text{H}_2) = 20$ bar; Stirring speed = 800 RPM. The numbers in T## are the values of the reaction temperatures.

Reaction ID	Regression function $Y = A + B1*X + B2*X^2$					
	A		B1		B2	
	value	error	value	error	value	error
T45	41.55	0.34	-11.85	0.59	0.66	0.19
T65	42.66	0.21	-22.26	0.37	2.83	0.12
T85	41.42	0.34	-53.78	1.72	14.31	1.59
T105	41.42	1.62	-87.93	8.24	46.79	7.65

4.3.3.1. Effect of metal composition on the activity of Ru-Pd NPs supported on MSU-F

The effect of the metal composition of bimetallic NPs on their activity for CAL hydrogenation is shown in Figure 4-11, with the activity of each catalyst defined as the conversion of CAL per mole of metal per hour. Under the same substrate concentration, the initial activity increased with increasing Pd fraction in the bimetallic NPs, reaching a maximum at 44 mol% Pd in the NPs (Pd40RuF). Further increases in the Pd fraction to 53 mol% (Pd50RuF) resulted in a significant decrease of the initial activity, with this value remaining relatively constant over Pd fractions ranging from 53 mol% to monometallic Pd NPs.

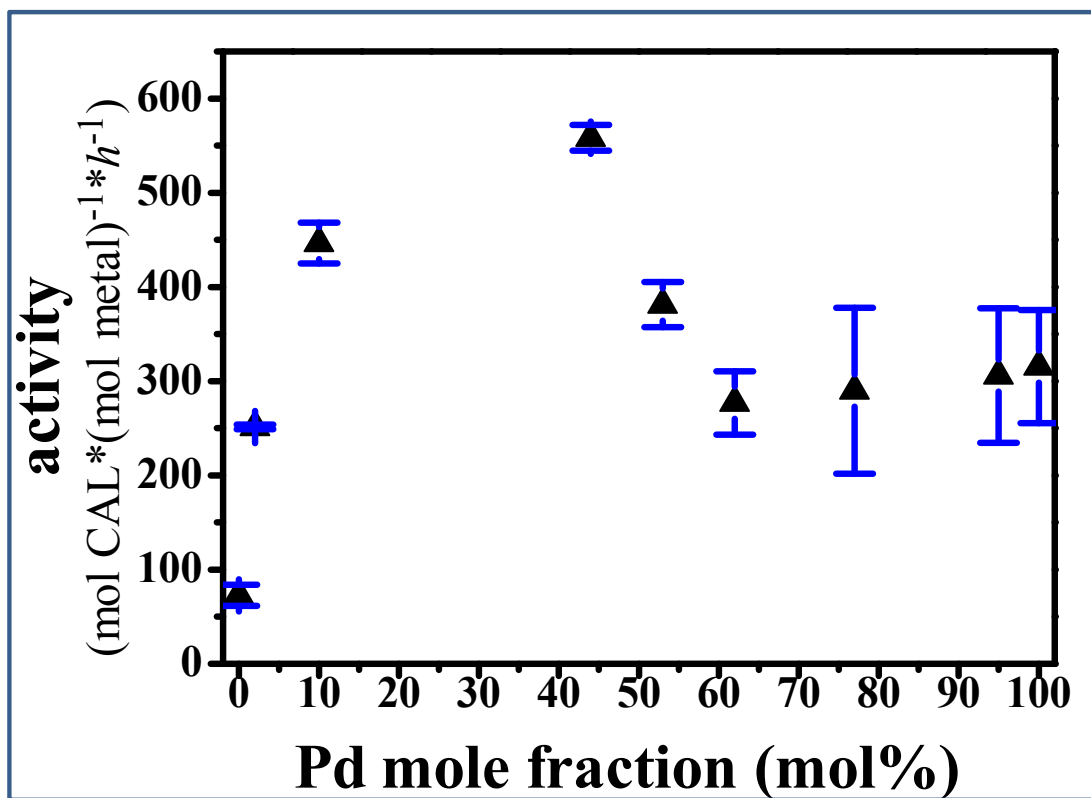


Figure 4-11 Catalytic activity as a function of Pd fraction for CAL hydrogenation over Ru-Pd NPs supported on MSU-F. Reaction conditions: 35 ml CAL solution in IPA (40 mM); $T = 65^{\circ}\text{C}$; $P(\text{H}_2) = 20$ bar; Stirring speed = 800 RPM. The activity of each catalyst is expressed as the initial rate of CAL consumption per mole metal per hour ($\text{mol CAL} \times (\text{mol metal})^{-1} \times \text{h}^{-1}$).

The turnover frequencies (TOF) of CAL hydrogenation over Ru-Pd bimetallic NPs and the monometallic NPs were estimated by normalizing the initial reaction rates to the total amount of exposed metal atoms on the supported NPs, which could be obtained from the metal dispersion determined by CO chemisorption (Table 4-4), without discriminating between Ru and Pd atoms. The TOF values for the reaction over the bimetallic NPs with Pd fraction of 10 mol% (Pd20RuF), 53 mol% (Pd50RuF), and 77 mol% (Pd80RuF), along with the monometallic Ru (WD170F-5NM) and Pd (Pd100F) NPs were calculated. The plot of the TOF values as a function of the metal composition is presented in Figure 4-12.

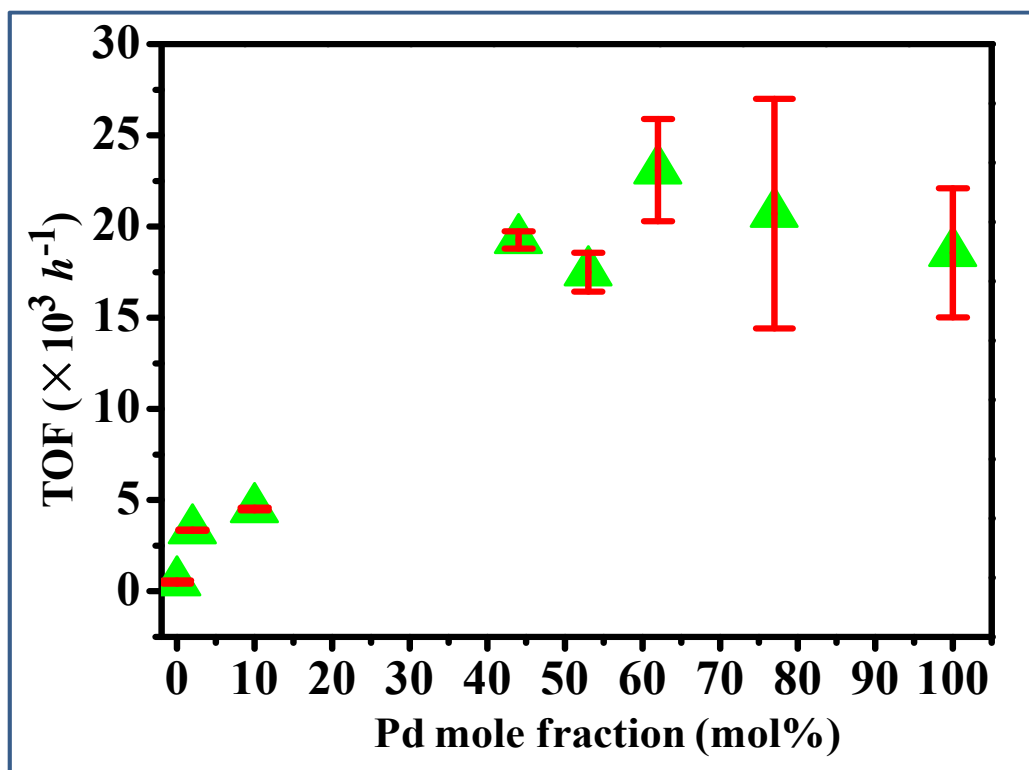


Figure 4-12 TOF as a function of Pd fraction for CAL hydrogenation over Ru-Pd NPs supported on MSU-F. Reaction conditions: 35 ml CAL solution in IPA (40mM); $T = 65^{\circ}\text{C}$; $P(\text{H}_2) = 20$ bar; Stirring speed = 800 RPM.

It can be seen from Figure 4-12 that the TOF for bimetallic NPs with Pd fractions of 10 mol% was higher than the monometallic Ru NPs at all reaction temperatures. The TOF increased with

increasing Pd fraction up to 53 mol% in the NPs. These results demonstrate the synergetic effect between Ru and Pd metals in the bimetallic NPs. This synergetic behavior has also been observed for CAL hydrogenation over Pt-Au bimetallic catalysts.^{25,26} Further increases in the Pd fraction up to monometallic Pd in the NPs did not significantly affect the TOF.

The effect of reaction temperature on TOF for CAL hydrogenation over Ru-Pd NPs is shown by the Arrhenius plots in Figure 4-13. The Arrhenius plots for all the reactions over each catalyst are linear with respect to the inverse reaction temperature. Thus, the apparent activation energy (E_A) and $\ln(r_0)$ values of each catalyst could be determined by linear regression within the selected reaction temperature range.

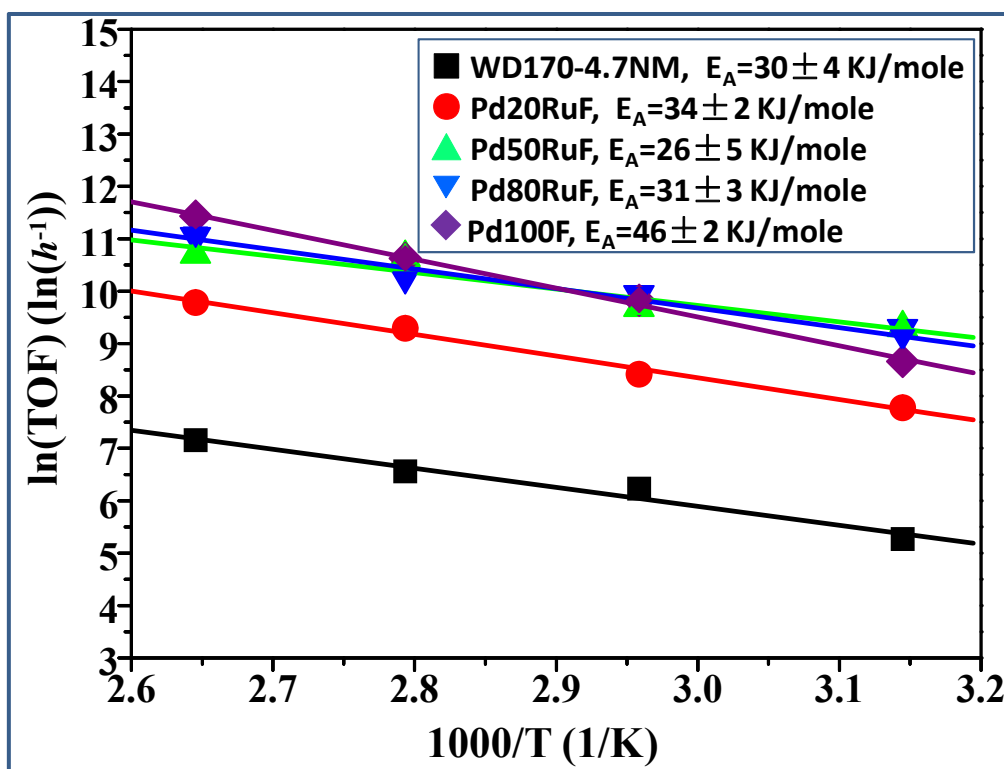


Figure 4-13 Arrhenius plots for CAL hydrogenation over bimetallic and monometallic NPs supported on MSU-F. Reaction conditions: 35 ml CAL solution in IPA (40mM); $T = 45-105^{\circ}\text{C}$; $P(\text{H}_2) = 20$ bar; Stirring speed = 800 RPM. Linear regression of the data for each catalyst gives the Arrhenius intercept $\ln(r_0)$ in the equation: $\ln(r) = \ln(r_0) - E_A/RT$.

The activation energy from the Arrhenius plots for CAL hydrogenation on monometallic Pd NPs (46 ± 2 kJ/mol) was higher than the value reported in the literature for traditional Pd/C catalyst (46 ± 2 kJ/mol).²⁷ This difference can be attributed to the influence of the support on catalytic activity. For example, it has been reported that a carbon support is beneficial for creation of additional adsorption sites and formation of spill-over hydrogen compared to an inert silica support.²⁸⁻³⁴ The activation energy for CAL hydrogenation over the supported Ru-Pd alloyed NPs decreased by about 15 kJ/mol compared to that for the reaction over monometallic Pd NPs. Thus, the synergy between Pd and Ru atoms has significantly decreased the activation barriers for the reaction. It is also observed that the activation energy is independent of the Pd fraction, given that the values are close to those for monometallic Ru NPs.

4.3.3.2. Effect of composition on the selectivity of Ru-Pd NPs supported on MSU-F

The profiles of product selectivity as a function of time for the reaction over Ru-Pd bimetallic NPs with different Pd fractions are shown in Figure 4-14, with selectivity defined as the ratio of the moles of the target product to the moles of total products formed. Unlike the case of CAL hydrogenation over monometallic Ru NPs where COL was the primary product (Figure 4-14a; details also in Figure 3-9), H₂CAL and H₂COL were the major products for CAL hydrogenation over monometallic Pd NPs. The product selectivity remained constant for substrate conversions ranging from 10% to 90% (Figure 4-14). Only a small amount of COL was produced at the beginning of the reaction, while the selectivity to COL decreased drastically with increased substrate conversion, and then remained at a low level (less than 10%) with the increase of substrate conversion to 100%. A significant difference in product selectivity was also observed for CAL hydrogenation over the traditional Ru and Pd catalysts supported on both carbon and

silica.³⁵ The higher selectivity for HCAL for the reactions over Pd catalysts can be explained by

a more favorable bonding between Pd and C-C than between Pd and C-O compared to Ru.³⁵⁻³⁹

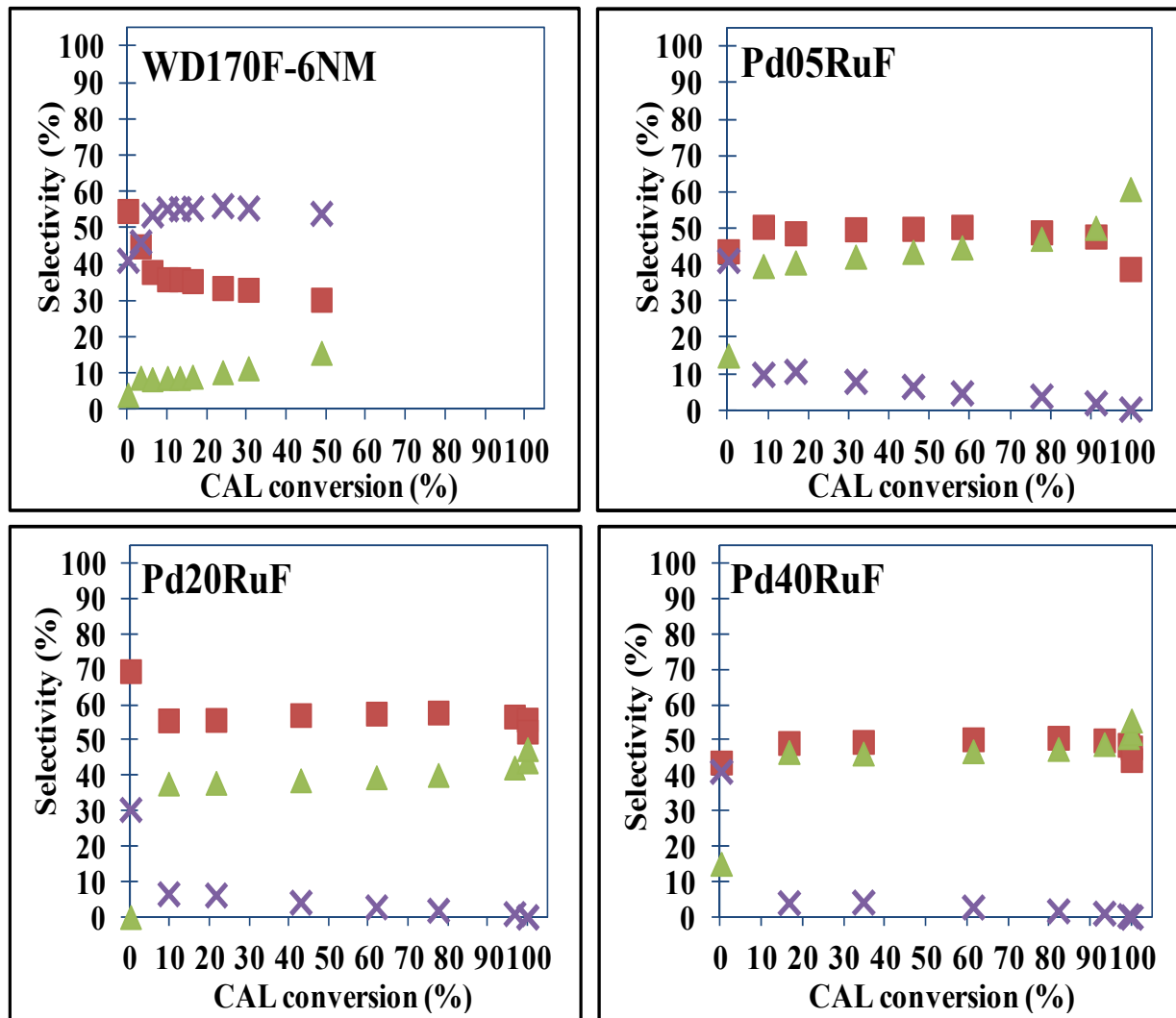
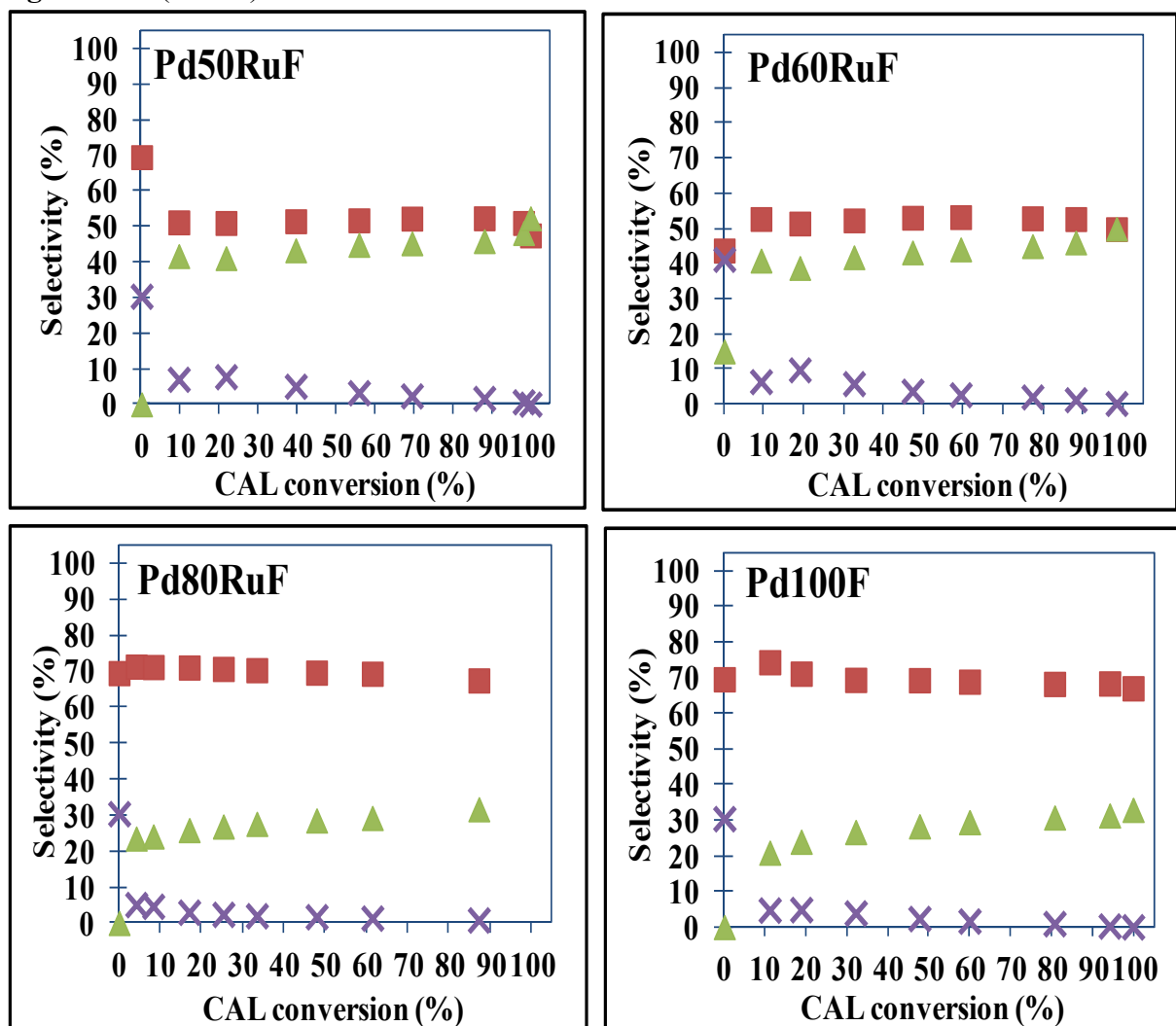


Figure 4-14 Product selectivity as a function of substrate conversion for CAL hydrogenation over Ru-Pd NPs supported on MSU-F. ■ HCAL; × COL; ▲ HCOL. Reactions conditions: 35 ml CAL solution in IPA (40mM); $T = 65^{\circ}\text{C}$; Stirring speed = 800 RPM.

Figure 4-14 (cont'd)



The effect of the Pd fraction of the bimetallic NPs on product selectivity was investigated at a substrate conversion of 50% (Figure 4-15). The selection of 50% percent substrate conversion as the analysis point is reasonable within our experimental data, since the selectivity-conversion profiles in Figure 4-10 show that the product selectivity of is fairly constant over CAL conversions of 35% to 90%. The monometallic Ru NPs have the highest selectivity to COL, but the addition of Pd to form the bimetallic NPs drastically decreased the selectivity of COL to less than 10%. The selectivity of HCOL first increased with increased Pd fraction in the bimetallic

NPs, then remained constant over Pd fractions between 10 mol% and 62 mol%. The selectivity begins to increase again with further increases in Pd fraction up to 77 mol % (Pd80RuF). There were no significant changes in the selectivity of HCOL for the reaction over monometallic Pd NPs and Ru-Pd bimetallic NPs when the Pd fraction is above 77 mol % (Pd80RuF). By contrast, the selectivity of HCOL has the opposite trend with increased Pd fraction in the bimetallic NPs. It can also be observed in Figure 4-12 that the product selectivity is insensitive to the initial substrate concentration under identical compositions of supported NPs. More detailed theoretical calculations would be needed to further understand the effect of the Pd fraction in Ru-Pd bimetallic NPs on the product selectivity of CAL hydrogenation.

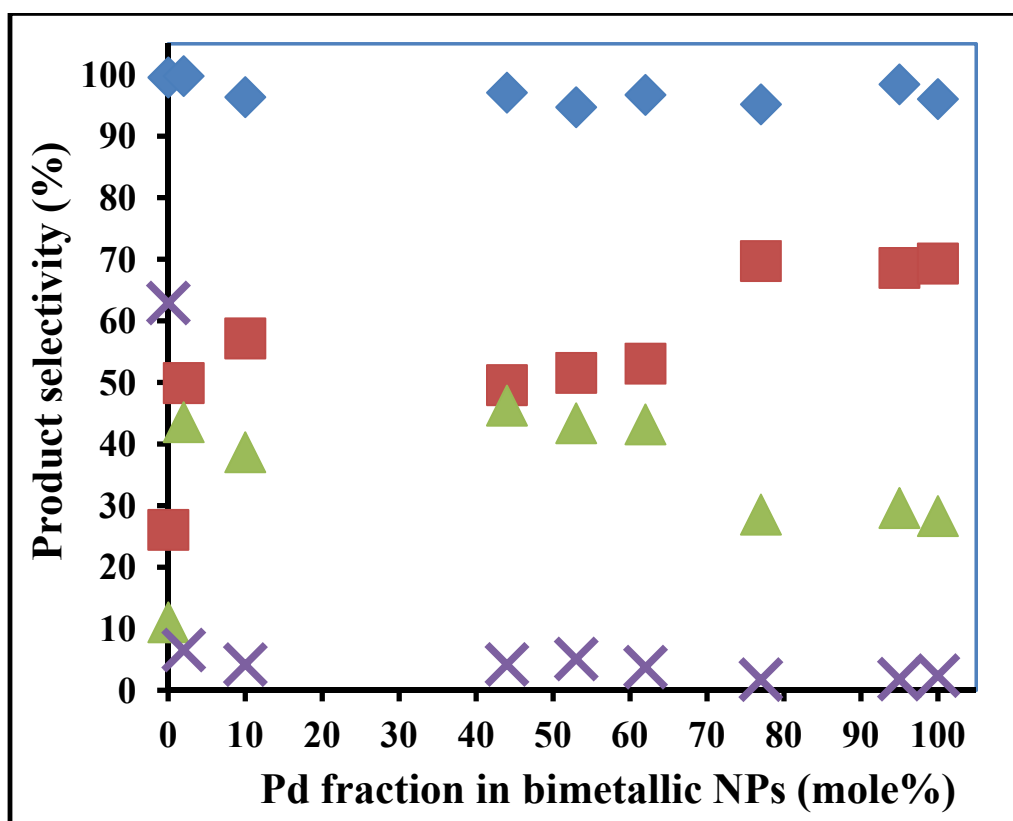


Figure 4-15 Product selectivity as a function of Pd fraction in the bimetallic NPs for CAL hydrogenation. Meaning of symbols: \blacklozenge material balance; \blacksquare HCOL; \times COL; \blacktriangle HCOL. Reaction conditions: 35 ml CAL solution in IPA (40mM); $T = 65^{\circ}\text{C}$; $P(\text{H}_2) = 20$ bar; stirring speed = 800 RPM. The product selectivity was investigated at the substrate conversion of 50% percent.

4.4. Summary

Ru-Pd bimetallic NPs with different metal compositions as well as monometallic Pd NPs were synthesized by polyol reduction of Ru and Pd metal precursors with PVP as the stabilizer. TEM data show that the predominant shape of the NPs synthesized using Ru(acac)₃ and Pd(acac)₂ as metal precursors are truncated spheres. A combination EDS line scan and elemental mapping analysis showed that the NPs are bimetallic in nature, and that the two metals (Ru and Pd) are homogeneously distributed in the NPs.

The NPs were well dispersed on the MSU-F support after deposition and thermal activation. Both the supported bimetallic and monometallic Pd NPs are spherical in shape with narrow size distributions. The supported bimetallic NPs retained an alloyed structure with a homogeneous distribution of the two metals (Ru and Pd) following thermal activation. The thermal treatment also improved the crystallinity of the supported NPs, as confirmed by powder XRD patterns, SAED, and HRTEM.

The supported bimetallic NPs gave higher TOF values than monometallic Ru NPs, with the enhancement proportional to the Pd fraction up to 53 mol% (Pd₅₀RuF) in the NPs. Further increases in the Pd fraction up to the monometallic Pd did not significantly affect the TOF values. The synergy between Pd and Ru atoms significantly decreased the activation barriers for the reaction, as indicated by about 15 kJ/mol decrease of the activation energy for CAL hydrogenation over supported Ru-Pd alloyed NPs than over the monometallic Pd NPs. CAL hydrogenation over the Ru-Pd bimetallic NPs as well as the monometallic Pd NPs produced either HCAL or HCOL as the major product within a broad substrate conversion range.

REFERENCES

REFERENCES

- (1) Jacobs, G.; Ghadiali, F.; Pisanu, A.; Borgna, A.; Alvarez, W. E.; Resasco, D. E. Characterization of the morphology of Pt clusters incorporated in a KL zeolite by vapor phase and incipient wetness impregnation. Influence of Pt particle morphology on aromatization activity and deactivation. *Applied Catalysis a-General*, 1999, *188*, 79-98.
- (2) Sikhwivhilu, L. M.; Coville, N. J.; Naresh, D.; Chary, K. V. R.; Vishwanathan, V. Nanotubular titanate supported palladium catalysts: The influence of structure and morphology on phenol hydrogenation activity. *Applied Catalysis a-General*, 2007, *324*, 52-61.
- (3) Piccolo, L.; Henry, C. R. NO-CO reaction kinetics on Pd/MgO model catalysts: morphology and support effects. *Journal of Molecular Catalysis a-Chemical*, 2001, *167*, 181-190.
- (4) Yanzhe Yua, B. F., Andreas Jentysa, Gary L. Hallera, J.A. Rob van Veenb, Oliver Y. Gutiérreza, Johannes A. Lercher Bimetallic Pt–Pd/silica–alumina hydrotreating catalysts Part I: Physicochemical characterization. *Journal of Catalysis*, 2012, *292*, 1-12.
- (5) Campbell, C. T. Bimetallic surface chemistry. *Annu. Rev. Phys. Chem.*, 1990, *41*, 775-837.
- (6) Fuggle, J. C.; Madey, T. E.; Steinkilberg, M.; Menzel, D. Photoelectron spectroscopic studies of adsorption of CO and oxygen on Ru(001). *Surface Science*, 1975, *52*, 521-541.
- (7) Rodriguez, J. A.; Goodman, D. W. The nature of the metal-metal bond in bimetallic surfaces. *Science (Washington, D. C., 1883-)*, 1992, *257*, 897-903.
- (8) Tao, F.; Grass, M. E.; Zhang, Y. W.; Butcher, D. R.; Aksoy, F.; Aloni, S.; Altoe, V.; Alayoglu, S.; Renzas, J. R.; Tsung, C. K.; Zhu, Z. W.; Liu, Z.; Salmeron, M.; Somorjai, G. A. Evolution of Structure and Chemistry of Bimetallic Nanoparticle Catalysts under Reaction Conditions. *Journal of the American Chemical Society*, 2010, *132*, 8697-8703.
- (9) Kleis, J.; Greeley, J.; Romero, N. A.; Morozov, V. A.; Falsig, H.; Larsen, A. H.; Lu, J.; Mortensen, J. J.; Dulak, M.; Thygesen, K. S.; Norskov, J. K.; Jacobsen, K. W. Finite Size Effects in Chemical Bonding: From Small Clusters to Solids. *Catalysis Letters*, 2011, *141*, 1067-1071.
- (10) Hammer, B.; Morikawa, Y.; Noerskov, J. K. CO chemisorption at metal surfaces and overlayers. *Phys. Rev. Lett.*, 1996, *76*, 2141-2144.

- (11) Hayden, B. E.; Rendall, M. E.; South, O. The stability and electro-oxidation of carbon monoxide on model electrocatalysts: Pt(111)-Sn(2×2) and Pt(111)-Sn($\sqrt{3} \times \sqrt{3}$)R30°. *J. Mol. Catal. A: Chem.*, 2005, 228, 55-65.
- (12) Kitchin, J. R.; Norskov, J. K.; Barteau, M. A.; Chen, J. G. Modification of the surface electronic and chemical properties of Pt(111) by subsurface 3d transition metals. *J. Chem. Phys.*, 2004, 120, 10240-10246.
- (13) Murillo, L. E.; Goda, A. M.; Chen, J. G. Selective hydrogenation of the CO bond in acrolein through the architecture of bimetallic surface structures. *Journal of the American Chemical Society*, 2007, 129, 7101-7105.
- (14) Ide, M. S.; Hao, B.; Neurock, M.; Davis, R. J. Mechanistic Insights on the Hydrogenation of α,β -Unsaturated Ketones and Aldehydes to Unsaturated Alcohols over Metal Catalysts. *Acs Catalysis*, 2, 671-683.
- (15) Wang, D. S.; Li, Y. D. Bimetallic Nanocrystals: Liquid-Phase Synthesis and Catalytic Applications. *Advanced Materials*, 2011, 23, 1044-1060.
- (16) Alayoglu, S.; Zavalij, P.; Eichhorn, B.; Wang, Q.; Frenkel, A. I.; Chupas, P. Structural and Architectural Evaluation of Bimetallic Nanoparticles: A Case Study of Pt-Ru Core-Shell and Alloy Nanoparticles. *Acs Nano*, 2009, 3, 3127-3137.
- (17) Nilekar, A. U.; Alayoglu, S.; Eichhorn, B.; Mavrikakis, M. Preferential CO Oxidation in Hydrogen: Reactivity of Core-Shell Nanoparticles. *Journal of the American Chemical Society*, 132, 7418-7428.
- (18) Alayoglu, S.; Nilekar, A. U.; Mavrikakis, M.; Eichhorn, B. Ru-Pt core-shell nanoparticles for preferential oxidation of carbon monoxide in hydrogen. *Nature Materials*, 2008, 7, 333-338.
- (19) Ferrando, R.; Jellinek, J.; Johnston, R. L. Nanoalloys: From theory to applications of alloy clusters and nanoparticles. *Chemical Reviews*, 2008, 108, 845-910.
- (20) Guzzi, L.; Boskovic, G.; Kiss, E. Bimetallic Cobalt Based Catalysts. *Catalysis Reviews-Science and Engineering*, 2010, 52, 133-203.
- (21) Jia, C. J.; Schuth, F. Colloidal metal nanoparticles as a component of designed catalyst. *Physical Chemistry Chemical Physics*, 2011, 13, 2457-2487.
- (22) Castillejos, E.; Jahjah, M.; Favier, I.; Orejón, A.; Pradel, C.; Teuma, E.; Masdeu-Bultó, A. M.; Serp, P.; Gómez, M. Synthesis of Platinum–Ruthenium Nanoparticles under Supercritical CO₂ and their Confinement in Carbon Nanotubes: Hydrogenation Applications (ChemCatChem 1/2012). *ChemCatChem*, 2012, 4, 1-1.

- (23) Alayoglu, S.; Eichhorn, B. Rh-Pt Bimetallic Catalysts: Synthesis, Characterization, and Catalysis of Core-Shell, Alloy, and Monometallic Nanoparticles. *Journal of the American Chemical Society*, 2008, *130*, 17479-17486.
- (24) Borodko, Y.; Habas, S. E.; Koebel, M.; Yang, P. D.; Frei, H.; Somorjai, G. A. Probing the interaction of poly(vinylpyrrolidone) with platinum nanocrystals by UV-Raman and FTIR. *Journal of Physical Chemistry B*, 2006, *110*, 23052-23059.
- (25) Sun, K. Q.; Hong, Y. C.; Zhang, G. R.; Xu, B. Q. Synergy between Pt and Au in Pt-on-Au Nanostructures for Chemoselective Hydrogenation Catalysis. *Acs Catalysis*, 2011, *1*, 1336-1346.
- (26) Alexeev, O. S.; Gates, B. C. Supported bimetallic cluster catalysts. *Ind. Eng. Chem. Res.*, 2003, *42*, 1571-1587.
- (27) Zhang, L. Q.; Winterbottom, J. M.; Boyes, A. P.; Raymahasay, S. Studies on the hydrogenation of cinnamaldehyde over Pd/C catalysts. *Journal of Chemical Technology and Biotechnology*, 1998, *72*, 264-272.
- (28) Su, F. B.; Lv, L.; Lee, F. Y.; Liu, T.; Cooper, A. I.; Zhao, X. S. Thermally reduced ruthenium nanoparticles as a highly active heterogeneous catalyst for hydrogenation of monoaromatics. *Journal of the American Chemical Society*, 2007, *129*, 14213-14223.
- (29) Blackmond, D. G.; Oukaci, R.; Blanc, B.; Gallezot, P. Geometric and electronic effects in the selective hydrogenation of alpha,beta-unsaturated aldehydes over zeolite-supported metals. *Journal of Catalysis*, 1991, *131*, 401-411.
- (30) Milone, C.; Crisafulli, C.; Ingoglia, R.; Schipilliti, L.; Galvagno, S. A comparative study on the selective hydrogenation of alpha,beta unsaturated aldehyde and ketone to unsaturated alcohols on Au supported catalysts. *Catalysis Today*, 2007, *122*, 341-351.
- (31) Dandekar, A.; Baker, R. T. K.; Vannice, M. A. Carbon-supported copper catalysts II. Crotonaldehyde hydrogenation. *Journal of Catalysis*, 1999, *184*, 421-439.
- (32) Prins, R. Hydrogen Spillover. Facts and Fiction. *Chemical Reviews*, 112, 2714-2738.
- (33) Maki-Arvela, P.; Hajek, J.; Salmi, T.; Murzin, D. Y. Chemoselective hydrogenation of carbonyl compounds over heterogeneous catalysts. *Applied Catalysis a-General*, 2005, *292*, 1-49.
- (34) Kluson, P.; Cervený, L. Selective Hydrogenation over Ruthenium Catalysts. *Appl. Catal. A-Gen.*, 1995, *128*, 13-31.

- (35) Lashdaf, M.; Krause, A. O. I.; Lindblad, M.; Tiitta, A.; Venalainen, T. Behaviour of palladium and ruthenium catalysts on alumina and silica prepared by gas and liquid phase deposition in cinnamaldehyde hydrogenation. *Applied Catalysis a-General*, 2003, 241, 65-75.
- (36) Oduro, W. O.; Cailuo, N.; Yu, K. M. K.; Yang, H. W.; Tsang, S. C. Geometric and electronic effects on hydrogenation of cinnamaldehyde over unsupported Pt-based nanocrystals. *Physical Chemistry Chemical Physics*, 2011, 13, 2590-2602.
- (37) Ruban, A.; Hammer, B.; Stoltze, P.; Skriver, H. L.; Norskov, J. K. Surface electronic structure and reactivity of transition and noble metals. *Journal of Molecular Catalysis a-Chemical*, 1997, 115, 421-429.
- (38) Delbecq, F.; Sautet, P. Competitive C=c and C=O Adsorption of Alpha-Beta-Unsaturated Aldehydes on Pt and Pd Surfaces in Relation with the Selectivity of Hydrogenation Reactions - A Theoretical Approach. *Journal of Catalysis*, 1995, 152, 217-236.
- (39) Cabiac, A.; Cacciaguerra, T.; Trens, P.; Durand, R.; Delahay, G.; Medevielle, A.; Plee, D.; Coq, B. Influence of textural properties of activated carbons on Pd/carbon catalysts synthesis for cinnamaldehyde hydrogenation. *Applied Catalysis a-General*, 2008, 340, 229-235.

Chapter 5 Conclusions and suggestions for future research

5.1. Conclusions

We have designed and synthesized ruthenium (Ru)-based catalysts with well-defined structures, and investigated the correlation between their structures and their catalytic performance for the liquid phase hydrogenation of bio-derived organic acids and aldehydes.

We first explored colloidal-based routes for preparation and activation of the supported Ru nanocatalysts. Three solution-based methods were evaluated to synthesize the colloidal Ru NPs: thermal decomposition with thioether as stabilizer, phase-transfer synthesis with amine as stabilizer, and polyol reduction with polymers as stabilizer. Of the three protocols, polyol reduction gave the best results for synthesizing monodisperse Ru NPs in high yield in a moderate reaction time over a broad range of reaction temperatures. Sonication-assisted colloidal deposition was more efficient than direct colloidal deposition for anchoring Ru NPs onto ordered mesoporous silica (MSU-F) support. Activation of the supported Ru NPs to remove the organic stabilizer used in the synthesis was explored using three thermal treatments: gentle oxidation at 150^oC, thermal reduction at 350^oC, and Argon-protected calcination at 650^oC. After the thermal treatments, the solid catalysts were characterized by several physical and chemical methods, followed by assessment of their reactivity by the aqueous phase hydrogenation of pyruvic acid (PyA) to lactic acid as a model reaction. The conclusion of these studies is that argon-protected calcination is the most efficient procedure for activating the - Ru nanocatalysts supported on MSU-F.

We then investigated the effect of particle size on the catalytic activity of the supported Ru NPs, using the liquid phase hydrogenation of cinnamaldehyde (CAL) as the model reaction. Colloidal

Ru NPs of different sizes were produced by polyol reduction under different synthesis conditions. It was observed that the formation of Ru NPs can occur under thermodynamic or kinetic control, with the final size of the NPs determined by a balance between the two pathways. After sonication-assisted deposition of the size-tuned Ru NPs on MSU-F and subsequent Ar-protected calcination, the Ru NPs were well-dispersed on the support, with no signs of agglomeration and no damage to the ordered structure of the MSU-F support. The uniformity and crystallinity of the supported Ru NPs in each catalyst also improved after thermal activation. The liquid phase hydrogenation of CAL over different sizes of supported Ru NPs produced COL, HCAL, and HCOL. COL was the primary product over all size ranges of the supported Ru NPs, but product selectivity was independent of particle size. However, particle size changes the density of active sites per unit surface area, thus affecting the activity of the catalysts. Finally, we correlated the composition of Ru-based bimetallic catalysts to their catalytic performance for CAL hydrogenation. The colloidal Ru-Pd bimetallic NPs as well as their monometallic counterparts were synthesized by polyol reduction of the metal precursors, impregnated into MSU-F support via sonication-assisted deposition, and activated through Ar-protected calcination. The supported NPs in each catalyst were well dispersed on MSU-F, with spherical shapes within a size range of 6 to 12 nm. The supported bimetallic NPs have an alloyed crystal structure, with a homogeneous distribution of the two metals. CAL hydrogenation over all the supported Ru-Pd bimetallic NPs and the monometallic Pd NPs produced either HCAL or HCOL as the major product, with the molar ratio of HCAL to HCOL strongly dependent on the metal composition of the catalysts. The supported bimetallic NPs have higher turnover frequencies (TOF) than the monometallic Ru NPs, presumably due to synergetic effects.

5.2. Suggestions for future research

5.2.1. Additional characterization to understand the structure of Ru-Pd bimetallic NPs supported on MSU-F

A combination of STEM-EDS analysis and power XRD diffraction has demonstrated that the supported Ru-Pd bimetallic NPs have an alloyed structure with a homogeneous distribution of Ru and Pd elements. Further characterizations are needed to confirm these observations. X-ray absorption spectroscopy (XAS), including both extended x-ray absorption fine structure (EXAFS) and x-ray absorption near edge structure (XANES) can be used to evaluate the electronic structure and the geometric atomic configuration in the local environment of the bimetallic NPs. The XANES spectra can be used to determine the valence state of the element and charge distribution of NPs in the sample. Theoretical fitting of the EXAFS data can provide information about the environment of local atoms, nearest-atomic neighbor arrangement (coordination numbers), and inter-atomic distance. A successful application of EXAFS was reported for characterization of Pt-Ru core-shell and alloy NPs.¹

High-energy x-ray diffraction, which is carried out on a synchrotron beamline, is another useful technique for understanding the structures of NPs. The diffuse scattering diffraction patterns over an extended range of wave vectors can be obtained in addition to the Bragg-like diffraction peaks on high-energy x-ray diffraction. Refinement of the high-energy x-ray diffraction data, combined with computational modeling such as reverse Monte Carlo simulations and atomic pair distribution function analysis, can provide more accurate structure and element distribution throughout the NPs.²⁻⁵

5.2.2. Mechanism-based kinetic modeling of CAL hydrogenation over supported Ru-Pd NPs

We compared our reaction data on CAL hydrogenation over the NPs supported on MSU-F with the latest reported kinetic models of CAL hydrogenation over traditionally prepared Ru or Ru-Sn sol-gel catalysts,^{6,7} and found discrepancies between our experimental data and the model predictions. We think a primary reason for this discrepancy is the difference between the reaction pathways of supported NPs and those over traditionally prepared Ru or Ru-Sn catalysts. The literature model does not consider transformations between reaction intermediates.^{6,7} However, intermediate transformations such as radical isomerization due to electron delocalizations, may have a significant effect on the reaction routes for CAL hydrogenation over supported NPs with well-defined compositions and structures. To model the kinetics of CAL hydrogenation over the supported NPs used in this study, further theoretical computations and simulation are necessary. Description of the chemical bond between the molecules and NP surfaces is the first step for modeling the reaction kinetics. Density functional theory (DFT) is an increasingly important tool for understanding surface chemistry.⁸⁻¹⁰ In DFT calculations, the interaction energies between molecules and atoms on the metal surface can be computed. The technique can also be used to obtain a set of other important parameters, including reaction free energies, activation energies, transition states, surface stability, and molecule vibration frequency.¹¹ Compared with other computational methods, DFT has the significant advantage of allowing the treatment of complex, extended systems with a good balance between accuracy and computational cost at a reasonable calculation speed.^{10,12-16} Several successful examples have been reported in applying DFT

calculations to investigation of the competitive routes for C=C and C=O hydrogenation over Au(111), Ag (111), Pt(111), Ru(0001) and Pt-Sn (111) surfaces.¹⁷⁻²³

In kinetic analyses which involve the modeling of overall reactions in terms of elementary steps, all possible elementary reactions are included in the mechanism and there is no assumption of a rate-limiting step.²⁴⁻²⁷ The activation energies and pre-exponential factors of each elementary reaction step are primary inputs for micro-kinetic analysis. The activation energies can be obtained directly from the DFT calculations, while the pre-exponential factors can be estimated by collision theory using transition state vibration frequencies given by DFT calculations.^{25,28}

The theoretical modeling, coupled with experimental results, could offer a better understanding of the reaction mechanisms and kinetics of CAL hydrogenation over supported NPs.

REFERENCES

REFERENCES

- (1) Alayoglu, S.; Zavalij, P.; Eichhorn, B.; Wang, Q.; Frenkel, A. I.; Chupas, P. Structural and Architectural Evaluation of Bimetallic Nanoparticles: A Case Study of Pt-Ru Core-Shell and Alloy Nanoparticles. *Acs Nano*, 2009, 3, 3127-3137.
- (2) Bedford, N.; Dablemont, C.; Viau, G.; Chupas, P.; Petkov, V. 3-D structure of nanosized catalysts by high-energy X-ray diffraction and reverse Monte Carlo simulations: Study of Ru. *Journal of Physical Chemistry C*, 2007, 111, 18214-18219.
- (3) Petkov, V.; Gateshki, M.; Niederberger, M.; Ren, Y. Atomic-Scale Structure of Nanocrystalline $Ba_xSr_{1-x}TiO_3$ ($x = 1, 0.5, 0$) by X-ray Diffraction and the Atomic Pair Distribution Function Technique. *Chem. Mater.*, 2006, 18, 814-821.
- (4) Petkov, V.; Ohta, T.; Hou, Y.; Ren, Y. Atomic-Scale Structure of Nanocrystals by High-Energy X-ray Diffraction and Atomic Pair Distribution Function Analysis: Study of $FexPd_{100-x}$ ($x = 0, 26, 28, 48$) Nanoparticles. *J. Phys. Chem. C*, 2007, 111, 714-720.
- (5) Petkov, V.; Parvanov, V.; Tomalia, D.; Swanson, D.; Bergstrom, D.; Vogt, T. 3D structure of dendritic and hyperbranched macromolecules by X-ray diffraction. *Solid State Commun.*, 2005, 134, 671-675.
- (6) Hajek, J.; Murzin, D. Y. Liquid-phase hydrogenation of cinnamaldehyde over a Ru-Sn sol-gel catalyst. 1. Evaluation of mass transfer via a combined experimental/theoretical approach. *Industrial & Engineering Chemistry Research*, 2004, 43, 2030-2038.
- (7) Hajek, J.; Warna, J.; Murzin, D. Y. Liquid-phase hydrogenation of cinnamaldehyde over a Ru-Sn sol-gel catalyst. 2. Kinetic modeling. *Industrial & Engineering Chemistry Research*, 2004, 43, 2039-2048.
- (8) Norskov, J. K.; Abild-Pedersen, F.; Studt, F.; Bligaard, T. Density functional theory in surface chemistry and catalysis. *Proceedings of the National Academy of Sciences of the United States of America*, 108, 937-943.
- (9) Gokhale, A. A.; Kandoi, S.; Greeley, J. P.; Mavrikakis, M.; Dumesic, J. A. Molecular-level descriptions of surface chemistry in kinetic models using density functional theory. *Chemical Engineering Science*, 2004, 59, 4679-4691.
- (10) Norskov, J. K.; Bligaard, T.; Rossmeisl, J.; Christensen, C. H. Towards the computational design of solid catalysts. *Nature Chemistry*, 2009, 1, 37-46.

- (11) Liebman, J. F. Density Functional Theory: A Practical Introduction, by David S. Sholl and Janice A. Steckel. *Mol. Cryst. Liq. Cryst.*, 2009, 515, 249-250.
- (12) Rossmeisl, J.; Skulason, E.; Bjoerketun, M. E.; Tripkovic, V.; Norskov, J. K. Modeling the electrified solid-liquid interface. *Chem. Phys. Lett.*, 2008, 466, 68-71.
- (13) Ertl, G. Reactions at surfaces: from atoms to complexity (Nobel lecture). *Angew. Chem., Int. Ed.*, 2008, 47, 3524-3535.
- (14) Bligaard, T.; Norskov, J. K.; Dahl, S.; Matthiesen, J.; Christensen, C. H.; Sehested, J. The Bronsted-Evans-Polanyi relation and the volcano curve in heterogeneous catalysis. *J. Catal.*, 2004, 224, 206-217.
- (15) Toulhoat, H.; Raybaud, P. Kinetic interpretation of catalytic activity patterns based on theoretical chemical descriptors. *J. Catal.*, 2003, 216, 63-72.
- (16) Hammer, B.; Norskov, J. K. Theoretical surface science and catalysis - calculations and concepts. *Adv. Catal.*, 2000, 45, 71-129.
- (17) Haubrich, J.; Loffreda, D.; Delbecq, F.; Sautet, P.; Jugnet, Y.; Becker, C.; Wandelt, K. Adsorption and Vibrations of alpha,beta-Unsaturated Aldehydes on Pt(111) and Pt-Sn Alloy (111) Surfaces. 3. Adsorption Energy vs Adsorption Strength. *Journal of Physical Chemistry C*, 2010, 114, 1073-1084.
- (18) Haubrich, J.; Loffreda, D.; Delbecq, F.; Sautet, P.; Jugnet, Y.; Krupski, A.; Becker, C.; Wandelt, K. Adsorption and vibrations of alpha,beta-unsaturated aldehydes on pure pt and Pt-Sn alloy (111) surfaces I. Prenal. *Journal of Physical Chemistry C*, 2008, 112, 3701-3718.
- (19) Haubrich, J.; Loffreda, D.; Delbecq, F.; Sautet, P.; Krupski, A.; Becker, C.; Wandelt, K. Adsorption of alpha,beta-Unsaturated Aldehydes on Pt(111) and Pt-Sn Alloys: II. Crotonaldehyde. *Journal of Physical Chemistry C*, 2009, 113, 13947-13967.
- (20) Loffreda, D.; Delbecq, F.; Vigne, F.; Sautet, P. Catalytic hydrogenation of unsaturated aldehydes on Pt(111): Understanding the selectivity from first-principles calculations. *Angewandte Chemie-International Edition*, 2005, 44, 5279-5282.
- (21) Loffreda, D.; Delbecq, F.; Vigne, F.; Sautet, P. Chemo-regioselectivity in heterogeneous catalysis: Competitive routes for C=O and C=C hydrogenations from a theoretical approach. *Journal of the American Chemical Society*, 2006, 128, 1316-1323.
- (22) Yang, X. F.; Wang, A. Q.; Wang, X. D.; Zhang, T.; Han, K. L.; Li, J. Combined Experimental and Theoretical Investigation on the Selectivities of Ag, Au, and Pt Catalysts for Hydrogenation of Crotonaldehyde. *Journal of Physical Chemistry C*, 2009, 113, 20918-20926.

- (23) Ide, M. S.; Hao, B.; Neurock, M.; Davis, R. J. Mechanistic Insights on the Hydrogenation of alpha,beta-Unsaturated Ketones and Aldehydes to Unsaturated Alcohols over Metal Catalysts. *Acs Catalysis*, 2, 671-683.
- (24) Broadbelt, L. J.; Snurr, R. Q. Applications of molecular modeling in heterogeneous catalysis research. *Applied Catalysis a-General*, 2000, 200, 23-46.
- (25) Hansgen, D. A.; Vlachos, D. G.; Chen, J. G. G. Using first principles to predict bimetallic catalysts for the ammonia decomposition reaction. *Nature Chemistry*, 2, 484-489.
- (26) Saliccioli, M.; Stamatakis, M.; Caratzoulas, S.; Vlachos, D. G. A review of multiscale modeling of metal-catalyzed reactions: Mechanism development for complexity and emergent behavior. *Chemical Engineering Science*, 66, 4319-4355.
- (27) Stoltze, P. Microkinetic simulation of catalytic reactions. *Progress in Surface Science*, 2000, 65, 65-150.
- (28) Madon, R. J.; Braden, D.; Kandoi, S.; Nagel, P.; Mavrikakis, M.; Dumesic, J. A. Microkinetic analysis and mechanism of the water gas shift reaction over copper catalysts. *Journal of Catalysis*, 281, 1-11.

APPENDICES

Appendix A

Reaction profiles for CAL hydrogenation over different size groups of Ru NPs supported on MSU-F

A. 1 CAL hydrogenation over the catalyst WD170F-5NM

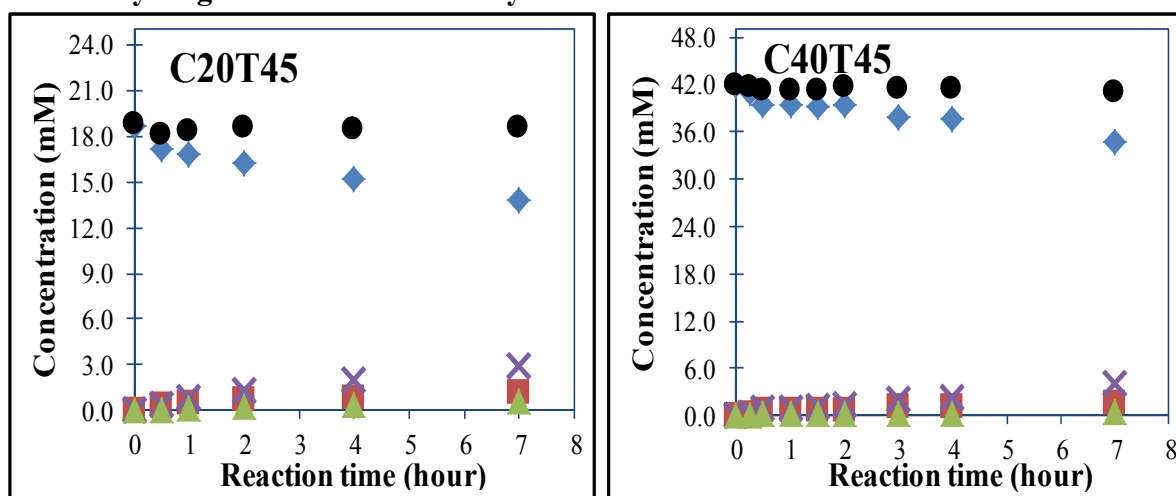


Figure A.1-1 Reaction profiles for CAL hydrogenation under reaction temperature of 45°C. ● material balance; ◆ CAL; ■ HCAL; ✕ COL; ▲ HCOL. The reaction conditions were described in Table 3-6. The numbers in C##T45 means the substrate initial concentration for the reaction.

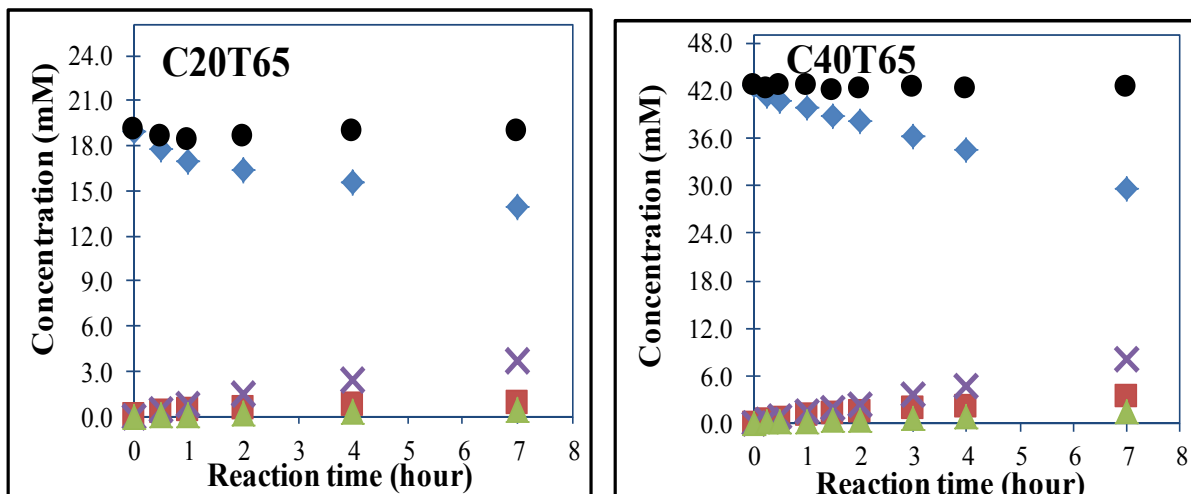


Figure A.1-2 Reaction profiles for CAL hydrogenation under reaction temperature of 65°C. ● material balance; ◆ CAL; ■ HCOL; X COL; ▲ HCAL. The reaction conditions were described in Table 3-6. The numbers in C##T65 means the substrate initial concentration for the reaction.

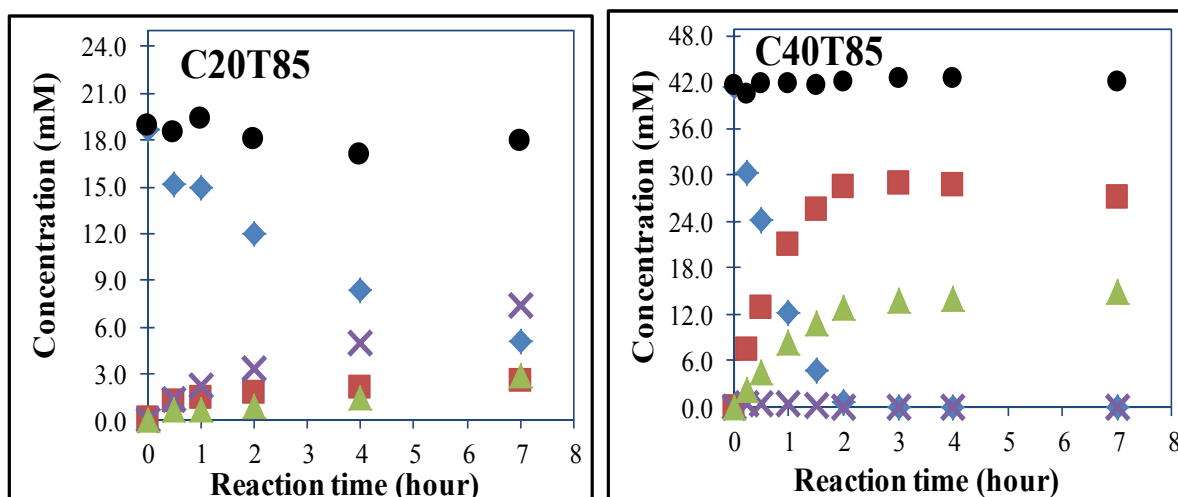


Figure A.1-3 Reaction profiles for CAL hydrogenation under reaction temperature of 85°C. ● material balance; ◆ CAL; ■ HCOL; X COL; ▲ HCAL. The reaction conditions were described in Table 3-6. The numbers in C##T85 means the substrate initial concentration for the reaction.

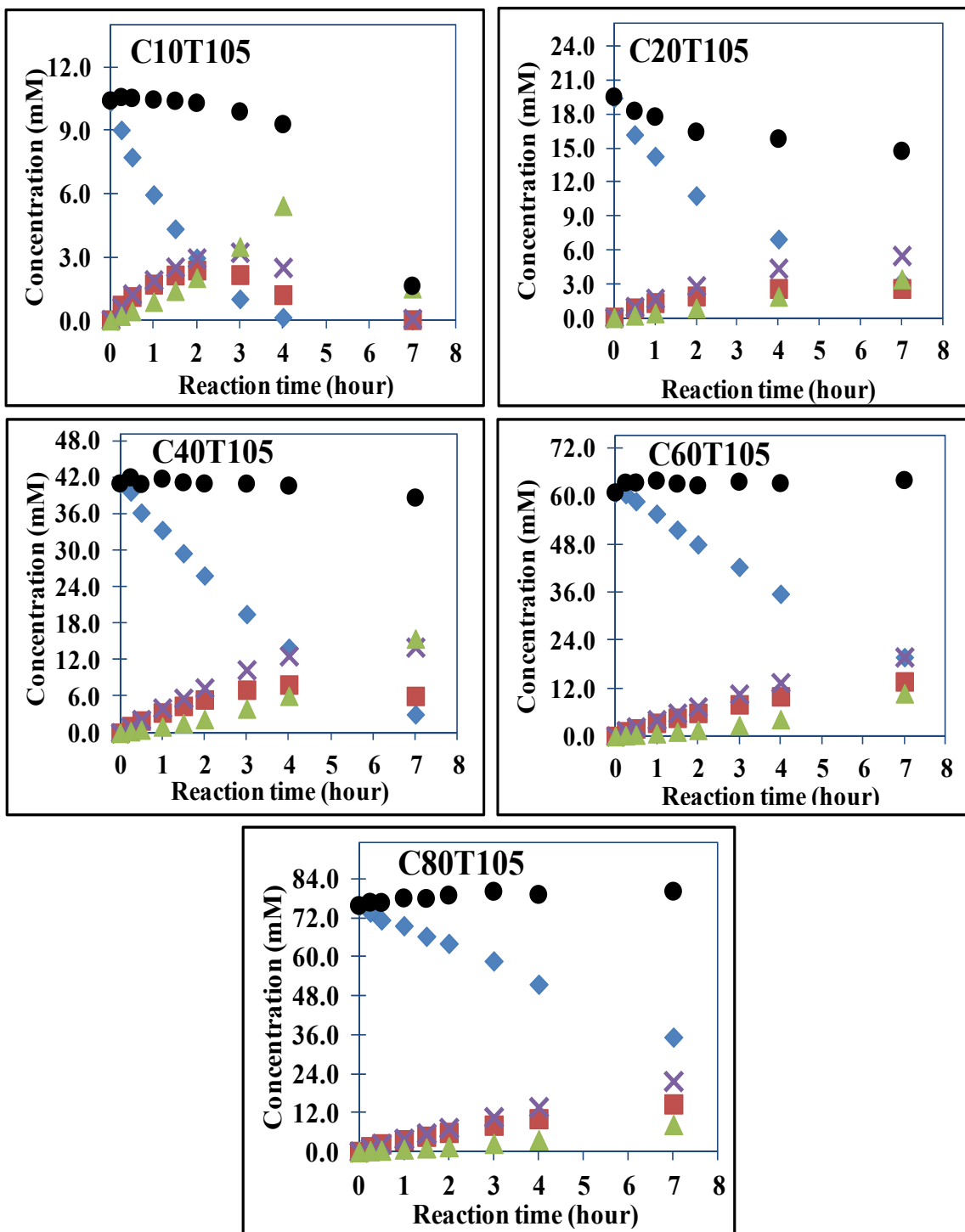


Figure A.1-4 Reaction profiles for CAL hydrogenation under reaction temperature of 105°C. ● material balance; ◆ CAL; ■ HCAL; X COL; ▲ HCOL. The reaction conditions were described in Table 3-6. The numbers in C##T105 means the substrate initial concentration for the reaction.

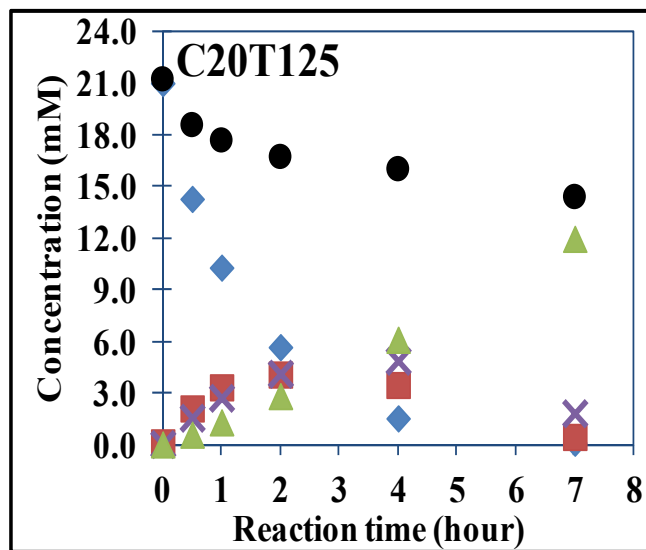


Figure A.1-5 Reaction profiles for CAL hydrogenation under reaction temperature of 125°C. ● material balance; ◆ CAL; ■ HCOL; X COL; ▲ HCOL. The reaction conditions were described in Table 3-6. The numbers in C##T125 means the substrate initial concentration for the reaction.

A. 2 CAL hydrogenation over Ru catalyst SG30F-6NM

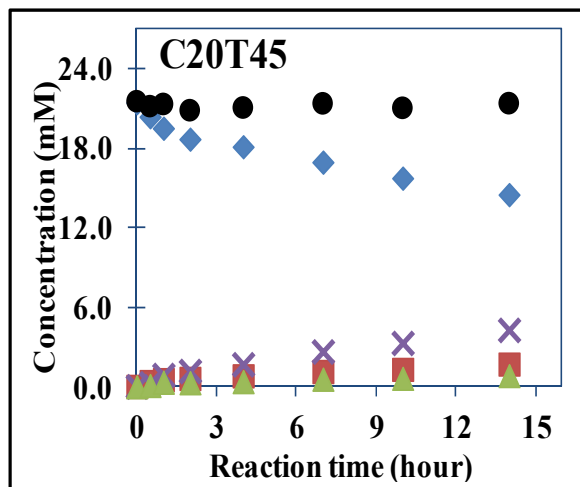


Figure A.2-1 Reaction profiles for CAL hydrogenation under reaction temperature of 45°C. ● material balance; ◆ CAL; ■ HCOL; X COL; ▲ HCOL. The catalyst was SG30F-6NM, and the reaction conditions were described in Table 3-6. The numbers in C##T45 means the substrate initial concentration for the reaction.

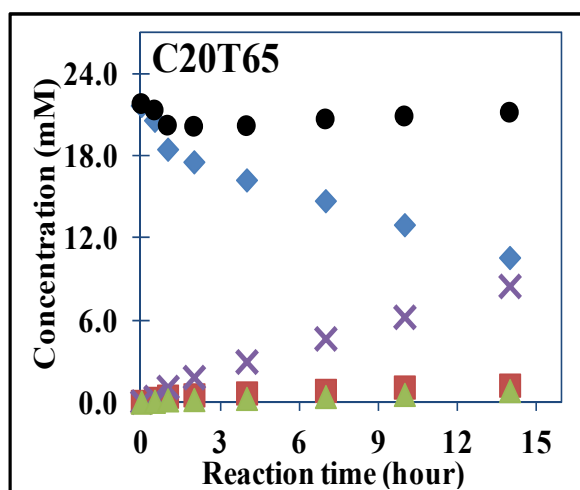


Figure A.2-2 Reaction profiles for CAL hydrogenation under reaction temperature of 65°C. ● material balance; ◆ CAL; ■ HCOL; X COL; ▲ HCOL. The catalyst was SG30F-6NM, and the reaction conditions were described in Table 3-6. The numbers in C##T65 means the substrate initial concentration for the reaction.

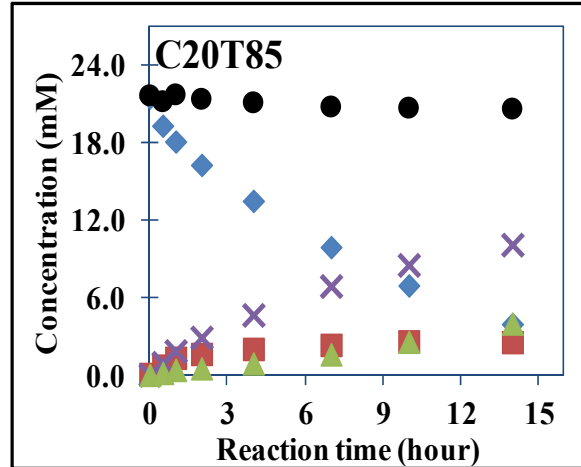


Figure A.2-3 Reaction profiles for CAL hydrogenation under reaction temperature of 85°C. ● material balance; ◆ CAL; ■ HCOL; ✕ COL; ▲ HCOL The catalyst was SG30F-6NM, and the reaction conditions were described in Table 3-6. The numbers in C##T85 means the substrate initial concentration for the reaction.

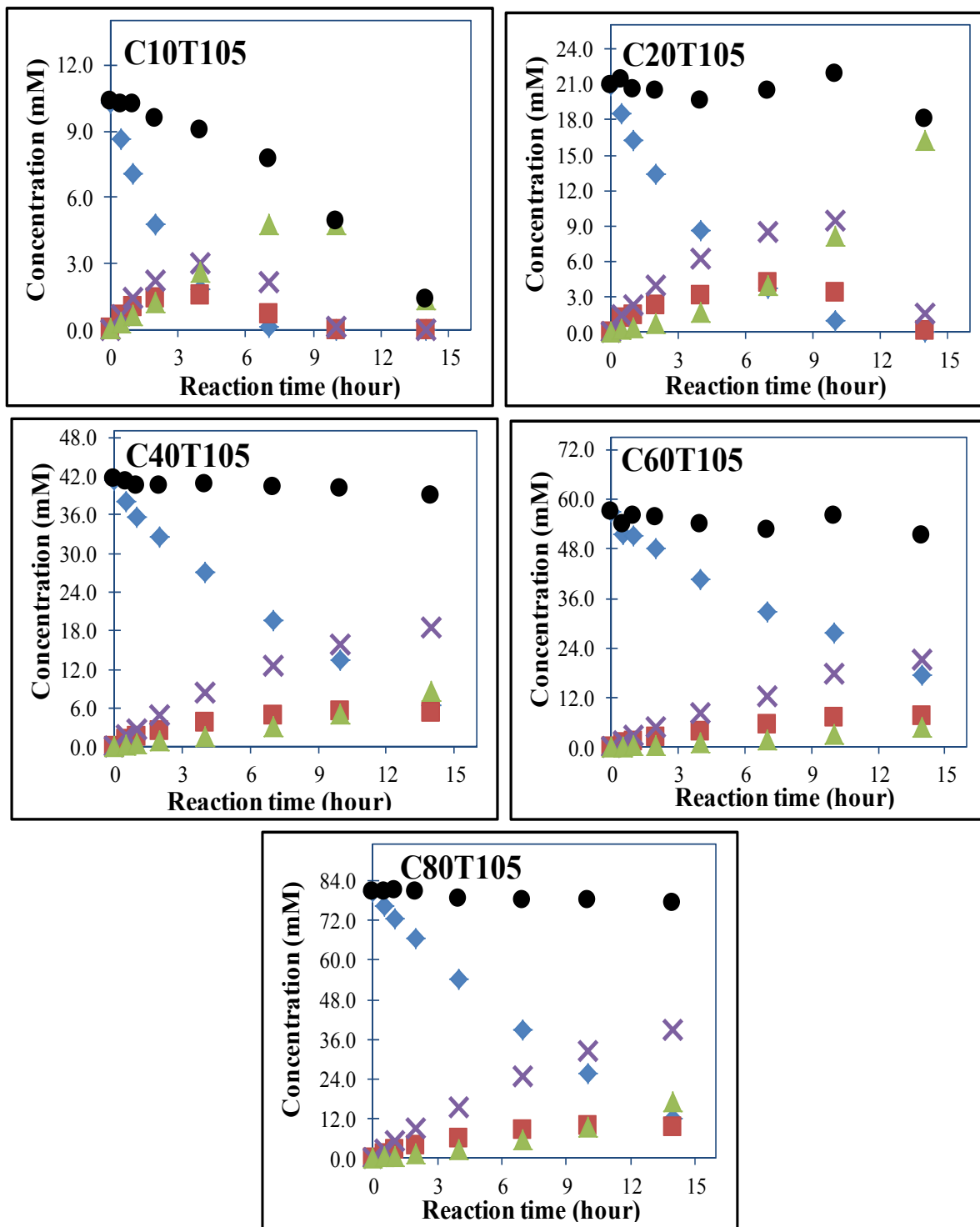


Figure A.2-4 Reaction profiles for CAL hydrogenation under reaction temperature of 105°C. ● material balance; ◆ CAL; ■ HCAL; X COL; ▲ HCOL. The catalyst was SG30F-6NM, and the reaction conditions were described in Table 3-6. The numbers in C##T105 means the substrate initial concentration for the reaction.

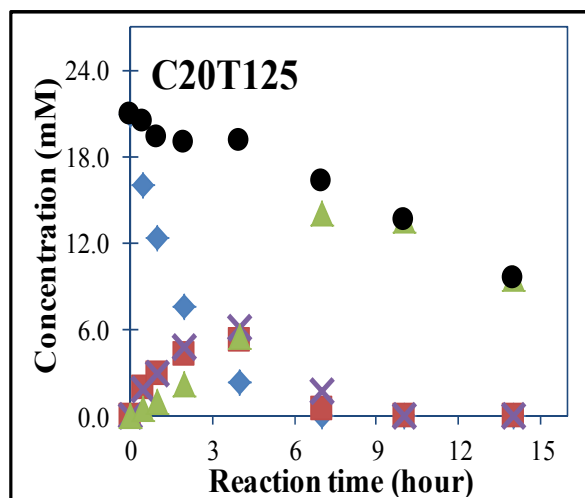


Figure A.2-5 Reaction profiles for CAL hydrogenation under reaction temperature of 125°C. ● material balance; ◆ CAL; ■ HCAL; X COL; ▲ HCOL. The catalyst was SG30F-6NM, and the reaction conditions were described in Table 3-6. The numbers in C##T125 means the substrate initial concentration for the reaction.

A. 3 CAL hydrogenation over Ru catalyst TW10F-25NM

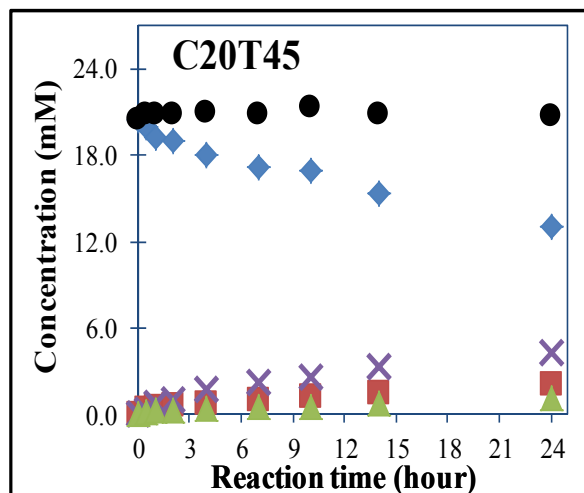


Figure A.3-1 Reaction profiles for CAL hydrogenation under reaction temperature of 45°C. ● material balance; ◆ CAL; ■ HCAL; ✕ COL; ▲ HCOL. The catalyst was TW10F-25NM, and the reaction conditions were described in Table 3-6. The numbers in C##T45 means the substrate initial concentration for the reaction.

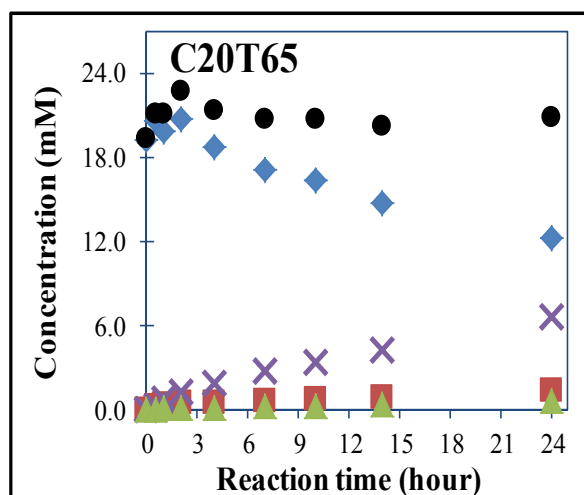


Figure A.3-2 Reaction profiles for CAL hydrogenation under reaction temperature of 65°C. ● material balance; ◆ CAL; ■ HCAL; ✕ COL; ▲ HCOL. The catalyst was TW10F-25NM, and the reaction conditions were described in Table 3-6. The numbers in C##T65 means the substrate initial concentration for the reaction.

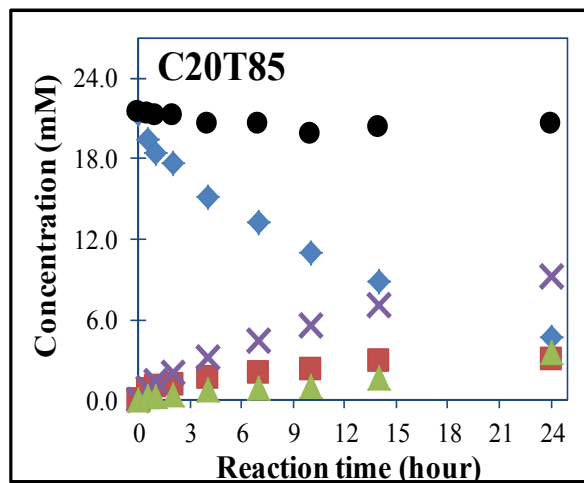


Figure A.3-3 Reaction profiles for CAL hydrogenation under reaction temperature of 85°C. ● material balance; ◆ CAL; ■ HCAL; ✕ COL; ▲ HCOL. The catalyst was TW10F-25NM, and the reaction conditions were described in Table 3-6. The numbers in C##T85 means the substrate initial concentration for the reaction.

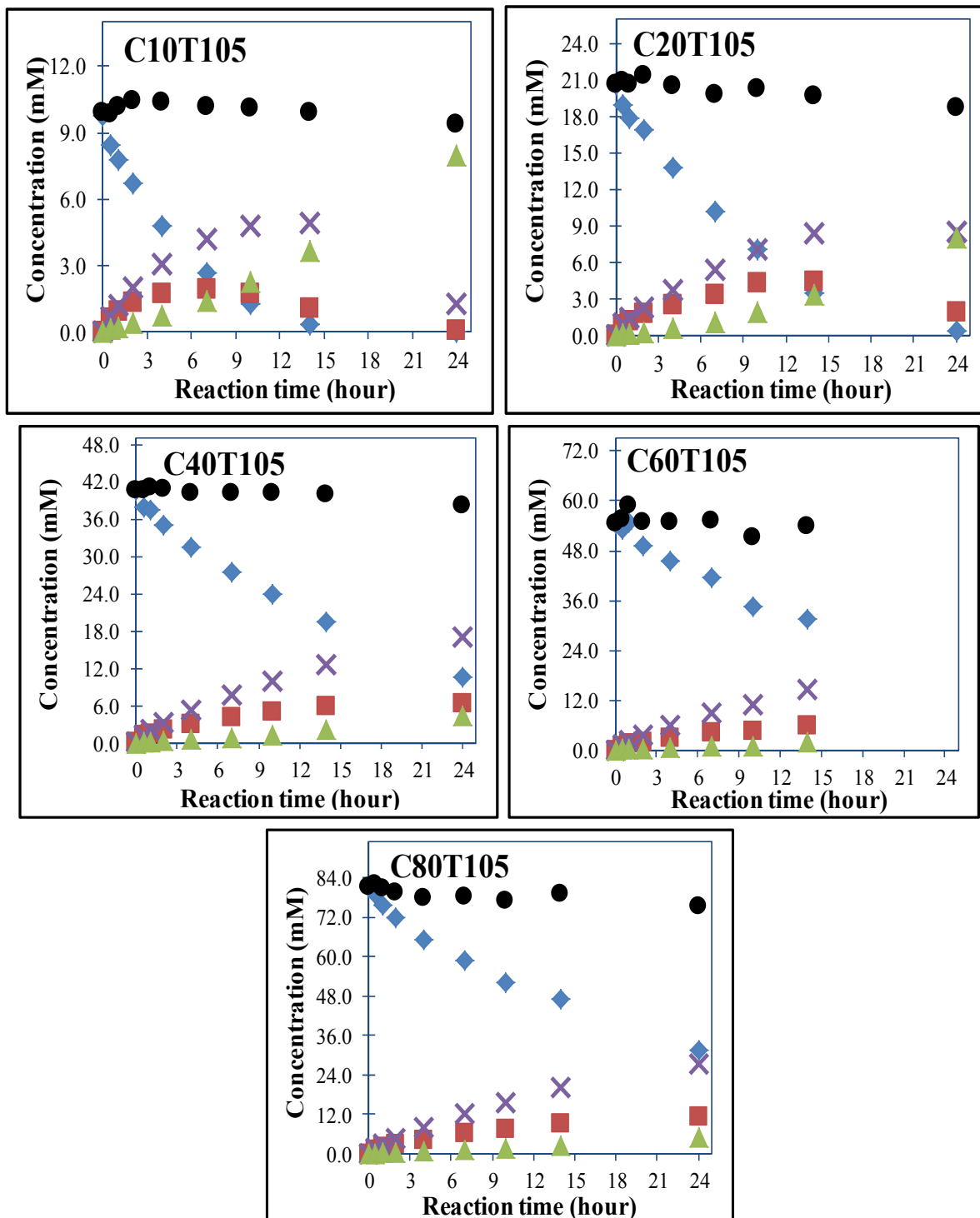


Figure A.3-4 Reaction profiles for CAL hydrogenation under reaction temperature of 105°C. ● material balance; ◆ CAL; ■ HCAL; ✕ COL; ▲ HCOL. The catalyst was TW10F-25NM, and the reaction conditions were described in Table 3-6. The numbers in C##T105 means the substrate initial concentration for the reaction.

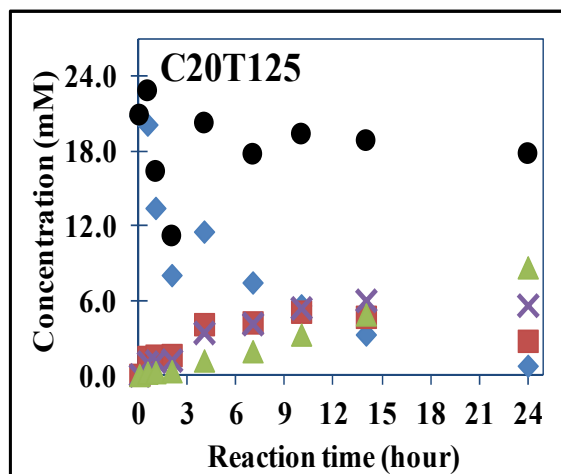


Figure A.3-5 Reaction profiles for CAL hydrogenation under reaction temperature of 125°C. ● material balance; ◆ CAL; ■ HCOL; × COL; ▲ HCOL. The catalyst was TW10F-25NM, and the reaction conditions were described in Table 3-6. The numbers in C##T125 means the substrate initial concentration for the reaction.

A. 4 CAL hydrogenation over Ru catalyst TW12F-67NM

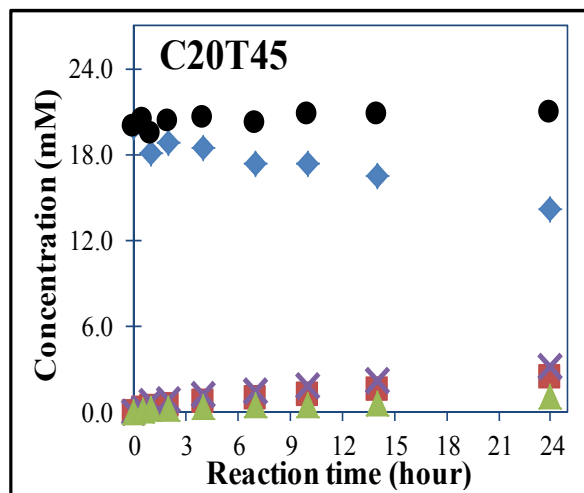


Figure A.4-1 Reaction profiles for CAL hydrogenation under reaction temperature of 45°C. ● material balance; ◆ CAL; ■ HCAL; ✕ COL; ▲ HCOL. The catalyst was TW12F-67NM, and the reaction conditions were described in Table 3-6. The numbers in C##T45 means the substrate initial concentration for the reaction.

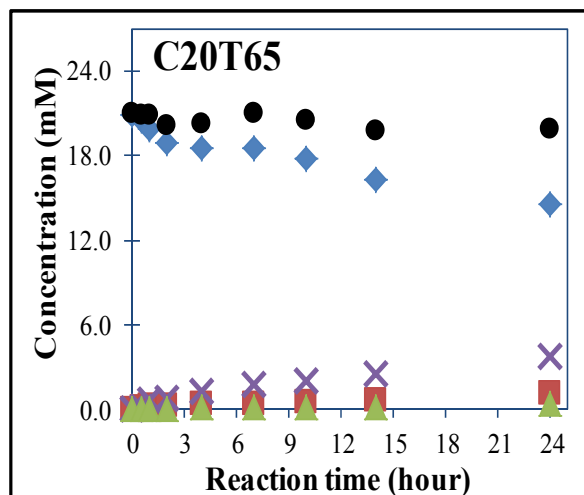


Figure A.4-2 Reaction profiles for CAL hydrogenation under reaction temperature of 65°C. ● material balance; ◆ CAL; ■ HCAL; ✕ COL; ▲ HCOL. The catalyst was TW12F-67NM, and the reaction conditions were described in Table 3-6. The numbers in C##T65 means the substrate initial concentration for the reaction.

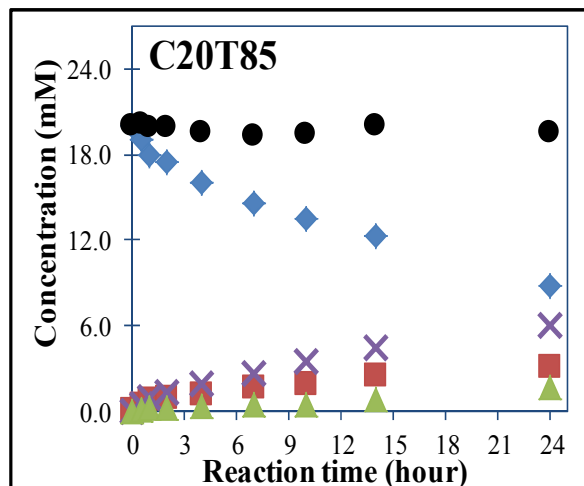


Figure A.4-3 Reaction profiles for CAL hydrogenation under reaction temperature of 85°C. ● material balance; ◆ CAL; ■ HCOL; ✕ COL; ▲ HCOL. The catalyst was TW12F-67NM, and the reaction conditions were described in Table 3-6. The numbers in C##T85 means the substrate initial concentration for the reaction.

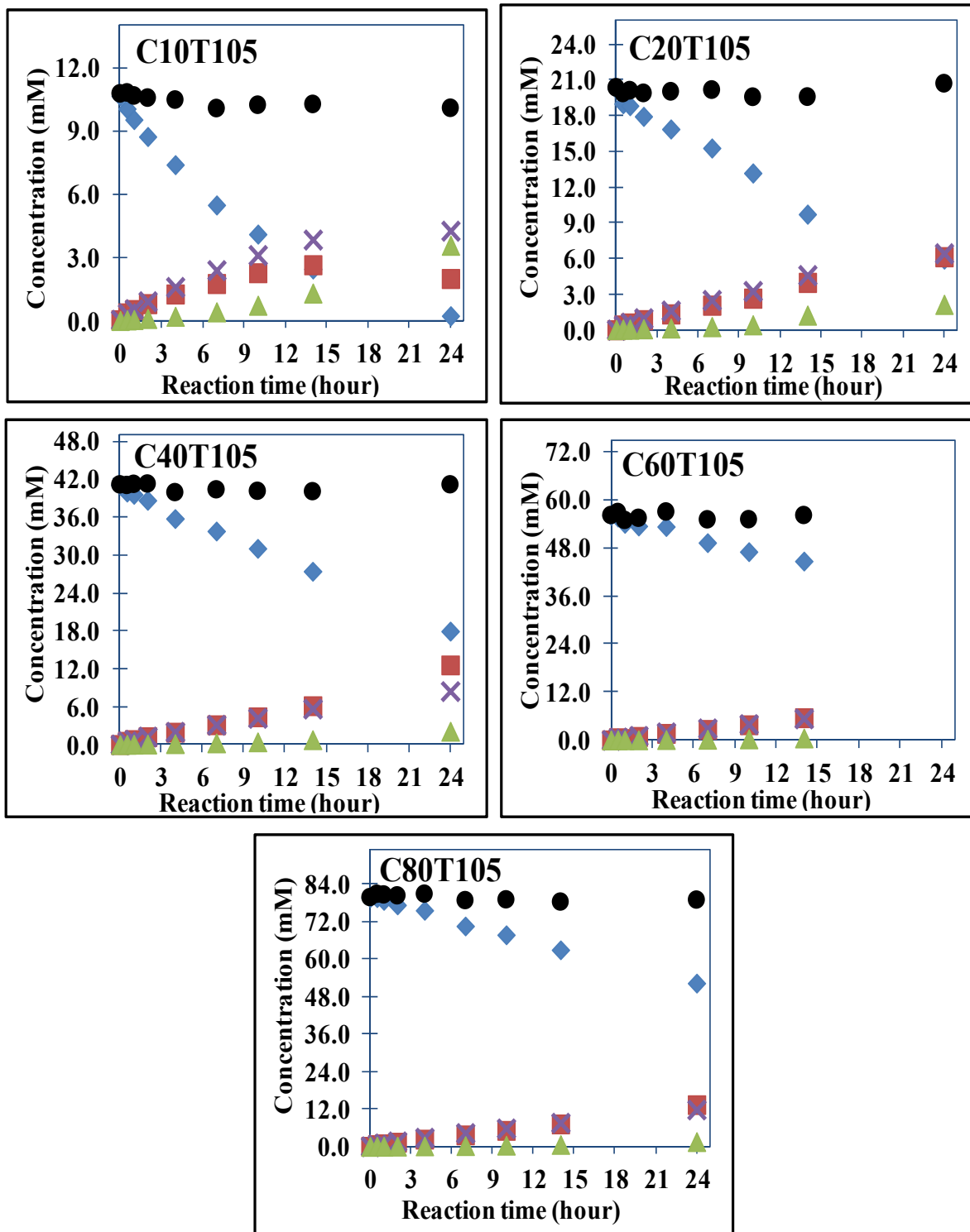


Figure A.4-4 Reaction profiles for CAL hydrogenation under reaction temperature of 105°C. ● material balance; ◆ CAL; ■ HCAL; ✕ COL; ▲ HCOL. The catalyst was TW12F-67NM, and the reaction conditions were described in Table 3-6. The numbers in C##T105 means the substrate initial concentration for the reaction.

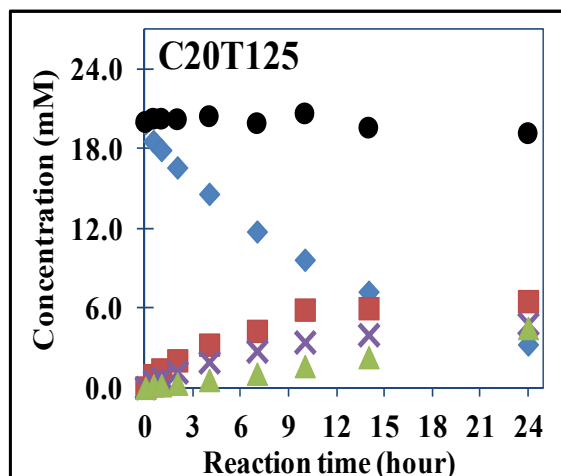


Figure A.4-5 Reaction profiles for CAL hydrogenation under reaction temperature of 125°C. ● material balance; ◆ CAL; ■ HCAL; ✕ COL; ▲ HCOL. The catalyst was TW12F-67NM, and the reaction conditions were described in Table 3-6. The numbers in C##T125 means the substrate initial concentration for the reaction.

A. 5 CAL hydrogenation over Ru catalyst TW16F-94NM

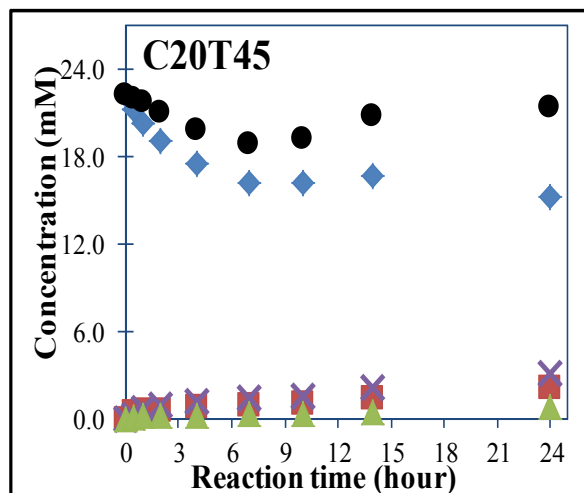


Figure A.5-1 Reaction profiles for CAL hydrogenation under reaction temperature of 45°C. ● material balance; ◆ CAL; ■ HCAL; ✕ COL; ▲ HCOL. The catalyst was TW16F-94NM, and the reaction conditions were described in Table 3-6. The numbers in C##T45 means the substrate initial concentration for the reaction.

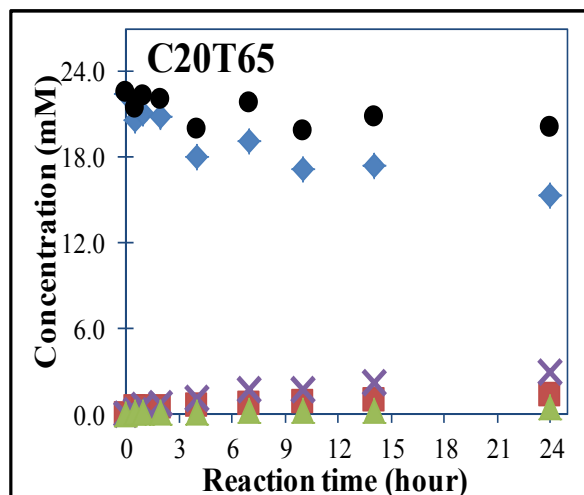


Figure A.5-2 Reaction profiles for CAL hydrogenation under reaction temperature of 65°C. ● material balance; ◆ CAL; ■ HCAL; ✕ COL; ▲ HCOL. The catalyst was TW16F-94NM, and the reaction conditions were described in Table 3-6. The numbers in C##T65 means the substrate initial concentration for the reaction.

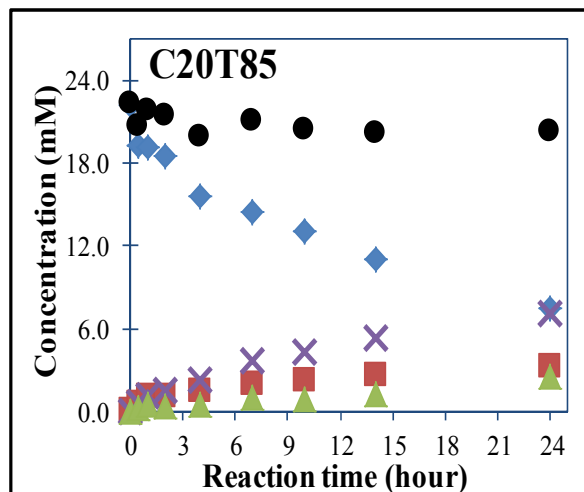


Figure A.5-3 Reaction profiles for CAL hydrogenation under reaction temperature of 85°C. ● material balance; ◆ CAL; ■ HCOL; × COL; ▲ HCOL. The catalyst was TW16F-94NM, and the reaction conditions were described in Table 3-6. The numbers in C##T85 means the substrate initial concentration for the reaction.

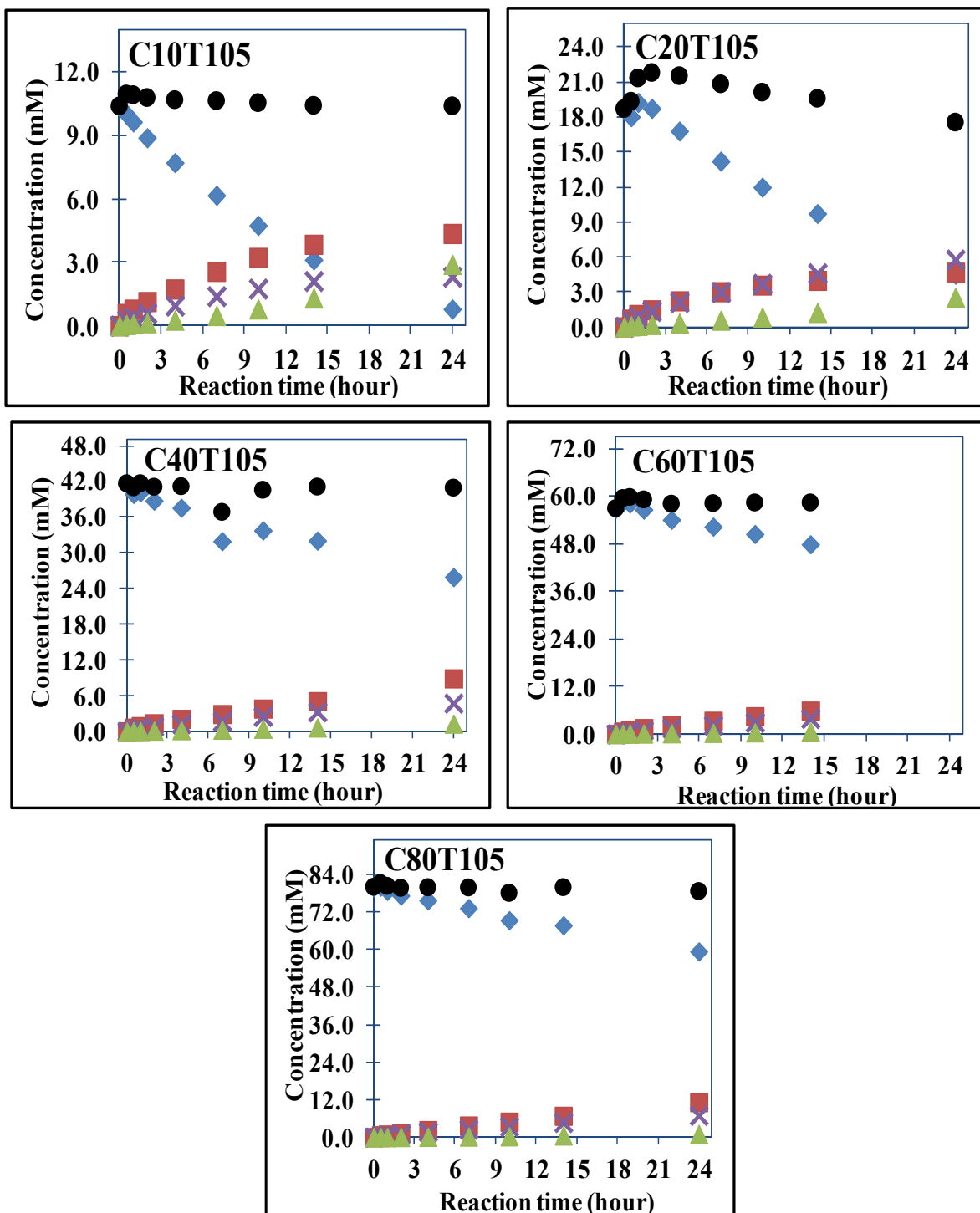


Figure A.5-4 Reaction profiles for CAL hydrogenation under reaction temperature of 105°C. ● material balance; ◆ CAL; ■ HCOL; X COL; ▲ HCOL. The catalyst was TW16F-94NM, and the reaction conditions were described in Table 3-6. The numbers in C##T105 means the substrate initial concentration for the reaction.

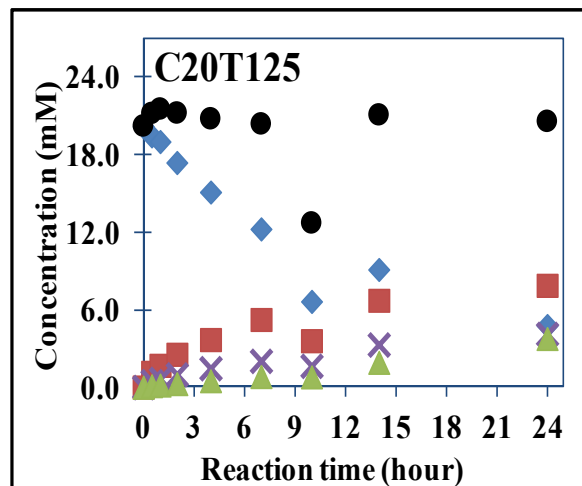


Figure A.5-5 Reaction profiles for CAL hydrogenation under reaction temperature of 125°C. ● material balance; ◆ CAL; ■ HCAL; ✕ COL; ▲ HCOL. The catalyst was TW16F-94NM, and the reaction conditions were described in Table 3-6. The numbers in C##T125 means the substrate initial concentration for the reaction.

Appendix B

Reaction profiles for CAL hydrogenation over Ru-Pd bimetallic NPs supported on MSU-F

B. 1 CAL hydrogenation over the bimetallic catalyst Pd05RuF

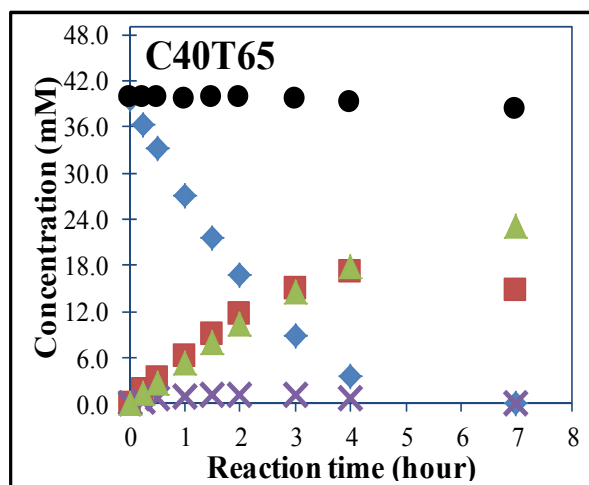


Figure B.1-1 Reaction profiles for CAL hydrogenation over the catalyst Pd05RuF. ● material balance; ◆ CAL; ■ HCAL; × COL; ▲ HCOL. Reaction conditions: 1.9×10^{-6} mole of metal (Ru+Pd) loading in each reaction; 35 ml CAL solution in IPA (40mM); $T = 65^{\circ}\text{C}$; $P(\text{H}_2) = 20$ bar; Stirring speed = 800 RPM. The numbers in C##T65 means the substrate initial concentration for the reaction.

B. 2 CAL hydrogenation over the bimetallic catalyst Pd20RuF

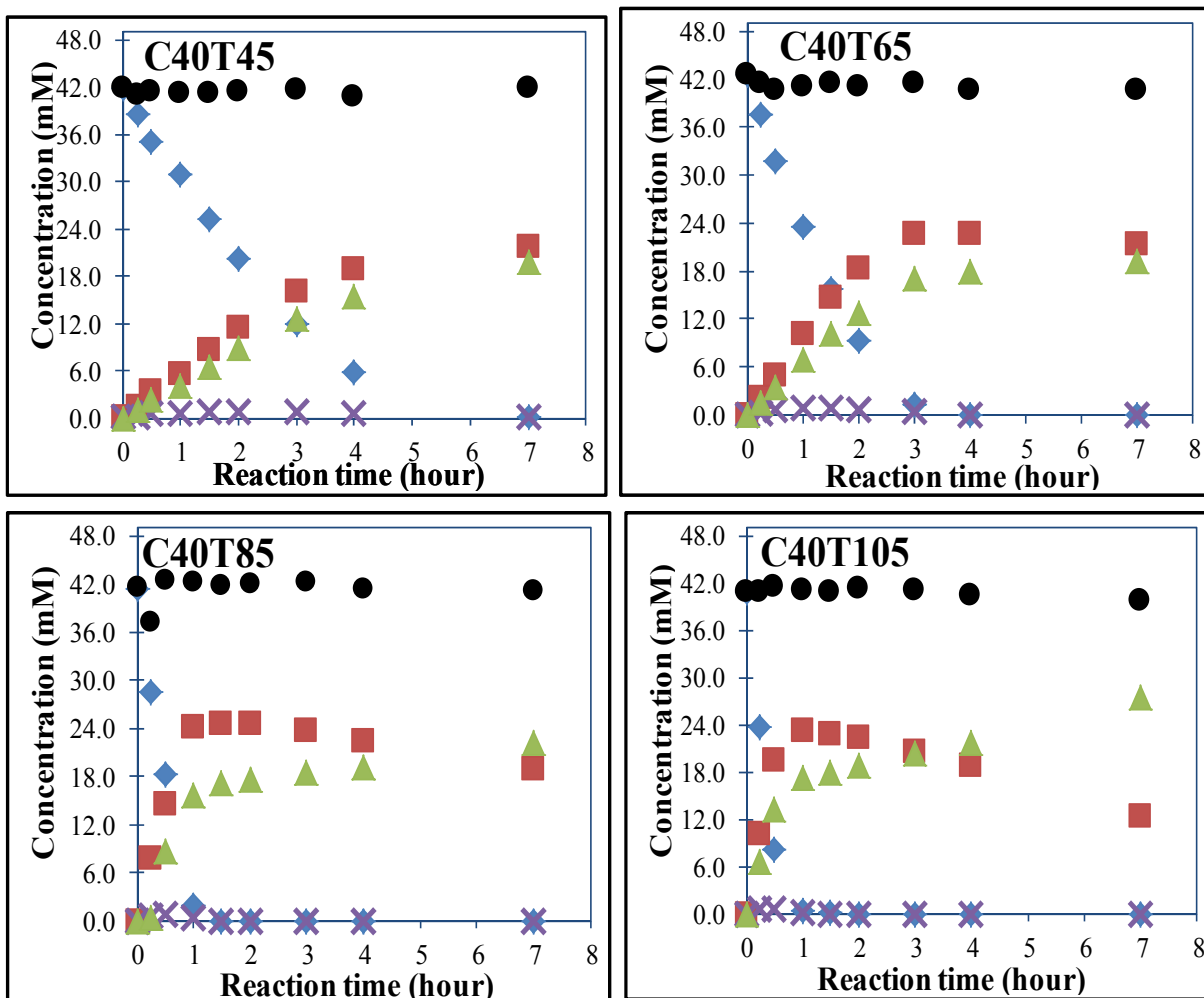


Figure B.2-1 Reaction profiles for CAL hydrogenation over the catalyst Pd20RuF. ● material balance; ◆ CAL; ■ HCOL; ✕ COL; ▲ HCOL. Reaction conditions: $\sim 1.9 \times 10^{-6}$ mole of metal (Ru+Pd) loading in each reaction (see Table 4-5); 35 ml CAL solution in IPA (40mM); $T = 65^\circ\text{C}$; $P(\text{H}_2) = 20$ bar; Stirring speed = 800 RPM. The numbers in C##T65 means the substrate initial concentration for the reaction.

B. 3 CAL hydrogenation over the bimetallic catalyst Pd40RuF

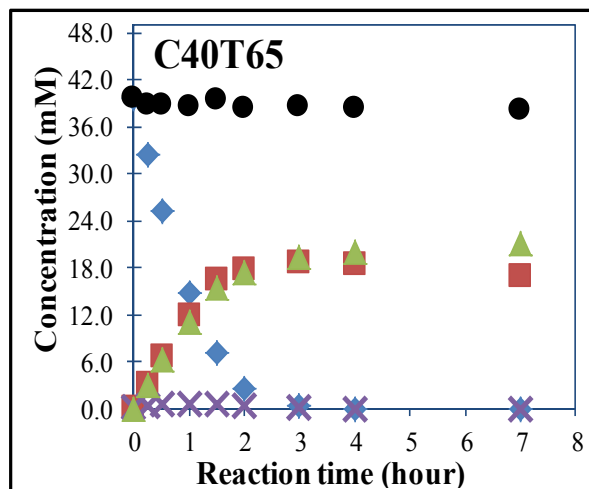


Figure B.3-1 Reaction profiles for CAL hydrogenation over the catalyst Pd40RuF. ● material balance; ◆ CAL; ■ HCOL; ▲ HCOL; × COL. Reaction conditions: 2.0×10^{-6} mole of metal (Ru+Pd) loading in each reaction (see Table 4-5); 35 ml CAL solution in IPA (40mM); $T = 65^{\circ}\text{C}$; $P(\text{H}_2) = 20$ bar; Stirring speed = 800 RPM. The numbers in C##T65 means the substrate initial concentration for the reaction.

B. 4 CAL hydrogenation over the bimetallic catalyst Pd50RuF

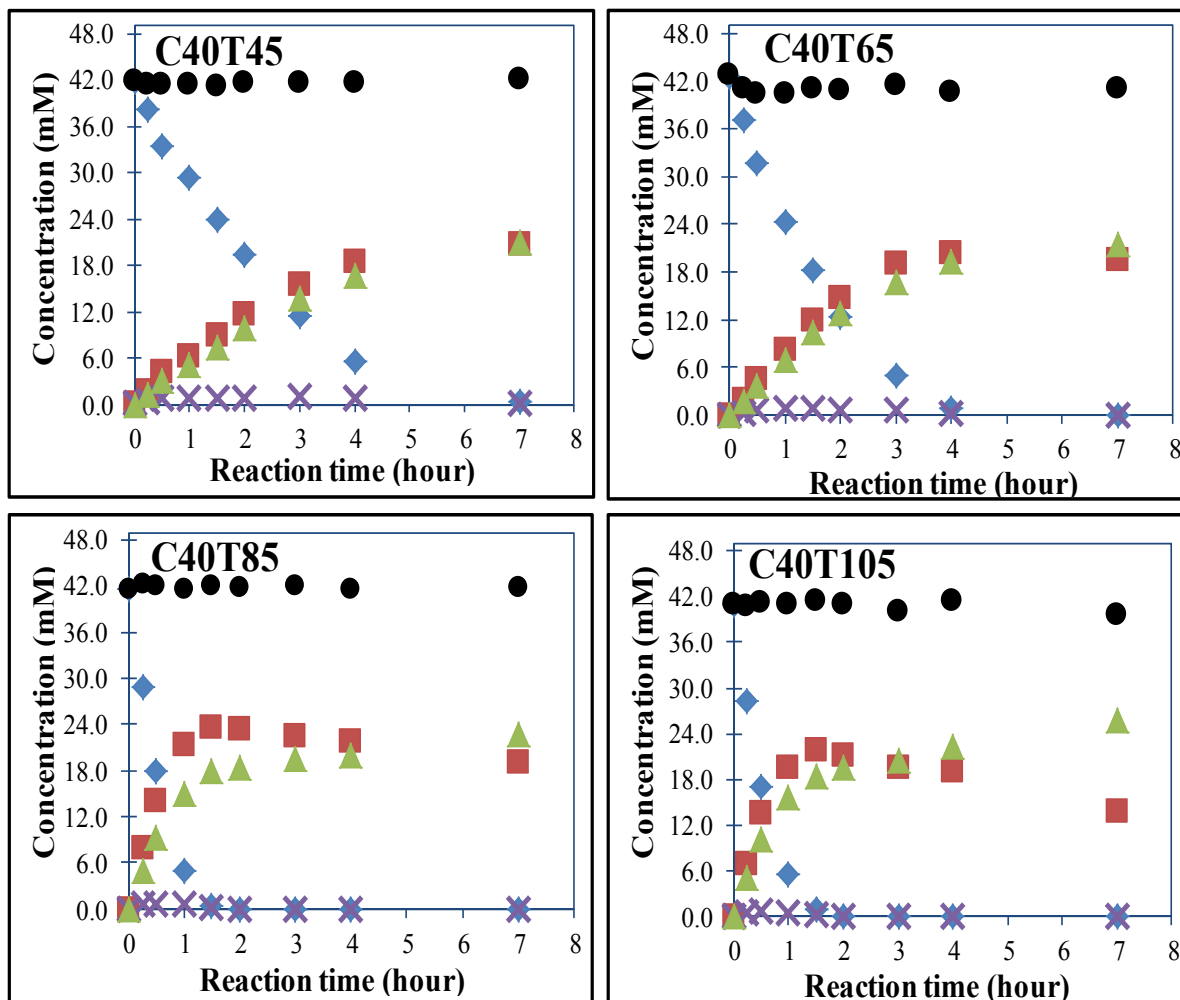


Figure B.4-1 Reaction profiles for CAL hydrogenation over the catalyst Pd50RuF. ● material balance; ◆ CAL; ■ HCOL; ✕ COL; ▲ HCOL. Reaction conditions: $\sim 1.9 \times 10^{-6}$ mole of metal (Ru+Pd) loading in each reaction (see Table 4-5); 35 ml CAL solution in IPA (40mM); $T = 65^\circ\text{C}$; $P(\text{H}_2) = 20$ bar; Stirring speed = 800 RPM. The numbers in C##T65 means the substrate initial concentration for the reaction.

B. 5 CAL hydrogenation over the bimetallic catalyst Pd60RuF

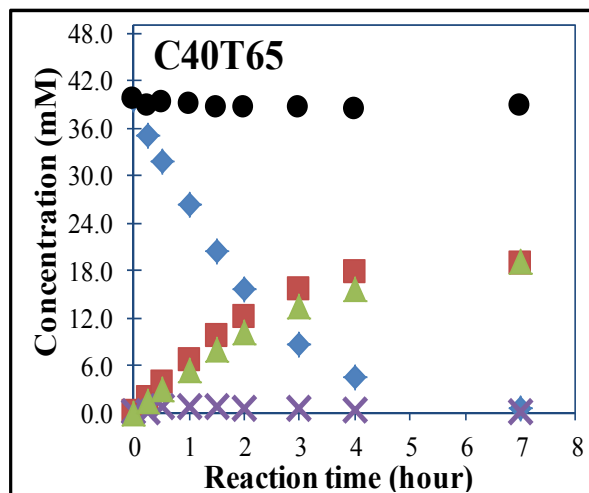


Figure B.5-1 Reaction profiles for CAL hydrogenation over the catalyst Pd60RuF. ● material balance; ◆ CAL; ■ HCOL; × COL; ▲ HCOL. Reaction conditions: 2.0×10^{-6} mole of metal (Ru+Pd) loading in each reaction (see Table 4-5); 35 ml CAL solution in IPA (40mM); $T = 65^{\circ}\text{C}$; $P(\text{H}_2) = 20$ bar; Stirring speed = 800 RPM. The numbers in C##T65 means the substrate initial concentration for the reaction.

B. 6 CAL hydrogenation over the bimetallic catalyst Pd80RuF

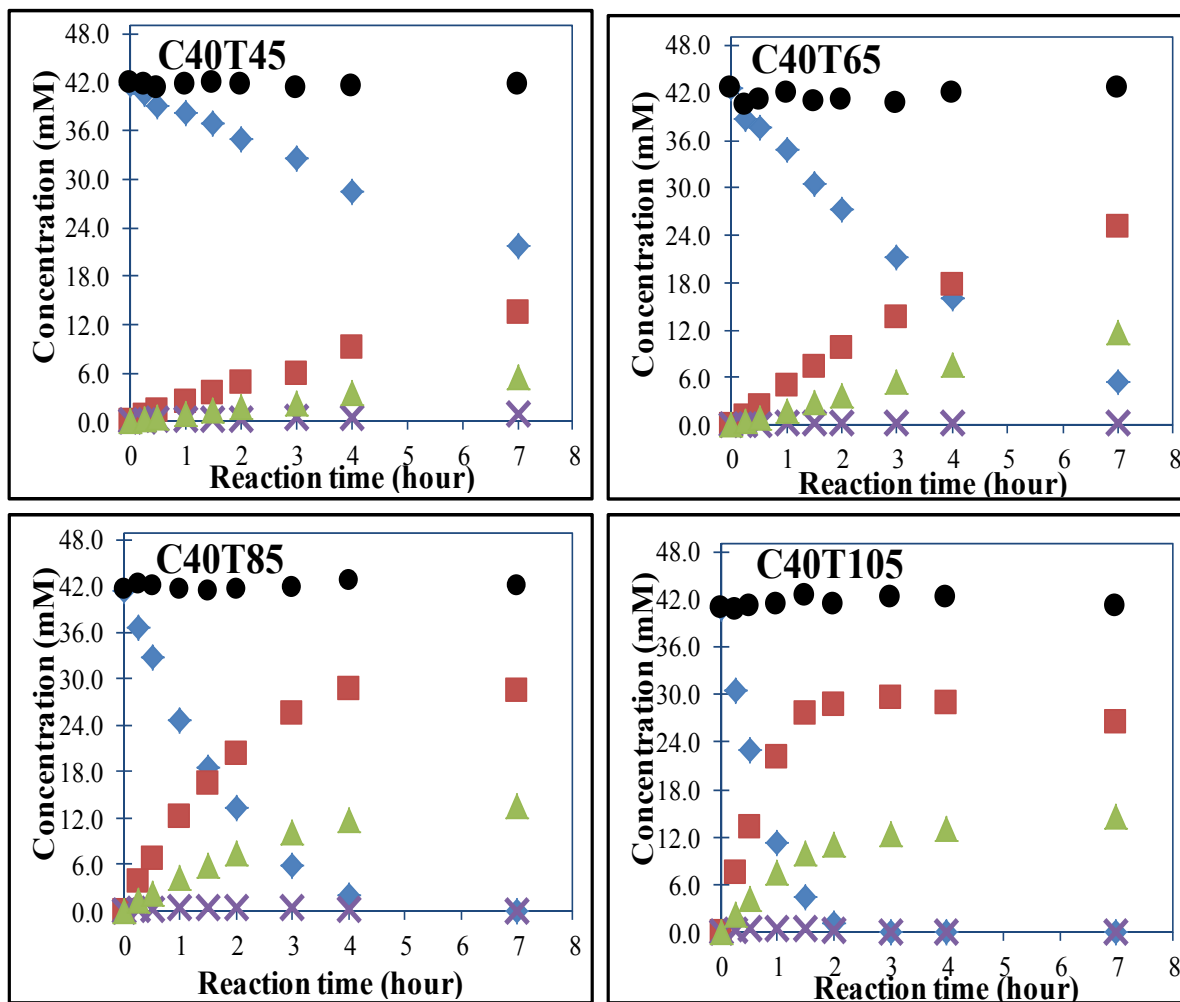


Figure B.6-1 Reaction profiles for CAL hydrogenation over the catalyst Pd80RuF. ● material balance; ◆ CAL; ■ HCOL; ✕ COL; ▲ HCOL. Reaction conditions: $\sim 1.9 \times 10^{-6}$ mole of metal (Ru+Pd) loading in each reaction (see Table 4-5); 35 ml CAL solution in IPA (40mM); $T = 65^\circ\text{C}$; $P(\text{H}_2) = 20$ bar; Stirring speed = 800 RPM. The numbers in C##T65 means the substrate initial concentration for the reaction.

B. 7 CAL hydrogenation over the bimetallic catalyst Pd95RuF

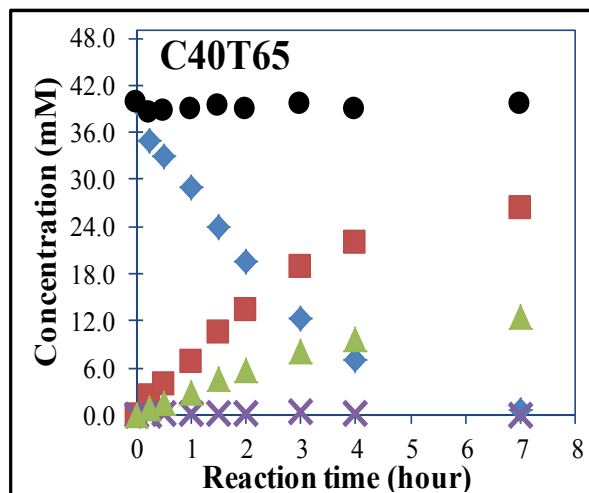


Figure B.7-1 Reaction profiles for CAL hydrogenation over the catalyst Pd95RuF. ● material balance; ◆ CAL; ■ HCOL; × COL; ▲ HCOL. Reaction conditions: 2.0×10^{-6} mole of metal (Ru+Pd) loading in each reaction (see Table 4-5); 35 ml CAL solution in IPA (40mM); $T = 65^{\circ}\text{C}$; $P(\text{H}_2) = 20$ bar; Stirring speed = 800 RPM. The numbers in C##T65 means the substrate initial concentration for the reaction.

B. 8 CAL hydrogenation over the bimetallic catalyst Pd100F

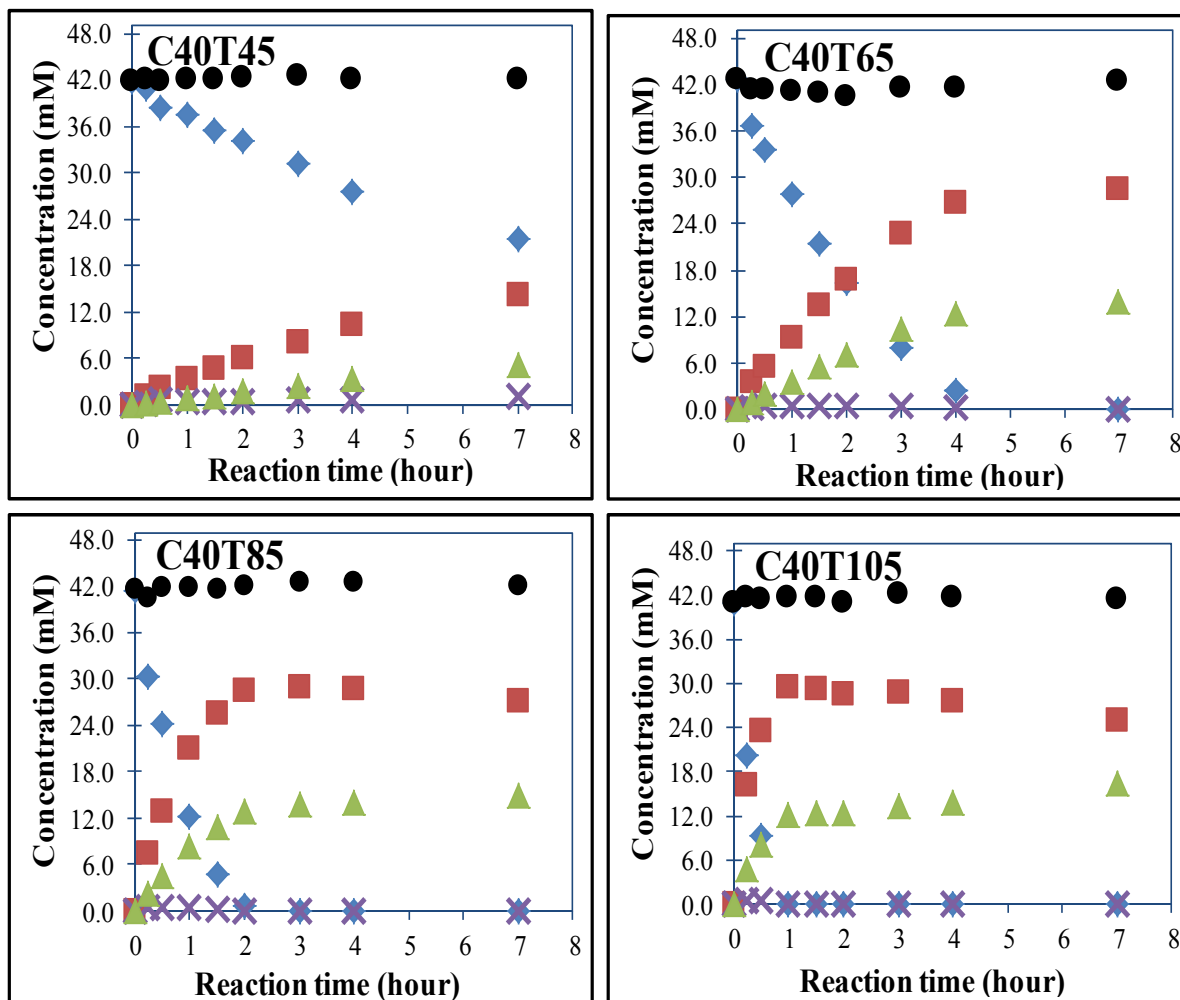


Figure B.8-1 Reaction profiles for CAL hydrogenation over the catalyst Pd100F. ● material balance; ◆ CAL; ■ HCOL; × COL; ▲ HCOL. Reaction conditions: $\sim 1.9 \times 10^{-6}$ mole of metal (Ru+Pd) loading in each reaction (see Table 4-5); 35 ml CAL solution in IPA (40mM); $T = 65^\circ\text{C}$; $P(\text{H}_2) = 20$ bar; Stirring speed = 800 RPM. The numbers in C##T65 means the substrate initial concentration for the reaction.